Department of Engineering, University of Leicester

PhD Thesis

This report is submitted in fulfilment of requirements for the degree of Doctor of Philosophy in Electrical Engineering.

Electromagnetic Characterisation and Modelling of Superconducting Wires and Coils for Engineering Applications

Bright Chimezie Robert

Department of Engineering, University of Leicester

June 2020

The law of his God is in his heart;
none of his steps shall slide

– KJV Bible.

Abstract

This thesis contributes to the broad understanding of the macroscopic electromagnetic behaviour of type-II superconducting wires (SC) under alternating and direct current (AC-DC) conditions, and the electromagnetic modelling of the second generation of high temperature superconducting (2G-HTS) coils for racetrack and pancake settings. In the first part, a comprehensive study of the effects of applying an AC transverse magnetic field to a type-II SC wire utilised for DC power transmission is presented. Likewise, the electromagnetic response of an AC superconducting wire that is simultaneously exposed to constant source (DC) of a transverse magnetic field has been analysed. Then, the second part deals with the study of the physical dependence of the hysteresis losses with the axial winding misalignment of superconducting racetrack and pancake coils subjected to AC applied transport current, made of commercial 2G-HTS tapes, which is a useful measure to understand the electromagnetic quantities of interest and the influence it could have on the coil performance in practical superconducting machines. Furthermore, the study is concluded with an exhaustive analysis of the impact of the material law selection on the numerical modelling of 2G-HTS tapes, which has allowed to establish a set of decision criteria that aims for the advising of computational modellers on what would be the most suitable material law in cases where, the need to quantify an electromagnetic quantity does not only depend on matching the experimental evidences, but where time and computing power are valuable resources to take into consideration. In summary, the undertaken studies focused on the local understanding of the physical properties of the wires and coils modelled, such as, the distribution of current density, the resulting magnetic flux, magnetic moments, and the AC-losses, where the findings can be used as a practical benchmark to understand the electromagnetic features of superconducting wires under such AC-DC conditions, and the inherent physical characteristics of any 2G-HTS racetrack or pancake coil for engineering applications.

Acknowledgments

The author would like to thank Dr. Harold Ruiz for his remarkable guidance, confidence, and support provided on this project. The assistance rendered with the installations of software, the purchase of a state of the art CPU for the exclusive use of this project, code development, and analysis of results is appreciated.

The author acknowledged the use of the high performance computing cluster facilities (ALICE) provided by the University of Leicester.

I also would like to thank the Niger Delta Development Commission (NDDC) scholarship scheme award of partially funded Ph.D. studies for three years.

I acknowledge the support of the east Midlands energy research accelerator (ERA) throughout the conferences and workshops attended that contributed to the contents of this thesis.

My sincere gratitude is deeply expressed to my family for their continuous support, my friends, and prayer power network (PPN) for their encouragement during these studies.

Thanks to the Student welfare service at the University of Leicester for their financial support for a family bereavement and COVID-19 pandemic.

I authorize to the University of Leicester for the distribution and reproduction of this report at internal level. Other uses beyond the ones considered for internal assessment of this report are not permitted, unless discussed with the author and agreed upon.

Contents

List of Figures

Preface

In the early 1900s, Heike Kamerlingh Onnes discovered the liquefaction of helium which facilitated the investigation of electrical resistance of metals at very low temperatures, leading in 1911 to the discovery of the superconductivity phenomenon, firstly observed in Mercury (Hg). It was the purest metals available at that time on which, below a cryogenic temperature of nearly 4.2 Kelvin ($-268.95\ ^\circ C$), it exhibited a sudden disappearance of its electrical resistivity. Then, within the continuous endeavours to ascertain other materials that show the phenomenon of superconductivity at suitably low temperature, in 1933 Walther Meissner and Robert Ochensenfield, found two different type of superconductors while investigating the behaviour of the magnetic properties of these materials under an external applied magnetic field, which has rendered the classification of what nowadays are called type-I and type-II superconductors.

On the one hand, type-I superconductors (SC-I) displayed full expulsion of the magnetic field, which is a remarkable characteristic of diamagnetism known as the Meissner effect. On the other hand, when the magnetic field penetrates the superconducting material, a mixed state of resistive (normal) and superconducting domains called vortex state, describes the distinctive characteristics of what are known as Type-II superconductors (SC-II). Therein, it is possible to evince a transition from the superconducting state to the normal state that allows the penetration of magnetic flux inside the SC sample via the formation of quantum vortices of magnetic flux. The vortex phenomenon in such SC samples make it possible for them to withstand strong magnetic fields, and therefore allow considerably higher current densities before losing its superconducting properties (quench). Therefore, these macroscopic magnetic properties in the mixed state are what makes the SC-II useful to be extensively considered in present-day applications to increase the electric transport current with

minimal loss of energy for significant applications in the technological and industrial sectors aided by the design of superconducting machines. In this sense, it is essential to understand the macroscopic electromagnetic behaviour of type-II superconducting wires exposed to alternating current (AC) and/or direct current (DC) conditions, in particular in the case of DC power transmission lines, since these systems will have to share the right of way of the existing AC network, to reduce the overall costs associated with the development of the superconducting cables.

Therefore, the first part of this thesis aims to present a comprehensive study of the effects of applying an AC transverse magnetic field to a type-II SC wire of rounded cross-section it utilised for direct current power transmission, which is captured under the theoretical framework of the critical state model and the numerical solution of Maxwell equations in the magneto quasi-steady approach. Therein, we disclose the local dynamics of the flux front profile of current density, the resulting density of magnetic flux, the total magnetic moment of the wire, and the curve of AC losses for different conditions of DC and transverse AC magnetic field, from which their analysis shows that our numerical results can be employed as a useful benchmark for determining the minimal losses and magnetic impact of DC SC lines subjected to external oscillating magnetic fields. Also, our results are compared with simplified analytical approaches, demonstrating the importance of considering the concomitant action of direct current and AC magnetic field by the use of numerical methods. The other significant findings include the influence of the direct current on virgin and premagnetised SC wires, and the most relevant characteristics on the magnetisation profiles of the SC wire, which evinced the identification of striking Boolean-like magnetic moments. For completion of the studies in part I of this thesis, a similar case was considered but analysing the effect of an AC transmission line of cylindrical cross-section, made of a type-II superconductor with critical current density J_c, that is simultaneously exposed to a constant source (DC) of a transverse magnetic field, and knowing the magnetisation features and AC-losses in such a system is relevant to understand the electromagnetic response of AC superconducting wires subjected to a constant source condition. We also report observations from the the local dynamics of current density of AC SC wires immersed in a constant transverse magnetic field, which has allowed us to define an adequate benchmark for the implementation of flux-tracking approaches in other 2D symmetries, such as SC strips, where the flux-front profile for isolated excitations can be formulated by exact geometrical expressions.

On the other hand, a reasonable number of superconducting wire manufacturers have moved to the development of second-generation high-temperature superconducting coils (2G-HTS) with rare-earth barium-copper oxide (REBCO)-

coated conductors, it due to the enormous progress in the technology of thin films and its fabrication. It offers higher transport current and magnetic field capability, presently considered as the most efficient and resilient technology for upgrading the existing electric power grid applications. Therefore, the formulation of modelling tools for describing the local electromagnetic and thermal properties of such 2G-HTS tapes and their use in high-power-density coils such as, but not limited to superconducting fault current limiters, transformers, power generators, industrial superconducting motors, permanent magnets, energy storage systems, and magnetic imaging machines, results of utter importance. These characteristics have now inspired the community of applied superconductivity for further exploration concerning the characterisation, electromagnetic modelling, and the physical and material understanding of the underlying superconducting arrangements, such as the optimal designing of superconducting coils and their integration in diverse superconducting technologies is achievable. Likewise, this understanding will improve their efficiency whilst reducing costs related to the use of conventional copper electromagnets in various kinds of electric power devices and the power grid.

In this sense, this has motivated the second part of this thesis which deals with the study of the physical dependence of the hysteresis losses with the axial winding misalignment of 2G-HTS racetrack-shaped and pancake-shaped coils, both subjected to an AC applied transport current, highlighting the influence this phenomena could have on the performance of practical superconducting machines. In particular, it discloses the effect of prospective winding misalignment factors in the macroscopical quantities of interest such as the hysteresis losses, magnetic field, and critical current density inside each turn of a typical 2G-HTS coil. Also, this part of the thesis unveils a comprehensive study of the impact of the material law selection on the numerical modelling of 2G-HTS tapes, which presents decision criteria aimed to advice computational modellers concerning adequate regimes for the material law selection.

This thesis aims to contribute to the understanding of the macroscopic electromagnetic behaviour of type-II superconducting wires exposed to AC-DC conditions and the electromagnetic modelling of 2G-HTS coils for racetrack and pancake settings. The thesis has been structured in two parts, with the following chapters devoted to present an exhaustive analysis of the fundamental electromagnetic properties of the abovementioned superconducting wires and coils from a macroscopic perspective, i.e., focused in the distribution of current density, magnetic field, and the AC-losses in such devices, systematically increasing the level of complexity from the computational point of view, associated to the underlying electromagnetic phenomena.

Chapter 1 aims to introduce a brief history of the superconductivity phe-

nomenon, and the fundamental theoretical background associated to the numerical methods that describe the electromagnetic properties of type-II superconductors, primarily captured by Bean's model. It reviews the classical statements of the critical state theory and electromagnetic problems in SC-II caused by free boundaries. It addresses an integral computational approach by introducing the Lagrangian for electromagnetic fields in infinitely long SC wires, i.e., formulating a 2D minimisation objective functional that reviews the general statements of variational theory and derived approaches for solving nonlinear minimisation problems within the general critical state theory for applied superconductivity.

In Chapter 2, the formulation abovementioned is applied on a rounded superconducting wire under different experimental scenarios, aimed to reproduce realistic conditions where a DC SC-II wire is subjected to the concomitant action of an external transverse oscillating (AC) magnetic field. The problem is then solved via *Lancelot*©, a software developed for large and nonlinear constrained extended Lagrangian optimisation techniques, aided by MatLab® for the handling and post-processing of data. The implemented sequence of steps allows the calculations of all the macroscopic electromagnetic quantities of interest without the need to include any arbitrary approaches or flux boundary condition for the practical solutions of SC-II under AC or DC conditions. For completeness, two cases are presented: a magnetically virgin DC SC wires under transverse AC magnetic field is analysed, and secondly a premagnetised DC SC wire under transverse AC magnetic field is considered for comparison. The numerical results obtained can be used as a useful benchmark for determining the AC losses and the influence of external oscillating magnetic fields exerted on SC-II DC wires. In particular, it reveals the dynamics of profiles of current density, the resulting magnetic flux and the magnetic moments, and the actual hysteretic AC losses of the wire. In addition, the results were compared with the simplified semi-analytical approaches of Gurevich et al., which demonstrated the importance of numerical methods when taking into account the simultaneous action of DC and AC magnetic fields. It unveils that the use of empirical or semi-analytical equations can underestimate the actual energy losses of a system, especially at low values of the applied magnetic field showing relatively small penetration of the profiles of current density, in comparison with the intensity of the transport current being applied. Likewise, this chapter analyses the effect of considering an AC power transmission line composed by a SC-II wire which is simultaneously subjected to a constant (DC) magnetic field. The observed electromagnetic features constitute semi-analytical approaches of flux-tracking for the dynamics of current density carrying an alternating transport current exposed to a constant magnetic field applied to a rounded superconducting wire. Also, the reported observa-

tions describe a suitable benchmark for the implementation of flux-tracking methods, in the case where the formulation of the flux-front profile for isolated excitations is not possible by exact geometrical expressions.

On the other hand, in the Part II of this thesis, Chapter 3 reviews the theoretical framework, computational conditions, and modelling strategy invoked for the numerical simulation of the 2G-HTS racetrack and pancake coils, either with or without winding misalignment features in the cross-section of a 20-turn superconducting coil, wound on a 5 cm mid-width former with a SuperPower Inc. surrounded copper stabiliser (SCS)-4050 tape. In detail, the numerical simulations were performed within the magneto quasi-steady approach, but using the numerical solution of the Maxwell equations under the theoretical framework of Kim's critical state model, extended to consider the magneto angular dependence of the in-field critical current for commercially available 2G-HTS tapes. Thus, Chapter 4 deals with the study of the physical dependence of the hysteresis losses with the axial winding misalignment of superconducting racetrack and pancake coils subjected to AC applied transport current, made of commercial 2G-HTS tapes. It is a useful measure to understand the electromagnetic quantities of interest of such coils in conditions, where it is possible to evince factors that alter the axial alignment between each turn of the wound coil and the influence it could have on their performance in practical superconducting machines. The turn-to-turn misalignment likelihood is conceivable either during the manufacturing of such coils or in their installation in real engineering applications, as well as in situations where coil deformations can be caused by electric shock, thermal, or mechanical pressure during fault events. The comprehensive analysis of the results disclosed in this chapter describes the influence of possible coil wound misalignments on the local electromagnetic properties of individual turns, which can be used as a benchmark to understand the physical characteristics of any 2G-HTS racetrack or pancake coil application under such experimental conditions.

Finally, Chapter 5 addresses a comprehensive study on the impact of the material law selection in the numerical modelling and analysis of the electromagnetic properties of SC-II racetrack coils, using a 2D H-formulation and other experimental conditions relevant to the solution of this problem. In particular, an evident influence of the magneto-anisotropic properties of the superconducting coil was revealed by directly comparing four different prevalent superconducting material law models, including the isotropic critical-state-like model, and three diverse versions of magnetically anisotropic model, namely as: the classical Kim's model, an empirical Kim-like model with perpendicular field dependence, and finally the magneto-angular anisotropic dependence of the in-field critical current density experimentally measured for SuperPower 2G-HTS tapes. The study focused on the similarities and differences between

the different material laws, by analysing the local distribution of current density inside different turns of the superconducting coil. It discloses intriguing features of the magnetic field near and over its innermost turn, and shows the calculated AC losses over the entire range of applied transport current ($I_{tr} \leq I_{c0}$), which allows to present certain decision criteria aimed to advice computational modellers on what material law is the most appropriate, in cases where the need to quantify an electromagnetic quantity does not only depend on matching the experimental evidences, but where time and computing power could be an impeding factor to render a numerical solution

Each one of the two parts in this thesis have its own introduction and conclusion sections, this with a combined list of references for the reader's convenience. It includes a comprehensive analysis of the results disseminated in peer-reviewed scientific journals, which are listed in the Appendix 5.3. The author expects that the reader will find this thesis a relevant contribution to the prevailing knowledge in applied superconductivity, attracting a broad community of physicists, engineers, and other scientists active in the exciting field of applied superconductivity.

May 2020, Leicester - UK.

Part I

Electromagnetic Modelling of Type-II Superconducting wires Exposed to AC-DC Excitations

The usefulness of type-II superconductors in technological applications is related to the local electromagnetic response of the superconductor under transverse magnetic field and different conditions of transport current, with very low but no negligible hysteresis, i.e., power dissipation [1]. Type-II superconductors are expected to be extensively used in the designing of direct current (DC) and alternating current (AC) applications due to its high transport current capability, nearly-zero resistive losses, and reduced use of space required for their application. However, despite the numerous successful demonstrations of HTS applications in areas such as electric power utilities, naval ship systems, industrial applications, wind turbines, electric aircraft systems, and else others [2–8] there has been slow commercial adoption of these technologies due to market acceptance and non stablished competitive prices against the most conventional approaches [3, 9]. Nevertheless, there has been major progress on the application of HTS cables for AC and DC power transmission, enabling the creation of the next generation of resilient power grids across different countries (see Figure 1) [10–18, 18–20]. These include the development and installation of a 2.5 km HTS DC cable in St. Petersburg electrical grid [21, 22], and the AmpaCity project in Germany consisting of the installation of a 10kV 40MVA HTS cable in the city of Essen, replacing their conventional 110 kV cables [23]. In more recent time, other projects such as the Icheon substation and Jeju power system projects in Korea, have successfully realised the installation of a 410 m length AC 22.9 kV 50 MVA-class HTS power cable core in 2010, and the installation of 101 m 80 kV 500 MW HTS DC cable in 2014, as part of the endevours taken by the Korean Electric Power Corporation (KEPCO) power grid [24–27]. Following the successful demonstration of these projects, KEPCO in 2017 launched the Shingal Project "world's first" to commercialise AC 23 kV HTS cables for actual grid, in existing underground utility tunnels connecting two substations, which was due for completion in July 2019 [15].

These recent progresses intend to meet near future's need for electricity in densely populated cities across the world, such as in Korea, UK, Russia, USA and so on, by replacing the existing power network of conventional class underground cables for high efficient and stabilised bulk transmission. In this sense, type-II superconductors are expected to be extensively used in the designing of DC and AC power grids due to its high transport current capability, nearly-zero resistive losses, and reduced use of space required for their application. Its usefulness to retrofit conventional cables is related to the local electromagnetic response of the superconductor under transverse magnetic field and different conditions of transport current, with capability to transmit high power at low voltage [1, 28]. However, these systems are likely to be integrated into the existing installed AC network, making it conceivable for HTS AC and DC

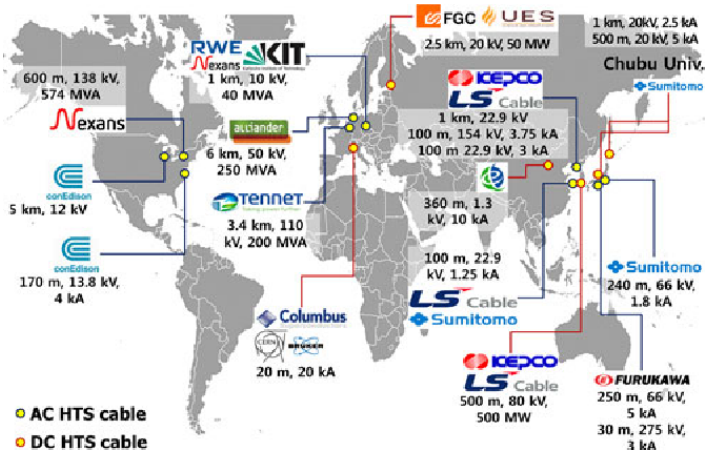

Figure 1: Overview of HTS power transmission cable projects worldwide [14].

power transmission cable to share the same duct connection to the power grid in real applications [14], which will reduce the costs of development linked to the superconducting cables without the need for increasing the right of way, given the severe restrictions that the right of way policies imply [29, 30]. Under these AC-DC conditions, the understanding of the electromagnetic response of the DC superconducting (SC) wires become cumbersome, as the added external magnetic field magnetises the wire with power losses increasing after each cycle. Therefore, it becomes crucial to understand the main parameters contributing to the hysteretic losses in superconducting wires subject to AC and DC conditions, and the impact that simultaneous field and transport current could carry under practical configurations, which could advise in the design of new kinds of applications for next generation power grid connections.

To begin, the sequence of steps depicted in the simplified flow chart presented in figure 2 illustrates the numerical method employed in Part I of this thesis. It shows a comprehensive study of the effects of applying an AC transverse magnetic field to a type-II SC wire of rounded cross-section, it utilised for direct current power transmission. Presented are the effects of considering a simultaneously exposed DC or AC transmission line of cylindrical cross-section and AC or DC transverse magnetic field, respectively. The theoretical framework of the critical state model, the computational approaches derived from the J-formulation, and the numerical results of this study can be used as a useful benchmark for the implementation of DC or AC transmission lines un-

der share of right of way conditions. This practical structure determines the maximum value of current dissipation, i.e., AC losses, under different practical configurations to understand the electromagnetic response of interest that such wires can offer under real situations.

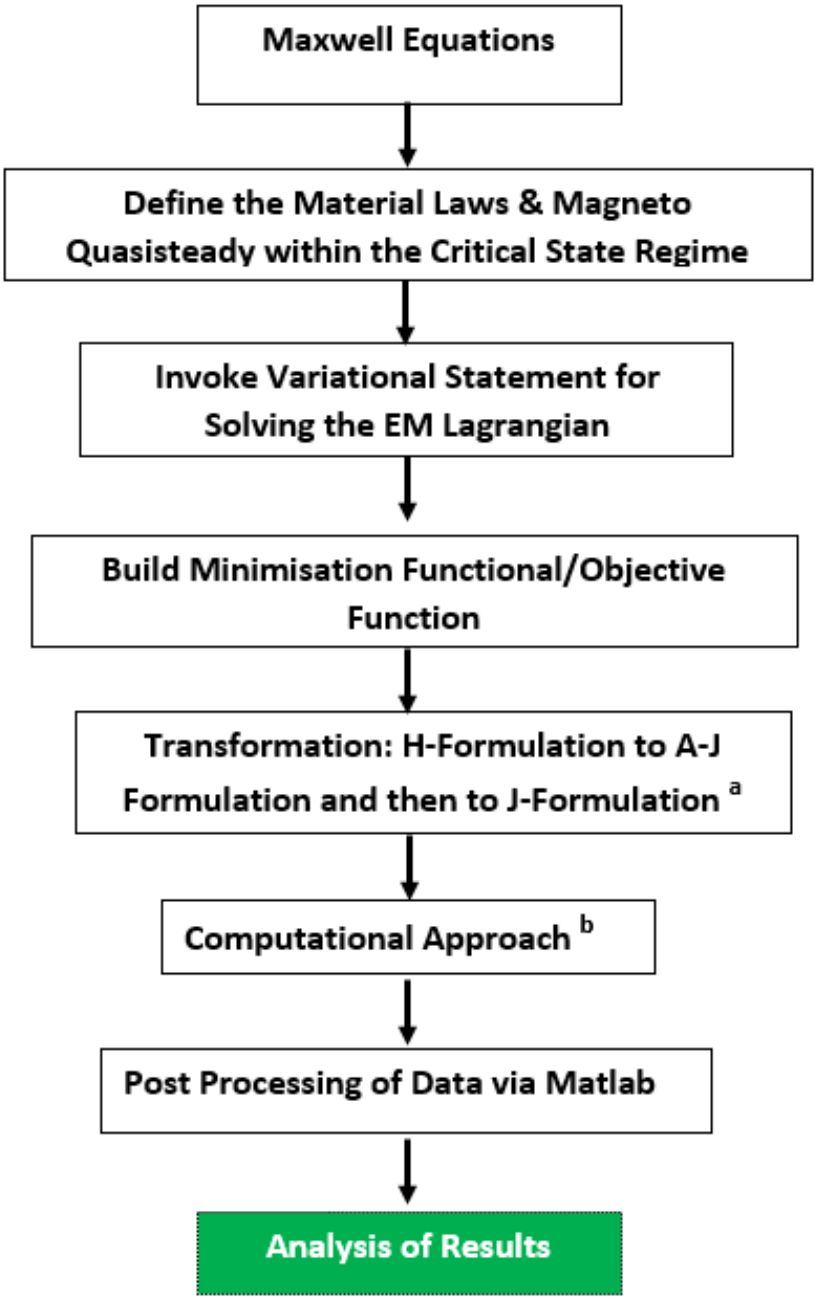

Figure 2: Simplified flow chart illustrating the overview of the numerical approach presented in Part I. [a] J-formulation enables a local integral solution of the Maxwell equation. [b] LANCELOT © was employed for the minimisation of the objective function.

Chapter 1

Introduction to applied superconductivity

In the early 1900s, Heike Kamerlingh Onnes discovered the liquefaction of helium which helped him to investigate the electrical resistance of metals at very low temperatures. At that time, the behaviour of the electrical resistance was predicted to decrease exponentially with temperature due to the scattering mechanism of individual electrons following the classical results of George Ohm (see Figure 1.1 (a)). However, after two decades, Onnes discovered the phenomenon of superconductivity [31], first observed in Mercury (Hg). It was cooled to a temperature of about 4.15 Kelvin ($-268.95°C$) to investigate the electrical resistance of such metal at extremely low temperatures, showing that below a cryogenic temperature of 4.2 K, mercury transits to a new state with almost negligible electrical resistance by showing a sudden drop from 0.1 Ω to less than 10^{-6} Ω, within a temperature gradient of just 0.01 K (see Figure 1.1 (b)). The residual resistivity was lowered by purifying metals such as, platinum, gold, and copper, which were better conductors at room temperature compared to mercury. However, the findings show that the residual resistivity of metals at a low temperature slightly depends on the purity level of the sample.

Concerning non-superconductors (normal metals), the resistivity increases with the rise of temperature as atomic vibrations in the material become intense, making them an obstacle to the free motion of electrons (electric current). Nevertheless, the understanding of the microscopic mechanisms governing the motion of electrons in the superconducting state resulted more complex than expected because the sudden drop of the electrical resistivity at a specific temperature, called the critical temperature of the material, T_c, could not be explained under the framework of classical theories.

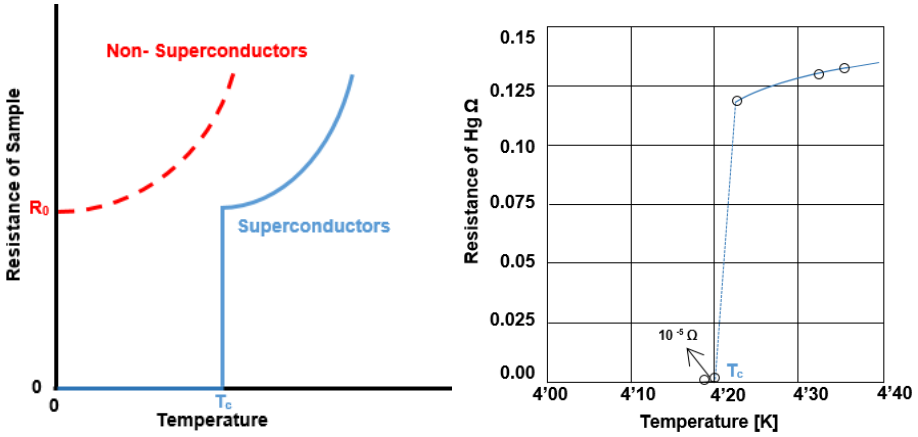

(a) (b)

Figure 1.1: (a) Expected behaviour of the electrical resistance in non- superconducting materials according to Ohm's law (red line), compared with the superconducting phenomena (blue line), and (b) experimental evidence for the occurrence of superconductivity in Mercury (Hg) at 4.2 K [31].

Although the physical understanding of the microscopic mechanisms underlying the theory of superconductivity is beyond the scope of this study, it is worth mentioning that the only accepted theory for the dynamics of electrons in the superconducting state (Cooper pairs) is the well-known BCS theory introduced in 1957 by the Nobel laureates J. Bardeen, L. N. Cooper and J. R. Schrieffer [32], which is a theory that relies on advanced concepts of quantum mechanics only applicable in a first approach, to pure metals like Mercury (Hg) and Lead (Pb). However, the phenomenon of superconductivity was also discovered in metal alloys such as Hg, Au, Sn, Pb, and PbSn, leading to a world competition for the search of more practical superconductors for engineering applications. For many years, endeavours have continued to discover other materials that exhibited the phenomenon of superconductivity at suitably low temperature. In the process, the German physicists Walther Meissner and Robert Ochensenfield investigated the behaviour of the magnetic properties of superconductors in applied magnetic field [33], finding that two different types of superconductors exist, namely type-I and type-II superconductors. The first exhibited striking diamagnetic characteristics, i.e., the expulsion of the magnetic field, and this phenomenon is known as Meissner effect, which is more obvious in type-I superconductors (see Figure 1.2), and the latter, the quantisation of magnetic flux (see Figure 1.3). Thus, the occurrence of the Meissner effect defined the introduction of a new critical parameter of the superconducting material, besides its critical temperature, T_c, where the material can lose its superconducting properties if the applied magnetic field exceeds its

critical magnetic field strength, H_c. The perfect diamagnetism of type-I superconductors implies the total expulsion of the magnetic field flux applied to the superconductor from the inside of the SC sample, with a maximum observable penetration length of the order of a few nanometres ($50 - 500\ nm$), called the London penetration depth, λ_L. It may be understood as the distance where the intensity of the applied magnetic field exponentially decays to zero from the external surface of the superconductor. Then, if the applied magnetic field exceeds the critical field H_c, the superconductor experiences a thermal quench, i.e., the transition from the superconducting state to the normal state.

Figure 1.2 (a) illustrates the behaviour of a superconductor (type-I) in an applied magnetic field H_a via two different routes, Zero Field Cooling (ZFC) and Field Cooling (FC). In the first, ZFC, the transition of the sample (a1) occurs at (b1) below the critical temperature T_c, with the magnetic field H_a applied at (c1), resulting in the occurrence of the diamagnetic behaviour. At this instant, if the applied magnetic flux density is removed or dropped to zero, it will show no evidence of trapped magnetic field contrary to what happens with a type-II superconductor. In this case, for a field $H_{c1} \ll H_a < H_{c2}$, a type-I SC shows the occurrence of magnetic vortices that generates a macroscopic pattern of magnetic flux lines comparable to the illustration of a perfect conductor (g2), if the SC is fully penetrated by the external magnetic field. It can be observed that it is not conceivable to discern (macroscopically) between a type-I superconductor and a perfect conductor during the ZFC route. It is because, in the hypothetical perfect conductors, there are no joule losses or dissipation of energy as a result of the zero electrical resistivity ($\rho = 0$). Therefore, by the principle of conservation of energy, the Maxwell-Faraday equation ($\nabla \times \mathbf{E} = -\partial_{\mathbf{t}}\mathbf{B}$), and Gauss's law ($\nabla \cdot \mathbf{E} = \rho/\epsilon_{\mathbf{0}} = \mathbf{0}$), any gradient of the magnetic field inside the SC is forced to produce a zero electrical field. Consequently, it is not conceivable to see lines of the magnetic field inside a perfect conductor in the ZFC condition. Because of this, it is not possible to see any trapped magnetic field inside the material described as a perfect conductor after dropping H_a back to zero. This phenomenon is macroscopically similar to the Meissner effect. However, type-I SCs are known to experience slight a penetration of the magnetic field that is not in agreement with the concept of a perfect conductor.

Moreover, by performing the same analysis under the FC condition, a more explicit way to visualise the difference between a type-I SC and the concept developed for perfect conductors can be achieved. For instance, in Figure 1.2, it can be noticed that the Meissner effect within type-I superconductors are always exhibited when $H_a < H_{c1}$. However, the concept of an ideal conductor implies that the original magnetic field inside the material must be kept locked even after the transition $T < T_c$, because no gradient of the magnetic field

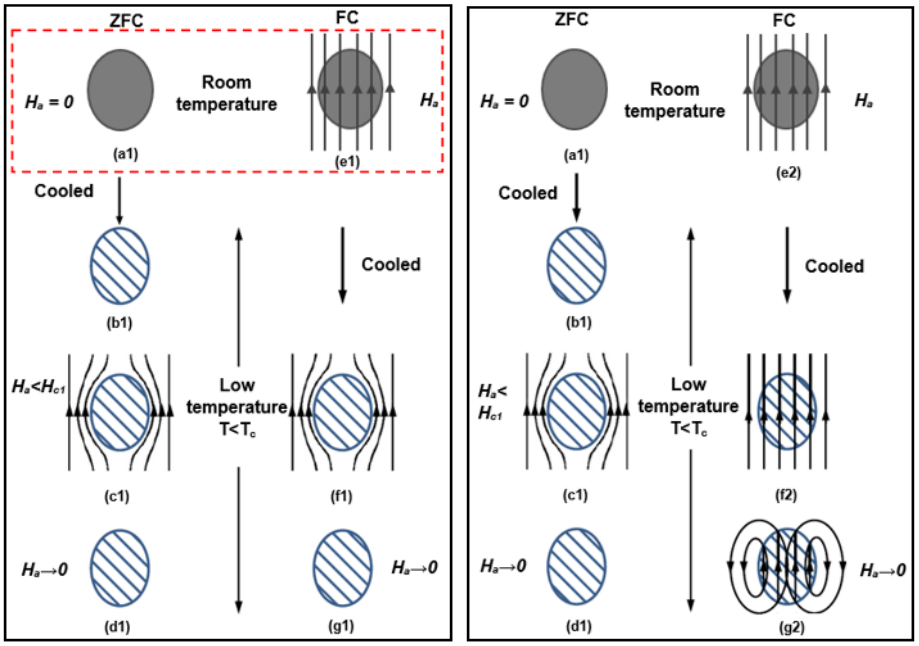

(a) (b)

Figure 1.2: Normal behaviour of (a) type-I superconductor, and (b) perfect conductors also known as ideal conductors, both in the presence of applied magnetic field and different temperatures. Illustrated are the Zero field cooling (ZFC) and Field Cooling (FC) conditions [34], with the behaviour of normal metals illustrated within the dashed red box.

could occur to keep with the condition of $\rho = 0$ and, at the same time preserve the overall integrity of Maxwell equations.

On the other hand, type-II superconductors allow the penetration of magnetic flux inside the sample through quantum vortices (see Figure 1.3 (a)). The occurrence of the vortex phenomenon was explained in 1957 by Soviet physicist, A. A. Abrikosov, who predicted that quantised amounts of magnetic flux were confined into vortex states inside the type-II superconductors, aligned parallel to the direction of the external magnetic field and arranged into triangular or hexagonal arrays of fluxons [35]. They appear when the external magnetic field strength reaches the lower critical field H_{c1}, penetrating the SC material from its surface towards its geometrical centre as the intensity of the applied magnetic field increases. These vortex states account for the interactions between the magnetic flux lines and the crystal lattice averaged by a flux pinning mechanism which controls the motion of vortices, occurring between the lower critical field H_{c1} and the upper critical field H_{c2} as shown in Figure 1.3 (b), after which the transition to the normal state occurs either by thermal acti-

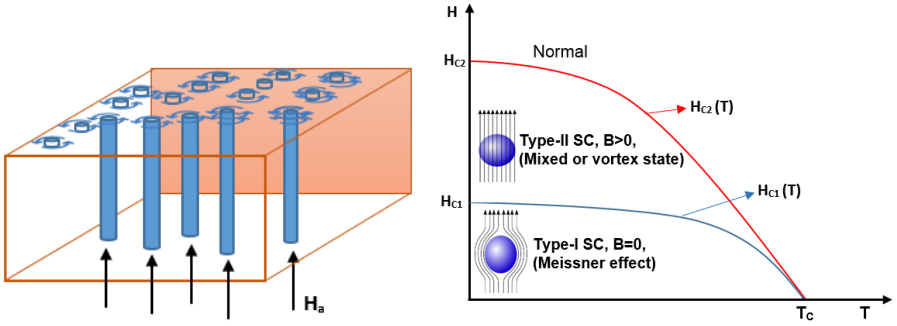

(a) (b)

Figure 1.3: (a) Illustration of the mesoscopic view of magnetic field penetration in the form of fluxons when a magnetic field H_a is applied to a type-II superconductor, and (b) shows the phase transition of type-I and type-II superconductors under external magnetic field as a function of the temperature.

vation of vortices leading to the phenomenon of flux creep or flux flow, or the direct destruction of cooper pairs.

However, within a macroscopical approach, the array of vortices can be assumed as a bundle of vortices located where macroscopic elements of the current of a size comparable with the dimensions of the sample occur. Consequently, the total amount of vortices inside the SC is averaged in a manner that the total amount of current and magnetic field that the SC material holds, before its transition to the normal state, gives the account of the existence of bundles of vortices. Moreover, the vortex in a superconducting sample can be understood as a circulating eddy current interacting with another current or with a magnetic field along its perpendicular axis, and parallel vortices repel [36]. Therefore, the applied transport current in the sample interacts with the vortices and moves them, as a result of the repulsion (Lorentz) force that occurs between them.

The different mechanisms that characterise the vortex motion in a type-II SC sample include (1) Flux pinning: gives place to the penetration and creation of vortices inside the SC sample, (2) flux creep: slight but controllable motion of vortices, (3) flux flow: uncontrollable motion of vortices and loss of SC properties, and (4) flux cutting: this is when the magnetic field is parallel to the direction of the current and can lead to entanglement and collapse of vortices inside the SC sample [37, 38]. However, this study considers only cases where neither flux flow nor flux cutting happen, either by the magneto quasi-steady approach or the symmetry of the problem. Thus, under the critical state condition which will be explained below, the macroscopic magnetic properties of type-II superconductors in the mixed or vortex regime will be studied.

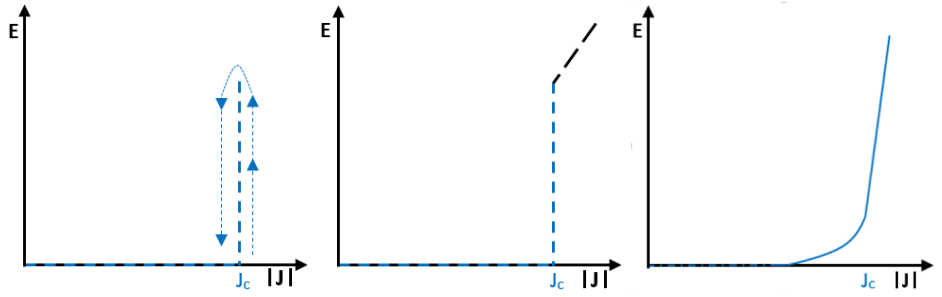

(a) (b) (c)

Figure 1.4: Illustration of the electric field law by the Bean's critical state model, with the curve in (a) illustrating the transient behaviour for $E(J)$ in a type II superconducting material, (b) the ohm's law statement for the transition to the normal state when $J > J_c$ (black dashed lines), and (c) a power law approach for reproducing the physical understanding of the CS regime for modelling the superconducting state.

1.1 *General Statements of the Critical State*

Charles Bean was the first to introduce the critical state model (CSM) in 1962 capturing the macroscopic magnetic properties of type-II SCs in the mixed or vortex state [39]. Bean proposed this model through the minimal complex mathematical equations [40] for one-dimensional samples (slabs), with extended principles to 2D symmetries (infinitely long wires of finite cross-section) like the case of SC wires. The problem can be extended to consider the concomitant action of a transverse magnetic field and longitudinal transport current where no analytical solution is possible. It recurs to the development of diverse numerical methods for describing the irreversible magnetisation of type-II superconductors. Following the Faraday's law of electromagnetic induction, in a perpendicular external magnetic field, macroscopic magnetisation currents of density J are induced inside a superconducting sample during time variations of the magnetic flux. The magnetic field penetrates the superconducting body in the form of superconducting electron current vortices, from the outer surface inwards of the SC as H_a increases with $H_{c1} < H_a < H_{c2}$ [41]. The magnetisation depends on the density of vortices, where each magnetic vortex transports the same quantity of magnetic flux, i.e., flux quanta. In the Bean's model framework, the forces pinning the vortices to sample inhomogeneities and the balance between the electromagnetic driving forces, both determine the distribution of vortices in type-II SCs. The varying external magnetic field causes the magnetic vortices to penetrate the SC sample into a metastable

state, such that small gradients of H_a allows the pinning of the entire network of vortices once more, resulting in the re-establishment of thermal equilibrium of the system during the transients between the flux creep to the flux pinning state. In other words, the system rapidly adapts itself to the oscillating external conditions due to the fast motion of the unpinned vortices. Therefore, a magneto quasistationary model which states that the occurrence of new vortices is achieved only at the regions of a distribution of current density where $J = \pm J_c$ appears.

The current density vector **J** (oriented in perpendicular direction to the magnetic field vector **B**) can only equal the specific critical value J_c determined by the flux density of the pinning forces ($J \times B = F_p$). This statement implies that during the transient states (see Figure 1.4), i.e., the period of the motion of vortices, only a certain amount of electric field can be created. It implies that when $J = \pm J_c$, locally, these domains must satisfy the condition of $E \neq 0$, and this is known as the critical state law. This law, together with Maxwell equations, provide a macroscopic model for describing the penetration of the magnetic field inside a type-II SC. Since the boundary between the flux free regions ($J = 0$) and those with elements of critical current ($J = \pm J_c$) is unknown, this model consists of a cumbersome system of equations and inequalities, which leads to a complicated free boundary problem that in most cases does not have an analytical solution [41, 42].

From the numerical point of view, and regardless of the type-II SC material, the CS model illustrated in Figure 1.4 suggests the constraint $J_i \leq J_c$, where 'i' defines the position of the element inside a superconducting mesh. It makes the numerical solving of the electromagnetic problem in type-II SC samples very difficult for arbitrary relations of external excitations (magnetic field or transport current). A noteworthy fact is that the power-law $E = E_c(J/J_c)^{n-1}$ in figure 1.4-(c) serves either as a simpler approximation of the $E(J)$ relation in the CS model or, with a smaller n, it can be employed to give an account for the thermally activated creep of magnetic flux in a type-II SC [43]. This fact is noted when specifically manufactured wires (materials or superconducting materials) are taking into account [44]. However, for the sake of generality, in part I of this study, only the CS-model is considered, although the impact of the $E - J$ power law into the modelling of commercially manufactured superconducting tapes and their applications in pancake and racetrack-shaped coils will be studied in the part II of this thesis.

The analytical solution to the CS problem with an external magnetic field is limited to the geometry of the sample and the field direction. However, there are two particular cases of idealised geometries where an exact analytical solution is viable, either the infinitely long cylinder in a parallel field or the study

of infinitely thin strips under transverse magnetic field. Beyond these geometries, for solving the problem of the free boundary, numerous front-tracking approaches have been developed [45]. Nevertheless, these approaches are not universal, and they are only useful and applicable in some cases where the topology of the free boundary is relatively simple, such like defining circles or ellipses, but unfortunately, when time-varying transport current and magnetic field are both simultaneously applied, it is not possible to recur to these simplified approaches. Therefore, it requires a more sophisticated formulation which will be presented in the later sections of this Chapter.

In particular, below the magnetic vector potential formulation for CS problems is utilised, where instead of approximating the current-voltage relation ($E-J$ power-law) for a specific material, the exact CS law $J \leq \pm J_c$ is invoked as in [46].

1.2 *Numerical Approach for Superconducting Wires*

As previously mentioned, the importance of determining the minimal energy loss of type-II SCs, i.e., the hysteretic losses inside practical superconducting samples under the conditions of a transverse magnetic field and transport current, taking into consideration the free boundaries created by the penetration of magnetic flux, resides in the ad-hoc knowledge of the local distributions of critical current density inside the superconductor. Moreover, analytical simplifications have been proposed since the 1970s for SC wires subjected only to one of these conditions (either transport current or magnetic field), where the flux front was presumed to be approached by the use of sinusoidal functions in SC cylinders such that the cross-section dimensions are much lesser than their length [47]. In this sense, analytical solutions are possible for the case of infinitely thin strips or slabs (one dimension samples) and cylindrical wire of cross-section with only transport current, but no applied magnetic field, as shown in Figure 1.5 (a), which can be calculated by the expressions [48]:

$$L = \omega \frac{\mu_0}{2\pi} R^2 J_c^2 \left[j - \frac{j^2}{2} + (1-j)Ln(1-j) \right], \tag{1.1}$$

with $j = J_{tr}/J_c$, and $J_{tr} = I_{tr}/(\pi R^2)$ or with the expression $L(B_{\mathtt{a}}) + L(I_{tr}), L(B_{\mathtt{a}}, I_{tr}^{dc})$ where evaluating the non-coupled dependence or AC/DC coupling can render an insufficient approximation for the calculation of the AC losses, thus, a false estimate of the AC losses. For instance, Figure 1.5 (a) depicts the dynamics of the magnetic flux lines (isolevels of the magnetic vector potential), and the current density profile for a long cylindrical wire of

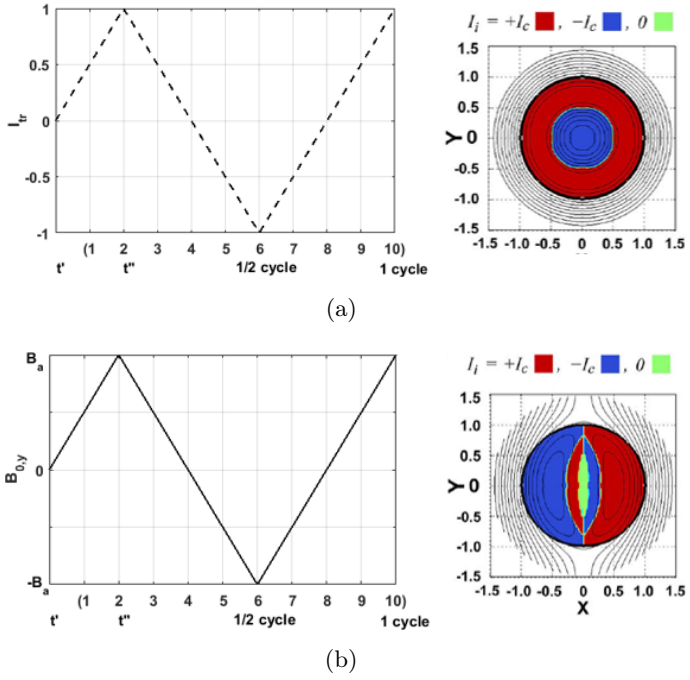

(a)

(b)

Figure 1.5: Sketch of the experimental process for a cylindrical superconducting wire of radius R exposed to (a) isolated AC excitations, transport current $I_{tr}(t)$ and (b) external magnetic field $B_{0,y}(t)$. Correspondingly, the current density profiles measured at the time step '9' are both shown at the right side of the figure.

length much greater than its radius R. The simulation therein considers an AC applied transport current condition with an experimental process near to complete a full cycle of the AC current (time step '9'). In this case, where only the transport current is applied; the total magnetisation (M) of the SC sample is zero, and the injected current acts as a 'screening' current, i.e., the current distribution in a region where $B(r_i) \neq 0$ fulfils the critical state condition $\mathbf{J_i} = \mathbf{J_c}$. It is worth mentioning then, that the time dynamics of the injected current is the source of the hysteretic losses (Joule's heat) in the regions where the flux transport occurs [40]. However, for a cylindrical wire immersed in an external magnetic field as shown in Figure 1.5 (b), exact analytical solutions are not possible, as there is no possible way to find an analytical expression for the dynamics of the flux-front shape. Then, the implementation of numerical analysis becomes the most practical solution for complex configurations were the SC wire or sample is simultaneously subjected to both transport current and transverse magnetic field. In this case, the asymmetrical distortion of the flux free region is conceivable, and the problem can be solved only by making use of sophisticated numerical approaches (see Figure 1.6).

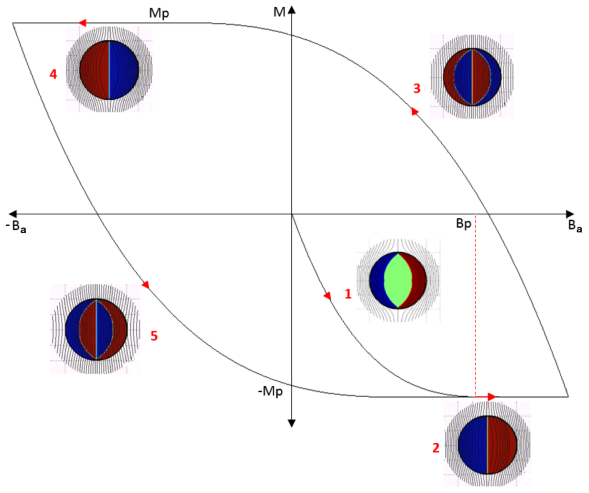

Figure 1.6: Magnetic hysteretic behaviour of a cylindrical SC wire under external magnetic field oscillations, accordingly with the time-dynamics for the external magnetic field excitation illustrated in Figure 1.5.

However, the results presented by Ruiz et al., in [40] have that the density of power dissipation ($\mathbf{E} \cdot \mathbf{J}$) is not uniform across the cross-section of the superconductor where the local profiles of current density appear, regardless of the fact that the material law assumes the CS condition $J_i = J_c$. This implies that locally, the value for the electric field (or $E = E_c$) cannot be a priori assumed, which justifies the fact that the current density is the physical variable constrained into the superconducting state, and not the electric field. In fact, concerning the case where only transport current is applied, the maximal power dissipation occurs homogeneously at the surface of the superconducting sample, but decreases to zero towards the flux front. The current distribution, in this case, can be easily calculated through the analytical expression in Equation 1.1, by following the boundary of the flux front that has a perfect circular shape. Thus, the flux front boundary is the penetration depth at which a local profile of current $I_i = \pm I_c$ transits to zero, following the time evolution of the injected current, as mentioned above. However, asymmetric deformations of the flux front occur when the SC wire is exposed to a magnetic field (absence of transport current), which reveals the occurrence of semi-elliptical shape flux fronts as described in [1].

Figure 1.5 (b) shows the electromagnetic response of an SC cylindrical wire subjected to the action of an oscillating external magnetic field $B_{0,y}(t)$ in the absence of transport current, from which the magnetic hysteretic behaviour observed in Figure 1.6 is obtained. Therein, it shows the magnetic flux lines and profiles of current density for a defined time evolution process (time-step) of the magnetisation loop, corresponding to Figure 1.5 (b). The magnetisation

loop represents the magnetisation (M) as a function of the applied magnetic field B_a, which illustrates the general behaviour of type-II SCs under transverse oscillating magnetic fields. Noticeably, when $B_a \geq B_p$, the SC sample is fully penetrated by the external magnetic field, resulting in a sample with no observable flux-free core, i.e., finite areas where $J = 0$, and B_p being the value of the applied magnetic field, known as the full penetration value expressed as:

$$B_p = \frac{2}{\pi}\mu_0 J_c R\,. \tag{1.2}$$

Therefore, after full penetration of the magnetic field, $B_a > B_p$, the magnetisation does not change as the distribution of lines of current cannot change any longer, unless the direction of the magnetic gradient $(B_a(t'') - B_a(t'))$ is reversed during the cyclic process $(t'' > t)$. As a result, the magnetisation curve saturates at a flat value (M_p). It is noticed that B_p can be expressed in terms of the units of $\mu_0 J_c R$, where $\mu_0 = 4\pi \times 10^{-7}$ $\left[NA^{-2}\right]$ is the magnetic permeability of vacuum. Thence, it results convenient to define the units of B as $(\mu_0/4\pi)J_c R$, such that an exact number for Equation 1.2 can be found, i.e., $b_p = 8$ in the case of a SC wire with cylindrical cross-section.

Recall that the key objective of this study in part I is to determine the electromagnetic properties of rounded type-II Superconductors for an arbitrary relation between the value of transport current and the amplitude of the applied magnetic field, which therefore requires the extension of all the concepts mentioned above. In this sense, the study introduces a sophisticated numerical method in order to determine the physical behaviour and electromagnetic performance of the superconducting wires under different conditions of electrical current (AC/DC) and magnetic field. The numerical/computational method relies on the solution of the Maxwell equations for superconductors under the critical state regime by means of a variational statement, which allows the calculation of all the macroscopic electromagnetic quantities needed without including any arbitrary approaches or flux boundary conditions. These calculations are essential for the practical solution of the electromagnetic properties of type-II superconductors. The derived results are crucial to allow accurate prediction, understanding, and ultimately the prototyping of SC cables, and also the calculation of the minimum energetic losses that these cables can provide in practical configurations.

1.3 *Electrodynamics of Type-II Superconductors*

As previously mentioned, the main distinctive attributes of the macroscopic electromagnetic behaviour of type-II SCs efficiently captured by Bean's CSM, come across a practical difficulty when solving the free boundary problem for varying magnetic field excitations which causes a radial asymmetry in the flux front region of rounded SCs. Nevertheless, the numerical methods discussed in chapter 1.2 are an effective and popular means to solve the problem in type-II SC wires. Knowledge of the flux front, i.e. the penetrating profiles of current density under practical configurations, is used to minimise the AC losses of the SC wires. It is achieved by determining its global magnetic properties such as the overall magnetisation of the sample, and the magnetic field lines distribution which utterly defines the dynamics of the flux front.

Thus, this section focuses on the use of numerical methods to solve the Maxwell equations (ME) under the MQS approach, and the theoretical framework of the variational principles. This is a significant step for reducing the numerical complexity of Maxwell equations for superconducting wires in a 2D approach (infinitely long wire compared to the cross-section dimensions), as it will be revealed in the forthcoming section. A noteworthy fact is that regardless of the material involved, Maxwell equations represent a unique solution to all electromagnetic phenomena [49], which presented in SI units can be defined as (bold notations in this represent vectorial quantities):

$$\nabla \times \mathbf{E} = -\partial_{\mathbf{t}}\mathbf{B} \qquad (\mathbf{Faraday's\ Law})\,. \tag{1.3}$$

$$\nabla \times \mathbf{H} = \partial_{\mathbf{t}}\mathbf{D} + \mathbf{J} \qquad (\mathbf{Ampère's\ Law})\,. \tag{1.4}$$

$$\nabla \cdot \mathbf{B} = \mathbf{0}, \quad (\mathbf{Gauss's\ Law\ for\ magnetic\ field})\mathbf{s}\,. \tag{1.5}$$

$$\nabla \cdot \mathbf{D} = \rho_{\mathbf{v}}, \qquad (\mathbf{Gauss'\ Law\ for\ electric\ fields})\,. \tag{1.6}$$

On the one hand, Equation 1.3, also known as Faraday's law, illustrates that any time variation of a magnetic field $\mathbf{B}$ inside a material can produce an induced current $\mathbf{J}$ due to the circulation of the electric field $\mathbf{E}$. Note that the magnetic field quantities, $\mathbf{H}$ and $\mathbf{B}$, vary in the context used. Recall that in the previous sections, the magnet flux density notation was $\mathbf{B}$ while the magnetic field is denoted by $\mathbf{H}$. However, in a SC, $\mathbf{B} = \mu_{\mathbf{0}}\mathbf{H}$ is conceivable, by assuming that the magnetic permeability of the superconductor equals the one of vacuum, which is generally the case for all type-II SCs. On the other hand, Equation 1.4 also known as Ampère's law shows that the flow of an

electric current J inside a material gives rise to a B field, which in the case of having the current density flowing in a single dimension, as it will be the case for long transmission lines, it implies that the resulting magnetic field circulates perpendicular to the direction of the applied current. However, it is worth mentioning that under certain circumstances, either caused by the geometry of the problem, or by the direction of applied currents or magnetic fields, it is possible to have situations where the magnetic field B can flow with a parallel component to the direction of the current density J, which give rise to the so called flux cutting mechanism [46]. However, in the two dimensional symmetry for the components of the magnetic field, as the considered in this study, where the direction of the applied magnetic field is always perpendicular to the infinite surface of the superconducting sample (perpendicular to the length of the SC wire), the generated magnetisation currents are in the same direction of the transport current (i.e., along the z-axis if the cross section of the SC sample lies on the plane xy), implying the nonexistence of flux cutting events which happen only when the magnetic field is parallel to the direction of the current density, and which could lead to the entanglement and collapse of the vortices. Likewise, the **B** field circulates the electric displacement field **D** when there are "free" or "bound" charges moving within the material, like in the case of dielectrics, but that are not observed or neglected in the case of superconductors, which transforms the Ampère's law to just $\nabla \times \mathbf{H} = \mathbf{J}$ in the case of type-II superconductors. Then, the Gauss's law for magnetic fields in Equation 1.5 implies that magnetic charges (monopoles) does not exist, i.e., the divergence of **B** or **H** field is always zero. It is used in superconductivity as a physical boundary condition.

Finally, the classical Gauss's law in Equation 1.6 shows that the divergence of **D** at any point in a space is nonzero if there is a "free" or "bound" electric charge density ρ_v present somewhere; otherwise, it is equals to zero, as it is the case for superconductors. Therefore, under appropriate considerations, it is possible to simplify the most relevant Maxwell equations for a superconductor, i.e., the Faraday's and Ampère's law, which describe a coupled system of time evolution field equations (Eq. 1.3 and Eq. 1.4). Both, jointly determine the distribution of supercurrents inside the SC material under appropriate boundary conditions and selection of $E - J$ material law.

As mentioned above, the calculations begin by defining the Maxwell equations in a macroscopic media of similar nature than vacuum. In an attempt to demonstrate this, let us start defining in general terms the electric displacement field **D** and the magnetic field **H**, where **B** is called the magnetic induction

which has components specified by:

$$D_i = E_i + 4\pi \left(P_i - \sum_{j=1} \frac{\partial Q_{ij}}{\partial r_j} + ... \right) , \tag{1.7}$$

and

$$H_i = B_i - 4\pi(M_i + ...) , \tag{1.8}$$

where $\mathbf{P}$ is the macroscopic density of the permanent and induced electric dipole moments in the material, Q_{ij} the components of the quadropole moments tensor $\mathbf{Q}$ relative to the coordinate systems origin $\mathbf{r}_j$ and $\mathbf{M}$ the local magnetic moment of the material, with the indices *i, j* running over the orthonormal components of the coordinate system, e.g., *x*, *y*, and *z* for Cartesian coordinates.

The Equation 1.7 and 1.8 are general definitions regardless of the material chosen. However, for a superconductor, any local magnetic moments of intrinsic nature, $\mathbf{M_i}$, are equal to zero, i.e. the material does not show any intrinsic magnetisation without applying an external magnetic field. Likewise, for a superconducting material, the polarisation $\mathbf{P} = 0$, as there are no "free" or "bound" electrons in the SC state, or at least, the macroscopically averaged magnetic dipole, electric dipole, and electric quadrupole being characterised by the quantities $\mathbf{M}$, $\mathbf{P}$, $\mathbf{Q}$, and related higher order quantities can be neglected even for those materials that exhibit a dielectric or ferromagnetic behaviour at their normal state ($\mathbf{T} > \mathbf{T_c}$).

Then, after these simplifications, the vectors, $\mathbf{B}$ and $\mathbf{E}$ are expressed in terms of the vector potential $\mathbf{A}$ and the scalar potential Φ, respectively. However, the resulting set of equations can only be solved when the resulting fields $\mathbf{D}$ and $\mathbf{H}$ are known as functions of $\mathbf{B}$ and $\mathbf{E}$, i.e., when the constitutive relations between these quantities are identified for the specific material or "space" where the Maxwell equations are to be solved [49]. Thus, we can define,

$$\mathbf{D} = \mathbf{D}[\mathbf{E}, \mathbf{B}] , \tag{1.9}$$

and

$$\mathbf{H} = \mathbf{H}[\mathbf{E}, \mathbf{B}] , \tag{1.10}$$

and analogously, due to Ampère's law, we can assume for general purposes that,

$$\mathbf{J} = \mathbf{J}[\mathbf{E}, \mathbf{B}] . \tag{1.11}$$

The links between these quantities are not certainly straightforward and could have a nonlinear behaviour due to hysteresis phenomena. Fortunately, this is not the case for most of the superconductors with practical applications such as those within the Yttrium Barium Copper Oxide (YBCO) or Bismuth Strontium Calcium Copper Oxygen (BSCCO) families (cuprates). However, it could be the case for exotic superconductors displaying intrinsic coexistence of ferromagnetism and superconductivity, such as UGe2, U(Rh, Co)Ge, ErRh4B4 and $HoMo_6S_8$ [50]. Therefore, by excluding these materials, we can say that for practical SCs (cuprates), the D(E) and H(B) functions show a linear response of the SC medium such that,

$$D_i = \sum_j \xi_{ij}\, E_{ji}\,, \tag{1.12}$$

and

$$H_i = \sum_j \mu_{ij}\, B_{ji}\,, \tag{1.13}$$

where E_{ji} and B_{ji} are the electric and magnetic field contributions of the j elements over the i elements in a discretised mesh of elements that compose the material. The tensors, μ_{ij} and ξ_{ij} are known as the inverse magnetic permeability and electric permittivity or dielectric tensor. These tensors summarise the linear response of the medium, which depends on the molecular, and possibly the crystalline structure of the material, and the bulk properties such as mass density. However, for SCs at a macroscopic level, it is possible to assume (in average) an isotropic behaviour (linear response) of $\mathbf{D}$ and $\mathbf{E}$ such that the tensors μ_{ij} and ξ_{ij} are diagonal as it is shown in Equations 1.14 and 1.15,

$$\mathbf{D}_{(\mathbf{r})} = \xi\, \mathbf{E}_{(\mathbf{r})}\,, \tag{1.14}$$

$$\mathbf{H}_{(\mathbf{r})} = \frac{\mathbf{1}}{\mu}\, \mathbf{B}_{(\mathbf{r})}\,. \tag{1.15}$$

Moreover, in all practical applications of type-II SCs, it is customary to consider situations where the local components of the magnetic field $\mathbf{H}_{(\mathbf{r})}$ along the SC are much higher than H_{c1}, and well below H_{c2}, usually in a way that it is possible to neglect the equilibrium magnetisation of the flux line lattice, as it would happen in the vacuum. Therefore, it is possible to use the following approach regardless of the composition of the (type-II) SC material:

$$\mathbf{H} = \frac{\mathbf{1}}{\mu_{\mathbf{0}}}\, \mathbf{B}\,. \tag{1.16}$$

Thus, the concurrent solution of Faraday's and Ampère's laws will determine the distribution of super-current inside of the SC sample, and they characterise the time dependence of the coupled system (see Equations 1.3 & 1.4). In this sense, the profile of the current density, $\mathbf{J}$, is updated by the induced transient electric field, which is determined through a suitable material relation $\mathbf{J}(\mathbf{E})$. For enabling this, it is possible to establish an additional condition by taking the divergence in both sides of the abovementioned laws and, recalling the integrability conditions of these equations (time derivatives and permutation of space):

$$\partial_t(\nabla \cdot \mathbf{B}) = \mathbf{0}\,,\ \partial_\mathbf{t}(\nabla \cdot \mathbf{D}) + \nabla \cdot \mathbf{J} = \mathbf{0}\,. \tag{1.17}$$

These equations allow introducing the "spatial initial conditions" which might define the presence of conserved electric charges, i.e.,

$$\nabla \cdot \mathbf{B}(t\,=\,0)\,,\ \ \nabla \cdot \mathbf{D}(t\,=\,0)\,=\rho_v(t\,=\,0)\,. \tag{1.18}$$

Note that the ρ_v in this context is the charge density, and not electrical resistivity. Thus, within this framework, evolution profiles such as $\mathbf{B}(\mathbf{r},t)$ and $\mathbf{E}(\mathbf{r},t)$ are determined by substituting $\mathbf{D}$, $\mathbf{J}$ and $\mathbf{H}$ into Equations (1.3) and (1.4) through the constitutive laws and applying relevant initial conditions. The transient variables $\mathbf{D}$, $\mathbf{E}$ and ρ_v are small and proportional to $\dot{\mathbf{B}} = \partial_t\mathbf{B}$ for a constant and slow sweep rate of the external excitations (transport current or/and magnetic field sources), while $\ddot{\mathbf{B}}$, $\dot{\mathbf{E}}$ and $\dot{\rho}_v$ are negligible. Thus, the MQS approximation is reduced to consider that the displacement current densities $\partial_t\dot{\mathbf{D}}$ are considerably lesser than the current density $\mathbf{J}$ in the bulk and disappear in a first order treatment, i.e. $\partial_t\dot{\mathbf{D}} \approx \mathbf{0}$. This causes a critical alteration in the mathematical structure of the Maxwell equations, where from Equation 1.4, $\dot{\mathbf{B}} = \mathbf{0}$, Ampère's law converts to a pure spatial condition and is no longer a time dependent equation. Therefore, the Ampère's law for the superconductor problem is reduced to:

$$\nabla \times \mathbf{H} = \mathbf{J}\,. \tag{1.19}$$

Note that with $\mathbf{B} = \mu_\mathbf{0}\mathbf{H}$, Ampère's law can be rewritten as $\nabla \times \mathbf{B} = \mu_\mathbf{0}\mathbf{J}$. Then by the integrability condition, Gauss law $\nabla \cdot \mathbf{B} = \mathbf{0}$, the divergence of the $\mathbf{J}$ vector equals to zero,

$$\nabla \cdot \mathbf{J} \approx \mathbf{0}\,. \tag{1.20}$$

It is worthy of mention that the Faraday's law is the distinctive time evolution equation in the MQS limit, then the evolution profile $\mathbf{B}(\mathbf{r},t)$ can be written as:

$$\partial_t\mathbf{B} = -\nabla \times \mathbf{E} = -\nabla \times [\rho(\mathbf{J})\ \mu_0\nabla \times \mathbf{B}]\ , \tag{1.21}$$

where $\rho(\mathbf{J})$ defines the electrical resistivity of the material. It could be a nonlinear and non-scalar (anisotropic) function that must incorporate the threshold or critical values for the mechanisms associated to flux depinning and flux cutting in the SC state, which are introduced via the critical state law:

$$\mathbf{J} = J_c[\mathbf{E}, \mathbf{B}] \quad if\, \mathbf{E} \neq 0\,. \tag{1.22}$$

The Equation 1.22 is the Bean's critical state assumption for the SC state discussed in chapter 1, which transforms into the classical Ohm's law, $J = \sigma\mathbf{E}$ for $J > J_c$ when the SC transits to the normal state (see Figure 1.4).

Bean's model states that only one value of $|J_c|$ can be identified if the electric field does not equal to zero, in other words, $\mathbf{J} = \pm\mathbf{J}_c$ if $\mathbf{E} \neq 0$. Therefore, the reduced Faraday's law in Equation 1.21 constitutes the H-formulation for applied superconductivity, which acts as a basis for all the variant electromagnetic formulations where the dependent variables can either be the fields $\mathbf{E}$ [51], $\mathbf{J}$ [52], or $\mathbf{A}$ [46, 53]. Consequently, the MQS approach is inherently implicit, no matter the formulation. At the same time, the MQS approach has been validated for frequencies as high as 300 MHz [54], from which there is a need for more complex formulations for a proper description of the macroscopic electromagnetic response of type-II superconducting materials at higher frequencies, although this is not the case for the majority of power systems lines which operate at 50 Hz or 60 Hz.

The numerical technique to solve a critical state problem is related to the outcome of the MQS assumption ($\partial_t\mathbf{D} \approx 0$), which is the MQS limit. Within this assumption, the initial condition must satisfy the Ampère's law $\nabla\times\mathbf{B}_n = \mu_0\mathbf{J}_n$, $\nabla\cdot\mathbf{B}_n = 0$, and $\nabla\cdot\mathbf{J}_n = 0$, and the penetrated field profiles inside the superconductor can be obtained by the finite-difference of the Faraday's law expression, using the inverse function $\mathbf{E}(\mathbf{J})$ of the conductivity law,

$$\begin{aligned} \mu_0\frac{\mathbf{H}_{n+1}-\mathbf{H}_n}{\Delta_t} &= -\nabla\times\mathbf{E}_{n+1} = -\rho\nabla\times\mathbf{J}_{n+1} \\ \mu_0\frac{\mathbf{H}_{n+1}-\mathbf{H}_n}{\Delta_t} &= -\rho\nabla\times\nabla\times\mathbf{H}_{n+1} \end{aligned} \tag{1.23}$$

where the Ohm's law has been assumed for an isotropic media, such that that the resistivity of the material will be later considered by the resistivity function ρ. Therefore, the field profile $\mathbf{H}_{n+1}$ can be determined by solving the obtained differential equation, Equation 1.23, if the "initial" distribution of magnetic field $\mathbf{H}_n$ is known, as well as the boundary conditions for the "current" instant $(n+1)\delta t$.

However, solving this equation still demands cumbersome and time-consuming processes as it still implies finding a global solution for the entire 3D space

inside and beyond the SC boundaries. This is the reason why further mathematical treatment is needed, i.e., invoking a minimisation procedure, which is the purpose of the next section.

1.4 *Variational Principle for Critical State Problems*

The numerical solution of the critical state problem is convoluted when considering the differential formalism of the Maxwell equations. Nevertheless, it is possible to formulate an equivalent variational theory for critical state problems, as shown in this section.

The variational principle is based on approaching the continuous evolution of the variables by the discretisation of time-steps, $\delta t = t" - t'$, with the accuracy of the solution increasing as δt tends to zero. In practical terms, the discretisation is performed over the path followed by the external sources. That is, either transport current or applied magnetic field, where the variational principle allows the selection of an arbitrary region $\Delta\mathbf{r}$ within the $\mathbf{J}$ space where the local changes of the magnetic field $\dot{\mathbf{B}}$ occurs. It could either depends on external magnetic fields, $\mathbf{B}_0$ and the position $\mathbf{r}$ of the elements of current $\mathbf{J}_i$ or both, in such a way that when the condition $\mathbf{J}_i = \pm\mathbf{J}_c$ is verified, only then will the non-dissipative flow of current occurs [46]. This condition also known as the material law for the critical state theory, is directly introduced as a further constraint into the system of equations to be solved which in the case of the variational formulation to be developed below, implies the direct definition of an inequality constraint on the main variables of the problem, which will result to be the current density elements $\mathbf{J}_i$ along the cross section of the SC wire, such that the material law is explicitly defined by the condition $|\mathbf{J}_i| \leq \mathbf{J}_c$. Alternatively, the material law can be introduced by a highly nonlinear power-law function between the electric field and the current density which will become more apparent as we progress towards Part II of this thesis, but for the sake of Part I all our results will be presented within the material law for the critical state in type II superconductors.

To be able to find the solution for the current density and minimise the functional in the so called $\mathbf{H}$-formulation, i.e., when $\mathbf{H}$ is the main accountable variable, we take into account a small path step Δt starting from some profiles of magnetic field $\mathbf{H}_n(\mathbf{r})$ to the final profile $\mathbf{H}_{n+1}(\mathbf{r})$, and the equivalent $\mathbf{J}_n(\mathbf{r})$ and $\mathbf{J}_{n+1}(\mathbf{r})$. This defines $\Delta\mathbf{H}$ as the variation of $\mathbf{H}$ between two successive

time steps, $\mathbf{H}_{n+1} - \mathbf{H}_n$. Also, this two configurations can be considered to be related by a fixed process that performs a linear step $\Delta\mathbf{H}$, in a way that $\mathbf{H}_{n+1} = \mathbf{H}_n + s\Delta\mathbf{H}$ with s$\in [0,1]\Delta t$. Note that the initial condition must satisfy the Ampère's law with negligible displacement current, as it has been demonstrated by Badia-Majos and Lopez in [55]. Then, solving the set of equations in Equation 1.23, a minimisation procedure must be implemented, considering $\mathbf{J}_{n+1}(\mathbf{r}) \in \Delta\mathbf{r}$. The abovementioned case is a minimisation problem within the framework of the variational calculus. It incorporates integral functionals of unspecified fields and their derivatives, with restrictions that can be analysed through the optimal control theory [56]. This relatively cumbersome procedure could be summarised by the integral inversion of Equation 1.23 with respect the field variable $\mathbf{H}_{n+1}$, as the field $\mathbf{H}_n$ is known, with which the left hand side of Equation 1.23 can be integrated as,

$$\int (\mathbf{H}_{n+1} - \mathbf{H}_n)\, d\mathbf{H}_{n+1} = \frac{H_{n+1}^2}{2} - \mathbf{H}_n \cdot \mathbf{H}_{n+1}\,, \tag{1.24}$$

and by doing the inverse process, the quasi-stationary change in the filed $\mathbf{H}_{n+1} - \mathbf{H}_n$ can be written as,

$$\frac{\partial}{\partial \mathbf{H}_{n+1}} \left(\frac{H_{n+1}^2}{2} - \mathbf{H}_n \cdot \mathbf{H}_{n+1} \right) = \mathbf{H}_{n+1} - \mathbf{H}_n\,, \tag{1.25}$$

The right hand term at Equation 1.23 is much cumbersome and cannot be transformed by direct integration over the field $\mathbf{H}_{n+1}$ due to its dependence with the spatial coordinates. However, by transforming the function $\nabla \times \nabla \times \mathbf{H}_{n+1}$ into its tensor representation, it is possible to prove that the $i-th$ component of this vectorial product can be written as function of its associated field momentums $\partial_{\chi_j} H_{n+1,\chi_i}$, with χ_j an orthogonal component of the system (x, y, or z in Cartesian coordinates) different to the component χ_i, such that

$$[\nabla \times \nabla \times \mathbf{H}_{n+1}]_{\chi_i} = -\frac{1}{2}\partial_{\chi_j} \frac{\partial}{\partial \left(\partial_{\chi_j} H_{n+1,\chi_i}\right)} [(\nabla \times \mathbf{H}_{n+1}) \cdot (\nabla \times \mathbf{H}_{n+1})] \tag{1.26}$$

Then, as any of the system of coordinates χ_i to be used has to be an orthogonal system, therefore the field components $\mathbf{H}_{n+1,\chi_i}$ and their associated momentums $\partial_{\chi_j} H_{n+1,\chi_i}$ are canonically independent such that for an isotropic material the Equation 1.23 can be rewritten by substitution of Equations 1.25 & 1.26 as,

$$\begin{aligned} &\mu_0 \frac{\partial}{\partial H_{n+1}, \chi_i} \left(\frac{H_{n+1}^2}{2} - \mathbf{H}_n \cdot \mathbf{H}_{n+1} \right) - \\ &\frac{\rho \delta t}{2} \frac{\partial}{\partial \left(H_{n+1}, \chi_j\right)} [(\nabla \times \mathbf{H}_{n+1}) \cdot (\nabla \times \mathbf{H}_{n+1})] = 0\,, \end{aligned} \tag{1.27}$$

such that the minimisation functional can be written as,

$$\begin{aligned}\mathcal{F} &= \text{Min}\int_{\Re^3}\left[\mu_0\left(\frac{H_{n+1}^2}{2}-\mathbf{H}_n\cdot\mathbf{H}_{n+1}\right)-\frac{\rho\delta t}{2}\left(\nabla\times\mathbf{H}_{n+1}\right)\cdot\left(\nabla\times\mathbf{H}_{n+1}\right)\right]dr^3\\ &= \text{Min}\int_{\Re^3}\frac{\mu_0}{2}|\mathbf{H}_{n+1}-\mathbf{H}_n|^2dr^3-\text{Min}\int_{\Re^3}\frac{\mu_0}{2}H_n^2dr^3\\ &-\text{Min}\int_{\Re^3}\frac{\rho\delta t}{2}\left(\nabla\times\mathbf{H}_{n+1}\right)\cdot\left(\nabla\times\mathbf{H}_{n+1}\right)dr^3\end{aligned} \tag{1.28}$$

Thence, it is to be noticed that the second minimisation integral in Equation 1.28 corresponds to the integral of a known parameter, as the field H_n is known, which is consequently for the minimisation process is considered as a constant rather than a variable, and therefore do not play any role into the minimisation itself other than defining the initial conditions of the system. On the other hand, it has been found that the third minimisation term depends explicitly of the Ampère's law for static fields $\nabla\times\mathbf{H}_{n+1}=\mathbf{J}_{n+1}$, where the current density after an excitation condition (applied magnetic field and/or transport current) is also a know value defined critical current density condition $\mathbf{J}_c$, which have been established by the Bean's model of superconductivity (Equation 1.22). Therefore, the minimisation functional can be simply reduced to

$$\mathcal{F} \quad = \quad \text{Min}\int_{\Re^3}\frac{\mu_0}{2}|\mathbf{H}_{n+1}-\mathbf{H}_n|^2dr^3\,, \tag{1.29}$$

as the solution of the first order differential equation for the functional field $\mathcal{F}_{n+1}$,

$$\frac{\partial\mathcal{F}_{n+1}}{\partial H_{n+1,\chi_i}}-\partial_{\chi_j}\frac{\partial\mathcal{F}_{n+1}}{\partial\left(\partial_{\chi_j}H_{n+1},\chi_i\right)}=0 \tag{1.30}$$

with a minimum at H_{n+1},χ_i. Here, it is to be noticed that this equation is identical to the Lagrangian action of a Hamilton equation with coordinates (H_{n+1}) and momentum $(\partial_{\chi_j}H_{n+1})$ canonically independent, and therefore the minimisation functional in Equation 1.29 can be understood as the minimum energy condition for the Faraday's law of discretised magnetic fields under a known $\mathbf{H}_n$ field and the Ampère's law as a physical constraint entered via the Bean's model for the material law

Probably a simple way to see this is by the Euler-Lagrange equation for electromagnetic (EM) field which can be used to solve the constrained minimisation problem. In this sense, following the conventional Lagrange multiplier method, the EM Lagrangian for Equation 1.23 is defined as:

$$\mathcal{L}=\frac{1}{2}|\Delta\mathbf{B}|^2+\mathbf{p}\cdot\left(\nabla\times\mathbf{H}_{n+1}-\mathbf{J}_{n+1}\right), \tag{1.31}$$

where $\Delta\mathbf{H}$ is the linear step approach $\mathbf{H}_{n+1} - \mathbf{H}_n \Rightarrow \dfrac{\partial \mathbf{H}}{\partial t}$.

The first term of the Lagrangian in Equation 1.31 is the energy gained by any change of external magnetic field, while, the second term corresponds to the response of the material in the presence of current density, which implies the Ampère's law $\nabla \times \mathbf{H} = \mathbf{J}$, and the inclusion of the Lagrange multiplier $\mathbf{p}$ which is aimed to preserve the integrability of Faraday's law. Thus, Euler's equation turns out to be:

$$\nabla \times \mathbf{H}_{n+1} - \mathbf{J}_{n+1} = 0\,, \tag{1.32}$$

where $\mathbf{H}_{n+1}$ and $\mathbf{J}_{n+1}$ are defined as the unknown solution for an arbitrary variation of $\delta\mathbf{p}$ and,

$$\nabla \times \mathbf{p} = -\mu_0 \Delta\mathbf{H}\,, \tag{1.33}$$

for any arbitrary variation $\delta\mathbf{H}$.

Now, taking into account the scalar electric potential Φ and the magnetic vector potential $\mathbf{A}$, the expression of the electric field $\mathbf{E}$ and the magnetic induction field $\mathbf{B}$ is:

$$\mathbf{E} = -\frac{\partial \mathbf{A}}{\partial t} - \nabla\Phi\,, \tag{1.34}$$

where $\nabla\Phi$ is constant. Then, as $\mathbf{B} = \nabla \times \mathbf{A}$, with the help of Equation 1.34 it is possible to identify that the Lagrange multiplier in Equation 1.33 is directly:

$$\mathbf{p} = -\Delta\mathbf{A}\,. \tag{1.35}$$

As $\mathbf{B} = \nabla \times \mathbf{A}$, the vector potential $\mathbf{A}$ is arbitrary to the extent that the gradient of some scalar function can be added without modifying the resulting magnetic field, with the invariance gauge of the Lagrange conditioner being defined by Equation 1.33. However, it cannot be any scalar function as the admissible physical states of the Lagrangian in Equation 1.31 need to fulfil Equation 1.34 and the condition $\mathbf{B} = \nabla \times \mathbf{A}$. Therefore, it is worth mentioning that the Lagrange conditioner, Equation 1.33 is valid for any arbitrary variation $\delta\mathbf{B}$. Nevertheless, not any variation $\delta\mathbf{B}$ is a physical solution of the system, because it must fulfil the Faraday's law (Eq. 1.3), which in discretised form can be written as,

$$\nabla \times (\mathbf{E}\Delta t) = -\Delta\mathbf{B}\,. \tag{1.36}$$

Consequently, the physical admissible Lagrangian within the CS regime need to fulfil the condition:

$$\mathbf{p} = \mathbf{E}\Delta t\,, \tag{1.37}$$

where the electric field in the critical state regime needs to be appropriately defined by the imposed material law $\mathbf{E}(\mathbf{J})$. Therefore, the time-averaged Lagrange density can be written within the MQS approximation as:

$$\mathcal{L} \equiv \frac{1}{2}(\Delta\mathbf{B})^2 + \mathbf{E}\cdot(\nabla\times\mathbf{B}_{n+1} - \mathbf{J}_{n+1})\Delta t\,. \tag{1.38}$$

On the other hand, It has been demonstrated already that it is possible to solve this Lagrangian by the optimal control principle in [55]. It establishes that the minimum of the Lagrangian only needs to be found inside of the regions of space where current density vector is allowed to be different to zero, what happens only in those regions of space $\Delta\mathbf{r}$ where $\mathbf{J}\cdot\mathbf{p}$ is maximum, i.e.,

$$\text{Min}\{\mathcal{L}\}|_{\mathbf{J}\in\Delta_\mathbf{r}} \equiv \text{Max}\{\mathbf{J}\cdot\mathbf{p}\}|_{\mathbf{J}\in\Delta_\mathbf{r}} \equiv \text{Max}\{\mathbf{E}\cdot\mathbf{J}\}|_{\mathbf{J}\in\Delta_\mathbf{r}}\,. \tag{1.39}$$

Therefore, Equation 1.39 suffices to determine the relationship between the directions of $\mathbf{J}$ and $\mathbf{E}$, noting that the maximal shielding condition is equivalent to the maximum projection rule. It means evoking the orthogonality condition of the electric field direction with the surface of $\Delta_\mathbf{r}$. In this sense, the Lagrange multiplier can be straightforwardly identified with the electric field of the problem as expressed in the latter part of Equation 1.39 (Maximal local shielding rule). This result is remarkably significant because now, we can solve the problem with a mesh of elements defining only the SC material domain, and not the entire 3D "infinite" space.

Furthermore, the rule of maximum projection is used to derive the functional for the minimisation procedure:

$$\mathbf{J}\cdot\mathbf{P} = \mathbf{J}\cdot\mathbf{E}\Delta t \equiv \mathbf{J}\cdot(-\Delta\mathbf{A} - \nabla\Phi\Delta t) = -(\Delta\mathbf{A} + \nabla\Phi\Delta t)\cdot\mathbf{J}\,, \tag{1.40}$$

where it applies the definition of the electric field, Equation 1.34, in discretised form. Notice that the Ampère's law was already applied in Equation 1.32 utilising the Lagrange multiplier. Faraday's law was obtained as an Euler equation to solve for the variational problem, which demonstrates consistency with the original set of Maxwell equations. Thus, with $\mathbf{B} = \nabla\times\mathbf{A}$, the minimisation functional of the system can be rewritten as:

$$\begin{aligned}\mathcal{F} \;=\; \text{Min}\int_{\Re^3}\mathcal{L}d^3\Re \;=\; \text{Min}\int_{\Re^3}[\frac{1}{2}(\Delta\mathbf{B})^2 - \Delta\mathbf{A}\cdot(\nabla\times\mathbf{B}_{n+1} - \mathbf{J}_{n+1}) \\ -\nabla\Phi(\nabla\times\mathbf{B}_{n+1} - \mathbf{J}_{n+1})\Delta t]\,.\end{aligned} \tag{1.41}$$

Then, by assuming the non-existence of gradients of charge densities that could exhibit the occurrence of intrinsic electric or magnetic fields as in the case of semiconductors or ferromagnetic materials, the scalar electric field potential $\nabla\Phi$ can be assumed to be equal to zero, an assumption generally valid

for conventional type II superconductors in the absence of transport current. Therefore, the third expression within the argument of the integral in Equation 1.41 can be neglected within the minimisation process, where the condition of transport current can be incorporated as an external constraint. Likewise, by incorporating the Bean's critical material law, the Ampère's law is intrinsically incorporated in the second term of this functional, such that for any physically valid solution given an initial field $\mathbf{B}_n$ known, the minimum of this functional relies only on the first term of the objective function, i.e., the solution of the problem can then be determined by the minimisation of the small functional below:

$$\mathcal{F} = \text{Min} \int_{\Re^3} \frac{1}{2} (\Delta \mathbf{B})^2 d^3\mathbf{r}\,, \tag{1.42}$$

where $\Delta\mathbf{B}$ is the magnetic field variance for successive time-steps $\mathbf{B}_{n+1} - \mathbf{B}_n$.

Equation 1.42 straightforwardly corresponds to the variational statement of one of the Maxwell equations. That is Faraday's law obtained for the case of type-II SCs by uncoupling the magnetic vector from the electric field. However, solving the functional for the magnetic sector (uncoupled) makes it also possible to derive the precise solution for the electric sector since $E = \dfrac{-\partial \mathbf{A}}{\partial t}$, with $B = \nabla \times \mathbf{A}$ in the case where there is no any local sources of B or E inside the system, an assumption that is valid for all practical type-II SCs. The underlying advantage of this formulation is that now, it is possible to avoid the extensive and numerically time-consuming integration of the equivalent partial differential equations (PDEs). Instead, it employs more straightforward algorithms for the solution of integrals. This significant benefit of the numerical minimisation constitutes the soundness of the so-called variational method. Consequently, merely the unknown components of the current are present for the computation, thus, reducing the number of the unknown variables. In the case where there is a problem with evident symmetry, further simplifications are possible, and as a consequence, one can easily solve 2D-3D problems within the above mentioned statements [46].

Even if there is an internal source of current from which we can no longer assume $\nabla\Phi = 0$, it is still possible to recover the value of the electric field, $\mathbf{E} = -\partial\mathbf{A} - \nabla\Phi$. This is done by adding only one more single variable, $C_t = \nabla\Phi$, which is calculated during the solution of the system at each time step, by simply ensuring that the physical condition E = 0 in those regions where either, there is a complete absence of magnetic flux, i.e., flux-free core regions, or $J = 0$ even after having a penetration profile (flux front) of the magnetic field inside of the superconducting material, is preserved.

Nevertheless, to solve Equation 1.42, the function that defines the magnetic field B (t) at each time step when there are elements of current inside the super-

conductors needs to be known. In this sense, chapter 2 of this thesis provides the derivations of the minimisation functional within the **J**-formulation for the specific case of 2D type-II SC wires exposed to transverse AC magnetic excitations, alongside its results and discussion.

Chapter 2

Electromagnetic Response of DC/AC Type-II Superconducting Wires Under AC/DC Magnetic Excitations

From a practical perspective, the opportunities of technological application and commercial value that type-II superconducting materials provide for DC power transmission cables and designing of DC power grids are notable, this mainly due to their compact design, high transport current capability [57], resilience properties of fault current limiter [58], and the low but non-negligible electric power hysteretic losses compared to normal conductors. In fact, the value of the electric power dissipation (losses) is one of the prevailing physical quantities which allow the assessment of the practical performance of superconductors for its technological deployment, as it serve as an indicative representation of the running costs associated to their long term operation. Therefore, understanding the physical meaning of the energy losses associated with SC materials under different electromagnetic perturbations (either magnetic field and/or transport current), is essential to give clarity on the conditions for which DC SC wires exposed to oscillating magnetic fields can compete with SC wires utilised for alternating current power transmission. Thus, this chapter is devoted to study the effects of applying an AC transverse magnetic field to a type-II SC wire of rounded cross-section, it utilised for direct current power transmission. It follows the theoretical framework of the critical state model and the numerical approaches derived from the so-called J-formulation

in Chapter 1, which allow a straightforward numerical solution of the problem. The results can be used as a practical benchmark for determining the minimal losses and magnetic impact of DC SC lines subjected to external oscillating magnetic fields, either when the direct current is applied to a magnetically virgin or a pre-magnetised SC wire, in a manner to allow us recognise a steady magnetic response after two to three cycles of the applied magnetic field.

Chapter 2.1 shows the transformation of the obtained minimisation principle in Equation 1.42 to a more familiar representation, where the variables of the problem are the magnetic vector potential **A** and the current density vector **J**, also known as the **A-J** formulation. It is then simplified for the numerical calculation into where **J** is the sole unknown variable when the inductance matrices of a system of coupled lines (elements) of current are known, with the computational method employed being discussed in Chapter 2.2. Then, the subsequent Chapter 2.3 introduces the computed numerical results for the case of type-II DC superconducting wires under AC magnetic excitations, disclosing the observed electromagnetic features such that a rapid saturation state of the SC wire characterised by a semi-square magnetisation loop, with evident Boolean characteristics that enable the possibility to use DC SC wires subjected to transverse AC magnetic field, for both transmissions of transport current and data. Also, a remarkable feature was observed for the calculation of the cyclic hysteretic losses (AC Losses) of the SC wire under these conditions. It was found that for the values of the applied magnetic field of amplitude $B_a \geq B_p \times (1 - I_a/I_c)$, being I_a either the amplitude of an AC or DC transport current, the AC losses, i.e., the amount of energy (heat) released by the SC wire is nearly the same. The observed Boolean feature for the SC wire is valid regardless of the experimental condition, i.e., DC or AC used for the transmission.

2.1 *Numerical Formulation*

Recall that when the flux free region in a magnetically penetrated superconductors is asymmetrically deformed, the practical solution of the electromagnetic problem demands to employ a numerical approach. Thus, as previously mentioned, the numerical method depends on resolving the differential form of Maxwell equations within the critical state regime, by arriving at a variational statement for the integral minimisation of the system, which allows a significant reduction of variables to solve the electromagnetic problem into the superconducting system. In an attempt to produce a formulation for the

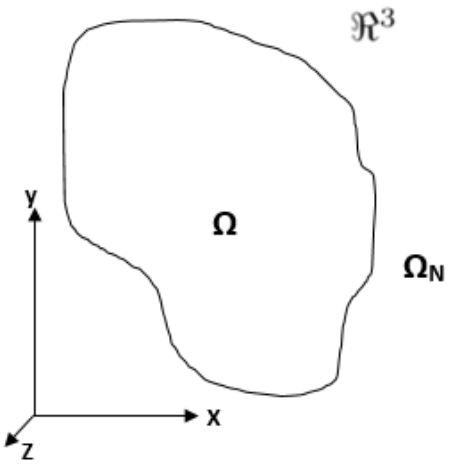

Figure 2.1: Pictorial representation of the 2D cross-section of a superconducting domain Ω in the $\Re^3$ space, which is used within the integral formulation described in Chapter 2. The outer volume $SC \setminus \Omega_N$ is incorporated only in PDE approaches such as the H-formulation.

computational method, and thus, enable the numerical calculation of the AC losses of rounded SC wires in arbitrary AC/DC regimes, here the variational approach of the $\mathbf{A} - \mathbf{J}$ formulation is derived, and then transformed to the so called **J**-formulation in a 2D approach.

Starting from the minimisation principle established in Equation 1.42, and recalling that $\mathbf{B} = \mu_0 \mathbf{H}$ in our case, the functional to minimise can be rewritten as:

$$\mathcal{F}\left[\mathbf{H}_{n+1}(\mathbf{x})\right] = \frac{1}{2} \int_{\Re^3} \left|\mathbf{H}_{n+1} - \mathbf{H}_n\right|^2, \tag{2.1}$$

which must satisfy Ampère's law at each calculated time step $n+1$, $\nabla \times \mathbf{H}_{n+1} = \mathbf{J}_{n+1}$, where the "magnetic" time step $\mathbf{H}_{n+1}$ is defined as $\mathbf{H}_n + d\mathbf{H}$ when the interval $d\mathbf{H}$ is known.

To derive the equivalence between the **H** and $\mathbf{A} - \mathbf{J}$ formulations, we start from the general form of the functional (Equation 2.1), having in mind that the only terms to minimise are those which are unknown, i.e., at the time step $n+1$. Therefore, $\mathbf{H}_n^2$ that defines the initial condition of a magnetic field

during the minimisation procedure is avoided, i.e.

$$\begin{aligned}\text{Min}\,\mathcal{F}[\mathbf{H}_{n+1}(\mathbf{x})] &= \text{Min}\left\{\frac{1}{2}\int_{\Re^3}|\mathbf{H}_{n+1}-\mathbf{H}_n|^2\right\}\\ &= \text{Min}\left\{\frac{1}{2}\int_{\Re^3}H_{n+1}^2-2\mathbf{H}_{n+1}\cdot\mathbf{H}_n+\mathbf{H}_n^2\right\}\\ &= \text{Min}\left\{\int_{\Re^3}\frac{H_{n+1}^2}{2}-\mathbf{H}_{n+1}\cdot\mathbf{H}_n\right\}.\end{aligned} \tag{2.2}$$

The above integral needs to be evaluated by separation of variables. As a consequence, the definition of the magnetic vector potential ($\mathbf{B}=\nabla\times\mathbf{A}$) is employed, so that with $\mathbf{H}=\frac{1}{\mu_0}\nabla\times\mathbf{A}$, we can redefine H_{n+1}^2 as:

$$H_{n+1}^2=\mathbf{H}_{n+1}\cdot\mathbf{H}_{n+1}=\frac{1}{\mu_0}\mathbf{H}_{n+1}\cdot\nabla\times\mathbf{A}_{n+1}\,, \tag{2.3}$$

and with the help of the following vectorial rule:

$$\nabla\cdot(\mathbf{F}\times\mathbf{G})=\mathbf{G}\cdot(\nabla\times\mathbf{F})-\mathbf{F}\cdot(\nabla\times\mathbf{G})\,, \tag{2.4}$$

and after some mathematical manipulations, it is possible to find that:

$$H_{n+1}^2=\frac{1}{\mu_0}\left[\nabla\cdot(\mathbf{A}_{n+1}\times\mathbf{H}_{n+1})+\mathbf{A}_{n+1}\cdot(\nabla\times\mathbf{H}_{n+1})\right]. \tag{2.5}$$

Thus, the first integral in Equation 2.2 can be written now as follows:

$$\int_{\Re^3}\frac{H_{n+1}^2}{2}=\frac{1}{2\mu_0}\left[\int_{\Re^3}\nabla\cdot(\mathbf{A}_{n+1}\times\mathbf{H}_{n+1})+\int_{\Re^3}\mathbf{A}_{n+1}\cdot\mathbf{J}_{n+1}\right]. \tag{2.6}$$

The Stokes' theorem is applied to evaluate the first term of this integral, which states that the line integral of a specific vector function of a closed path, equals to the integral of any bounded surface for that path [59]. Consequently, it is noticed that the first term of the integral in Equation 2.6 allows defining a surface bounding the space $\Re^3$ at the infinite, and by reminding that any magnetic field on the infinite equals to zero, thanks to the Stokes theorem this first integral equals to zero, i.e.,

$$\int_{\Re^3}\nabla\cdot(\mathbf{A}_{n+1}\times\mathbf{H}_{n+1})=\oint_{S(\Re^3)}\mathbf{A}_{n+1}\times\mathbf{H}_{n+1}=0\,. \tag{2.7}$$

On the other hand, evaluating the second integral in Equation 2.6 will require the separation of variables into two volumes. These are the current densities inside the superconducting volume (Ω) and the external volume ($\Re^3\setminus\Omega$),

i.e. outside of the superconducting material (see Figure 2.1), which is translated into the following expressions,

$$\int_{\Re^3} \mathbf{A}_{n+1} \cdot \mathbf{J}_{n+1} = \int_{\Omega} \mathbf{A}_{n+1} \cdot \mathbf{J}_{n+1}(\Omega) + \int_{\Re^3 \setminus \Omega} \mathbf{A}_{n+1} \cdot \mathbf{J}_{n+1}(\Re^3 \setminus \Omega)\,. \quad (2.8)$$

Therefore, the magnetic vector potential can be defined as the sum of the local contributions and the external sources by applying the same separation of variables, and this means that:

$$\mathbf{A}_{n+1}(\Re^3) = \mathbf{A}_{n+1}(\Omega) + \mathbf{A}_{n+1}(\Re^3 \setminus \Omega)\,. \quad (2.9)$$

Thus, Equation 2.8 can be rewritten as:

$$\begin{aligned} \int_{\Re^3} \mathbf{A}_{n+1} \cdot \mathbf{J}_{n+1} = &\int_{\Omega} \mathbf{A}_{n+1}(\Omega) \cdot \mathbf{J}_{n+1}(\Omega) + \int_{\Omega} \mathbf{A}_{n+1}(\Re^3 \setminus \Omega) \cdot \mathbf{J}_{n+1}(\Omega) \\ &+ \int_{\Re^3 \setminus \Omega} \mathbf{A}_{n+1}(\Omega) \cdot \mathbf{J}_{n+1}(\Re^3 \setminus \Omega) \\ &+ \int_{\Re^3 \setminus \Omega} \mathbf{A}_{n+1}(\Re^3 \setminus \Omega) \cdot \mathbf{J}_{n+1}(\Re^3 \setminus \Omega)\,. \end{aligned} \quad (2.10)$$

Here, the underlying advantage of using a separation of variables as the one performed above, is the possibility to use the charge conservation principle $\nabla \cdot \mathbf{J} = 0$ over the whole $\Re^3$ space. Also, for the second and third terms in Eq. 2.10, one can take advantage of the duality condition in the expression for the interaction energy for a system of electrical currents at the space a and b, i.e., $\int_a \mathbf{A}_b \cdot \mathbf{J}_a = \int_b \mathbf{A}_a \cdot \mathbf{J}_b$, such that Equation 2.10 can be rewritten as:

$$\begin{aligned} \int_{\Re^3} \mathbf{A}_{n+1} \cdot \mathbf{J}_{n+1} = &\int_{\Omega} \mathbf{A}_{n+1}(\Omega) \cdot \mathbf{J}_{n+1}(\Omega) \\ &+ 2 \int_{\Omega} \mathbf{A}_{n+1}(\Re^3 \setminus \Omega) \cdot \mathbf{J}_{n+1}(\Omega) \\ &+ \int_{\Re^3 \setminus \Omega} \mathbf{A}_{n+1}(\Re^3 \setminus \Omega) \cdot \mathbf{J}_{n+1}(\Re^3 \setminus \Omega)\,. \end{aligned} \quad (2.11)$$

The equation 2.11 can be understood as follows:

1. The first term of the integral considers the electromagnetic energy inside the SC sample at the time step $n+1$, where the solution is to be determined.

2. The second term considers the set of electromagnetic perturbations induced inside the SC sample as the effect of the action of the external sources $\mathbf{A}_{n+1}(\Re^3 \setminus \Omega)$, i.e., the electromagnetic energy produced by the external source to create any profile of current $\mathbf{J}_{n+1}(\Omega)$ inside the SC sample.

3. Finally, analogously to the second term, the third term in this expression considers the set of electromagnetic perturbations or current densities that could be induced but now outside of the SC sample to complete the integral over the whole $\Re^3$ space.

Consequently, Equation 2.6 can be finally rewritten as:

$$\begin{aligned}\int_{\Re^3} \frac{H_{n+1}^2}{2} &= \frac{1}{2\mu_0}\int_{\Omega} \mathbf{A}_{n+1}(\Omega)\cdot\mathbf{J}_{n+1}(\Omega) \\ &+ \frac{1}{2\mu_0}\int_{\Omega} \mathbf{A}_{n+1}(\Re^3\setminus\Omega)\cdot\mathbf{J}_{n+1}(\Omega) \\ &+ \frac{1}{2\mu_0}\int_{\Re^3\setminus\Omega} \mathbf{A}_{n+1}(\Re^3\setminus\Omega)\cdot\mathbf{J}_{n+1}(\Re^3\setminus\Omega)\,.\end{aligned} \tag{2.12}$$

Likewise, the second term from the main Equation 2.2 is evaluated following the same arguments abovementioned, although for the sake of brevity this demonstration is avoided in this thesis, but instead, we show that the original functional to minimise, Equation 2.2, can be now written in a less complex way for its numerical processing, with elements well delimited into specific regions of the space where the physical variables have analogous meanings through the following functional:

$$\begin{aligned}\mathcal{C} &= \mathrm{Min}\,\mathcal{F}\left[\mathbf{H}_{n+1}(\mathbf{x}) := \mathrm{Min}\,\mathcal{F}\left[\mathbf{A}\,,\mathbf{J}(\mathbf{x})\right]\right. \\ &= \frac{1}{2\mu_0}\int_{\Omega} \mathbf{A}_{n+1}(\Omega)\cdot\mathbf{J}_{n+1}(\Omega) + \frac{1}{\mu_0}\int_{\Omega} \mathbf{A}_{n+1}(\Re^3\setminus\Omega)\cdot\mathbf{J}_{n+1}(\Omega) \\ &- \frac{1}{\mu_0}\int_{\Omega} \left[\mathbf{A}_n(\Omega)+\mathbf{A}_n(\Re^3\setminus\Omega)\right]\cdot\mathbf{J}_{n+1}(\Omega)\,.\end{aligned} \tag{2.13}$$

Then, if the vectorial potential $\mathbf{A}_n$ is known for an initial distribution of current $\mathbf{J}_n$, the above functional can be solved and this method is commonly known as the $\mathbf{A}-\mathbf{J}$ formulation. This formulation can ultimately be reduced to a simple $\mathbf{J}$ - formulation if the self-and mutual-inductance matrices for the elements of current can be analytically derived, which is the case for the 2D longitudinal symmetries considered in this Chapter, where the 2D geometry implies the assumption of a cylindrical cross-section of SC wire with a radius much smaller than its length.

The critical state theory for the macroscopic modelling of the electromagnetic features of type-II SCs [39, 45, 46, 60] has allowed to predict and explain various experimental phenomena, including the magnetisation and demagnetisation of SCs under crossed and rotating magnetic field experiments [61–65], the low pass filtering effect in the magnetic moment of AC SC wires [66], and strong patterns of localisation of the density of power losses inside the

SC materials under magnetic and electrical stress conditions [40, 67]. Moreover, the critical advantage of why the numerical modelling of type-II superconductors employs this geometry, relies on the fact that one can efficiently compare the numerical results with exact or semi-analytical approaches. It allows a straightforward understanding of the physics involved while a phenomenological benchmark for the implementation of practical applications is being developed.

Nevertheless, the minimisation procedure is continued in terms of identifying the function that determines the magnetic vector potential, ultimately reducing the problem to the calculation of inductance matrices that allow a clear recognition of the set of elements that plays a particular role in the minimisation procedure. For instance, inside the superconductor, it is assumed that the injected transport current can be defined as a local source that therefore, can be introduced as an external constraint. Thus, each resulting element of current inside the SC in a 2D approach can be defined by an infinitely long line of current which produces a magnetic vector potential defined as:

$$\mathbf{A}(\mathbf{r}) = \frac{\mu_0}{4\pi} \int \frac{\mathbf{J}(\mathbf{r}\,')}{|\mathbf{r} - \mathbf{r}\,'|} d^3\mathbf{r}\,' = \frac{\mu_0}{4\pi} \int_{\Omega'} \frac{\mathbf{J}(\mathbf{r}\,')}{|\mathbf{r} - \mathbf{r}\,'|} d\Omega' \,, \tag{2.14}$$

being $\mathbf{r}$ the position where the calculation of the magnetic vector potential takes place, and $\mathbf{r}\,'$ the position where the element of the current is situated.

From Equation 2.14 the minimisation procedure is reserved to take into account the magnetic dynamics into the superconducting volume (Ω), where the charge conservation condition $\nabla \cdot \mathbf{J}(\Omega)$ must be ensured. Therefore, the volume integral ($d^3r\,'$) is transformed to a surface integral accounting for the cross section (Ω') of the lines of (superconducting) current. Then, by discretisation of $\Delta A = A_{n+1} - A_n$, the minimisation principle in Equation 2.13 can be rewritten as:

$$\begin{aligned} \mathcal{C} = & \frac{1}{2\mu_0} \int_{\Omega} [\mathbf{A}_{n+1}(\Omega) \cdot 2\mathbf{A}_n(\Omega)] \cdot \mathbf{J}_{n+1}(\Omega) \\ & + \frac{1}{\mu_0} \int_{(\Omega)} \Delta\mathbf{A}(\Re^3 \setminus \Omega) \cdot \mathbf{J}_{n+1}(\Omega) \,, \end{aligned} \tag{2.15}$$

where by the use of Equation 2.14, the argument of the first integral above can be rewritten as,

$$\begin{aligned} \mathbf{A}_{n+1}(\Omega) - 2\mathbf{A}_n(\Omega) &= \frac{\mu_0}{4\pi} \int_{\Omega'} \frac{\mathbf{J}_{n+1}(\mathbf{r}\,')}{|\mathbf{r} - \mathbf{r}\,'|} - \frac{\mu_0}{2\pi} \int_{\Omega'} \frac{\mathbf{J}_n(\mathbf{r}\,')}{|\mathbf{r} - \mathbf{r}\,'|} \\ &= \frac{\mu_0}{4\pi} \int_{\Omega'} \frac{\mathbf{J}_{n+1}(\mathbf{r}\,') - 2\mathbf{J}_n(\mathbf{r}\,')}{|\mathbf{r} - \mathbf{r}\,'|} \,, \end{aligned} \tag{2.16}$$

from which is possible to demonstrate that the minimisation principle in Equation 2.1 can be defined as:

$$\begin{aligned}\mathcal{F}\left[\mathbf{A}(\cdot)\,,\mathbf{J}\in\Delta\mathbf{r}\right] = \int_{\Omega}\int_{\Omega'}\frac{\mathbf{J}_{n+1}(\mathbf{r}')\cdot\left[\mathbf{J}_{n+1}(\mathbf{r}')-2\,\mathbf{J}_{n}(\mathbf{r}')\right]}{|\mathbf{r}-\mathbf{r}'|}d^2r\,'d^2r \\ +\frac{8\pi}{\mu_0}\int_{\Omega}\Delta\mathbf{A}_a(\Re^3\setminus\Omega)\cdot\mathbf{J}_{n+1}(\mathbf{r})\,d^2r\,,\end{aligned} \tag{2.17}$$

where the vector potential in the second integral refers only to external electromagnetic sources, which for the case of an external magnetic field $\mathbf{B}_a$, with $\Delta\mathbf{B}_a = \mathbf{B}_{a,\,n+1} - \mathbf{B}_{a,\,n}$, results proportional to $\mathbf{B}_a \times \mathbf{r}_j$.

The objective function $\mathcal{C}$ is now expressed in Cartesian coordinates to reveal the inductance matrix formulation, that is practical in defining the current density vectors $\mathbf{J}_i$ in terms of the intensity of the flux current infinite elements $\mathbf{I}_i(\Omega)$. So, if we assume that the "infinite" length of the SC wire extends along the z-axis, the problem is reduced to consider elements of current with a cross-section area $\partial_{xy} = dx\,dy$, and the current flowing in the $\hat{\mathbf{z}}$ direction, i.e., it is possible to demonstrate that:

$$\mathbf{J}_n(\mathbf{r})d\,r = I_{n,x}\,d\hat{\mathbf{x}} + I_{n,y}\,d\hat{\mathbf{y}} + I_{n,z}\,d\hat{\mathbf{z}} = I_{n,z}\,d\hat{\mathbf{z}}\,, \tag{2.18}$$

with $I_{n,z} = J_{n,z}\,dx\,dy$, and $d\hat{\mathbf{z}} = \hat{u}_z dz$.

Consequently, the first term into the minimisation functional, Equation 2.17, which includes only the local terms (Ω or $\Omega' \in SC$) can be rewritten as:

$$\mathcal{C}_{local} = \int_{z,}\int_{z'\in\Omega}\frac{\eta_{n+1}\;\eta\,'_{n+1}\,d\hat{\mathbf{z}}\cdot d\hat{\mathbf{z}}'}{|\mathbf{r}-\mathbf{r}'|} - 2\int_{z,}\int_{z'\in\Omega}\frac{\eta_{n+1}\;\eta\,'_{n}\,d\hat{\mathbf{z}}\cdot d\hat{\mathbf{z}}'}{|\mathbf{r}-\mathbf{r}'|}\,, \tag{2.19}$$

where the η functions indicate current intensity of the flux lines and N is the total number of finite elements of current. Thus, in terms of a discrete mesh of finite elements, the objective function can be written as:

$$\begin{aligned}\mathcal{C}_{local} = \frac{1}{2}\sum_{i=1}^{N}\sum_{j=1}^{N}I_{i,n+1}\,I_{j,n+1}\oint_{z,}\oint_{z'\in\Omega}\frac{d\hat{z}\cdot d\hat{z'}}{|\mathbf{r}-\mathbf{r}'|} \\ -\sum_{i=1}^{N}\sum_{j=1}^{N}I_{i,n+1}\,I_{j,n}\oint_{z,}\oint_{z\in\Omega}\frac{d\hat{z}\cdot d\hat{z'}}{|\mathbf{r}-\mathbf{r}'|}\,.\end{aligned} \tag{2.20}$$

Here, one can notice that the remaining integrals depend only on the fixed positions of the finite elements inside the SC mesh (Ω), and the solution for this integral is known as the inductance matrix:

$$\mathrm{M}_{\mathcal{Z}} = \oint_{z,}\oint_{z'\in\Omega}\frac{d\hat{z}\cdot d\hat{z}'}{|\mathbf{r}-\mathbf{r}'|} := \mathrm{M}_{ij,z} = \sum_{i=1}^{N\in\Omega}\sum_{j=1}^{N\in\Omega}\frac{d_{z,i}\;d_{z,j}}{|\mathbf{r}_i-\mathbf{r}_j|}\cos\alpha_{ij,z}\,, \tag{2.21}$$

where $\alpha_{ij,z}$ represents the angle formed between the positions of the vectors $\mathbf{r}_i$ and $\mathbf{r}_j$ over the plane xy (in our case). In consequence, a generalisation of the minimisation functional accounting for the local terms of current in Cartesian coordinates could be written as follows:

$$\begin{aligned}\mathcal{C}_{local} = &\frac{1}{2}\sum_{i=1}^{Nyz}\sum_{j=1}^{Nyz}\xi_{i,n+1}\ \mathrm{M}_{ij}^{x}\ \xi_{j,n+1} + \frac{1}{2}\sum_{i=1}^{Nxz}\sum_{j=1}^{Nxz}\psi_{i,n+1}\ \mathrm{M}_{ij}^{y}\ \psi_{j,n+1}\\ &+\frac{1}{2}\sum_{i=1}^{Nxy}\sum_{j=1}^{Nxy}\eta_{i,n+1}\ \mathrm{M}_{ij}^{z}\ \eta_{j,n+1} - \sum_{i=1}^{Nyz}\sum_{j=1}^{Nyz}\xi_{i,n+1}\ \mathrm{M}_{ij}^{x}\ \xi_{j,n}\\ &-\sum_{i=1}^{Nxz}\sum_{j=1}^{Nxz}\psi_{i,n+1}\ \mathrm{M}_{ij}^{y}\ \psi_{j,n} - \sum_{i=1}^{Nxy}\sum_{j=1}^{Nxy}\eta_{i,n+1}\ \mathrm{M}_{ij}^{z}\ \eta_{j,n}\,,\end{aligned}$$

where the ξ, η, and ψ defines the intensities of current for the components of the flux lines. On the other hand, the contribution to the minimisation functional made by the external sources, i.e.,

$$\mathcal{C}_{sources} = \frac{8\pi}{\mu_0}\int_{\Omega}[\mathbf{A}_{n+1,a} - \mathbf{A}_{n,a}]\cdot\mathbf{J}_{n+1}(\mathbf{r})d^2r\,, \tag{2.22}$$

can be calculated by having in mind that the vector potential $\mathbf{A}$ that describes a magnetic uniform induction, i.e., with $\mathbf{B}$ being uniform in the space, can be expressed as:

$$\mathbf{A}_a = \frac{1}{2}\mathbf{B}\times\mathbf{r} = \frac{\mu_0}{2}\mathbf{H}\times\mathbf{r}\,. \tag{2.23}$$

Thus, by assuming that the applied magnetic field $\mathbf{H}_a$ is perpendicular to the surface of the superconductor with finite dimensions along the x and y axis, and physical reciprocity along the z axis, we can define the components of the applied field $\mathbf{H}_a$ as:

$$\mathbf{H}_a = (H_{ax}, H_{ay}, 0)\,. \tag{2.24}$$

It is to be noticed that in this case, the applied magnetic field has been considered to be uniform along the whole space, regardless of its direction. However, all the statements above mentioned, which have been used for the introduction of the general minimisation functional for type II superconductors, and consequently of Equation 2.17, are equally valid for non-homogeneous applied fields, with the exemption that that the components of the external applied magnetic field components would need to be defined as spatial coordinates dependent functions. Thus, and for the sake of simplicity, within the approach of uniform applied magnetic field, the magnetic vector potential $\mathbf{A}_a$ results:

$$\begin{aligned}\mathbf{A}_a &= \frac{\mu_0}{2}(H_{x,a}\hat{u}_i + H_{y,a}\hat{u}_j)\times(x\hat{u}_i + y\hat{u}_j + z\hat{u}_k)\\ &= \frac{\mu_0}{2}(H_{x,a}y - H_{y,a}x)\hat{u}_z\,.\end{aligned} \tag{2.25}$$

Having determined the external vector potential $\mathbf{A}_a$ into the superconducting volume produced by an external magnetic source, we can finally rewrite the component $\mathcal{C}_{sources}$ of the minimisation functional ($\mathcal{C} = \mathcal{C}_{local} + \mathcal{C}_{sources}$) in discretised form as:

$$\begin{aligned}\mathcal{C}_{sources}\frac{8\pi}{\mu_0}\int_\Omega \Delta\mathbf{A}_a\cdot\mathbf{J}_{n+1}(\mathbf{r})d^3r &= \frac{8\pi}{\mu_0}\int_\Omega \frac{\mu_0}{2}\Delta(H_{a,x}y - H_{a,y}x)\,I_{z,n+1}d\Omega \\ &= 4\pi\sum_{i=1}^{N\in\Omega}(y_i\Delta H_{a,x} - x_i\Delta H_{a,y})I_{i,n+1} \\ &= 4\pi\sum_{i=1}^{N\in\Omega}\left[y_i(H_{a,x,n+1} - H_{a,x,n}) - x_i(H_{a,y,n+1} - H_{a,y,n})\right]I_{i,n+1}\,.\end{aligned} \tag{2.26}$$

Thus, we have implemented a time-discretisation for the different components of the applied magnetic field $\mathbf{H}_a$, such that together with Equations 2.13 & 2.22, this forms a complete general formulation for 2D type-II superconductors easily implemented into minimisation algorithms for the numerical solution of the problem. The critical state law, $|I_i| \leq |I_c|$ and the transport current condition are the only two additional constraints (equations) that need to be included to solve the problem, where the latter reads as follow:

$$\int_\Omega \mathbf{J}\cdot\,\hat{n}d\Omega = I_{tr} \therefore \sum_{i=1}^{N\in\Omega} I_{i,n} = I_{tr,n}\,. \tag{2.27}$$

Thus, the problem has been reduced to the specific geometry or shape of the finite elements defining the mesh that represents the SC region (Ω), and consequently the calculus of the fundamental inductance matrices, which is a topic well studied in the literature [68–70]. Also, as the inductance matrix values are time-independent, their calculation can be done before the minimisation process, reducing the computing time.

Moreover, the general formulation for 2D type-II superconductor derived from Equation 2.22 & 2.26 is known as either J-formulation or the integral formulation of the critical state model [40, 71], which allows determining the local dynamics of current density profiles. It is comparable to numerical solutions utilising other finite element methods, but which focus on the direct numerical solution of the set of partial differential equations of Maxwell (Equations 1.3 - 1.6), such as the so-called H-formulation [72]. It is a versatile, broadened numerical method that avoids the use of a minimisation algorithm to solve problems, but at the expense of considering the entire $\Re^3$ space, and not only the SC domains Ω (Figure 2.1). However, it can be implemented in popular FEM modelling packages used in academia and industry as well, such as COMSOL Multiphysics [61–63], such that the solution to many problems in complex geometries where the inductance matrices are unknown can be addressed.

Nonetheless, in Part I of this study, a free software licence called *Lancelot* [73], was used for the computational minimisation process in MatLab. *Lancelot* has the advantage of automatically adjusting the penalty parameter and Lagrange multiplier estimates. This ensures the convergence of the constrained optimisation problem to a global solution, which is done through implementing the convex region or trust-region approach into the quadratic model of the optimisation function or augmented Lagrangian function, and within the constraints that characterised the physics behind the control variable. Afterwards, the use of either direct-matrix or truncated conjugate-gradient algorithm systematically modifying the trusted region size, facilitates the improvement of the quadratic model in a manner to avoid the propagation of local minima. The reader is advised to refer to Lancelot [73, 74] for more technical details on its application, and how other problems can be solved, as a description of this computational package and the algorithms that support it are beyond the scope of this thesis. Likewise, the computational method that has been implemented in this part of the study for the solution of the minimisation functional (Equation 2.1), has been already described in a detailed manner in [1]. Still, for the ease of the reader, the following subchapter presents a brief summary of the computational scheme invoked in this study, where the extent of additional computational packages for data handling and post processing could be visualised.

2.2 *Computational Scheme*

This part of the study focuses on implementing the derived **J**-formulation into a computational method capable of handling large nonlinear optimisation problems. Recall that only the unspecified components of current within the superconducting sample ($\mathbf{J}_{n+1}$) are present for the computation. Thus, this significantly reduces the number of the unknown variables when compared to the **H** or $\mathbf{A}-\mathbf{J}$ formulation as **J** is only confined within the Ω (Figure 2.1). Numerically, this framework aims to obtain a reasonable understanding of how the critical state problem is approached from the computational point of view and in a practical manner, but without discussing the algorithms of minimisation that can be found by default in many computational packages commercially available. Instead, the list of case-oriented packages below, summarise the computational tools employed to handle different stages of the numerical process for a thorough engineering analysis and understanding of the physical properties of the SC system in this study:

1. Design a grid of finite elements for Ω,
2. Define the time-space dependent experimental conditions of the system $(H_a(t), I_{tr}(\mathbf{r}, t))$,
3. Create hyper matrices for proper storage of large amount of data,
4. Calculate the inductance matrices and call a global minimisation algorithm such as *Lancelot*,
5. Compute the magnetisation of the system,
6. Compute the magnetic vector potential locally,
7. Compute the resulting electric field,
8. Compute the resulting magnetic field,
9. Compute the instantaneous and hysteretic energy losses of the system, and finally
10. Plot the results obtained at the level of detailed required.

First of all, designing a grid makes it possible for a superconducting volume (Ω) to be described as a set of elements $(\Delta\Omega_i)$, and distinctively defining them by a current density that flows across the coordinates $(\mathbf{r}_i)$. Afterwards, the inductance coefficient matrices are calculated between the elements $\mathbf{J}(\mathbf{r}_i)$ and $\mathbf{J}(\mathbf{r}_j)$ for the entire set of conceivable couples $(\mathbf{r}_i, \mathbf{r}_j) \in \Omega$, with the result saved on the computer hard drive. It is worth mentioning that these values need to be saved at each iteration (time-step) by the solver, and therefore the resulting files can sometimes be substantially large (in the order of gigabits). However, if this occurs, Matlab employs the hyper matricial formalism for data storage, such that it is possible to create tridimensional (i, j, k) matrices with, for instance, the i, j elements storing physical information for elements situated at the coordinates x_i, y_i respectively, whilst the k-layer identifies the time-step number within a discretised experimental process. Therefore, the subsequent stage is to define the experimental conditions or the temporal evolution of the EM sources such as $I_{tr}(t)$, $H_a(t)$, or both.

The time domain is introduced through adequate steps of a small path for the external electromagnetic sources, i.e., the experimental conditions need to be linked by finite difference expressions in a manner that $\Delta\mathbf{H}_0 = \mathbf{H}_{n+1} - \mathbf{H}_n$, with the related distribution of current $\mathbf{I}_{n+1}$ playing the role of the unknown variable. Then, it is noticed that the latter part of Equation 2.26 contains precisely the expression of the temporal evolution of the external magnetic field along the x and y directions. Furthermore, as the values of the elements of

current at the initial time-step, $\mathbf{I}_n(\mathbf{r})$, are assumed to be known beforehand, for instance by assuming that $I_{tr} = 0$ at $t = 0$, it is possible to calculate the linear elements inside the argument of the objective functional before proceeding with the minimisation. In practical terms, the time stepping for the AC external excitations is introduced by the discretisation of the peak to peak positive values of at least 1000 time-steps for adequate numerical convergence within an error tolerance of less than $|1 - J_i/J_c| < 10^{-6}$ between internal minimisation processes [73]. Likewise, it is worth mentioning that although the calculations here presented are non-dependent on the frequency of oscillation of the electromagnetic excitations, these are expected to be valid at last for frequencies below the radio frequencies spectrum ($< 20KHz$) [75–77], where the majority of power transmissions systems operates at just 50 Hz to 60 Hz.

A noteworthy fact is that the objective function size hugely relies on the formulation of the mathematical problem and its intrinsic geometry (if any). For instance, concerning the objective function, the most common and preferable way to reduce the number of the computing elements is subdividing or splitting the problem into relatively loose linked subsystems. It implies that internal operations that do not rely on the variables of the minimisation need to be assigned to preconditioners or external operations that can be calculated outside the minimisation algorithm, such as the case of the inductance matrices which do not depend on the time evolution of the electromagnetic quantities. In this way, using available software with standard optimisation tools like *Lancelot* [73] allows more rapid incursion of the variables, thus, lessening the computational time.

In summary, in order to minimise an objective function into *Lancelot*, the minimisation functional needs to be expressed into a standard input format (SIF) file, which enables the communication between the subprograms and the optimisation algorithms provided by *Lancelot*. Therefore, defining the optimisation problem in the SIF decoder would involve writing one or more files, in an orderly manner that satisfies the role of the introduced set of preconditioners for the objective function. At this point, the input elements for the objective function or the minimisation functional have been arranged, correspondingly with the number of variables and the time evolution that relies on the experimental conditions. Into the SIF, the objective function is subdivided into at least two groups that are the quadratic elements (nonlinear) and the linear elements of the minimisation functional. Also, the first derivative of the element variables can be included if an analytical solution is known, although this is not mandatory. Even the Hessian matrix (second-order partial derivatives of a scalar field or scalar-valued function, usually a square matrix) of the objective function can also be included if the second-order partial derivatives of the entire set of the minimisation variables are known. Otherwise, it considers

a finite difference method as a means of approximating the derivative of the nonlinear element functions. For this reason, it is vital to assure the adequate definition of mathematical constraints with a physical meaning. If not, the system could converge to unrealistic solutions.

In the event of complications in the numerical convergence due to numerical noise, *Lancelot* enables the use of lists of scaling factors that are applied separately to variables and general constraints before initialising the optimisation. This approach allows the groups of elements in a highly nonlinear optimisation to be handled effectively as those herein considered. However, we do not recommend the use of scaling factors, and instead, we recommend the reduction of the time stepping. The latter is the approach considered here to ensure efficient convergence. After this, given the solution of the problem, i.e., getting the profiles of current $I_{i,n+1}$ across the entire section Ω, the calculation of all the other physical quantities such as $\mathbf{A}$, $\mathbf{B}$, $\mathbf{E}$ and the derived quantities such as magnetisation and energy losses is conceivable. Thus, the next section will be focused on the results derived from the electromagnetic response of rounded SC wire exposed to a transverse magnetic field and transport current (Figure 2.2).

2.3 *SC DC Wires Under Transverse Oscillating (AC) Magnetic Field*

In an attempt to replicate the conditions where the influence of accommodating a DC SC wire into existing duct banks could be studied and how these relate to the most popular semi-analytical approaches, in this subchapter a comprehensive study of the electromagnetic modelling of type-II rounded superconducting wires (infinitely long wire compared to the dimensions of its cross-section) is presented. It illustrates the physical behaviours related to its local electrodynamics under the simultaneous action of an oscillating external magnetic field $B_{0y}(t)$, and DC transport current $I_{tr}(t)$. This experimental condition constitutes a further step in the attempt to understand and observe the response of the electromagnetic properties and the local effects associated to the hysteretic losses inside type-II SC wires. In this sense, to assist the reader in visualising the conditions that can describe different situations in which it is possible to obtain numerical solutions for the interplay between the above electromagnetic excitations, the study considers the effect of introducing two different cases in terms of the magnetisation state of the SC wire (see Figure 2.2 & 2.3), with their experimental processes described as follows:

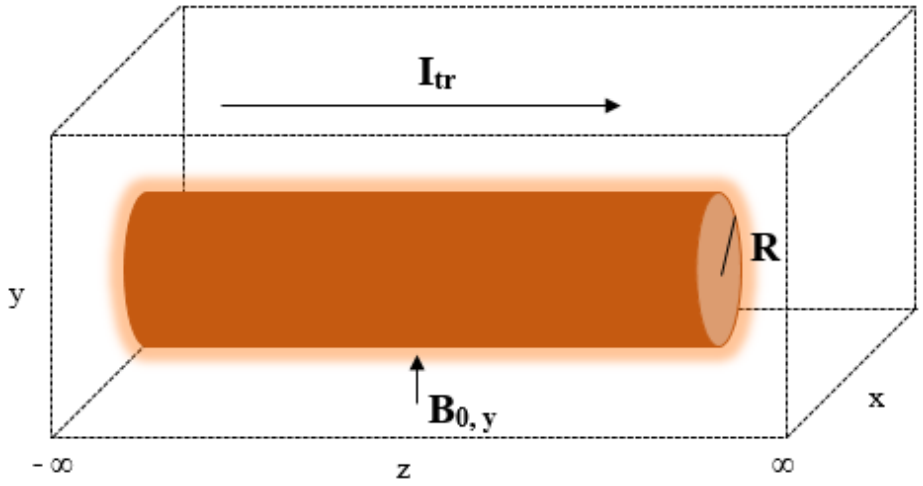

Figure 2.2: Pictorial representation of the experimental configuration showing an infinitely long rounded SC wire of radius R exposed to a transverse magnetic field and longitudinal transport current over the xy plane.

1. The DC transport current is applied (injected) to a SC wire until reaching a maximum value (I_a) after which it remains constant. Then, an oscillating magnetic field of amplitude B_a (see Figure 2.3 (a)) is applied, and the energy losses of the system is studied. In this sense, the SC sample is considered as magnetically virgin (zero magnetisation) before the activation of the AC field.

2. In this case we assume that before triggering the DC transport current, the SC wire is previously magnetised. To simulate this condition, firstly, the wire is subjected to an oscillating (AC) magnetic field of specific amplitude. Once a full magnetic hysteretic cycle is achieved, the ramp of transport current I_{tr} is activated until it reaches a maximum DC value. Then, a new hysteretic behaviour starts, covering the simultaneous action of the AC field and DC current regardless of the initial magnetisation of the SC wire(see Figure 2.3 (b)).

Thus, this part of the study focuses mainly in the two essential electromagnetic measurable quantities from the macroscopical point of view. Firstly, the hysteretic AC losses of the rounded SC wire per unit volume (Φ) and time, with finite cross-section Ω, and for a cyclic excitation of frequency ω, which is calculated by the closed integral of the local density of power dissipation ($\mathbf{E}\cdot\mathbf{J}$) after the period elapsed for the magnetic relaxation of the profiles of current density, i.e., for the hysteretic cycle ($h.c$), according to the following equation:

$$L = \omega \oint_{h.c.} dt \int_{\Phi} \mathbf{E}\cdot\mathbf{J} d\Phi \,, \tag{2.28}$$

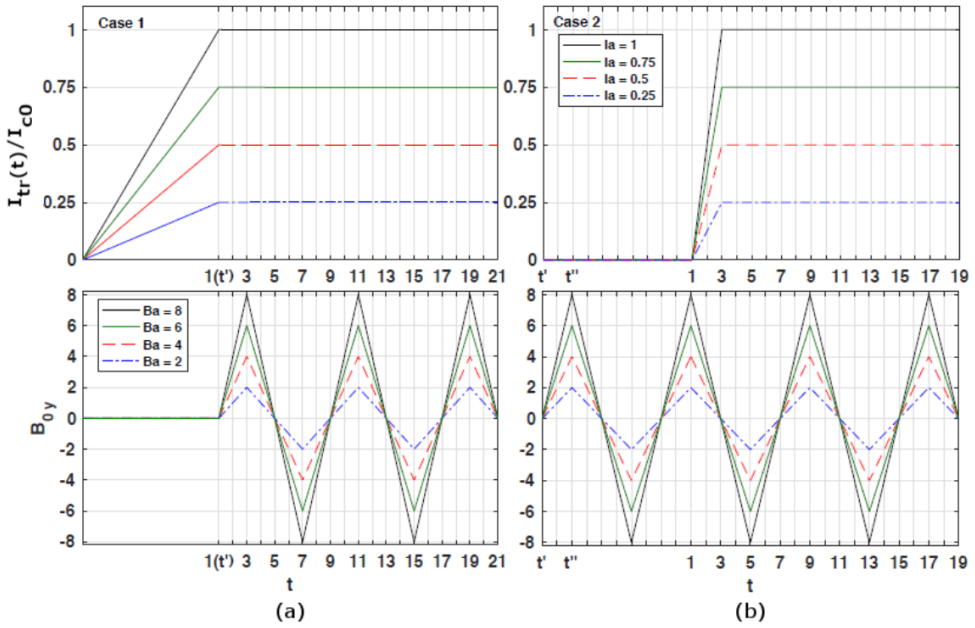

Figure 2.3: Sketch of the time-dependent experimental process analysed in this chapter, where a rounded type-II SC wire as the one illustrated in Figure 2.2, is subjected to the simultaneous action of an external magnetic field, B_{0y} (in the units of $(\mu_0/4\pi)J_cR$), and transport current $I_{tr}(t)$ (top and bottom panes), of amplitudes B_a and I_a, respectively. (a) left pane or case 1, represents the situation when the DC current is applied to a magnetically virgin SC sample, whilst in the right pane (b) the case 2 shows an analogous situation but for a premagnetised sample.

where the duration or time steps defining the beginning and end of the hysteretic cycle can be achieved either by inspection of the numerical results for the profiles of current density, or by the symmetry of the derived magnetisation loop as it will be shown in the following subsections. Thus, the second macroscopic quantity to be studied, i.e, the magnetisation of the SC sample, will be represented by a magnetisation loop which can be calculated as the integral of the local magnetic moments (per unit length, I) inside the superconducting wire, as follows:

$$\mathbf{M} = \frac{l}{2}\int_{\Omega} \mathbf{r} \times \mathbf{J} d\Omega \,, \tag{2.29}$$

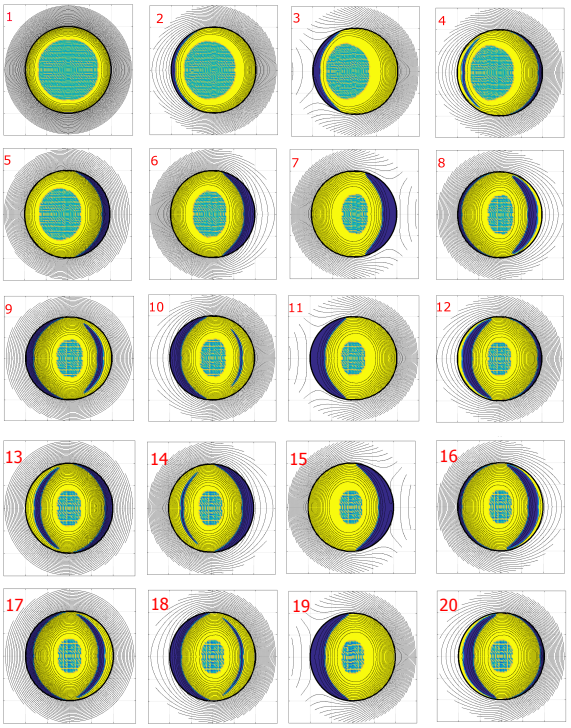

Figure 2.4: Evolution of magnetic flux lines and their corresponding current profiles inside the SC rounded wire of radius R, for an AC magnetic field of amplitude $B_a = 2$ (low field) and a DC transport current of moderate intensity $I_{tr} = 0.5I_c$, accordingly with the experimental process shown in Figure 2.3 (a). Darker (blue) regions indicates zones with negative elements of current density $J_i = -J_c$, and the lighter (yellow) regions correspond to $J_i = +J_c$, otherwise (green) it corresponds to the flux free core where J_i and B_i are both equal zero. Subplots are labelled according to the monotonic branch of the experimental processes depicted in the Case 1 of Figure 2.3.

2.3.1 *Magnetically Virgin DC SC wires under transverse AC magnetic field*

A rounded type-II SC wire (Figure 2.2) which is at the same time exposed to both, an AC external magnetic field and an injected DC transport current is being explored. It shows a comprehensive view on the physical characteristics of the local distribution of profiles of current density J_i, evolving as a function of time when considering the experimental process displayed in Figure 2.3 (a). The time step '1' in Figure 2.3 is also labelled as the first subplot for easy visualisation, such that each additional time step considers an added field gra-

dient of $\Delta B = B_a/2$. As observed therein, the SC sample is initially subjected to a linear ramp of transport current, until it reaches the desired DC value. Therefore, the profiles of current density before t', i.e., the time step when the external magnetic field is activated, shows the classical concentric behaviour with elements of current occurring from the sample's surface towards its geometrical centre, as the intensity of the transport current I_{tr} increases. The resulting profile of current density at this time step, '1', for a maximum transport current $I_a = 0.5I_c$ is displayed in the first subplot of Figure 2.4. Then, after t', the applied transport current remains in the DC condition, while an oscillating AC magnetic field of $B_a = 2(\mu_0/4\pi)J_cR$ is being applied perpendicularly to the surface of the SC wire (see Figure 2.2). Thus, before reaching the first peak of the AC magnetic field at the time step '3', it is possible to observe in Figure 2.4 the diverse patterns of evolution for the flux front profile, where it displays the competition between the introduced magnetisation currents and the injected transport currents. This results in a noticeable distortion of the axisymmetric orientation of the original circular flux front profile, found at t', i.e., when $I_{tr} = I_a$ and $B_{0y} = 0$, to the time step '3' when $I_{tr} = I_a$ and $B_{0y} = B_a$. However, the circular shape of the flux front profiles are expected to be slightly distorted during the first cycle of AC magnetic excitation for an AC magnetic field (no transport current) [66] of non-dimensional units $b_a = B_a/B_P \leq i_a$, being $B_P = 8\ (\mu_0/4\pi)J_cR$ the analytical solution for the minimum value of applied magnetic field needed to saturate the magnetic moment of the SC wire, and $i_a = I_a/I_c$ with I_c the critical current of the SC wire. This distortion affects the position of the centre of the flux free core (current free region) causing it to displace from the geometrical centre of the SC sample towards its left side given the positive slope of the applied magnetic field, which adds positive profiles of magnetisation currents at the positive x-quadrants of the SC body.

On the other hand, a more acute distortion and displacement of the flux front profile is observed if $b_a > i_a$. It is due to the added profiles of magnetisation current, which could eventually lead to the entire disappearance of the flux free core in the SC wire when B_a reach B_p, i.e., $b_a = 1$. It is worthy of mentioning that in the case of DC superconducting wire under AC field conditions (see Figure 2.3 (a)), the origin of the deformation of the flux front profile is not caused by the consumption of magnetisation currents, as it is the AC wires considered in [40, 66]. It is because the applied transport current considered in our case is constant. Consequently, the total domain occupied by the current profiles cannot change; instead, it redistributes across the cross-section of the SC sample. Therefore, the occurrence of magnetisation currents exerts a Lorentz force in the presence of external AC field, which push the distribution of local elements with transport current density $J_i = J_c$ inwards.

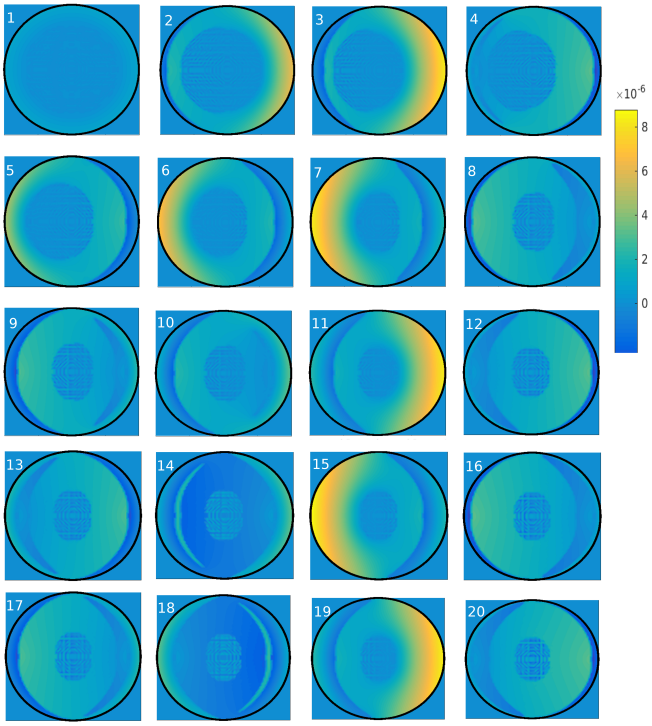

Figure 2.5: Local density of power dissipation $\mathbf{E} \cdot \mathbf{J}$ corresponding to the current density profiles shown in Figure 2.4.

It results in the reduction of the total domain of the flux free core until its disappearance, due to the intensity of the applied magnetic field being enough to saturate the SC sample (see Figure 2.6). The outcome of the Lorentz force introduced into the system through the presence of magnetisation currents increases the local density of power dissipation, also called local energy losses $\mathbf{E} \cdot \mathbf{J}$ (see Figure 2.5). This fact provides a direct explanation of why the AC losses in SC wires exposed to AC fields and DC transport currents are higher compared to the ones subjected to both AC field and AC transport current. In this sense, this study presents a similar comparison between numerical and semianalytical approaches [48] as the one shown in [40] & [66], where from the authors' knowledge it is the first time when proper numerical calculations of the AC losses of SC rounded wires subjected to AC field and DC conditions are shown. It demonstrates that in reality, the use of empirical equations such as the Gurevich approaches [48], can underestimate the actual energy losses of the system even for low values of the magnetic field and transport current.

Continuing with our discussion on the physical features of the distribution of elements of current density profiles, as shown in Figure 2.4 for the experimental condition displayed in Figure 2.3 (a). Therein, the first peak-to-peak

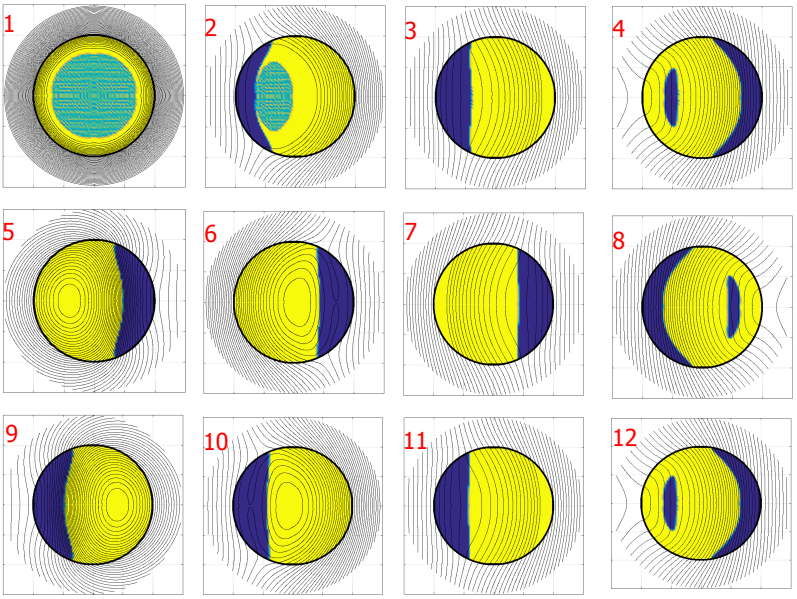

Figure 2.6: Same as Figure 2.4 but for $B_a = 8$ (high field) and a DC transport current of moderate intensity $I_{tr} = 0.5I_c$.

cycle accounts for the time elapsed between the time steps '3' to '11', i.e., the first cycle of the AC field, and it cannot be considered for the calculation of the actual AC-losses of the SC wire. This is because of the size of the flux free core which keeps changing during this period until reaching the smallest possible area with a null magnetic field gradient, i.e., the global state of minimum energy. In simpler terms, the distribution of profiles of current density at the time step '3' and '11' (peak-to-peak) do not convolute to each other, which can be easily seen by observing the corresponding profiles of current density (Figure 2.4). It results in a net energy loss not accounted for when the first cycle of the AC field is considered as the foundation for the calculation of the AC-losses. However, when the second cycle is considered, i.e., from the time step '11' to '19', it can be seen in Figure 2.3 (a), how the distribution of current density across the SC sample returns to its initial state of hysteretic magnetisation. Therein, the hysteretic losses of the SC wire (per cycle) do not depend any longer on the previous magnetic history, i.e., the profiles of the flux front along the subsequent cycles become identical to those between time steps '11' to '19'. Consequently, this phenomenon can also be observed in the patterns of the local density of power dissipation (Figure 2.5), and the corresponding magnetisation curve displayed in Figure 2.7, where the magnetisation loop $M_y(B_{0y})$ does not close at the end of the first cycle of the AC field

excitation. However, when the applied AC magnetic field is intense enough to saturate the SC wire with DC transport current, before completing the first AC cycle, as observed in Figure 2.6, the AC losses therein can be calculated from the magnetic history included during this period (time steps '3' to '11'). It shows then a negligible variation of the magnetisation loop after the first cycle, observed in Figure 2.7.

On the other hand, it is possible to observe that in all the cases, the occurrence of magnetisation currents flowing in the opposite direction of the injected current is always discernible from the transport current profiles. However, it is not possible to discern the elements of 'positive' current density $J_i = J_c$ that correspond either to the magnetisation currents or transport current (see Figure 2.5 or 2.6). This fact also explains why it is not appropriate to compute the AC losses as the simple sum of isolated excitations. However, studying the density of power dissipation at a local level, i.e., inside the SC sample, within the magneto-quasi steady approach [46], it is possible to observe (see Figure 2.5) that the maximum dissipation of energy by the thermal activation of vortices always occurs in the active zones. It is where the patterns of transport current are present (see Figure 2.4), and also are being pushed inwards due to the occurrence of magnetisation currents exerting Lorentz Force at the outer layers of the SC. This flows in the same direction as the injected transport current previously discussed above. This behaviour is axisymmetric along the axis dominated by the direction of the applied magnetic field (y-axis, see Figure 2.2). Nevertheless, due to the lack of Lorentz force compensation along the x-axis by the non-homogeneous distribution of profiles of current density $J_i(\mathbf{r}) = J_c$, the release of energy is also asymmetric along its orthonormal.

Nevertheless, concerning the magnetisation loops derived from our experimental conditions, a very striking feature is observed in Figure 2.7. Therein, as the DC transport current increases, the shape of the magnetisation loop becomes more squared-shaped, reaching the saturation of the magnetic moment $M_y(B_{0,y})$ at AC magnetic field of amplitudes lower than $B_p = 8$. In this sense, contrary to what is commonly expected for the DC SC wires under transverse AC magnetic field, the saturation of the magnetic moment of the SC wire is conceivable at a field lower than the full penetration field ($B_p = 8$). This occurrence can be observed after two full cycles of an AC field of intensity as low as $B_a \geq 2$ for DC currents greater than $I_{tr} = 0.75I_c$, or even for low DC currents such as $I_{tr} = 0.25I_c$ with $B_a \geq 5$. The phenomenon observed in Figure 2.7 implies that when the SC wire exhibits the full saturation state, there is the possibility to achieve a fast transition from the magnetically stable region with a positive (or negative) constant magnetic moment towards its counter magnetic moment of the same amplitude. Therefore, it reveals the possibility to establish well-defined Boolean data type in DC superconducting

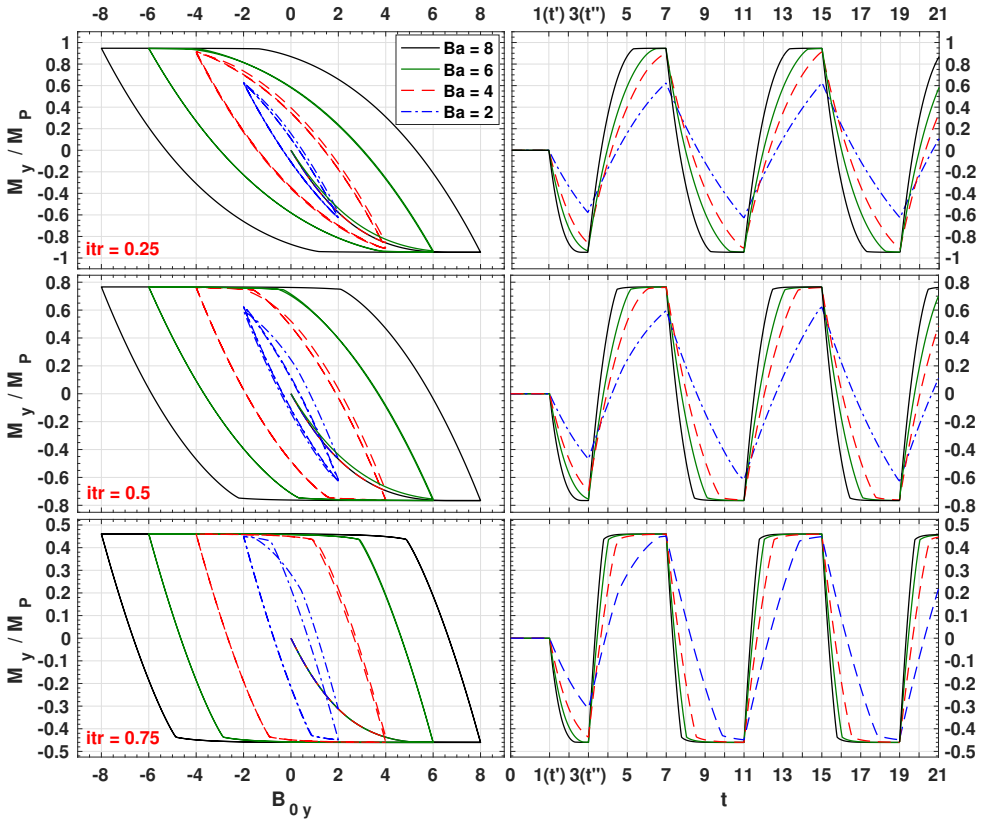

Figure 2.7: Dimensionless magnetisation curves (M_y/M_P) as function of the AC applied magnetic field B_{0y} and the temporal/experimental process displayed for Case 1 shown in Figure 2.3 (a). $M_P = 2J_cR^3/3$ is the analytical solution for the magnetic moment of the sample when it is fully penetrated by a field $B_P = 8$ with zero transport current. Recall that units for B are $(\mu_0/4\pi)J_cR$, R is the radius of the SC wire, and I_{tr} is given in units of I_c.

wires that are subject to transverse AC magnetic fields. In other words, under the right conditions of direct transport current and AC applied magnetic field, the usefulness of a superconducting wire goes beyond the incredibly low losses that SC materials provide (compared with conventional conductors) and their resilience properties under power fault conditions [58]. It also considers the possibility of transferring magnetic logic data without interfering with the transmission of transport current, and regardless of the amplitude of B_a utilised for the sending and receiving a magnetic logic data, the DC condition is always the same (neglecting any losses added by the SC joints). Thus, the transmission of magnetic logic data depends on the history of the transverse magnetic excitation B_0, and it might be conceivable with proper cryptographic conditions alongside a well-defined Boolean structure.

Thus, the evolution of the magnetic moment M_y in Figure 2.7 as a function of the time-dependent external magnetic excitation $B_{0y}(t)$ (see Figure 2.3) is analysed in detail. This is to show how to read a Boolean logic from the magnetic moment profile of DC superconducting wires subjected to AC transverse magnetic field. Let us recall that under the critical state regime, the resulting magnetisation loop for type-II SCs given the experimental condition; $I_{tr} < I_c$ and $B_{0y} > 0$ valid for at least frequencies lower than 300 MHz [54], depends on the field amplitude B_a. It does not depend on the frequency and time-dependence of the function that describes the oscillation of the external magnetic field $B_{0y}(t)$, either triangular or sinusoidal. Nevertheless, at a time-step t, the actual value of the magnetic moment at a specific value of applied magnetic field depends on its history, i.e., on its current value $B_{0y}(t)$ and on the sign of its rate of change $\Delta B_{0y}(t) = B_{0y}(t) - B_{0y}(t-1)$. Thus, the study reveals that for an experimental condition where $I_{tr} \geq 0.5I_c$ and $B_a \geq 6$, it exhibits two well-defined regimes of saturation with maximum or minimum magnetic moments. It shows the applied magnetic field range from 0 to $\pm B_a$, and constant level of the magnetic moment at $\mp M_{p'}$, where $M_{p'}$ is the resulting saturated magnetic moment, usually less than $M_p = 2/3(J_c R^3)$, which is the maximum magnetic moment achievable by SC wire when $I_{tr} = 0$, i.e., in the absence of transport current. This view is understood by observing the magnetisation curves at $I_{tr} = 0.75I_c$ (bottom pane) and $B_a \geq 6$ (solid lines) in Figure 2.7. It is noticed that the magnetic moment therein is constant $M_{p'} \approx 0.4601$ for any magnetic field within the regime of the time steps '5' and '7', i.e., from $B_{0y} = 0$ to $B_{0y} = -B_a = -6$. On the other hand, when the slope of the change rate of the oscillating magnetic field sign varies from $B_{0y} = -B_a$ to $B_{0y} = 0$, i.e., between the time steps '7' and '9', the polarity of the magnetic moment quickly converts to $-M_{p'}$. The same occurrence is observed for lower amplitudes of the magnetic field $B_a = 4$. The results differ with 2.43% smaller magnetic moment at $B_{0y} = 0$ and $M_{p'} \approx -0.44489$ at the time step '5', and $M_{p'} \approx 0.44489$ at the time step '9'. It generates a minimum error margin for defining Boolean states at external AC fields of amplitudes as low as $B_a = 4$.

The same analysis is performed but for lower intensities of the DC transport current, $I_{tr} = 0.5$ (mid-pane of Figure 2.7), which experiences the same Boolean behaviour for the magnetic moment, $M = \pm M_{p'} = \pm 0.7661$ obtained between the intervals of applied AC field $B_{0y} = 0$ to $B_{0y} = \mp B_a$ with $B_a \geq 6$ (solid lines). Therefore, we can conclude on two key facts from the findings in this section. Firstly, is that for any value of the AC applied magnetic field with both negative intensity and negative tendency $\Delta B_{0y}(t)$, the magnetic moment of the wire keeps at the positive saturation value $M_{p'}$. Secondly, for the positive intensity of the applied field and a positive tendency $\Delta B_{0y}(t)$, the magnetic

moment of the wire corresponds to the negative state $M_{p'}$. Otherwise, the magnetic moment of the SC wire will be defined between the transient states $\pm M_{p'}$, and it allows to define a third logic input for $|M| \neq M_{p'}$ with the sign of B_{0y} different to the sign of ΔB_{0y}. Also, this result is valid for a premagnetised SC wire before triggering the DC transport current, as shown in the Chapter 2.3.2.

2.3.2 *Premagnetised DC SC Wires Under Transverse AC Magnetic Field*

In an attempt to understand the possibility of observing patterns of magnetisation loops as the ones described above, but in more general conditions where the superconducting wire can be previously magnetised (Figure 2.3 (b)), a similar study to case 1 is performed. This condition takes into account the premagnetisation of the SC wire after completing a full hysteresis cycle of $B_{0y}(t)$ before the simultaneous action of the transport current.

Comparable to the results displayed in Figure 2.4, Figure 2.8 presents the dynamics of magnetic flux lines and profiles of current density for a low amplitude of the external magnetic field, $B_a = 2$, and moderate-intensity of the DC transport current, $I_{tr} = 0.5$. It can be seen that the main difference between these two figures corresponds to the initial state ($t = 1$). It is a condition where the SC wire reaches the DC value before applying the AC field (Case 1), or the SC wire is premagnetised before turning on the DC transport condition (Case 2). Therefore, it results in an initial flux-front of circular or semi-elliptical shape, respectively.

For Case 1, a cyclic hysteretic behaviour can be seen after 3/4 of the AC magnetic excitation, i.e., from the time step '7', as shown in Figure 2.3 (a). Observed therein is a cyclic behaviour between positive peaks of the magnetic field (the time steps '11' to '19'), i.e., the second positive peak-to-peak cycle of B_{0y} or the first negative peak-to-peak cycle (time steps '7' to '15'). However, when the SC wire is premagnetised (Figure 2.8), a hysteretic cyclic behaviour is not stablished until time step '9' to '17', i.e., during the third peak-to-peak cycle of the oscillating magnetic field. This process that spans two peak-to-peak cycles of B_{0y} is the stabilisation period of the profiles of current density, also known as magnetic relaxation. Nonetheless, once this period is overcome, the resulting evolution of magnetic flux lines and the corresponding profiles of current density inside the SC wire for either the magnetically virgin or premagnetised condition does not depend on the magnetic history of the SC

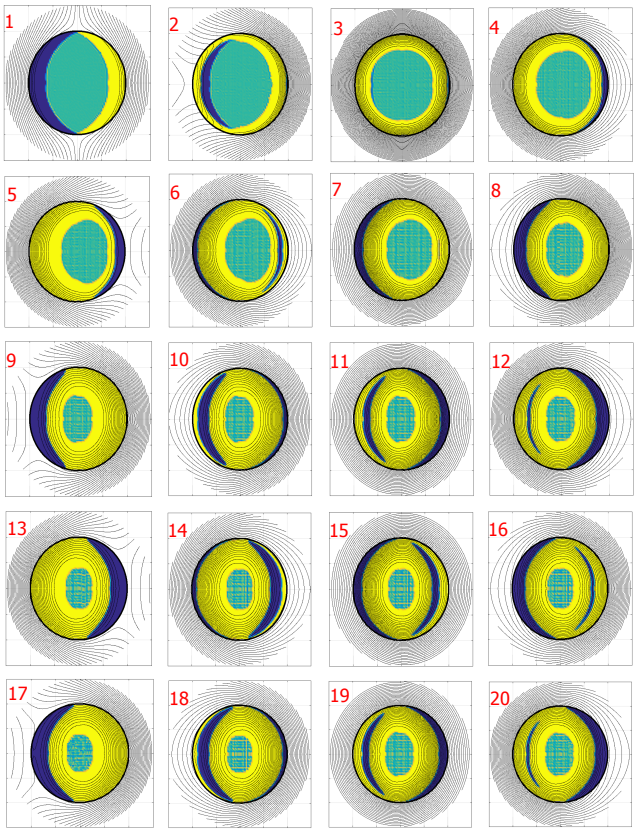

Figure 2.8: Same as Figure 2.4 but for the Case 2 in Figure 2.3 (b).

wire. Furthermore, a direct comparison of the subplots '11' to '19' in Figure 2.4, with the corresponding subplots '9' to '17' in Figure 2.8 reveals this observation. Therein, it shows that the dynamics of the magnetisation loops produced by the oscillating magnetic field remains the same after the magnetic relaxation moment is overcome, regardless of the initial magnetisation condition of the DC superconducting wire.

Likewise, for high field conditions $B_a = 8$ or $b_a = 1$, the same result can be observed by a direct comparison between the profiles of current density and lines of the magnetic field for case 1 and 2, displayed in the subplots 3 to 11 in Figure 2.6 and subplots 9 to 17 in Figure 2.9, respectively. In this instance, the stabilisation process in Case 1 lasts for only 1/4 of the AC magnetic excitation, with full saturation of the SC wire reached within this period. Consequently, after overcoming the magnetic stabilisation period, the dynamics of the magnetisation loops produced by the oscillating magnetic field remains the same, regardless of the initial magnetisation condition of the DC superconducting wire. The evidence of its magnetic history can be

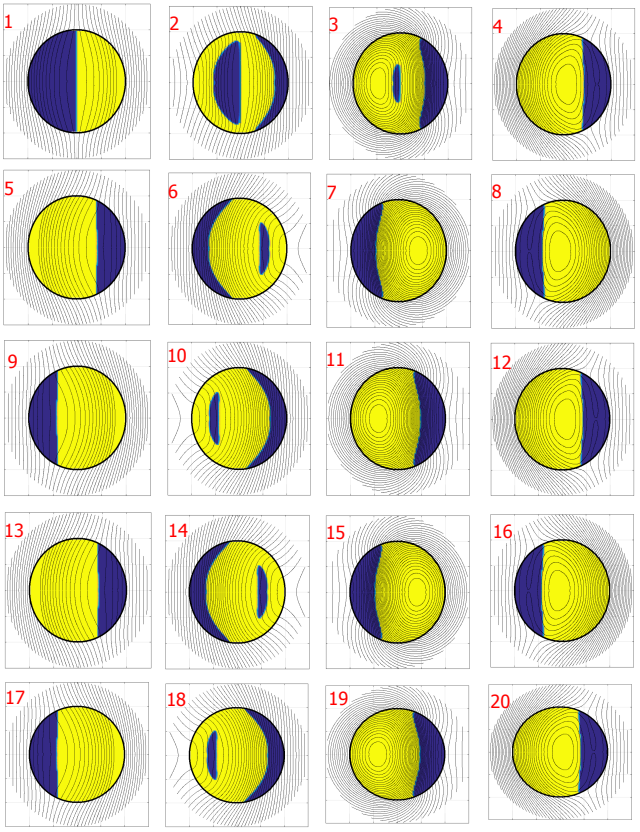

Figure 2.9: Same as Figure 2.4 but for the Case 2 in Figure 2.3.

seen only through the magnetic moment for the first cycle of the magnetic excitation displayed in Figure 2.10. In other words, Figure 2.7 shows the quasi-square shape of the magnetisation loops that have been observed previously for magnetically virgin SC DC wires and their intrinsic Boolean characteristics for specific values of B_a and I_{tr}. They appear to be a general characteristic of considering SC wires with DC conditions for the transport current and a simultaneous AC transverse magnetic field, regardless of the magnetic history of the SC wire. Therefore, by selecting the right cycles of hysteretic behaviour, we have found that the resulting AC-losses in both systems is the same (see Figure 2.11). Although it is worth mentioning that the specific density of power losses during the stabilisation process differs from each other, and it is not relevant for practical applications. The magnetic logic phenomena found in this study, adds to the list of remarkable physical features observed in rounded SC wires, such as the reported magnetic low pass filter phenomena [66], and the robust localisation of power density losses [40].

Although, the magnetically virgin or premagnetised condition of a DC SC

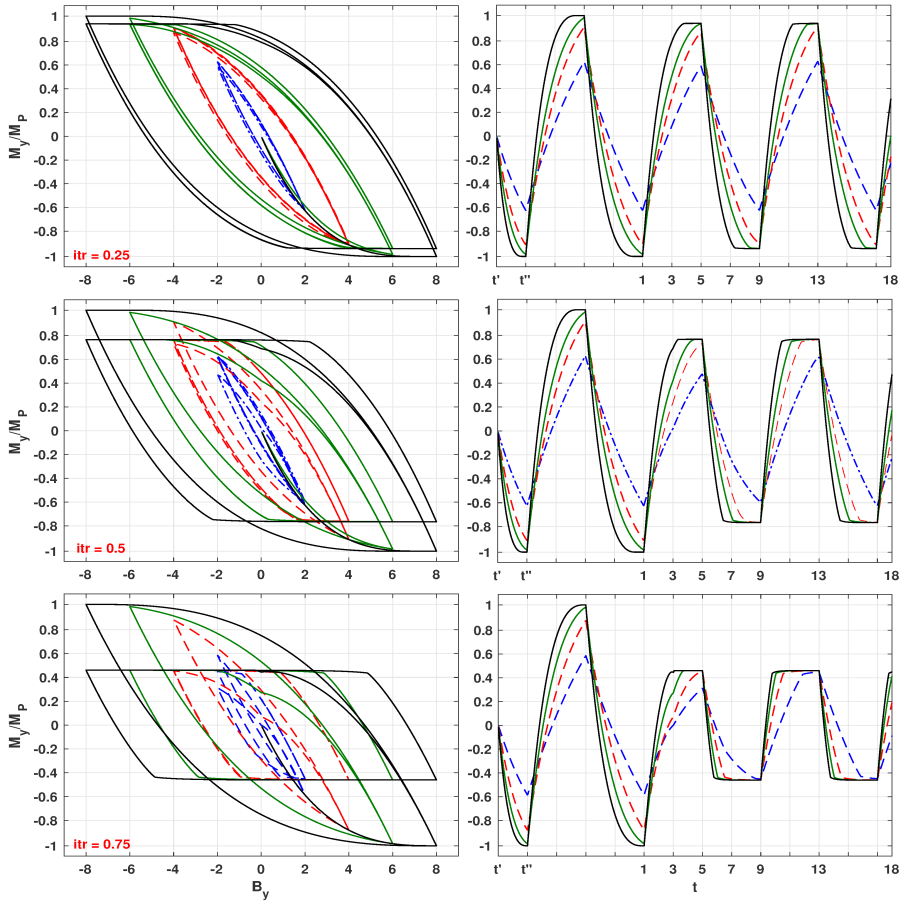

Figure 2.10: Same as Figure 2.7 but for the experimental conditions of Case 2 (premagnetised sample), displayed in Figure 2.3.

wire subject to transverse AC magnetic fields presents a remarkable feature of boolean characteristics observed at full saturation state of the magnetic moment, the practical realisation of this condition can be challenging when B_0 needs to be applied precisely at a designated section of the SC wire, as our 2D model implies that the magnetisation current loops are closing at the sending and ending terminals of a very long SC wire. Though, we have validated our statements by the detailed analysis of the profiles of current density, the time-dynamics of the magnetisation curves, and the strict comparison of our numerical results with popular semi-analytical approaches for the calculation of the AC-losses detailed in the section, an experimental validation is left for future works and is considered out of the scope of this thesis. However, our published papers in [78–80] intend to motivate other scientists to instigate the experimental realisation of magnetisation states with the macroscopic Boolean-like properties described above.

2.3.3 *Hysteretic AC losses*

It is worth mentioning that the interest of studying rounded SC wires lies on the fact that exact analytical approaches can be found for the calculation of the AC losses when isolated excitations, transport current or transverse magnetic field, are considered, serving as a benchmark for the estimation of the AC losses in practical applications.

Even though the collection of reliable experimental data is rather challenging due to unavoidable pitfalls in the measurement procedures, we have found that it is common to assume that the heat released by an SC wire under both I_{tr} and B_{0y} can be estimated by the linear sum between the contributions of these excitations are considered separately [67, 81–84]. Moreover, much research dealing with this problem argue that electromagnetic measurements can separately determine the transport losses and the magnetisation losses, at least for low values of the magnetic field or high transport current densities [67, 85–87]. However, when both electromagnetic sources are applied simultaneously in an AC regime, as demonstrated in [66], the competition between the magnetisation currents and the injected current lines involving axisymmetric distributions of the screening currents, impedes the use of simplified approaches, as a robust localisation of the local density of magnetic flux, as well as of the local density of power losses, makes it remarkably difficult to differentiate the role on the AC losses introduced by magnetisation currents and the inductive terms of the injected lines of transport current, which can be calculated by [40]:

$$\Delta L_{ind} = -\frac{\mu_0}{2}\int_{\Omega} \mathbf{B}_{r_i}\cdot\Delta\mathbf{B}_{r_i}dr\,. \tag{2.30}$$

Moreover, by using the semi-analytical approach of Gurevich et al. for a DC SC wire under AC magnetic field [48] which is defined by the function:

$$L(B_{\mathtt{a}}, I_{tr}^{dc}) \equiv \frac{8B_p^2}{3\mu_0}\begin{cases} b_{\mathtt{a}}^3\left(1-\frac{1}{2}b_{\mathtt{a}}\right) & ,\ \forall\quad b_{\mathtt{a}} < i_{\mathtt{a}}^{\dagger} \\ i_{\mathtt{a}}^{\dagger 3}\left(1-\frac{1}{2}i_{\mathtt{a}}^{\dagger}\right)+\left(1+i_{\mathtt{a}}^2\right)\left(b_{\mathtt{a}}-i_{\mathtt{a}}^{\dagger}\right) & ,\ \forall\quad b_{\mathtt{a}} \geq i_{\mathtt{a}}^{\dagger}\ , \end{cases} \tag{2.31}$$

where we have introduced the dimensionless parameter $i_a^{\dagger} = 1 - i_a^{2/3}$, with $i_a = I_a/I_c$, and $b_a = B_a/B_p$, we have found that for low values of the magnetic field $B_a < B_p/2$, the semi-analytical approach of Gurevich et al. underestimates the actual contribution of the inductive losses due to the motion of local lines

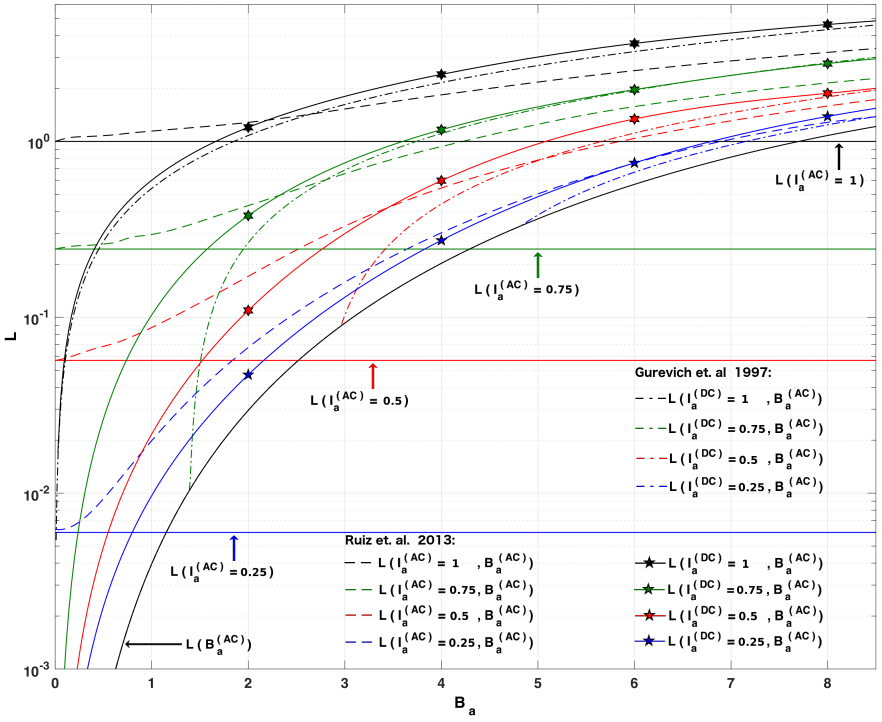

Figure 2.11: Hysteretic AC losses per cycle of a DC SC wire subjected to a transverse AC magnetic field of amplitude B_a, and different intensities of the DC transport current $I_a = I_c/4$, $I_c/2$, $3I_c/4$, or I_c. Our results (solid lines with symbols) are compared with the semi-empirical approach of Gurevich et. al. [48] for DC current and AC field conditions (dash-dotted-lines), and also with the numerical results of Ruiz et. al. [40] for synchronous AC field and AC current conditions (dashed-lines). The curve of AC losses for the SC wire under the AC field and zero transport current is also shown, $L(B_a^{(AC)})$, as well as the AC losses for the SC wire when it is subjected to an AC transport current and no magnetic field, $L(I_a^{(AC)})$, which act as reference for the values of I_{tr} (horizontal lines).

of transport current caused by the magnetic pressure exerted by the AC field, particularly when $b_a < i_a^{\dagger}$.

In the case reported in [40], it demonstrated that when both the applied magnetic field and the transport current are AC excitations, the actual hysteretic AC losses of the SC wire are in general higher than the ones estimated by the isolated excitations. A similar case is obtained for a transport current DC condition, where physically, the AC losses increase due to the rise in the magnetic pressure exerted by the magnetisation currents over the lines of injected/transport current. It leads to the deformation of the flux front profile, rather than consumption of magnetisation currents due to the oscillation of I_{tr}. Thus, as observed in Figure 2.11, for high values of the magnetic field

$B_a \geq B_p/2 = 4$, the attained values of the AC losses are nearly the same with the values obtained in the case of AC field and AC transport current [66]. Moreover, we have found that regardless of the experimental condition, i.e., with the SC wire either subjected to a DC or AC transport current, the resulting AC losses are nearly the same in both situations with the sample immersed in a transverse oscillating magnetic field, provided that the condition $i_a^* = 1 - i_a \leq b_a$ is satisfied, with $i_a = I_a/I_c$ and $b_a = B_a/B_p$. This assertion is important as it defines the limit from which the technological advantages of using SC wires for DC applications sharing the right of way with AC lines, competes with the case of using the SC wire for the sole transmission of AC current. Also, for completeness, the next Chapter 2.4 discloses the influence of a DC magnetic field in an AC SC wire (opposite of the previous study in Chapter 2.3), as the right of way may introduce such scenario for transmission lines.

2.4 *Magnetisation Characterisation of AC Type-II Superconducting Wires Exposed to DC Magnetic Fields*

In this section, we consider the effects that a constant magnetic field source has on a superconducting AC transmission line of cylindrical cross-section with critical current density J_c, as shown in Figure 2.12. In particular, the calculation of all the macroscopic electromagnetic quantities of interest such as the magnetic field, magnetic moment, and power density of energy losses, was performed by employing the numerical method and theory introduced in [46]. As in the previous Chapter 2.3, this section presents the analysed time-dependent distributions for the flux front profiles of local current density, magnetic flux, magnetisation characteristics, and energy density dissipation, where the analysis of the rounded SC wire allowed us to establish semi-analytical approaches of flux-tracking for the local dynamics of the current density of AC SC wires immersed in a constant transverse magnetic field. Also, it defines a satisfactory benchmark for the implementation of flux-tracking approaches in other 2D symmetries, such as SC strips, where exact geometrical expressions can formulate the flux-front profile for isolated excitations.

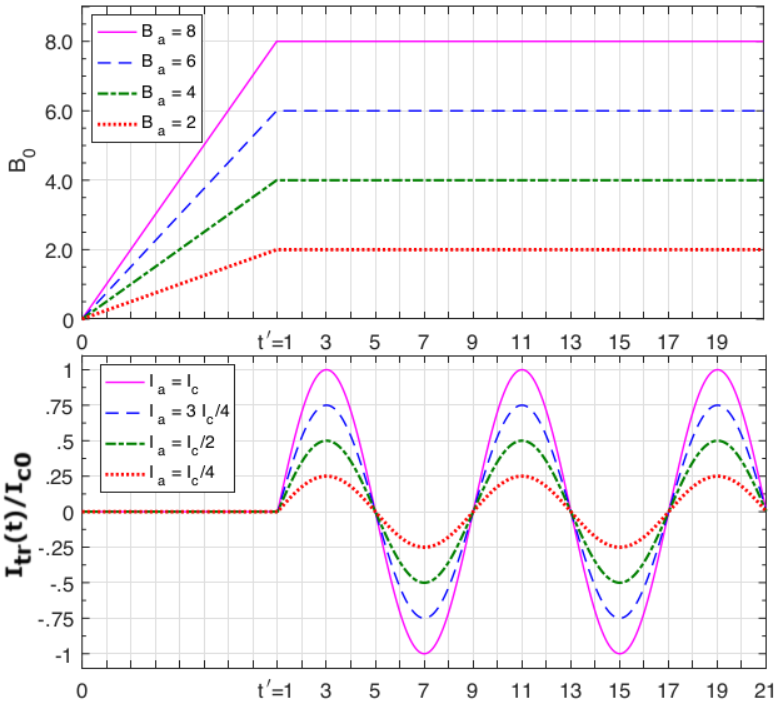

Figure 2.12: Time evolution of the electromagnetic excitations for longitudinal transport current (I_{tr}) and transverse magnetic field $B_{0,y}$, that are applied to a cylindrical SC wire of radius R lying over the plane xy. The amplitude of the AC transport current, I_a, is given in units of $J_c\pi R^2$, and B units are $(\mu_0/4\pi)J_cR$.

2.4.1 *Dynamics of Flux Front Profiles*

Presented in Figure 2.13 is the local distribution of profiles of current density into the critical state regime, $J_i = \pm J_c$, where it is possible to identify the intricate shapes of the flux front profile with clear elliptical field-like distributions of current embedded into well-defined rings of transport current. It can be observed therein that in Figures 2.12 & 2.13, the SC wire is premagnetised from the virgin condition $J_i = 0$ up to $t = t'$, i.e., $B_a > 0$ with $I_a = 0$, subsequently, the AC transport current (I_{tr}) is initially applied after the time step t' corresponding to the subplot labelled $t = 1$. Afterwards, the intensity of the applied magnetic field B_a (in units of $(\mu_0/4\pi)J_cR$) remains constant. Therefore, instantly after the concomitant action of both I_{tr} and B_0 is achieved, i.e., after $t' = 1$, the common field-like shape of the flux front profile observed in Figure 2.13 is deformed by the injection of finite lines carrying the transport current while satisfying the condition, $\int J_i dxdy = I_{tr}$.

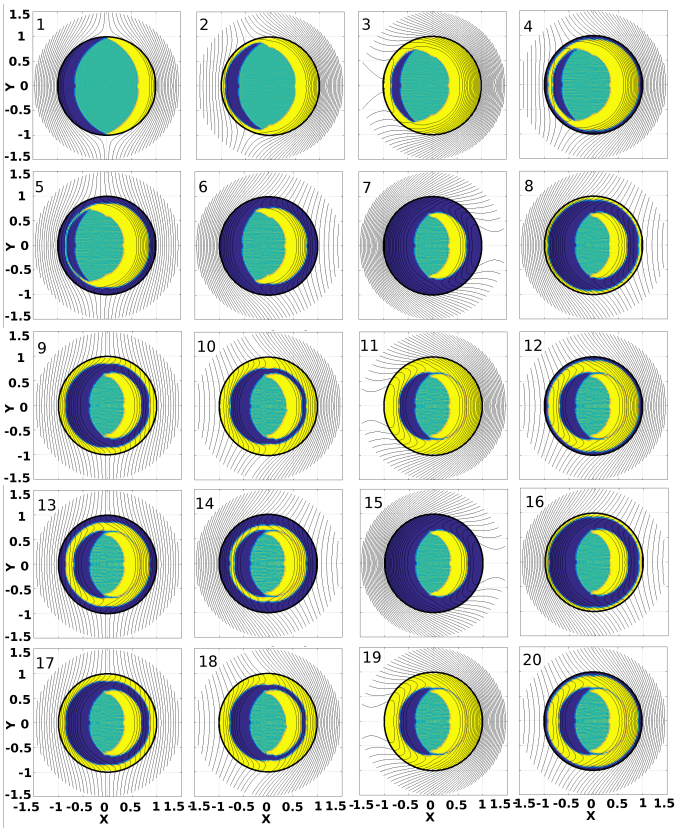

Figure 2.13: Flux front dynamics in a cylindrical superconducting wire of radius R exposed to the electromagnetic excitations depicted in Figure 2.12, with an AC I_{tr} of moderate amplitude, $I_a = 0.5I_c$, and a DC magnetic field of amplitude $B_a = 2$. Darker (blue) regions indicates critical state zones with $J_i = -J_c$, and the lighter (yellow) regions correspond to $J_i = +J_c$, otherwise $J_i = 0$ (green zone) defines flux free conditions.

This is understood by observing the dynamics of the flux front profiles of the current density in Figure 2.13 at the subplot labelled $t = 1$ $(B_a > 0, I_a = 0)$ & $t = 2(B_a > 0, I_a > 0)$. In this sense, the presence of the I_{tr} introduces a large deformation of the axisymmetric orientation of the observed flux front profiles, it due to the competition between the injected transport current and the magnetisation currents inside the SC. Moreover, this affects the geometrical centre of the flux free core, i.e., the regions without current density, causing it to be displaced towards the left side of the SC sample given the positive slope of the injected I_{tr}. In other words, the introduced local elements of transport current to the SC-sample consume the magnetisation current lines at the negative abscissa of the cylindrical wire, while at the same time, it exerts a Lorentz force pushing the magnetisation currents at the other side of the SC body inwards.

However, the symmetry of the ordinate elements of current are preserved as the B_0 direction is not changed.

The phenomenon of consumption and displacement linked to the magnetisation currents described above can be observed exclusively for the first three-quarters of the cyclic transport current, i.e., until it reaches the second peak $(-I_a)$ of the transport current excitation at the time step $t = 7$. Therefore, as it exceeds this period, therein, the unequivocal characteristic of the magnetic relaxation is evinced, illustrating the distortion and the dynamics of the magnitude of the flux front profile, as shown in Figure 2.13. Then, a cyclic hysteresis behaviour of the distribution of the profiles of current density is achieved, evidently by comparing the subplots labelled $t = 7$ and $t = 15$. It establishes an adequate state for the actual contribution of the AC losses, being calculated in the cyclic hysteresis regime. Also, as observed in Figure 2.13 after overcoming the magnetic stabilisation period, the size and dynamics of the flux core is unaltered as the applied magnetic field remains constant while the intensity of the I_{tr} is not as large as to fulfil the entire cross-section of the SC. In fact, by paying attention to the flux front dynamics after $t = 7$, it is possible to identify a circular flux front profile which is typical of the dynamics of the transport current inside a type-II superconductor. This finding is relevant for the calculation of the current-like flux front profile in the hysteretic cyclic regime using exact analytical methods [48], from which the boundary of the flux front agrees with the axisymmetric circumference of radius:

$$r = R\sqrt{1 - \frac{I_{tr}}{I_c}}\,, \tag{2.32}$$

which confines the magnetisation currents inside the transport current limit $I_{tr} = I_a$, i.e., $r_a = R\sqrt{1 - I_a/I_c}$.

Consequently, this formulates an inner secondary flux front profile, which allows identifying the distribution of profiles of current density produced by the external magnetic field with a centred semi-elliptical flux free core (see for example rows 3-5 in Figure 2.13). It can be calculated, however, by employing diverse semi-analytic approaches like the ones reported by Ashkin [88], Wagner [89], and Gömöry et al. [90], up to different levels of accuracy. Therefore, the use of Gömöry's approach which can realise precision levels of nearly 99.9%, by introducing a single semi-empirical variable, ε, which defines the semi-major axis (εr_a) of the elliptical flux front profile, such that the *position* of the inner flux front for the field-like current distribution can be calculated as:

$$r_\varepsilon(\theta) = \frac{\varepsilon\ r_a}{\sqrt{cos^2(\theta) + \varepsilon^2 sin^2(\theta)}}\,, \tag{2.33}$$

where θ is the angular direction enclosing the elliptical flux front profile of the

field-like distribution in a round SC wire, ϵ can be ascertained from the magnetisation measurements (see Figure 2.14 & 2.15) with $M(\varepsilon) = -(2/3)H_{p'}(1-\varepsilon^2)$, and $H_{p'} = \mu_0^{-1}B_p\sqrt{1-I_a/I_c}$. The later define the condition for the full penetration of magnetic flux inside the superconducting wire, with ε ranging from 0, i.e., accounting for the disappearance of the flux free core, to 1, i.e., when the field-like flux front coincides with the current-like flux front, or inner surface of radius r_a that limits the distribution of magnetisation currents.

2.4.2 *Magnetisation Features and Hysteretic Losses*

Following the earlier arguments, it is possible to state that as long as $I_a < I_c$, then $r_a \neq 0$ and consequently, the SC wire can show profiles of magnetisation current. Thus, if it is assumed that the superconducting wire is premagnetised before activating the AC transport current, i.e., for $t \leq t'$ where $I_a = 0$ and $B_a = 8$ (see Figure 2.12), the magnetisation curve as a function of the transport current will exhibit a monotonic increment of M_y reaching the saturation value of the magnetic moment $M_p = (2/3)J_cR^3$ (see Figure 2.14). Then, when the AC transport current is activated, i.e., at $t' > 1$ where $I_a > 0$ and $B_a = 8$, the lines of injected transport current consume the lines of magnetisation current, which reduces the overall magnetisation of the SC wire until a threshold, $I_a = I_c$ prompting a complete disappearance of the magnetisation signal (Figure 2.14 & 2.15). However, for $I_a < I_c$ and $B_a > 0$, as demonstrated previously that the full penetration of the magnetic field (or profiles of current density) is achieved at the field $H_{p'}$, which is always smaller than H_p by the factor $\sqrt{1-I_a/I_c}$. In this sense, for $B_0 > H_{p'}$, the stabilisation period of the profiles of current density span from the first three quarters of the applied AC transport current up to $t = 7$, afterwards, showing a hysteretic cyclic behaviour with the resulting magnetisation indicating a flat line from $t = 7$, as shown in Figure 2.15 . The flux free core which might be observed during this magnetic stabilisation period eventually disappears, leading to the stabilisation of the finite magnetic moments inside the circumference of radius r_a. Therefore, the calculation of the maximum magnetisation of a premagnetised rounded SC wire with AC transport current is conceivable by employing the semi-analytical approach $M_p = -(2/3)J_cr_a^3$, written as a function of I_a as follows,

$$M_p'(I_a) = -\frac{2}{3}J_cR^3\left(1-\frac{I_a}{I_c}\right)^{3/2}. \tag{2.34}$$

This result implies that for moderate amplitudes of applied transport current i.e., $I_a = 0.5$, the SC wire can obtain a maximum dimensionless magnetisation

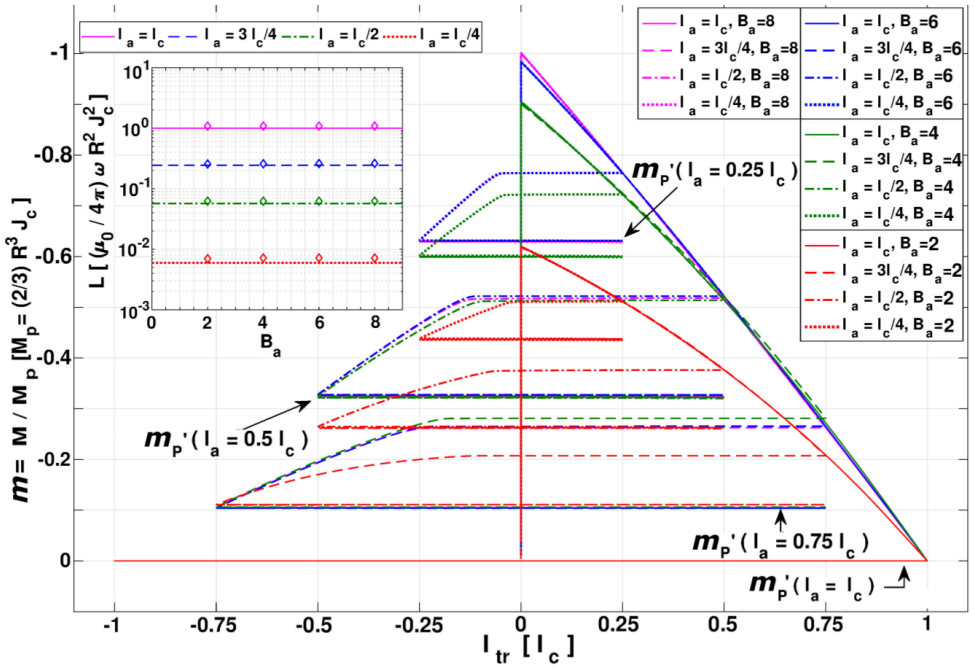

Figure 2.14: Dimensionless magnetisation curves ($m = M_y/M_p$, being the renormalised magnetic moment) as function of the AC transport current I_{tr} under the experimental conditions displayed in Figure 2.12. $M_p = 2J_cR^3/3$ is the analytical solution for the magnetic moment of the SC sample when the field $B_p = 8$ fully penetrates it, in the absence of transport current. Recall that units for B_a are $(\mu_0/4\pi)J_cR$, R is the radius of the SC wire, and I_{tr} is given in units of I_c. Presented in the inset is our numerical results (solid symbols) for the calculation of the monotonous hysteresis losses per cycle of the transport current. Therein, the solid lines correspond to the analytical solution described by Equation 2.38. L is shown in units of $(\mu_0/4\pi)\omega R^2 J_c^2$ per cycles of frequency ω.

of $m'_p = M'_p/M_p = -0.3535$, which is in good agreement with our numerical results presented in Figure 2.14. Furthermore, m'_p can only be reached for $B_a > B_p\sqrt{1-0.5} \approx 5.65$, and although the difference between the resulting magnetic moment for $B_a > 4$ and I_a is almost negligible, for lower magnetic fields showing a broad flux-free core (Figure 2.13) a smaller magnetisation plateau, $m'(I_a = 0.5, B_a = 2) \approx -0.262$ can be observed. Therefore, for $B_a < B_p\sqrt{1 - I_a/I_c}$, the existence of a flux free core inside a SC rounded wire subjected to AC transport current and DC magnetic field can be seen from the macroscopic measurement of the magnetic moment of the wire, when $|m| < |m'_p|$. Otherwise, for the experimental conditions depicted in Figure 2.12, and after the cycle of magnetic-stabilisation, a constant magnetisation plateau (m'_p) is discerned, which does not depend on the time dynamics of the transport current.

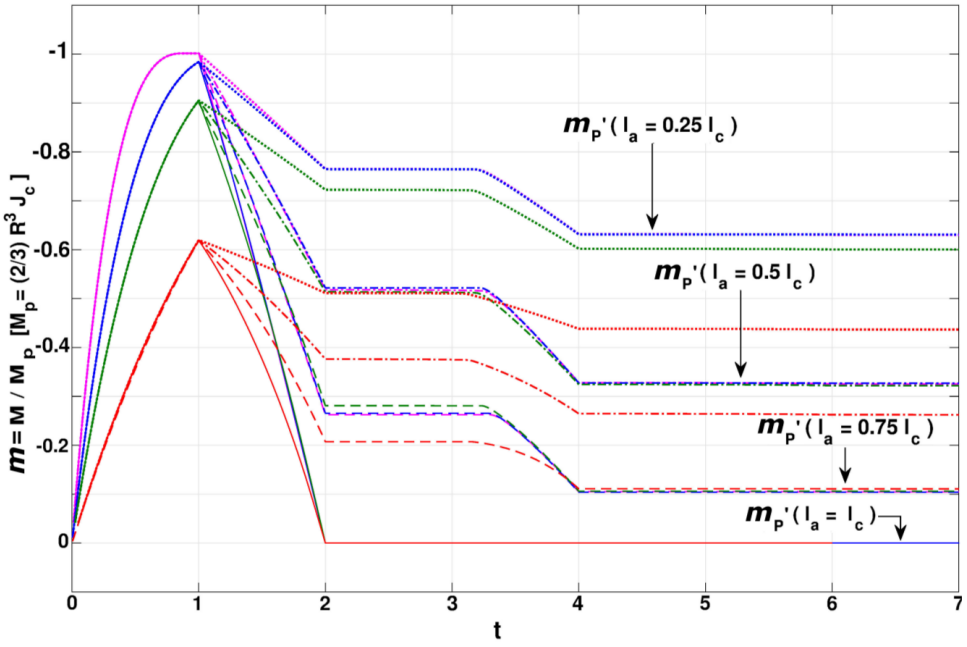

Figure 2.15: The dimensionless magnetisation curves shown in Figure 2.14 but as function of time.

Finally, concerning to the density of power losses ($\mathbf{E} \cdot \mathbf{J}$) for the conditions depicted in Figure 2.12,, the first cyclic excitation defines a period of magnetic stabilisation, where the profiles of current density that contribute to the magnetisation are regrouped into the r_a boundary, showing a constant field-like profile afterwards. In this sense, under these conditions it is satisfactory to calculate the cyclic hysteretic losses from the second cycle of I_{tr} once the magnetic relaxation period has passed.

Furthermore, the symmetry of the problem gives way for $\nabla\phi = C_t\hat{\mathbf{u}}_k$ to become an integration constant, provided that the electric field vector is defined in terms of the magnetic vector potential as $\mathbf{E} = -\partial_t\mathbf{A} - C_t\hat{\mathbf{u}}_k$. Therefore, the contributions of the external magnetic field and the induced/injected transport current can be grouped into separate vector potentials for the elements of the current $J_i(\mathbf{r}_i)$, i.e.,

$$\mathbf{A}_{ext}(\mathbf{r}_i) = \mathbf{B}_0 \times \mathbf{r}_i \,, \tag{2.35}$$

and

$$A_{self} = \mu_0 \pi J_i/(4\pi) \,, \tag{2.36}$$

representing the self inductance contributions, and

$$A_{mut} = -\mu_0 J_i ln(r_{ij}^2)/(4\pi) \tag{2.37}$$

for the mutual inductance contributions between the $i \to j$ finite elements of current of circular cross-section [66, 91]. Therefore, the induced elements of current, $A_{ind} = A_{self} + A_{mut}$, explicitly contribute to the AC-losses, demonstrating that the variation of J_i only occurs inside the flux front boundaries for current-like distributions, $r_a < r < R$. Thus, although observed in our numerical calculations is a minimal increase in the integration constant C_t as a consequence of the magnetic stabilisation period, the left-top inset in Figure 2.14 shows that, concerning a rounded SC wire subjected to a constant transverse magnetic field and AC transport current, the AC-losses per unit time can be calculated by the analytical solution [48],

$$L = \omega \frac{\mu_0}{2\pi} R^2 J_c^2 \left[j - \frac{j^2}{2} + (1-j)Ln(1-j) \right] . \tag{2.38}$$

with $j = J_{tr}/J_c$, and $J_{tr} = I_{tr}/(\pi R^2)$.

Thus, our findings suggest that after overcoming the period of magnetic stabilisation, it is conceivable to evince a semi-analytical expression to track the evolution of the flux front profile at least in this case, where a DC magnetic field is applied to an AC superconducting wire. Also, the experimentally extracted macroscopic quantities of the SC wire such as the maximum magnetic moment, M_p, and the AC-losses, L, both are accurately determined through the simplification of considering firstly "current-like" flux front profiles for the dynamics of $I_{tr}(t)$, and secondly the embedding of a constant "field-like" distribution. Thus, it is worth mentioning that taking into account the generality of our approach and the analysis of the results, these findings could be extended to SC strips with elliptical cross-section [90], and in fact to any other 2D symmetry where semi-analytical approaches of flux front-tracking could be known.

Conclusions I

The critical state theory for the magnetic response of type-II superconductors in a vortex state is summarised in Chapter 1, highlighting the use of variational methods and computational techniques with the fundamental structure based on inductance matrices, offering a meaningful method for reducing the numerical complexity of Maxwell equations when solving the macroscopic electrodynamics of superconducting wires in a 2D approach.

Contrarily to cases where the topology of the free boundary that defines the geometry and evolution of flux fronts is relatively simpler, and analytical solution can be found, e.g., as in an infinitely long superconducting cylinder in a parallel field or, the study of infinitely thin SC strips, the experimental condition of the concomitant action of time-varying transport current and magnetic field where it is not possible to apply simplified analytical approaches is thoroughly studied. In this sense, the macroscopic electromagnetic behaviour of DC/AC type-II superconducting wires under AC/DC magnetic excitations is captured by the numerical solution of the Maxwell equations under the framework of the critical state principle and the so-called integral formulation, also known as J-formulation, in Chapter 2. In this sense, we presented a systematic analysis of the electromagnetic characteristics and local effects linked to dynamics of current density, magnetic field, magnetic moment, and hysteretic losses inside type-II superconductors of rounded cross-section. Thus, in Chapter 2.3, the DC type-II superconducting wires of cylindrical shape under transverse AC magnetic fields have been analysed, where it has been found that the superconducting wire quickly develops a saturation state for relatively low amplitudes of the applied magnetic field, B_a, with $|M_p|$, characterising the limits of magnetisation loops that exhibit a striking Boolean-like behaviour. The occurrence of a Boolean-like logic from the magnetic moment profiles is evinced regardless if the SC wire is magnetically virgin or premagnetised where boolean-like $\pm M_p$ states can be measured with the sign's rule defined by the sign of the slope $\Delta B_{0y}(t)$.

Concerning the calculation of AC losses, let us recall that exact analytical approaches can be found for isolated excitations conditions, $I_{tr}(t)$ or $B_{0y}(t)$, with the assumption that the heat dissipation by an SC wire under both ex-

citations can be estimated by the linear sum between their individual contributions [67, 81–84], at least for cases with low values of magnetic field or high transport current [67, 85–87]. However, when both electromagnetic sources are in AC regime, the use of the existing semi-analytical approaches significantly underestimates the actual AC losses of the system, which has been already demonstrated in [66]. Likewise, we have demonstrated that the AC losses of a DC rounded SC wire, either magnetically virgin or premagnetised condition that is exposed to a further an oscillating transverse magnetic field, cannot be predicted accurately by semi-analytical approaches such as the ones proposed by Gurevich et al. [48].

Thus, for the practical implementation of superconducting DC wires sharing the right of way with AC lines, this study reports that for relatively low values of a magnetic field, $B_a \leq B_P/2 = 4$, being B_P the analytical value for the full penetration field in the absence of transport current, I_{tr}, the use of semi-analytical approaches for the calculation of AC-losses leads to a significant underestimation of the actual contribution of the induction losses. This phenomena is particularly relevant at dimensionless fields $b_a < 1 - i_a^{2/3}$, being $b_a = B_a/B_P$, and $i_a = I_a/Ic$ the amplitude of an AC or DC transport current, it due to the local motion of flux front profiles being dominated by the occurrence of transport current. Nevertheless, we have found that regardless of the nature of the transport current, either DC or AC, when a transverse oscillating magnetic field greater than the classical limit $b_a = (1 - i_a)$ is applied to the SC wire, the difference between the obtained AC losses in both situations results to be negligible, indistinctly of the approach used (semi-analytical or numerical). For example, the obtained values of the AC losses for $B_a \geq B_P/2$ are nearly the same with those attained in [66] for the case of AC field and AC transport current. Thus, the actual limits from which the estimation of the AC-losses can be used as an asset for the deployment of DC SC wires sharing the right of way with AC lines, against the sole use of SC wires for the transmission of AC transport current, are established.

Finally, in Chapter 2.4 we studied the action of a constant magnetic field applied to a rounded superconducting wire of radius R and critical current density J_c, carrying an alternating transport current of intensity I_a, under the theoretical framework of the critical state model and the numerical solution of Maxwell equations in the magneto quasi-steady approach. The analysis of the time-dependent distributions for the flux front profiles of local current density, magnetic flux, and cycles of the magnetic moment has allowed us to establish semi-analytical approaches of flux-tracking for the local dynamics of the current density of AC SC wires immersed in a DC magnetic field, from which all the macroscopical electromagnetic quantities of interest such as the magnetic field, magnetic moment, and power density of energy losses can be

calculated. We have demonstrated that under the abovementioned experimental conditions, it is possible to realise a set of well-established semi-analytical expressions to track the evolution of the flux front profile after overcoming the magnetic relaxation which spans during the first cycle of oscillation of $I_{tr}(t)$, where two plateaus with constant magnetic moment can be measured. During this period of stabilisation, a marked redistribution of the lines of magnetisation current is observed due to the Lorentz force that has been added by the insertion of finite lines of transport current density, which satisfy the integral condition $\int J_i d\Omega = I_{tr}$, being Ω the cross-section area of the SC wire. The observed resulting distribution of profiles of current density $J_i = \pm J_c$ or 0 during this cycle, follows a cumbersome dynamics which precludes a semi-analytical description of the flux front profile. However, once the SC wire reaches the cyclic monotonic behaviour, we have identified a cyclic monotonic behaviour with well-defined flux-front boundaries, with clear signatures of *current-like* and *field-like* flux front profiles. On the one hand, the dynamics of the flux front profile is confined during the monotonic regime to a region of the space, constrained by the condition $r_a < r < R$, with $r_a = R\sqrt{1 - I_a/I_c}$, where circular "current-like" profiles of current density occur. On the other hand, the inner limit r_a defines the outer boundary of semi-elliptical "field-like" profiles of current density contributing to the overall (constant) magnetisation of the superconducting wire. Therefore, the results presented reveal that there is no need for cumbersome numerical algorithms to determine the distribution of profiles of current density and the experimentally extracted macroscopic quantities of the SC wire such as the maximum magnetic moment, M_p, and the AC-losses, L. Both the M_p and the L can be determined accurately through the simplification of considering, firstly, "current-like" flux front profiles for the dynamics of $I_{tr}(t)$, and secondly, the embedding of a constant "field-like" distribution. It is worth mentioning that taking into account the generality of our approach and the analysis of the results, the findings here for a cylindrical superconducting wire define an adequate benchmark for the implementation of flux-tracking approaches in other 2D symmetries, such as SC strips with elliptical cross-section [90], where exact geometrical expressions can formulate the flux-front profile for isolated excitations.

Part II

Electromagnetic Modelling of 2G-HTS REBCO Coils: Racetrack and Pancake Configuration

In recent years, the majority of superconducting wire manufacturers have moved to the development of the so called second-generation (2G) of high-temperature superconductors (HTS) made of coated conducting (CC) tapes with REBCO materials, where RE stands for Rare Earth elements such as Gadolinium, (Gd), Yttrium (Y), or Europium (Eu), and B is for Barium, C for copper, and O for Oxygen (see Figure 2.16). This is due to their enormous progress in the deposition technology and fabrication of thin films in the past decade, which has positioned the 2G-HTS REBCO tapes as the basis of nearly all current and envisaged high-power density applications taking advantage of the local electromagnetic properties of type-II superconductors [34, 92–96]. Examples of these superconducting applications can be seen in superconducting fault current limiters (SFCL) [97–100], transformers, power generators [101–103], industrial superconducting motors [104–107], permanent magnets [108, 109], superconducting energy storage systems [110–112], and magnetic imaging machines [113, 114], where the 2G HTS tapes are mainly used within the design and testing of coils and cables, for both AC and DC applications [115, 116]. Therefore, an understanding of the macroscopic measurable quantities such as magnetic field, critical current density, $\mathbf{J}_c$, and AC losses of superconducting coils are essential subjects in the physics and engineering of applied superconductivity [96, 112, 115, 117–120].

Several works reporting on the electromagnetic properties of coated conductor coils, either by experimental measurements [115, 121–124] or numerical computations [119–121, 123–127], have focused on the understanding of the AC losses of HTS racetrack-shaped [128–131] and pancake-shaped coils [96, 132, 133] (see Figure 2.17) due to their importance on multiple engineering applications. Within these kinds of studies, one of the most determining factors which needs to be considered when fostering a superconducting application is the actual estimation of the AC losses of the employed coils, because it utterly defines the optimal design, performance, and cost assessment of a superconducting machine [116]. However, it is well-known that the type-II superconducting materials used for the fabrication of 2G-HTS tapes are extremely prone to be affected by external and induced changes in the electromagnetic excitations, which results in very complex local distributions of current density and flux front profiles, both being the physical source of the hysteresis losses [79, 80]. In fact, in the case of a superconducting coil, each one of its turns that carries a certain amount of current affects the electromagnetic performance of the other turns by magnetic induction, where both the local profiles of transport current and magnetisation currents appears. Nonetheless, these local profiles are complicated to see at the level of each one of the superconducting tapes that conform the coil, and from a computational point of view, the large aspect ratio of the 2G-HTS tapes can imply a significant computational burden re-

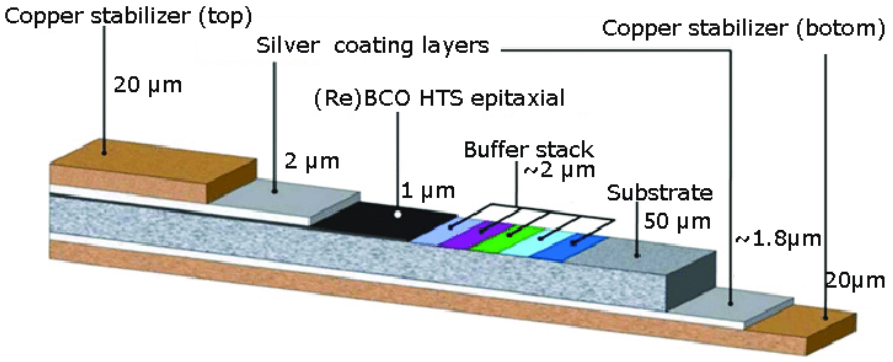

Figure 2.16: Configuration of SuperPower 2G-HTS Wire (coated conductors), based on (RE)BCO (rare earth barium copper oxide elements) materials [134].

gardless of whether or not the system of derived inductance matrices is solved by differential [116, 135, 136] or integral [119, 137, 138] approaches. Thus, the running of extensive numerical studies in applied superconductivity is somehow limited to the computational resources and time that might be available for the case of study, even if the symmetry can be reduced to a 2D axisymmetric geometry (like in the case of a racetrack or pancake coil) or when a simplified meshing approach can be invoked. However, performing these kind of computational challenges is of remarkable importance as the actual costs concerning the experimental testing and manufacturing of these devices might not be permissive.

When studying a superconducting coil made of 2G-HTS tape, the most common practice is the assumption that all the turns of the coil are perfectly aligned and maintained throughout any manufacturing or assembling process. This assumption is undoubtedly a complicated statement to sustain, as in reality, possible misalignment between the coil turns (tapes) is likely to occur, either during the coil manufacturing, their assembling in practical applications, or even due to possible axial alterations caused by extrinsic magnetic, thermal, or mechanical pressure over the coil turns. These scenarios have left questions concerning their practical importance from both the engineering and physics perspectives such as: How does an unintentional misalignment in the winding of a superconducting coil impact its energy losses and magnetic field profile? Is the commonly assumed factor negligible? Or can it deteriorate or improve the coil energy efficiency features? In this sense, the influence of the winding misalignment factor on the energy losses of superconducting coils under AC conditions remains a fundamental physical and engineering problem to be solved.

Thus, Part II of this thesis is motivated by the long standing questions

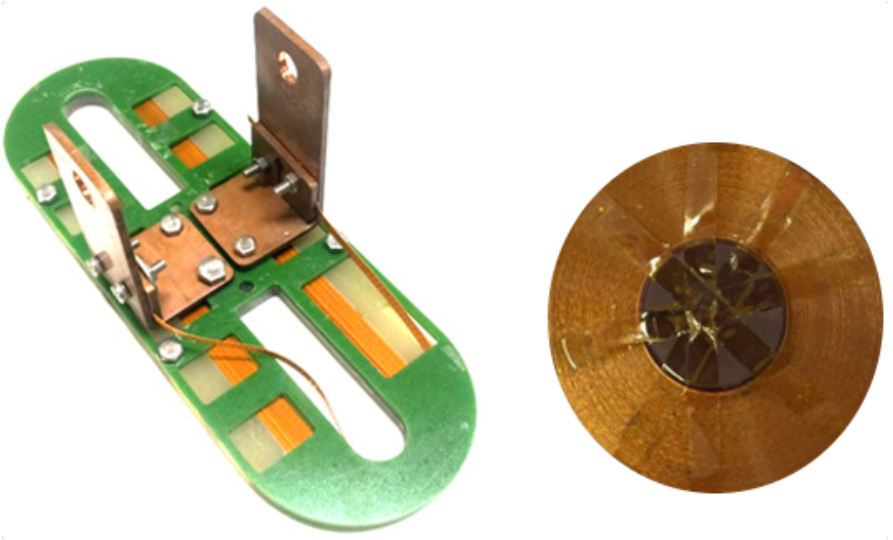

Figure 2.17: Practical configuration of (a) racetrack-shaped coil made of SCS4050 2G tape [139], and (b) YBCO pancake-shaped coil wound from Superpower 4 mm wide copper stabilised CC tape [140] .

abovementioned, and their practical importance from both the engineering and physics perspectives, bearing in mind the computational effort involved. Therefore, we have studied different topological experimental conditions to disclose how systematic turn-to-turn misalignments in the winding of 2G-HTS coil could impact the hysteresis losses, magnetic flux features, and the distribution of critical current density within such coils when they are subjected to alternating currents (discussed in Chapter 3 & 4). In particular, the presented models utilised a unified numerical approach supported by high-level meshing conditions and a generalised description of experimentally measured material laws in 2G-HTS tapes [141], which focus more on the local understanding of the physical properties of the coils, rather than on commonly used mesh simplifications for reducing the expected computational burden.

It is worth mentioning that several modelling strategies have been developed for the formulation of the modelling tools for describing the electromagnetic and thermal properties of the vast majority of 2G-HTS tapes. However, concerning to the inherent complexity of the $E-J$ material law which governs the electrical properties of such superconducting tape, no strong agreement has been reached, as widely different material laws can render similar results depending on the physical quantity being studied [142–144]. Nonetheless, regardless of the 2G-HTS tape used, a certain consensus has been reached in terms of describing the current-voltage characteristics of all type-II superconductors as a power law, $V \propto (I/I_c)^n$, with $n \gg 1$. This power-law from a computational

point of view, renders the well-known form of the material law for the electric field, also known as the E-J power law, $\mathbf{E}(\mathbf{J}) = E_0 \cdot \mathbf{J}/J_c \cdot (|\mathbf{J}|/J_c)^{n-1}$. Also in a macroscopical approach, it allows the solution of the Maxwell equations inside the superconducting domains within diverse mathematical formulations, for a broad range of experimental measurements [108, 116, 120, 128, 138, 143, 145–152].

However, the simulation of the electromagnetic behaviour of 2G-HTS coils presents serious challenges, especially in conditions where one needs to consider the in-field dependence of the critical current, I_c, such as concerning the direction and intensity of the magnetic field per coil-turn, as pointed out in early experiments that measured the magnetic field distribution and AC loss of HTS thin films in superconducting coils [115, 153]. Furthermore, most published research focused either on the simplification of numerical models to enable faster computational algorithms for relatively large or complex geometries, or on the reproduction of specific experimental evidence such as the hysteresis losses, magnetisation curves, or the measurement of the magnetic field at different positions, where there are robust changes in the amplitude of the critical current density. Besides, it is well-known that the computational models usually invoke an overall estimate of the critical current density J_c of the entire coil, it due to the enormous complexity associated with the experimental measurement of the critical current density at each turn of a superconducting coil, and also, by taking into account the considerable uncertainty in the reproducibility of the experimental measurements caused by the non-homogeneity of the electric field inside the superconducting tape (both across its length and along its width). Thus, such estimations are considered; generally, by matching the numerical results of a particular model with any specific physical quantity that can be measured by further experimental methods. However, this does not give a definite solution to the challenges associated to the selection of the appropriate material law for the cases of interest, but opens some central questions, such as Are computational modellers using a sound material law for the superconducting tapes? And, is this material law valid for the study of any other macroscopic electromagnetic quantity?

In an attempt to answer these questions, in Chapter 5 we analysed how the selection of different material laws in the numerical modelling of superconducting coils can strongly influence the accurate estimation of macroscopically measurable physical quantities, such as the critical current density of each coil turn, the magnetic field near the coil armature, and the accounting of the hysteresis losses per cycle under self-field current conditions. The main findings from our numerical results offer decision criteria aimed to advice computational modellers concerning the selection of the material law for 2G-HTS coils, especially when not only a physical quantity needs to be quantified to

match the experimental evidence, but in situations where the consideration of the computing time is crucial. Our study adopts a numerical model based on the implementation of the H-formulation into available finite-element methods (FEM) for the solution of Maxwell equations [154]. Reminding Chapter 1, the governing equations explicitly invoked in our case are the Faraday's and Ampére's laws, where the superconducting material is usually introduced by using a non-linear E-J relation which describes the electrical conductivity of the material [155]. However, regardless of the formulation, in the case of strong discontinuities of the materials' properties and highly non-linear materials, like the superconductors, or in the presence of geometries with sharp corners, the FEM discretisation of the second-order differential operator ($\nabla \times \nabla \times$) and the use of nodal elements can give rise to ill-conditioned inductance matrices, which might cause the iterative solution of the Partial Differential Equation (PDE) system to converge gradually with a large dispersion of values in the results [156]. Nevertheless, the use of edge elements [157–160] overcomes the above problems, and this has already been validated in previously published works on the general case of eddy currents [161], and superconductors [156]. This implies that utilising FEM in both cases guarantees the continuity of the tangential component and the possible discontinuity of the normal component. Therefore, we built our model based on edge elements, and the high non-linearity problem of superconducting materials was solved through the first-order PDE system. This is directly formulated in terms of the components of the magnetic field $\mathbf{H}$, eliminating the use of the magnetic vector potential [161–163] that was employed in Part I, at the expense of considering the whole space and not only the area occupied by the superconducting domains (see Figure 2.1). Also, this method offers the following advantages [155]:

1. The use of the first-order element disregards the use of second-order derivatives, and this indirectly satisfies the condition of zero divergence of the magnetic field, $\nabla \cdot \mathbf{H} = 0$.

2. The components of the magnetic field as state variables are very practical for imposing boundary conditions, usually in the case of symmetric or axisymmetric geometries.

3. The variables of the magnetic field are readily available in the solution, it implies that differentiating of the electromagnetic potentials is not required, which may introduce some inaccuracy in the numerical values.

Based on these considerations, a numerical method based on the finite element software; COMSOL Multiphysics [164] is introduced in our study, which provides a suitable environment for solving PDE systems by edge finite element methods. This is an attempt to describe the physical understanding

of misalignment factors replicating the effect of possible imperfections in the alignment of 2G-HTS wound pancake and racetrack coils and later on, the impact of material law selection for a 2G-HTS coil. We simulate different REBCO coil configurations wound on a 5 cm mid-width in racetrack and pancake formers, these made of 20 turns 4 mm tape-width of commercially available 2G HTS tape (SuperPower-SCS4050) at $77K$ self-field condition with the critical current as 114 A [134]. Also, it was modelled with a high-level meshing strategy to overcome the computational challenges imposed by the large aspect ratio of the superconductor layer within such tape (4 $mm \times 1$ μm) representing the cross-section of the coils at its mid-section and neglecting the influence of the U-turns. This kind of simulation is a powerful tool for estimating the current distribution inside each one of the turns of the superconducting coil and its magnetic field distribution, although a vast number of mesh nodes is required in order to achieve satisfactory accuracy. As a consequence, it results in a computationally demanding problem, which in our case (about 140 cases), implies simulations of single cases which can span for up to four days within workstations equipped with an Intel® i7-6700k CPU @ 4GHz core processor with 32GB RAM. Thus, part II of the thesis is organised as follows:

Chapter 3 summarises the physics framework and modelling strategy invoked for the numerical simulation of the 2G-HTS racetrack and pancake coils either with or without winding misalignment features, considering the cross-section of a 20-turn superconducting coil made with SuperPower Inc. SCS4050 tape [134]. Chapter 4 deals with the study of the physical dependence of the hysteresis losses with the axial winding misalignment of 2G-HTS racetrack and pancake coils subjected to AC applied transport current, highlighting the influence it could have on their performance of practical superconducting machines. In particular, it discloses the effect of prospective winding misalignment factors in the macroscopical quantities of interest such as the hysteresis losses and critical current density inside each turn of a typical 2G-HTS coil, and their relation with the magneto-angular dependence of the in-field critical current density $J_c(B, \theta)$ of the 2G-HTS tape. Finally, Chapter 5 addresses a comprehensive study of the impact of the material law selection on the numerical modelling and analysis of the electromagnetic properties of SuperPower Inc. SCS4050 2G-HTS tapes that constitute a coil. It is focused mainly on the similarities and differences between the different material laws in terms of their macroscopic measurable quantities, which presents decision criteria aimed to advice computational modellers concerning adequate regimes for the material law selection.

It is worth mentioning that the findings analysed in this study can be used as a practical benchmark to determine measurable quantities such as critical current density inside different turns of the superconducting coil, magnetic field

and relative AC losses for any 2G-HTS racetrack or pancake coil application.

Chapter 3

Computational Models and the 2D H-Formulation

The use of the H-formulation can be traced back to Pecher and Kajikawa in 2003 [165, 166], and since then, several modelling strategies have been developed for performing the numerical simulation of 2G-HTS coils with a high degree of accuracy. Therefore, in this study numerical simulations of racetrack-shaped coils are performed within the framework of the celebrated 2D H-formulation in Cartesian coordinates [108, 135, 155, 167], where the effect of the U-ends can be neglected for sufficiently large racetrack coils as demonstrated in the work of Enric Pardo et. al., [128, 129]. Likewise, pancake-shaped coils are modelled under the polar axisymmetric approach, where the centre of the coil is placed at the z-axis [96, 133], following the geometry imposed by the graphics user interface (GUI) of COMSOL Multiphysics 5.3a [164]. Additionally, a most general form of the material law for describing the E-J properties of the 2G-HTS tapes at liquid nitrogen temperature is invoked, extending the conventional Kim's critical state model to an experimentally validated magneto angular dependent $E - J$ power law [141], therefore, taking into account an appropriate consideration of the magneto-angular anisotropy properties of 2G-HTS tape. Thus, this section summarises the theoretical framework and modelling strategy employed for the numerical simulation of 2G-HTS racetrack and pancake coils, either with or without winding misalignment features, by considering the cross-section of a 20-turn superconducting coil under a high level meshing detail.

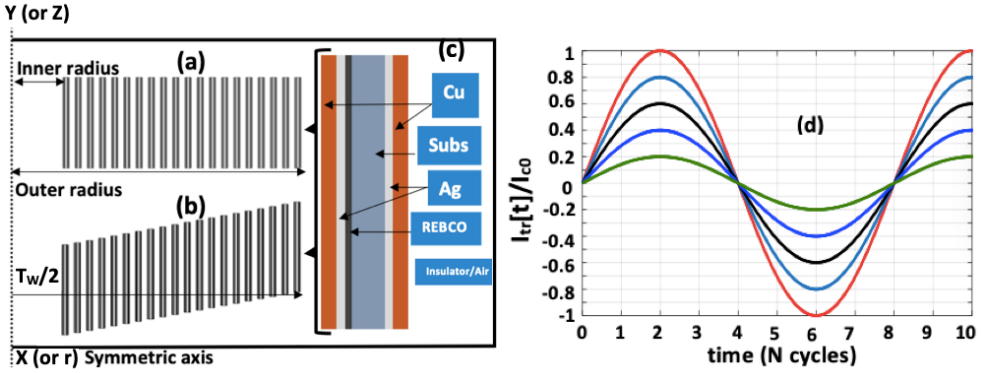

Figure 3.1: Schematics of the cross-section of the 20 turns 2G-HTS racetrack and pancake coil geometries considered for the (a) perfectly aligned winding case, and (b) when the coil is subjected to a non-uniform winding displacement ($\delta_m = 100\ \mu m$), with a half the tape width ($T_w/2$) misalignment between the innermost and outermost tapes. In (c) an individual 2G-HTS tape (not to scale) as a period array of unit cells is shown for illustrative purposes. Finally, (d) shows the time dynamics of the applied transport current with time steps labelled at each $\pi/4$ cycles.

3.1 *Electromagnetic Modelling of Racetrack and Pancake Coils*

The analysis of the electromagnetic features of racetrack and pancake HTS coils, with or without winding deformations, begins by assuming a cross-section of a 20-turn wound coil on a 5 cm mid-width former, using a SuperPower Inc. SCS4050 tape [134] (Figure 3.1). This tape of 4 mm width and overall thickness of approximately 0.1 mm, is conditioned by a self-field critical current density (i.e., the critical current density measured in the absence of external magnetic field) of $I_{c0} = 114$ A, this measured for long linear sections within the standard 1 μV cm^{-1} electric field criterion at which $E_0 = 1 \times 10^{-4}$ Vm^{-1} [141, 168]. This tape consists of a type-II superconducting thin film made of Yttrium Barium Copper Oxide (YBCO) with a large aspect of 1 μm thickness times 4 mm width, split into at least 4×115 finite elements for enabling a sufficiently high resolution for the proper analysis of the flux front profiles and, the distribution of current density along and across each turn of the 2G-HTS coil (see Table 3.1).

All layers of the SCS4050 tape with exemption of the buffer stack have been modelled (see Figures 2.16 & 3.1), for which it is worth reminding that the fabrication of the YBCO layer involves metal-organic chemical vapour deposition (MOCVD) over a heteroepitaxial layer of 0.2 μm (the buffer), deposited by

Table 3.1: Physical and computational characteristics for modelling the SCS4050 superconducting tape [134, 141, 168]

2G-HTS layers [134]	T_{th} [mm]	$T_{th(l)}$	T_w [mm]	$T_{w(l)}$
Top covering stabiliser Cu_1	0.02	2	4	200
Top overlayer Ag_1	0.002	1	4	200
YBCO (HTS)	0.001	3	4	200
Substrate	0.05	2	4	200
Bottom overlayer Ag_2	0.0018	1	4	200
Bottom covering stabiliser Cu_2	0.02	2	4	200

T_{th} refers to the material thickness which has been divided into $T_{th(l)}$ layers for attaining a local description of the physical variables. Likewise, the width characteristics are defined by T_w and $T_{w(l)}$ respectively, with $T_{th(l)} \times T_{w(l)}$ defining the total number of elements composing a material domain. The material layers totalled to the thickness of $< 0.1\ mm$, and are presented in the order shown in Figure 3.1 (c).

sputtering on a Hastelloy C-276 substrate of 50 μm ($\rho = 1.25 \times 10^{-9} \Omega m$), and then coated at the top and bottom by a thin Ag layer of $\sim$2 μm ($\rho = 2.7 \times 10^{-9} \Omega m$). This composition offers efficient uniform electrical contact with the Cu electro-thermal stabiliser layers of 20 μm thickness ($\rho = 1.97 \times 10^{-9} \Omega m$) each deposited at the top and bottom heterostructures of the 2G-HTS tape. Thus, within the numerical scope of this study, the thickness of the buffer layer is neglected, which implies that for transport currents under the critical threshold, I_{c0}, neither current is expected to flow across the buffer, nor magnetisation signal is expected to be added. Furthermore, in the 2D approach, all physical properties are considered to be homogeneous along the entire length of the 2G-HTS tape used, which is a valid approach for reproducing a wide range of experimental evidences as shown in [108, 169]. Moreover, the computational efforts applied to overcome the massive aspect ratio of the YBCO layer, are sufficiently enough to discern on a micro-level the corresponding physical features of the racetrack and pancake coil, as it will be shown in Chapter 3.2.

Recalling that Maxwell equations define the rules that describe the behaviour of current density, electric and magnetic field, and different formulations can represent these equations according to the chosen state variables (vector-scalar potentials $A-\phi$, current potential $T-\omega$, E-field or H-field com-

ponents) [155], in principle all different formulations commonly used to solve Maxwell equations with numerical models are equivalent, but the solutions of the corresponding PDE by means of finite element methods can differ. Studies have recognised the use of 'edge' (also 'vector') elements as the most effective for non-linear electromagnetics [160], thus, this study adopts the direct H components formulation, which in the case of 2D problems is reduced to the system of the two transverse components of the magnetic field, although the principle of using magnetic field components can be extended to the three-dimensional case. Thus, a detailed description of the magnetic field formulation employed for the model conditions of the racetrack and pancake coils are presented below

We begin with the two relevant Maxwell equations that govern the 2D H-formulation solved by the finite element software, COMSOL Multiphysics, where the Ampére's law is already defined within the quasi-static approximation [137] in Equation 1.19, and for Faraday's law (Equation 1.3), it can be rewritten as:

$$\nabla \times \mathbf{E} = -\mu_0 \mu_r \frac{\partial \mathbf{H}}{\partial t}\,, \tag{3.1}$$

where the components of the magnetic field $\mathbf{H}$ in Cartesian coordinates are given by the vector:

$$\mathbf{H} = \begin{vmatrix} H_x \\ H_y \\ H_z \end{vmatrix}. \tag{3.2}$$

Analogously, as the nabla operator, ∇, in Cartesian coordinates (x, y, z) can be written as:

$$\frac{\partial}{\partial x}\hat{\mathbf{u}}_x + \frac{\partial}{\partial y}\hat{\mathbf{u}}_y + \frac{\partial}{\partial z}\hat{\mathbf{u}}_z\,, \tag{3.3}$$

therefore, the curl of the electric field in $\hat{\mathbf{u}}_x, \hat{\mathbf{u}}_y, \hat{\mathbf{u}}_z$ directions can be written as:

$$\nabla \times \mathbf{E} = \begin{vmatrix} \hat{\mathbf{u}}_x & \hat{\mathbf{u}}_y & \hat{\mathbf{u}}_z \\ \dfrac{\partial}{\partial x} & \dfrac{\partial}{\partial y} & \dfrac{\partial}{\partial z} \\ E_x & E_y & E_z \end{vmatrix}, \tag{3.4}$$

or which is the same, by resolving the determinant:

$$\nabla \times \mathbf{E} = \hat{\mathbf{u}}_x \left(\frac{\partial E_z}{\partial y} - \frac{\partial E_y}{\partial z} \right) - \hat{\mathbf{u}}_y \left(\frac{\partial E_z}{\partial x} - \frac{\partial E_y}{\partial z} \right) + \hat{\mathbf{u}}_z \left(\frac{\partial E_y}{\partial x} - \frac{\partial E_x}{\partial y} \right). \tag{3.5}$$

According to the symmetry of the racetrack coil, the 2D approximation means that only the cross-section of the conductor is considered (see Figure 3.2 (a)),

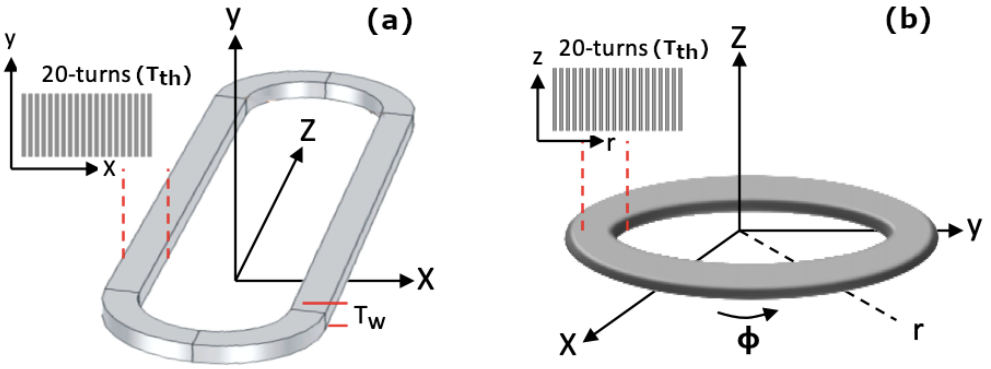

Figure 3.2: (a) Illustration of a racetrack coil lying over the plane xz, and the 2D cross section of the coil arm at the plane xy, which for a racetrack coil of length much greater than the former width (T_w), allows the neglecting of the U-turns [128]. (b) Same as in the left figure, but displaying axially symmetric axis (r, ϕ, z) of a pancake coil.

assuming that the length of the coil along the z- direction is at least five times bigger than its transversal width, an ansatz that has been demonstrated by comparing the results between 2D and 3D models, where an integral method splitting the straight and U-turns section renders the same results [128]. As a consequence, the induced magnetic field will have two transverse components, $\mathbf{H} = (H_x, H_y)$, with the profiles of current density inside the superconducting material flowing in the z- direction in order to screen the external magnetic field $\mathbf{H}_0$. Therefore, the electric field has one longitudinal component that flows only in the z- direction, i.e., E_z, as the current density is defined by J_z, which allows to define the vector components of magnetic field, current density, and electric field as:

$$\mathbf{H} = \begin{vmatrix} H_x \\ H_y \\ 0 \end{vmatrix} , \ \mathbf{J} = \begin{vmatrix} 0 \\ 0 \\ J_z \end{vmatrix} , \ \mathbf{E} = \begin{vmatrix} 0 \\ 0 \\ E_z \end{vmatrix} , \tag{3.6}$$

therefore, from Equation 3.5, Faraday's law can be rewritten as:

$$\nabla \times \mathbf{E} = \frac{\partial E_z}{\partial y}\hat{\mathbf{u}}_x - \frac{\partial E_z}{\partial x}\hat{\mathbf{u}}_y = -\mu_0\mu_r\frac{\partial \mathbf{H}}{\partial t} , \tag{3.7}$$

which in the column vectorial notation employed by COMSOL, it can be rewritten as:

$$\nabla \times \mathbf{E} = \begin{vmatrix} \frac{\partial E_z}{\partial y} \\ -\frac{\partial E_z}{\partial x} \\ 0 \end{vmatrix} = -\mu_0\mu_r \begin{vmatrix} \frac{\partial H_x}{\partial t} \\ \frac{\partial H_y}{\partial t} \\ 0 \end{vmatrix} . \tag{3.8}$$

On the other hand, similar to the previous procedure, it is easy to demonstrate that the curl of the magnetic vector in Ampére's law (Equation 1.19) can be represented as:

$$\nabla \times \mathbf{H} = \hat{\mathbf{u}}_x \left(\frac{\partial H_z}{\partial y} - \frac{\partial H_y}{\partial z} \right) - \hat{\mathbf{u}}_y \left(\frac{\partial H_z}{\partial x} - \frac{\partial H_y}{\partial z} \right) + \hat{\mathbf{u}}_z \left(\frac{\partial H_y}{\partial x} - \frac{\partial H_x}{\partial y} \right) . \quad (3.9)$$

Therefore, the current density which is allowed only in the z- direction allows to rewrite this equation as:

$$\mathbf{J} = \begin{vmatrix} & 0 & \\ & 0 & \\ \dfrac{\partial H_y}{\partial x} & & -\dfrac{\partial H_x}{\partial y} \end{vmatrix} , \quad (3.10)$$

which implies that Ampére's law can be used to describe the relationship between the local profiles of current density flowing in the z- direction, and the perpendicular component of the magnetic field (H_x, H_y).

Finally, in the case of a type-II superconducting material, the electric field behaviour is modelled by the $E - J$ power law which can be expressed as:

$$\mathbf{E} = E_0 \left(\frac{\mathbf{J}}{J_c} \right)^n = E_0 \, sgn\,(J) \left(\frac{|\mathbf{J}|}{J_c} \right)^n , \quad (3.11)$$

where J_c is the critical current density defined with the standard electric field criterion $E_0 = 1 \times 10^{-4} V m^{-1}$. The exponent n is the $E-J$ power relationship that indicates the period of the sudden transition from the superconducting state to the normal state, where the greater the power 'n', the closer the E-J law model approaches the critical state. Thus, given that $J_x = J_y = 0$, and in the same manner, $E_x = E_y = 0$, in the case of the electric field $\mathbf{E} = E_z \hat{\mathbf{u}}_z$ in the isotropic assumption, i.e., neglecting the dependence of $\mathbf{J}$ with the magnetic field or any other material property [170], we get:

$$E_z = E_0 \left| \frac{J_z}{|\mathbf{J}|} \left(\frac{|\mathbf{J}|}{J_c} \right)^n \right| . \quad (3.12)$$

Thus, in COMSOL Multiphysics the superconductors are somehow considered as Ohmic materials but with a highly non-linear dependence between the electric field and the current density, where material properties definitions such as electrical conductivity (σ) or electrical resistivity $(\rho = \sigma^{-1})$ must be entered as an analogous Ohm's law. In this sense, in order to preserve the integrability of Ohm's law across all the domains, where for normal metals Ohm's law is defined by the classical equation $\mathbf{J} = \sigma \mathbf{E}$, in the case of a SC material we can write Ohm's law as:

$$|\mathbf{J}| = \rho^{-1} |\mathbf{E}(\mathbf{J})| \Rightarrow \rho = \frac{|\mathbf{E}(\mathbf{J})|}{|\mathbf{J}|} . \quad (3.13)$$

Recall that Equation 3.11 describes the $E-J$ power law, thus, substituting Equation 3.11 into Equation 3.13 gives:

$$\rho = \frac{E_0}{|\mathbf{J}|}\left|\frac{\mathbf{J}}{J_c}\right|^n = \frac{E_0}{|\mathbf{J}|}\left(\frac{|\mathbf{J}|}{J_c}\right)^n , \tag{3.14}$$

which introduces the main difference between modelling a SC and a normal conductive material from the computational perspective, although this will have significant effects on the physical variables of the system as it will be shown in the following chapters.

Thus, the components of the resistivity expressed in the column vector representation of COMSOL means that:

$$\begin{vmatrix}\rho_x\\ \rho_y\\ \rho_z\end{vmatrix} = E_0 \begin{vmatrix} 0 \\ 0 \\ \dfrac{1}{|\mathbf{J}|}\left(\dfrac{|\mathbf{J}|}{J_c}\right)^n \end{vmatrix} . \tag{3.15}$$

However, the validity of a model is defined by the actual experimental evidences, and in this sense, besides the generality of Maxwell equations, and therefore the mathematical and computational formalism described above, it is the material law that describes the critical current density of a superconducting material, J_c, which can actually lead to more conclusive results from the quantitative point of view, beyond the general qualitative agreement that the pure critical state model for an isotropic J_c and high power index n in the $E-J$ power law could render. Thus, the most general material law that is capable of describing the $E-J$ properties of the 2G-HTS tapes at 77K, could be modelled using the isotropic relationship based on a generalised Kim's model [171]:

$$J_c(\mathbf{B}) = \frac{\mathbf{J}_{c0}}{\left(1+\dfrac{|\,\mathbf{B}\,|}{B_0}\right)^{\alpha}} , \tag{3.16}$$

which has been extended to include an experimentally validated function for the magneto angular anisotropy of the infield critical current density of a vast number of 2G-HTS tapes [141, 172] in our model. Therefore, in our model the simplified function for the magnetically anisotropic J_c law can be written as:

$$\mathbf{J}_c(\mathbf{B},\theta) = \frac{\mathbf{J}_{c0}}{\left(1+\epsilon_\theta\left(\dfrac{\mathbf{B}}{B_0}\right)^{\alpha}\right)^{\beta}} , \tag{3.17}$$

where the self-field critical current $\mathbf{I}_{c0} = 114\text{A}$ corresponds to the actual 2G-HTS tape SCS4050, with a critical current density $\mathbf{J}_{c0} = 28.5\text{GA/m}^2$. Thus,

B_0 and α are the so-called Kim's field parameters, β is the flux creep exponent, and ϵ_0 is the Blatter's angular anisotropy factor defined as:

$$\epsilon_\theta = \sqrt{\gamma^{-1}\sin^2(\theta) + \cos^2(\theta)}\,, \tag{3.18}$$

which is a function of the electron mass anisotropy ratio (γ) that moderates the angular dependence of the YBCO layer inside the 2G-HTS tape, and θ is the angular direction of the magnetic field $\mathbf{B}$ at the element of the SC mesh where the material law is being applied. The constant parameters, B_0, α, β, and γ depends only on the specific characteristics and fabrication of the superconducting tape as reported in [141, 172], where the parameter values used in this study correspond to the particular case of the Superpower SCS4050, which read as: $B_0 = 240\ mT$, $\alpha = 1$, $\beta = 1.5$, $\gamma = 5.02$, and $n = 30.5$. Moreover, it is worth mentioning that other material law approaches and their impact on the numerical modelling of superconducting coils are discussed in Chapter 5.

On the other hand, the pancake coil is modelled within the 2D axisymmetric environment of COMSOL Multiphysics, where the H-formulation can also be implemented but in cylindrical coordinates [135, 155, 173]. To derive the field variables that will be computed by the H-formulation of the Faraday's law, for obtaining the univocal solution of the profiles of current density through Ampére's law, we begin by transforming the nabla operator "∇" from Cartesian coordinates (x, y, z) to cylindrical coordinate (r, ϕ, z) (Figure 3.2 (b)), which are related by the transformation functions, $x = r\cos(\phi), and y = r\sin(\phi)$, resulting in:

$$\nabla = \frac{\partial}{\partial r}\hat{\mathbf{r}} + \frac{1}{r}\frac{\partial}{\partial \phi}\hat{\boldsymbol{\phi}} + \frac{\partial}{\partial z}\hat{\mathbf{z}}\,. \tag{3.19}$$

Figure 3.2 (b) depicts the axially symmetric configuration, from which the two dependent variables of H_r and H_z will represent the components of the magnetic field $\mathbf{H}$ in the problem. Likewise, the profiles of current density $\mathbf{J}_\phi$ inside each one of the turns of the 2G-HTS tapes and the induced electric field $\mathbf{E}_\phi$, both flow in the $\phi-$ direction, from which the relationship between the electric field and the current density, i.e., the superconducting $E - J$ power law, has to be defined in accordance with the material properties of the actual 2G-HTS tape used during the manufacturing of the coils. Thus, the $\nabla \times \mathbf{E}$ in Faraday's law can be written as,

$$\nabla \times \mathbf{E} = \begin{vmatrix} \frac{1}{r}\hat{r} & \hat{\phi} & \frac{1}{r}\hat{z} \\ \frac{\partial}{\partial r} & \frac{\partial}{\partial \phi} & \frac{\partial}{\partial z} \\ E_r & rE_\phi & E_z \end{vmatrix} = \begin{vmatrix} \frac{-\partial E_\phi}{\partial z} \\ \frac{1}{r}\frac{\partial (rE_\phi)}{\partial r} \end{vmatrix}. \tag{3.20}$$

Then, substituting the components of **H** and **E** into Equation 3.1, the 2D description of the axisymmetric model for the field variables computed by the so-called H-formulation of Faraday's law can be written as:

$$\begin{vmatrix} -\dfrac{\partial E_\phi}{\partial z} \\ \dfrac{1}{r}\dfrac{\partial (rE\phi)}{\partial r} \end{vmatrix} = -\mu_0 \begin{vmatrix} \mu_r \dfrac{\partial H_r}{\partial t} \\ \mu_r \dfrac{\partial H_z}{\partial t} \end{vmatrix} . \tag{3.21}$$

Concerning the Ampére's law in Equation 1.19 which can be used to describe the relation between the current density **J** and the components of magnetic field (H_r, H_z), with **J** only in the ϕ direction, the derivation of the $\nabla \times \mathbf{H}$ is equivalent to the $\nabla \times \mathbf{E}$ in Equation 3.20, such that the Ampére's law can be rewritten by the differential expression for the current density **J**

$$\mathbf{J} = J_\phi = \frac{\partial H_r}{\partial z} - \frac{\partial H_z}{\partial r} . \tag{3.22}$$

Coupling the above Equations where Faraday's law in Equation 1.19 can be rewritten as, $\partial_t(\mu_0 \mu_r \mathbf{H}) + \nabla \times \mathbf{E} = 0$, with $\mathbf{E} = \rho \nabla \times \mathbf{H}$ makes it possible for the H-formulation to be solved by the FEM software in COMSOL Multiphysics [164] as:

$$\mu \frac{\partial \mathbf{H}}{\partial t} + \nabla \times (\rho \nabla \times \mathbf{H}) = 0 . \tag{3.23}$$

Moreover, to satisfy the condition of zero divergence of the magnetic field in COMSOL, the most effective way is the use of edge elements of the first order, which assures the continuity of the tangential component of the magnetic field from one element to the adjacent one [174].

The Equations for current density (Equation 3.10 for the racetrack coil, and Equation 3.22 for the pancake coil), electric field (Equation 3.12), and the two transverse components of magnetic field for the different symmetry conditions with prescribed appropriate boundary conditions (Equation 3.8 for the racetrack coil, and Equation 3.21 for the pancake coil), constitute the numerical model employed for simulating the macroscopic electromagnetic behaviour of 2G-HTS coils. Then, to include the transport current condition, our simulation adopts integral constraints for the current density **J** over the cross-section of the racetrack and pancake coils, such that at each one of the turns of the coil the transport current is defined as the integral of the current density derived by the model, i.e.:

$$\mathbf{I}_i(t) = \int_{\Omega_i} \mathbf{J}_i(t) d\Omega , \tag{3.24}$$

where Ω_i indicates the area of the cross section of the REBCO layer within the i-th turn of the superconducting coil.

Then, it is to be noticed that although the axisymmetrical conditions of the pancake coil allows to model this as a single array of stacked tapes in the 2D representation of its cross-section, in the case of a racetrack coil a further boundary condition must be invoked, otherwise the left and right arms of the coil must me modelled (see Figure 3.2). Thus, by the symmetry of the problem, and in order to consider one single arm of the racetrack coil, a Dirichlet boundary condition ($H_x = 0$) is imposed at the centre axis of the coil former (5 cm width) neglecting the effect of the U-ends of the coil. Likewise, in the case of the pancake coil a further boundary condition can be added at the centre of the coil, i.e., at the z-axis over the origin of the coordinate system in COMSOL, where $H_r = 0$, which although is not mandatory, it can help into the numerical convergence of the PDE system, as the boundary conditions determine the validity of the current and magnetic simulations within the model. Besides, other than taking the advantage of the axisymmetric conditions of the model for achieving minimal computing time, further symmetry conditions could be imposed for a perfectly wound coil, such that only either its top or bottom half would need to be considered, thus, achieving nearly a 50% reduction in the number of elements within the domains describing the SC coil. However, for misaligned windings dual axisymmetrical reductions cannot be imposed resulting in the compulsory modelling of the entire width of the coil for attaining results under the same physical and computational benchmark. Thus, although additional homogenisation meshing techniques comparable to the ones presented in [116, 148, 169] could be applied to encapsulate the average behaviour of bundles of 2G-HTS tapes, i.e. modelling multiple turns of the coil into singular domains for faster computation, employing these approaches in misaligned coils will inherently impede a physical insight at local level, i.e., within each turn of the SC coil, in particular when the profiles of transport or induced current in a single turn result transposed into bulk-like descriptions (covering multiple coil turns), except if the number of turns in the coil is large enough such that the local distribution of profiles of current density within sequential turns, is expected to show the same position for the flux front profiles within the size of the smallest homogenised element. Nevertheless, from the physical perspective, where computing time reductions are not of uttermost importance, an accurate definition for the size of homogenised domains requires to have an ad hoc knowledge on the distribution of profiles of current density, this being one of the cornerstones contributed by this study.

Then, in order to implement the physical model conditions above described for the racetrack and pancake coil within the partial differential equations form of COMSOL Multiphysics, the derived PDE of the Faraday's law in Equation 3.8 (or Equation 3.21) needs to be presented with its variables appropriately defined into their corresponding cells inside the GUI of the COMSOL

model builder. Therefore, it is imperative to understand how to insert the components of the derived H-formulation into the designated cells inside COMSOL to avoid incorrect solutions. In this sense, the general form PDE interface is expressed, by default, with the following equation coefficients:

$$e_a \frac{\partial^2 \mathbf{H}}{\partial t^2} + d_a \frac{\partial \mathbf{H}}{\partial t} + \nabla \cdot \Gamma = f \,, \tag{3.25}$$

where e_a is the mass coefficient, d_a, is the damping or mass coefficient, Γ, the conservative flux vector, and f is the source term.

In the case of the flux terms, the divergence operator is executed on each row discretely, and it is defined as:

$$\nabla \cdot \Gamma = \nabla \cdot \begin{bmatrix} \begin{bmatrix} T_{11} \\ T_{12} \end{bmatrix} \\ \begin{bmatrix} T_{21} \\ T_{21} \end{bmatrix} \end{bmatrix} = \begin{bmatrix} \nabla \cdot \begin{bmatrix} T_{11} \\ T_{12} \end{bmatrix} \\ \nabla \cdot \begin{bmatrix} T_{21} \\ T_{21} \end{bmatrix} \end{bmatrix} \,, \tag{3.26}$$

where $\nabla = [\partial_x, \partial_y]$ in Cartesian coordinates, i.e., for the case of the Racetrack coil (Equation 3.8), and the divergence of the conservative flux vector matrix in Equation 3.26, this can be simplified further as:

$$\nabla \cdot \Gamma = \begin{bmatrix} [\partial_x, \partial_y] & \begin{bmatrix} T_{11} \\ T_{12} \end{bmatrix} \\ [\partial_x, \partial_y] & \begin{bmatrix} T_{21} \\ T_{21} \end{bmatrix} \end{bmatrix} = \begin{bmatrix} \partial_x T_{11} + \partial_y T_{12} \\ \partial_x T_{21} + \partial_y T_{22} \end{bmatrix} \,, \tag{3.27}$$

where, the components, T_{11} , T_{12} , T_{21} , T_{22} correspond to:

$$\Gamma = \begin{bmatrix} T_{11} \\ T_{12} \\ T_{21} \\ T_{22} \end{bmatrix} = \begin{bmatrix} 0 \\ E_z \\ -E_z \\ 0 \end{bmatrix} \,. \tag{3.28}$$

Then, the mass terms on the left hand side of Equation 3.25 result to zero, because the second order of the general PDE form do not need to be accounted, i.e, $e_a \partial_t^2 \mathbf{H} = 0$. Similarly, the damping term is given by:

$$d_a \frac{\partial \mathbf{H}}{\partial t} = \begin{bmatrix} d_{a11} \\ d_{a12} \\ d_{a21} \\ d_{a22} \end{bmatrix} = \begin{bmatrix} \mu_0 \\ 0 \\ 0 \\ \mu_0 \end{bmatrix} \,. \tag{3.29}$$

These derived values in the above matrices are inserted into the designated cells for the conservative flux variables in the COMSOL GUI, whilst the constraints and boundary conditions are inserted by selecting the corresponding

edge or material domains, respectively. Further information about how to include boundary or constraint conditions can be found in the User Manual available for each one of the COMSOL Multiphysics versions [164], which due to its generality and availability it is not included in this thesis.

The computational time required in our model simulation is consequentially dependent on the mesh density used for discretisation of the tapes, the number of turns and the intensity of the applied current. As mentioned previously, speed up computation is also achieved by taking advantage of the characteristics of the edge element, and the smooth convergence of the solver could be challenging to achieve depending on the features of the PDEs. For instance, in cases were boundary conditions or equations are highly nonlinear, specific control approaches could improve the convergence and obtain an accurate solution. However, refining the time step and mesh (mapped mesh, see Figure 3.3) can result in smoother convergence, but this effects the speed of the solver, thus, increasing the computational time.

From the technical point of view, the average computing times for one thousand time steps per I_{tr} cycle in the case of having a perfectly wound or misaligned coil, both show a negligible difference, providing that the same current conditions are maintained. On the one hand, the computing time for a single case of a racetrack coil model under the reduced mesh conditions described in Chapter 3.1, ranges from approximately 5 hours for cases with current amplitudes $I_a = 0.1 I_{c0}$, up to approximately 22 hours for cases with $I_a = I_{c0}$, i.e., the time increases in terms of the intensity of the applied transport current relating to a specific case investigated in this study. On the other hand, the computation for the Pancake coil model can take between 2 days for very low intensities of the applied current, $I_a = 0.1\ I_{c0}$, up to 6 days for the threshold current $I_a = I_{c0}$, within workstations equipped with an Intel® i7-6700k CPU @ 4GHz core processor with 32GB RAM. In this sense, multiple CPUs have been used for the simulation; otherwise, the study can take up to 31 days of full computing time for each coil configuration on a single CPU, where the computing time can be even doubled if a more standard CPU of 3.0 GHz clock rate, 4 MB L2 cache, and 16 GB RAM memory is used, according to our own computational benchmark.

Finally, we consider it worthy to mention the technical issue that has been encountered when plotting the normalised current density profiles within the HTS domains, using the 'Cut line 2D' plotting functionality of COMSOL for the post-processing and analysis of results. This because a large community of superconductivity researchers have adopted this method for displaying the local profiles of normalised current density, J/J_c, inside each one of the turns of the superconducting coil in a *'not-to-scale'* fashion, as a means to surpass

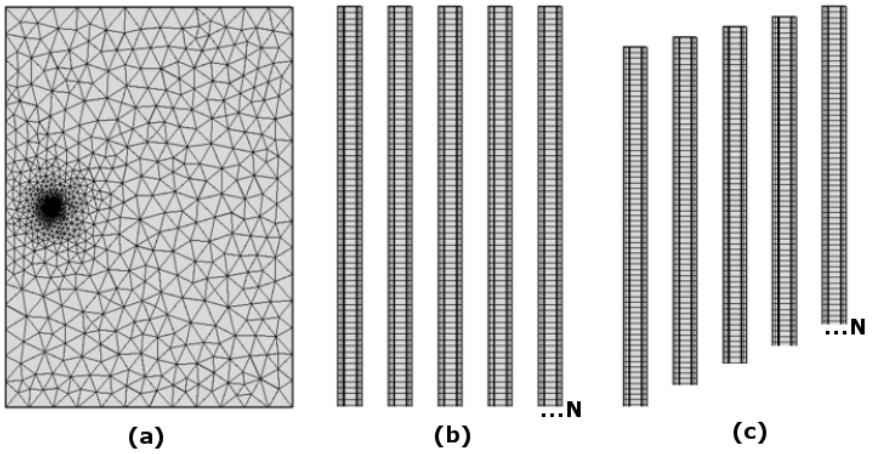

Figure 3.3: (not to scale) Represents the mesh structure of 2D domains used in this work, showing (a) the free triangular mesh for the air subdomain with a high density of elements near the cross-section of the 2G-HTS coil, and (b) the inner domain mesh of rectangular elements for the the cross-section of perfectly aligned 2G-HTS tapes for the racetrack and pancake coil with (c) representing the case of non-uniform wound coil. Notice that the space between tapes here represents the insulation between the coil turns, and the meshing of these domains, as well all the layers of the 2G-HTS tape modelled (see Table 3.1) are not displayed for easy visualisation of the misalignment effect between coil turns.

the large aspect ratio of the HTS tape. However, a 'cut line 2D' calculates the averaged current along the thickness of a *"cylinder"* (actually a rectangular domain in the 2D model) whose thickness and width commonly matches (at least) the dimensions of the YBCO layer into the 2G-HTS tape, therefore hiding the actual local distribution of profiles of current density where well defined flux front profiles could be distinguished. For instance, from the physics perspective, the use of a 'cut line 2D' approach to display the average profiles of current density for low to moderate amplitudes of the applied current ($I_a \leq 0.7\ I_{c0}$), may give the false impression of having a large flux-free core region inside the HTS layers, because the average of the current on the superconducting regions dominated by the occurrence of magnetisation currents results to be zero. Therefore, for an appropriate representation of the local profiles of current density, we recommend exporting the calculated values over the entire mesh of elements defining the HTS domains for post-processing, analysis, and plotting into an external software such as MATLAB. In this way, the displayed flux front profiles could give a better account of the concomitant occurrence of transport and magnetisation currents inside each one of the turns of the HTS coil.

3.2 *Particular Specifications for the modelled Coils*

The cross-section of both the racetrack and Pancake coils were designed systematically to accommodate the simulation of perfectly aligned winding configurations or the non-uniformity cases (see Figure 3.1). The latter consists of geometrical turn-to-turn misalignments within the bundle of the parallel 2G-HTS tape starting from the innermost turn towards the outermost turn in increments of $\delta_m = (T_w/4) \times (N-1)$, with T_w being the overall width of the tape, N the number of turns, and δ_m the collateral turn misalignment factor, replicating the scenario of a deformed wound coil. In particular, our simulations consist of a distinctive misalignment factor of $\delta_m = 20\ \mu m$, 25 μm, 30 μm, 50 μm, and 100 μm between the adjacent turns, or in a more general perspective, innermost to outermost turn-misalignment of $T_w/10$, $T_w/8$, $T_w/6$, $T_w/4$, and $T_w/2$. In other words, the magnitude of the misalignment factors δ_m shown in this study correlate to the overall displacement between the innermost and the outermost turn of the coils (racetrack and pancake-shaped), also called the coil deformation, which is indicated as a function of the tape width, T_w. In this sense, the $\delta_m = 100$ μm assumed for a 20 turns SCS4050 coil is the maximum lateral misalignment between the innermost and outermost turn of half of the tape-width (2 mm).

Thus, the assumed condition $\delta_m = 100\ \mu m$ defines the maximum tolerance for the misalignment between adjacent tapes, without compromising the mechanical and electrical properties of the 2G-HTS tape at each turn. In this sense, greater misalignments are unlikely to happen as it is improbable to evince a scenario where the imbalance between the positioning of the innermost and outermost turns of a laminar coil will be higher than half of its tape-width, unless the number of turns in the coil is much greater than 20. Nevertheless, the threshold value for the misalignment factor depends on the maximum width of the HTS tape that could be displaced out of a collinear configuration (perfect winding) without exhibiting delamination behaviours (i.e., localised damage to the microstructure of the tape), due to shear stresses between the different turns of the HTS coil [175], which could be mitigated by the use of adequate insulation systems such as the inclusion of a soft metallic layer in YBCO CCs tapes, or the extrinsic reinforcement with solder fillets lamination as currently applied for RABiTS [131, 176, 177]. Therefore, for the case of the SCS4050 tape that has been considered in this study, the maximum misalignment factor $\delta_m = 100\ \mu m$ is a plausible threshold value, as this has been already demonstrated that for up to a $5 - MPa$ applied stress level, with a $8 \times 3\ mm$ width anvil, the shear stress at less than 250 μm from the tape

edges results negligible [178].

Moreover, for a 20 turns 4 mm tape-width coil, the deformation of 0.4 mm to 2 mm can be understood as a coil deformation range of $T_w/10$ to $T_w/2$ for large coils. Certainly, these deformations are likely to occur in a coil with larger number of turns, which might seem exaggerated within the size of the coil that has been considered in this study at the expense of achieving numerical convergence under a reasonable computing time. However, it is worth highlighting that for the sake of generality of this study, all physical features are being presented in renormalised units of the turn-to-turn misalignment factor δ_m, in such way that the results presented are valid for racetrack or pancake coils with a greater number of turns. This is because the distribution of profiles of current density presented for our exemplar 20 turns case will render a sufficiently large resolution for enabling direct use of homogenisation meshing techniques [116] or multi-scale models [169], where a single one of our modelled superconducting coil turns could reproduce the electromagnetic response of a whole stack. For example, in a 1000 turns racetrack coil with turn-to-turn displacements as small as 0.4 μm, the average distribution of profiles of current density in a single stack of 50 turns, will be represented by the local distribution of profiles of current density inside one of our generic 20-turns coil, in the same relative position, such that based on the homogenisation techniques the calculations of the AC losses are expected not to yield to errors larger than 2.5%. Moreover, it has to be noticed that our simulation results for turn-to-turn displacements of $\delta_m < 20$ μm exhibit negligible differences of ($< 2\%$) between the AC losses for perfectly wound coils and the deformed coils, and therefore all the simulations presented in this thesis will be for turn-to-turn displacements no smaller than 20 μm.

Therefore, based on the above considerations, the simulations in this study takes into account ten different amplitudes of the alternating transport current, I_a, with six cases of racetrack and pancake coils conformed to distinctive misalignment factors of $\delta_m = 0, 20$ $\mu m, 25$ $\mu m, 30$ $\mu m, 50$ μm, and 100 μm. In this sense, the study of both coils consisted in the analysis and computation of one hundred and twenty cases, whose computing time depends on the high mesh resolution of the physical domains and the computer specs (processors and RAM) employed. In fact, the computational burden imposed by the SCS4050 2G-HTS large aspect ratio (0.1 mm thickness $\times$ 4 mm width) presents computational challenges (see Figure 3.3), considering that in our case we need substantial resolution to account for the local behaviour of the physical variables within the individual turns of the coil, where the winding misalignments are in the order of microns. Thus, our meshing strategy is to split the 20 turns of the 2G-HTS tape into 221 domains comprising the six-layered structure considered for the internal structure of the individual turns, and their surrounding

environment. It is therefore to be noticed that homogenisation techniques such as the ones proposed in [116] do not apply to our study, this mainly due to the geometry, dimensions, and the specific nature of our problem, although these can mitigate the computational burden for the modelling of a perfectly or uniform wound coil, corresponding to the case with $\delta_m = 0$. Thus, we have found that for a relative tolerance between internal solutions for the field variables superior than $1E-6$, and a minimum absolute tolerance of $1E-8$, a mesh of 31500 quad elements for the tape-domains renders the same solution than an equivalent mesh with approximate 15000 quad elements, as long as the number of triangular, edge, and vertex elements of the mesh used for the surrounding spaces (commonly called air domains) double the number of quad elements. This computational insight is important, because it allows us to define a minimal element ratio in specific domains where "extra elements" or an "extremely" fine mesh is required e.g., in cases where a micro level resolution is required (as it is our case), and also in situations where it is necessary to simplify or reduce the number of sublayers for meshing the overall structure of the 2G-HTS tape. For instance, a 31500 quad elements mesh implies that each identified ReBCO layer into the cross-section of the coils modelled could be divided into 7 sublayers, each containing 75 elements across the width of the tape, and similarly, the Cu and substrate layers can be divided into 4 sublayers each, with the Ag modelled as a single layer. However, with the simplified mesh approach in Table 3.1, it is possible to reduce the mesh to about less than half of the number of elements, with conceivable results within the same tolerance levels than in the finest mesh. This has allowed us to reduce the number of sublayers to its minimum, i.e., 3 for the YBCO layers, 2 for the substrate, 2 for the Cu layers, and 1 for the Ag layers, whilst maintaining our fundamental focus of being able to account for current density flux at the local level.

Chapter 4

Electromagnetic Features of 2G-HTS Racetrack and Pancake Coils Subjected to Winding Deformations

Most of the reported numerical studies on superconducting racetrack coils [116, 130, 155, 174] or pancake coils [96, 114, 117, 119, 122, 123, 127, 136, 179, 180] refer to perfectly wound magneto-isotropic coils subjected to certain transport current conditions (also called self-field conditions) aiming to explain specific experimental evidence, or to improve their electromagnetic performance by novel optimisation approaches. However, none of these previous studies has proven to have a sufficiently accurate resolution, capable to allow a full physical description on the local time dynamics of flux front profiles inside the individual superconducting turns of a 2G-HTS coil. Therefore, considering cases where the experimental conditions might have shown possible deformations in the coils winding, and the understanding on how this phenomena can impact the measurement of relevant macroscopical quantities, such as the AC Losses, has been evasive. This is probably due not only to the computational challenges explained in Chapter 3, but to the success of applying either reductions on the degrees of freedom for the superconducting tape or, common meshing homogenisation techniques applied to the cross-section of perfectly wound coils, both capable of rendering “acceptable" estimations of the AC losses within a $10\% - 20\%$ average deviation from the experimental measurements, which can be the result as well on many other experimental factors. Still, it is question that has remained open for decades, and tackling this problem is the purpose of this chapter.

In fact, due to the length-scale implicit in the possible misalignment of non-uniform wound coils, where the lateral displacement between the innermost and the outermost turn of a coil could easily exceed 10% of 2G-HTS tape width, it can be intuitively expected that the induced changes in the AC losses, if any, could be within the same order than the error tolerance aforementioned. Therefore, this implies that simplified meshing minimisation techniques for misaligned coils would not give a proper account of the physical mechanisms involved, unless the observation of local changes on the distribution of current density inside the superconducting layers of the coil turns is conceivable. In this sense, to the author's best of knowledge, this is the first study that presents an exhaustive study on how the local profiles of current density inside individual turns conforming, either the pancake or racetrack coil; with or without winding misalignment geometries, evolve in time within AC transient states of an applied current of different amplitudes (Fig 3.1(d)), covering from very low transport current profiles ($I_{tr} = 0.1\ I_{c0}$), up to the critical current threshold value I_{c0}.

Specifically, this chapter presents a comprehensive study on the local electrodynamics at micron level for the second generation of a magnetically anisotropic high-temperature superconducting racetrack and pancake coils, both wound on a 5 cm mid-width former with different configurations comprising perfectly wound and winding misalignment characteristics. In particular, special attention has been given to the influence of the turn-to-turn lateral misalignment factor on the local electromagnetic properties of individual turns, which has been analysed by considering six different coil arrangements and ten amplitudes for the applied alternating transport current, I_a, together with an experimentally determined function for the magneto-angular anisotropy properties of the critical current density, $J_c(B, \theta)$ [141] of the Superpower SCS4050 tape. The study adopts high-level meshing considerations in order to get a realistic account of the local and global electromagnetic properties of 20 turns racetrack and pancake coils. It includes a mapping of the flux front dynamics with well-defined zones for the occurrence of magnetisation currents, transport currents, and flux-free cores, which simultaneously enables an adequate resolution for determining the experimental conditions when turn-to-turn misalignments of the order of 20 μm-100 μm can lead not only to the increment of the AC losses, but also to a striking reduction of their AC losses which we have found to be connected to the actual disappearance of the flux-free core inside the superconducting coil. Our results for the time dynamics of the flux front profiles of current density for the perfectly wound racetrack and pancake coils, and its counterpart, coils with a clear misalignment in its winding pattern are both presented. Noteworthy patterns of transport and magnetisation currents are disclosed at the micron level, i.e., across the thickness of the 1 micron

YBCO layer that compose the SC structure of the 4mm 2G-HTS tape, and over each one of the turns of the racetrack and pancake coil. These observed patterns build a generalised framework for our discussion (disclosed in the later sections) of the curves of AC losses for misaligned racetrack and pancake coils which can be used as a practical benchmark to determine the relative hysteresis losses for any 2G-HTS racetrack or pancake coil application respectively. The reader is encouraged to download and zoom the high-resolution Figures (4.1, 4.2, 4.3, & 4.4) for a better understanding of the results presented in this study, such that a better visualisation and understanding of the distribution of current profiles could be achieved were applicable.

4.1 *Local Characteristics of Perfectly Wound Coils*

Previously we mentioned that the numerical computing time for any of the models considered in this study could be extensively reduced by simplifying the number of elements inside the individual turns of the superconducting domain that constitute the coil, even up to the limit of considering a 1D strip geometry for each one of the HTS layers, therefore eliminating the aspect-ratio problem. However, within this approach, it becomes unlikely to observe the physical nature of the local profiles of current density as the occurrence of magnetisation currents, i.e., currents flowing in opposite direction within the superconducting tape, cannot be seen within this strategy. Moreover, the ReBCO materials used for the manufacturing of 2G-HTS tapes are well known to be affected by the intensity and direction of externally applied magnetic fields [39, 137, 181], which can diminish the intensity of the critical current density $J_c(B, \theta)$ [141], or cause intricate distributions of current density profiles inside the superconducting material [78, 80, 108, 109, 182]. Therefore, the minimum approach that could be considered is to model each HTS layer as a 2D system with a minimum of 2 sub-layers across their thickness, such that opposite magnetisation currents can appear within each HTS domains. Still, this level of resolution might not be sufficient for the case of misaligned coils, as the deformation of the flux front profiles will initially occur at the lateral edges of the individual turns as the transport current is applied, where a denser mesh of elements will be required to account for the displacement of successive turns, reason why at least three sublayers should be considered for the describing the YBCO layer, with a sufficiently large number of elements distributed across the width tape as discussed in the previous chapter (see Table 3.1).

Thus, defining the exact symmetry of the flux front profile in the presence

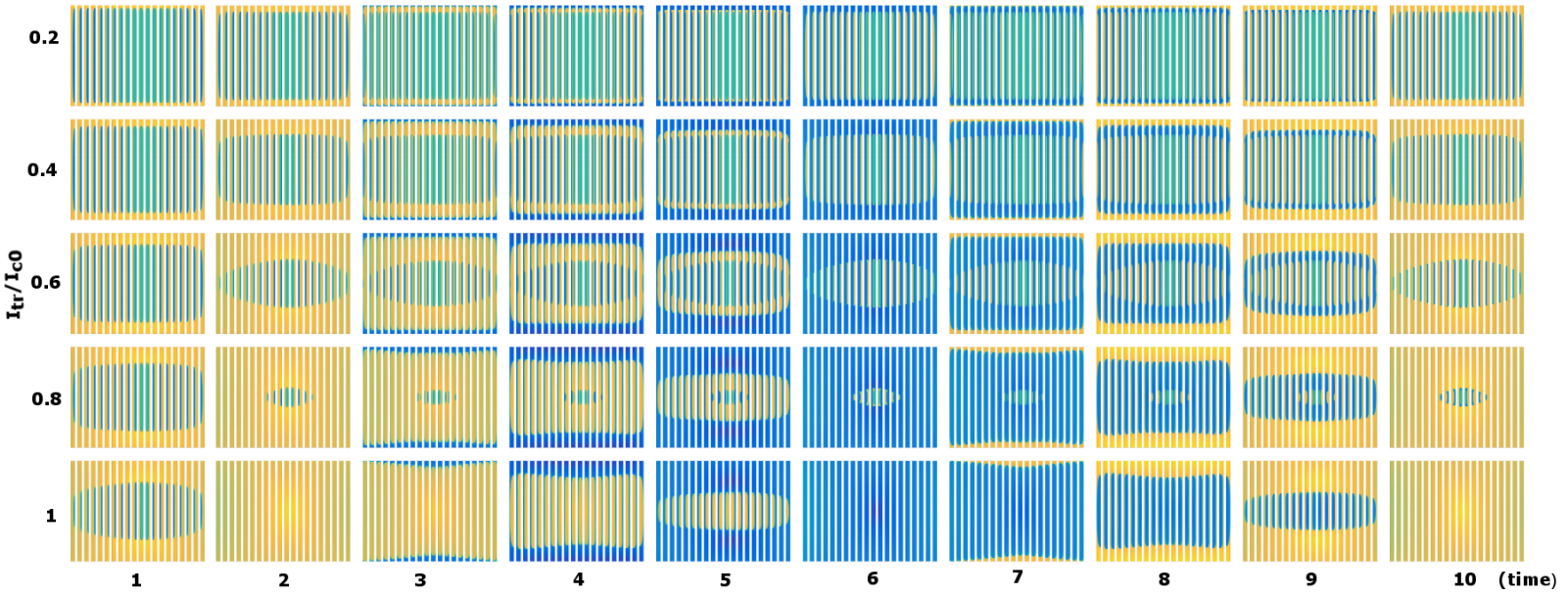

Figure 4.1: (color online) Evolution of the normalised current density J/J_c in a perfectly wound pancake coil ($\delta_m = 0$; Fig 3.1 (a)) made of 20 HTS layers under alternating transport current conditions of amplitude I_a. Darker coloured (blue) regions indicate zones with negative elements of current density $J_i = -J_c$, lighter coloured (yellow) regions correspond to $J_i = +J_c$, otherwise (green) corresponds to the flux free core where J_i and B_i are both equal zero. Subplots are labelled in accordance with the monotonic branch of the experimental processes depicted in Fig. 3.1 (d), starting from the time-step 1 at the leftmost pane to the time-step 10 at the rightmost pane of the figure.

of transport current is relatively complex, although it can be determined with the use of a refined mesh across the thickness of the HTS tapes. For instance, let us consider the case of perfectly aligned wound HTS coils composed of a stack of 2G-HTS tapes, as shown in Figure 3.1 (a). Therein, the occurrence of transport current on each of these 2D HTS layers that correspond to the wound turns of the HTS coil, indicates the manifestation of inductive magnetisation currents across the thickness of the tape, which therefore implies that if a single sublayer is considered for each HTS domains, the regions with magnetisation currents will be computed as flux free-regions, and thus, rendering a mathematically valid but physically incorrect result. Consequently, it will impede the computation of the magnetisation losses of the system, particularly for low intensities of the applied transport current ($I_a < 0.5\ I_{c0}$), i.e., when the magnetisation currents take a dominant role, with discrepancies that could yield more than 50% the actual AC losses in the system, as it has been reported in for wires of circular or rectangular cross-sections. On the other hand, for higher intensities of I_a, we have found that the discrepancy between the numerical results for the strip (1D) approximation and the 2D single or homogenised layer approximations [116, 183] is reduced from about a 20% discrepancy for $I_a = 0.8 I_{c0}$ to a 7% when $I_a = I_{c0}$, which is the typical range of operation for the HTS wire. This is because the area occupied by the transport current density profiles for $I_a \geq 0.8\ I_{c0}$ is much higher than the area occupied by magnetisation currents and the flux-free core, phenomena illustrated at the time step '5' and '6' of Figures 4.1 & 4.2. These figures show the distribution of current density profiles for the perfectly wound coil as a function of time, connected to the unit time steps illustrated in Figure 3.1 (d), for different intensities of the applied current, where the high order meshing level within our calculations (see Table 3.1) allows to locally discern the physical nature between the different profiles of current density inside of each 1μm thick superconducting layers.

It is to be noticed that in Figure 4.1 & 4.2, almost no difference was obtained in the observed local distribution of current density profiles, meaning that no physical discernment between the dimensions of the local flux front profiles for the local electromagnetic response of pancake and racetrack HTS coil can be seen. For this reason, the analysis of the local characteristics for perfectly wound racetrack and pancake coils would be based on Figure 4.1. Therein, it displays the normalised profiles of current density for 1/2 cycles of the applied current ($I_{tr} = I_a sin(\omega t)$), with amplitudes ranging from $0.2\ I_{c0}$ up to the threshold value I_{c0} for the self-field critical current condition measured on an individual HTS tape [141]. In Figure 4.1, approximately 30% of the turns (6 central layers) for the low amplitude of the applied transport current $I_a = 0.2\ I_{c0}$, show a collective 'bulk' behaviour with an observable flux-free

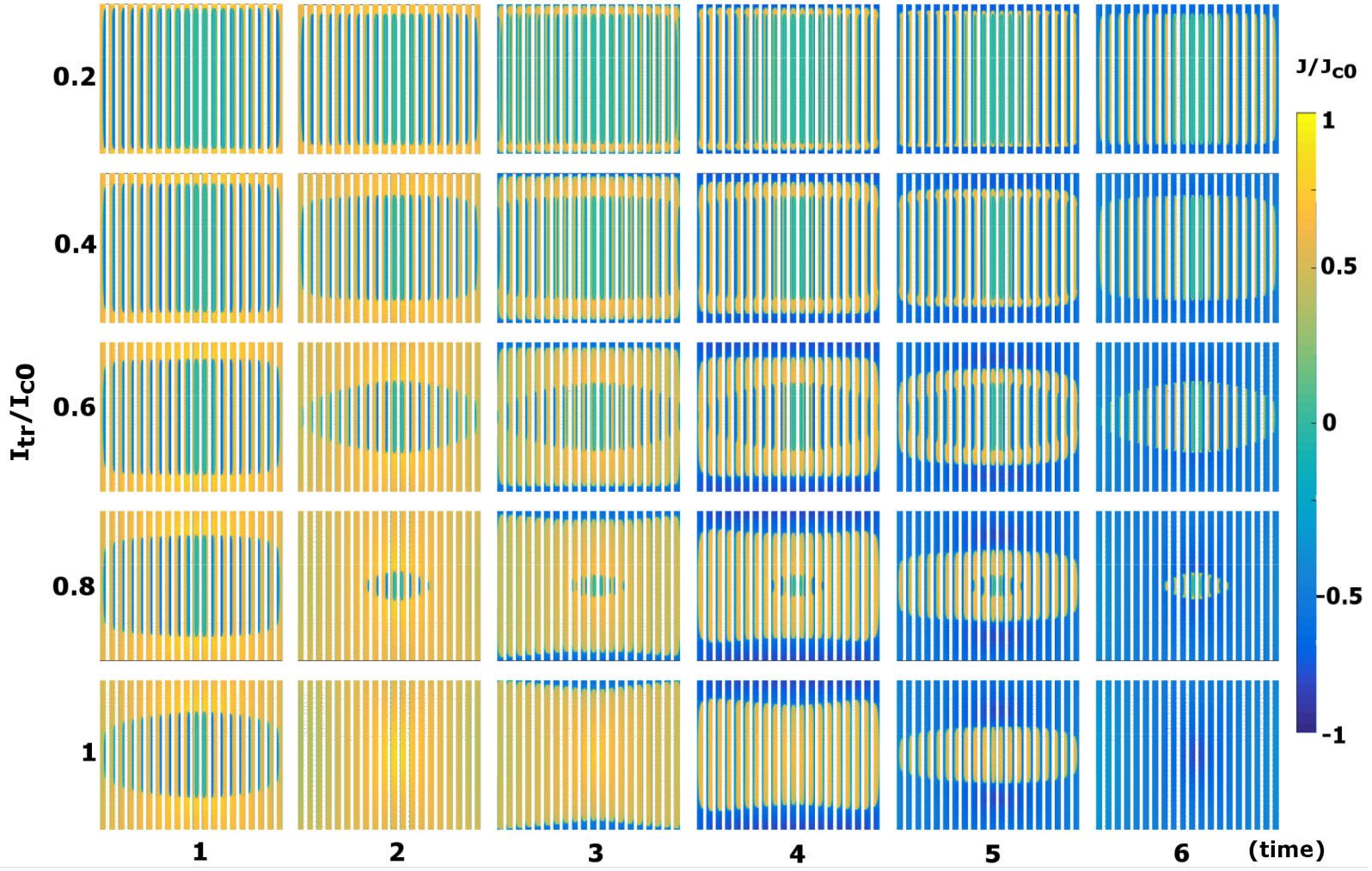

Figure 4.2: Normalised profiles of current density J/J_{c0} within the ReBCO layers (not to scale) of a 20 turns HTS racetrack coil in the configuration shown in Fig. 3.1 (a), and with applied AC currents of amplitude $I_{tr} = I_a/I_{c0}$ =0.2, 0.4, 0.6, 0.8, and 1.0 (top to bottom, respectively). Time evolution is presented as a sequence of labelled columns in accordance with the time steps displayed in Figure 3.1 (d).

core (green zones) with no visible magnetisation currents [184], i.e., showing that the central turns of the coil are only affected by the extrinsic source of transport current density at the top and bottom of each HTS turn. However, the remaining turns, i.e., the inner and outer seven turns of the coil, show a clear dominance of magnetisation currents along the width of each tape, and these turns are confined by the flux front profile that separates the transport current density (local profiles of current, $\mathbf{J}_i$, flowing in a single direction across the whole thickness of the tape) from the magnetisation currents which fully penetrate each turn. Thus, although a homogenised or coarser mesh could give a qualitatively valid macroscopic description of the electromagnetic properties of the HTS coil, as power losses are in the region dominated by the transport current [185], it is evinced that models simpler than the one considered in this study will not be able to give a proper account for the magnetisation losses of the system. Furthermore, as the amplitude of the applied transport current increases, the number of turns that become fully penetrated by magnetisation currents increase as well, hence reducing the size of the central flux-free core that disappears when $I_a \geq 0.9\ I_{c0}$ at the time step '2' in Figure 4.1.

Besides, the material law governing the electrodynamics of realistic 2G-HTS tapes and their measured magneto-angular anisotropy [141] plays a dominant role in the observed features of the local distribution of current profiles, which could not be observed at their full extent by simplified material laws such as the critical state model [181]. For instance, before analysing the peak-to-peak hysteretic behaviour that occurs between the time step '2' and '6' in Figure 4.1, the influence of increasing the transport current for a DC application can be analysed by simply observing the evolution of the profiles of current density along the second column of subplots displayed in this figure. From this viewpoint, it can be seen that under the critical state condition, the local profiles of current density must ensure the condition $\mathbf{J}_i = \pm\mathbf{J}_{c0}$, which implies that for $I_a < I_{c0}$, each turns will have to show the occurrence of magnetisation currents around the radial axis of the coil, otherwise, the system will not be able to satisfy the transport current condition $I_{tr} = \int J_i\, d\Omega_i$. Therefore, under the critical state condition, the local distribution of profiles of current density for $I_a \leq 0.6\ I_{c0}$ will show a comparable symmetry to the one depicted in Figure 4.1, with the exception that the $\mathbf{J}_i$ across the width of each turn will equal $\mathbf{J}_{c0}$ for transport current profiles and $\pm\mathbf{J}_{c0}$ for magnetisation currents. On the other hand, for $I_a > 0.6\ I_{c0}$, the length of the semi-major axis of the quasi-elliptical flux-front profile which delimits the transition from transport current profiles with the occurrence of magnetisation currents remains constant, whilst the position of the co-vertices linearly approaches the geometrical centre of the coil, reducing the length of the semi-minor axis of the flux front, until the full transport current condition $I_{tr} = I_{c0}$ is reached. Consequently,

this implies that for moderate to high currents ($0.6\ I_{c0} \leq I_{tr} \leq 0.9\ I_{c0}$), the critical state model will render a slight overestimation of the magnetisation losses that decreases as I_{tr} increases. This occurrence is due to the consumption of magnetisation currents [40], which explains why the CS model is still a very successful physical approach despite neglecting the magneto angular anisotropy of the real HTS material [137].

Nevertheless, the introduction of the experimentally measured power-law dependence between the critical current density on the direction and intensity of an external magnetic field, results into a more accurate description of the electromagnetic properties of 2G-HTS tapes [141]. In this case, assuming the simplified Kim's model [171], i.e., the critical current dependence on only the magnetic field with no angular factor $J_c(\mathbf{B})$, both the local distribution of current density and the temporal process of the flux-front profiles for $I_a > 0.6 I_{c0}$ displays a better qualitative resemblance with the profiles of current density illustrated in Figure 4.1, where instead of showing a constant current density across all the elements of the superconducting tape with induced magnetic field as in the CS model, the critical current density diminishes from J_{c0} at the geometrical centre of the coil towards the edges of outermost and innermost turns. Notably, at this current levels and before changing the direction of the applied transport current, it was found that no meaningful differences are observed between Kim's model (Equation 3.16) and the generalised magneto-angular model introduced in Equation 3.17. However, taking into account the angular anisotropy characteristics of J_c a remarkable difference at applied currents $I_a > 0.6\ I_{c0}$ is evinced, by showing a concave shape of the flux-front profile beyond the peak current $I_{tr} = I_a$ (time step '2' in Figures 4.1 & 4.2) and the time step when $I_{tr} = 0$ (time step '4', respectively). Therein, it is noticed that the intensity of the critical current across each coil turns is strongly affected by the intensity of the self-field, such that at the innermost and outermost turns, it has been found that their average I_c shows a detriment of up to 50% the I_{c0} value, decreasing radially towards the centre of the wound tapes in a similar fashion to what has been reported in stacks of 2G-HTS tapes with simplified $J_c(B)$ models [136, 180].

The manifestation of the concave feature in the distribution of flux front profiles can be seen in the regions where the sign of the slope of the applied transport current as a function of time changes, but not the direction of the applied current, i.e., between time steps '2' to '4' and '6 ' to '8' in Figure 3.1 (d), which correspond to the profiles of current density in Figure 4.1 at time step '3' and '4', and '7' and '8', respectively. The subtle aperture of the flux front profile concavely shaped at the bottom and top sides of the pancake or racetrack coil can be understood as the predominant physical feature on the local electromagnetic response of an HTS coil with magneto-angular anisotropy, where

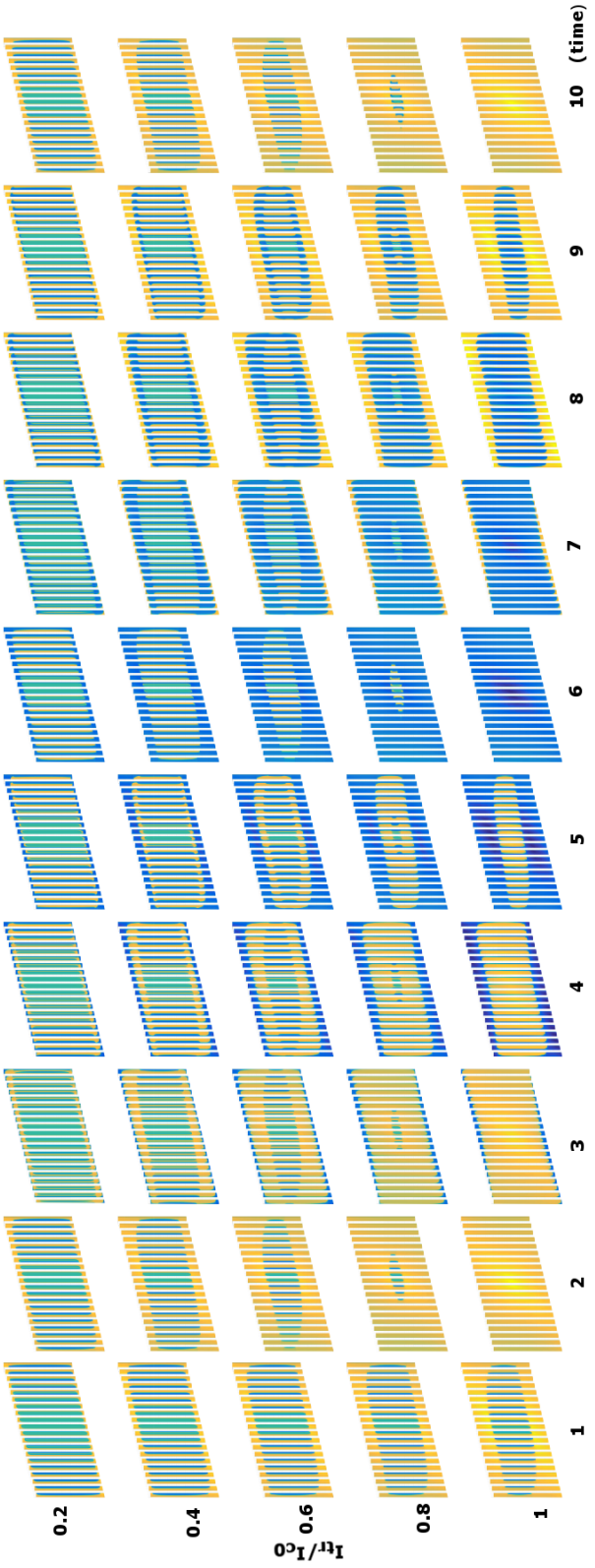

Figure 4.3: Same as Fig 4.1 but considering a deformed wound coil with turn-to-turn displacement of up to the maximum misalignment factor ($\delta = 100\mu m$).

the individual HTS grains [137, 171, 186–188] of the HTS tape respond differently to the changes on the intensity and direction of the inductive of applied magnetic field across each coil turns .

4.2 *Deformations in the Current Density Profiles by Lateral Displacement in the Coil Winding*

For the sake of illustration and ease visualisation of results for the case of misaligned coils (Figure 3.1 (b)), in Figures 4.3 & 4.4 we present the local distribution of profiles of current density inside each of the superconducting domains within a 20 turns SCS4050 2G-HTS tape conforming either a pancake or a racetrack coil, respectively, configured with a maximum lateral turn-to-turn displacement of $\delta = 100\ \mu m$. This considers an extreme case where the local displacement between the innermost and outermost turns could reach up to half the width of the wound tape, which although is much likely to happen in much greater coils, still it allows to present general qualitative description of the underlying phenomena. In fact, as mentioned in Chapter 3, even though the $\delta = 100\ \mu$m turn-to-turn displacement results in exaggerated deformation for a 20 turns coil, however, this condition is still relevant for coils with number of turns greater than 100, where the maximum δ_m condition has been already established to be $\delta_m \leq 250\ \mu m$ [175]. In fact, a turn-to-turn axial deformation higher than 250 μm is known to result in the delamination of 2G-HTS tapes, if the applied magnetic stress level ($B^2/2\mu_0$) is higher than $5 - MPa$ [178], a scenario conceivable in a superconducting coil operating at moderate to high transport currents. As a consequence, for larger coils the profiles of current density shown in Figures 4.3 & 4.4 can be understood as the homogenisation of the local profiles of current density into 20 sub-domains sectioning the thickness of the coil, each one representing the averaged positioning and intensity of the current density into stacks of tapes of relative dimensions [120, 183]. Thus, provided that the macroscopic electromagnetic quantities are presented under the base of the results obtained for perfectly aligned coils, our results and conclusions are not limited to the coil dimensions but instead focused on invoked physical principles and material laws.

The most representative physical feature that can be observed in the local distribution of current density profiles for misaligned coils in Figure 4.3 and Figure 4.4, is the progressive deflection of the originally semi-elliptical vertices of the flux front profile when $\delta_m = 0$ (perfectly wound coil), towards the upper and bottom edges of the innermost and outermost turns of the coil respec-

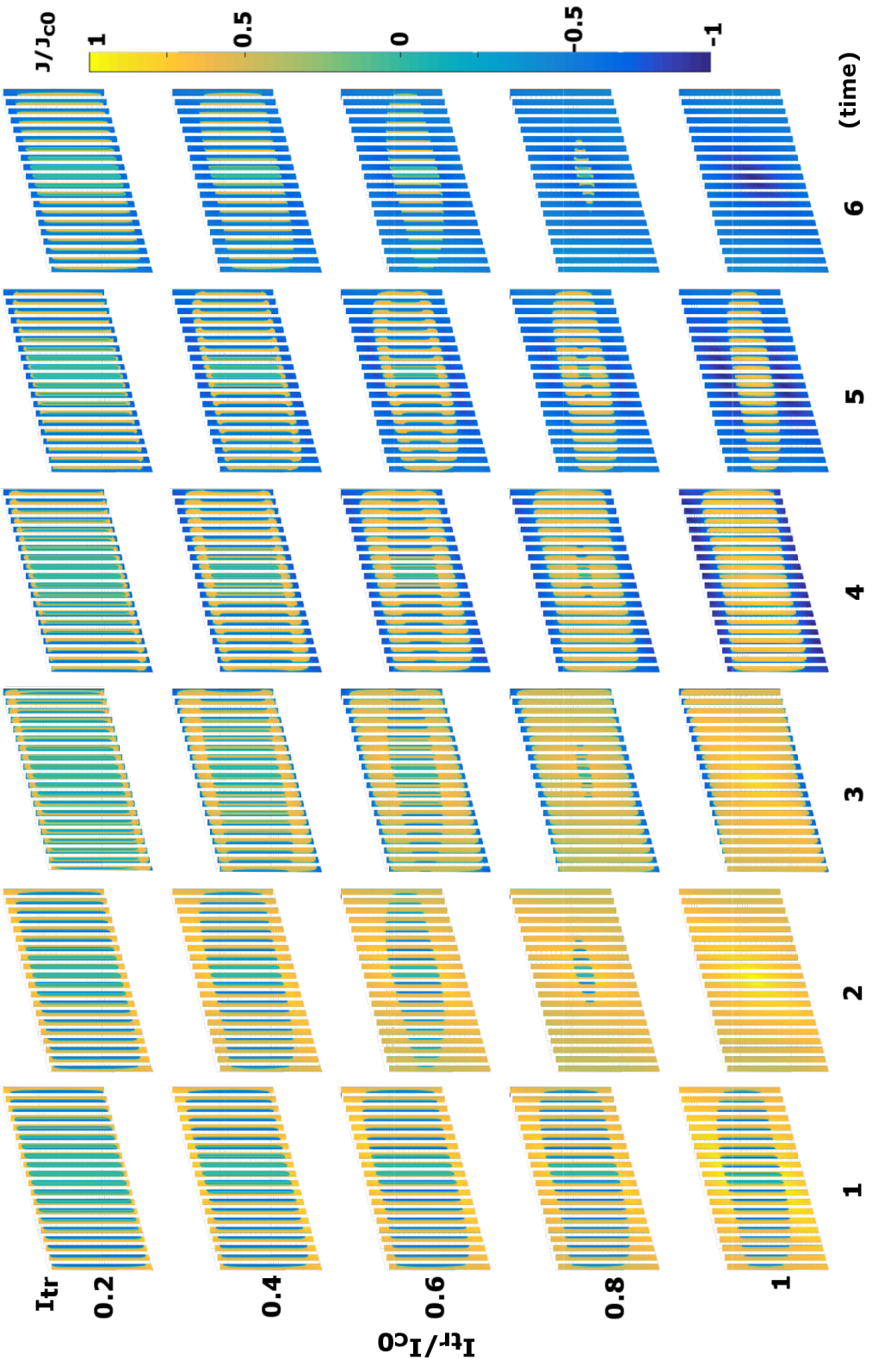

Figure 4.4: Same as Fig 4.2 but for the misaligned coil shown in Figure 3.1 (b).

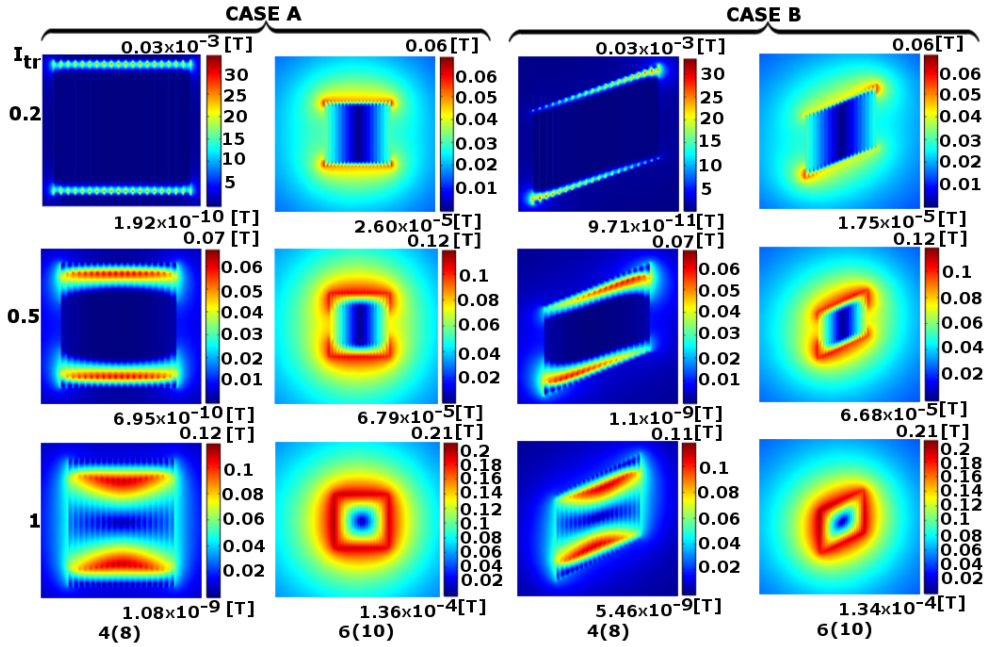

Figure 4.5: Magnetic flux density $|B|$ generated by the current density profiles displayed in (Case A) Figure 4.2 and (Case B) Figure 4.4 at the time steps '4' and '6' (or 8 and 10) displayed in Figure 3.1 (d), with $I_a = 0.2I_{c0}$ (top row), $0.5I_{c0}$ (middle row), and I_{c0} (bottom row).

tively, manifesting a clockwise repositioning of the co-vertices that results in a "worm-like" flux-front shape. This occurrence on the flux front profile has been observed to be more acute towards the outermost and innermost coil turns, which suggests that local distribution of current density within each turns is no longer symmetric between the upper and bottom half widths of the 2G-HTS tapes, implying that symmetry reductions along the y-axis cannot be applied when winding deviations are present. In other terms, this repositioning of the semi-elliptical vertices is caused by the breakdown in the ordinal symmetry of the mutual inductance between the turns of the coil, causing an imbalance in the local magnetic field experienced at the lateral edges of the tape, as shown in Figure 4.5. Therein, the magnetic flux density $|B|$ generated by the current density profiles of $I_a = I_{c0}$, for instance, at the lower corner of the innermost turn of the non-uniform coil, either for a pancake coil or a racetrack coil renders a magnetic field of approximately 129.65 mT, which is lower than the magnetic field created by the uniformly wound coil ($\sim$ 140.87 mT) at the same position. Moreover, this reduction in the local magnetic field at one of the opposite edges of the coil-turns, results in an increment of the local intensity of the critical current density, creating easier flow paths for the lines of

transport current which "push" the magnetisation currents towards the opposite edges, in a similar way to what happens in isolated AC superconducting wires that are subject to synchronous and asynchronous magnetic field excitations [40]. Consequently, the microscopic motion of the magnetisation currents across each one of the individual turns results reflected in a lateral inversion of the current density profiles across the innermost and outermost 2G-HTS tapes, which ultimately will result in a coherent deviation of the local density of power losses $\mathbf{E} \cdot \mathbf{J}$ that alters the hysteresis losses of the HTS coil. Likewise, it is worth noticing that this change in the symmetry of the distribution of profiles of current density and the consequent imbalance on the magnetic field along the originally axisymmetric cut-lines of the perfectly wound coil, which has now suffered an axial deformation, could lead up to a 8% difference in the experimental readings for the magnetic field intensity and homogeneity, which can be of vital importance on the reliability figures for the readings of magnetic imaging applications [113] or high energy physics applications [189].

4.3 *Impact on the AC-losses by Winding Deformations*

The prediction of the AC Losses of high power density superconducting devices is already a classical subject commonly covered through different electromagnetic formulations and material law models for the $\mathbf{E} - \mathbf{J}$ properties of type-II superconductors, where the hysteretic AC losses per unit time and the superconducting volume (Φ) for cyclic excitations of frequency ω can be calculated by integration of the local density of power dissipation $\mathbf{E} \cdot \mathbf{J}$ as follows:

$$L = \omega \oint_{f.c.} dt \int_{\Phi} \mathbf{E} \cdot \mathbf{J} d\Phi \,. \tag{4.1}$$

Here, *f.c.* denotes a full cycle of the time-varying electromagnetic sources after the magnetic relaxation period, i.e., after the first half cycle of the applied transport current in absence of an external magnetic field in our case. Otherwise, if the situation considers an applied magnetic field which could also change direction along the cycle, the magnetic relaxation period can take several cycles to accommodate the local consumption of magnetisation currents, by the concomitant action of the transport current in cross-field and rotating field configurations [40, 80, 109, 182].

The critical aspect behind Equation 4.1 is that the prediction of the local effect for the AC losses depends not only on the difference between the accumulated power losses at the peak current values, but on the actual history

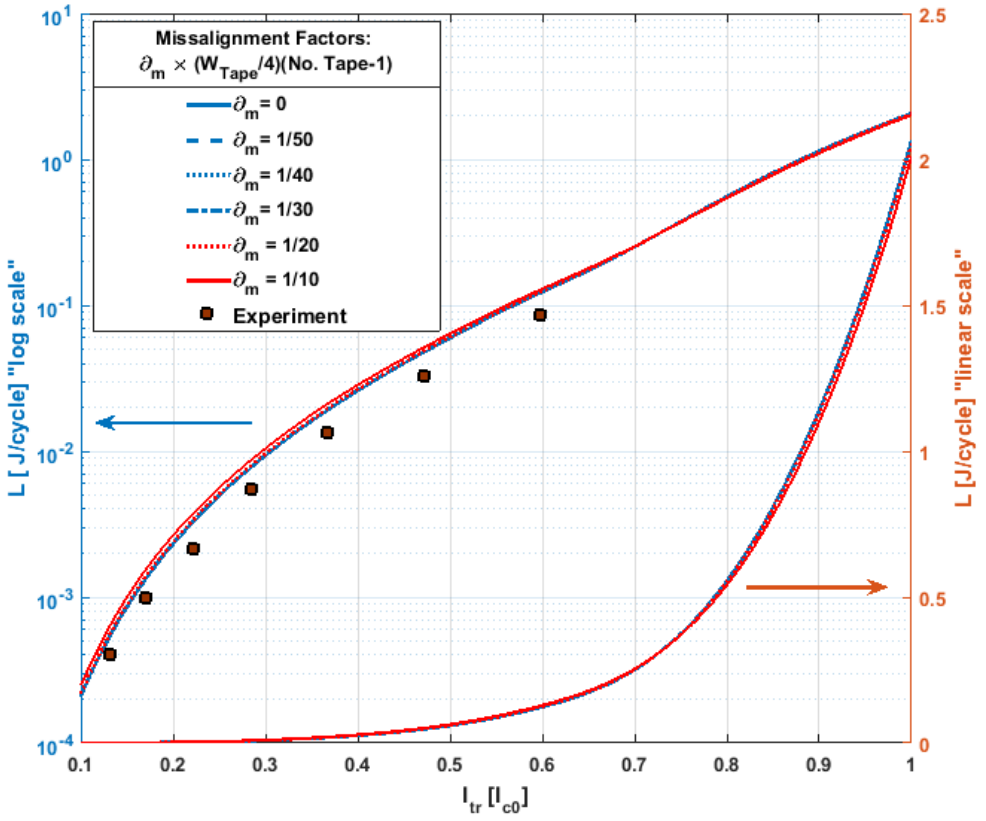

Figure 4.6: Hysteretic AC losses per cycle for diverse misalignment factors in the winding precision of 2G-HTS pancake coils presented as a function of the amplitude of the applied transport current, compared with the experimental measurements reported in [190].

of the local distribution of profiles of current density and electric field inside the superconducting domains. Consequently, due to the large aspect ratio of the 2G-HTS tapes, it is reasonable to accept a 10% to 20% relative tolerance between the experimental and numerical evidences, when the later considers a simplified mesh of finite elements as previously discussed. Additionally, the popular practice of displaying the results of the AC-losses plot is in *logarithmic* scale, as shown in Figure 4.6, impedes an adequate physical analysis of the AC losses curves, as the visual impact on the difference between the experimental and numerical data is scaled down, particularly for low to medium applied currents $I_a < 0.7\ I_{c0}$, i.e., during the period for which the occurrence of magnetisation currents can be easily seen [40, 106].

Though, while it could be argued that our findings for AC-losses of perfectly aligned pancake or racetrack coils could be more accurate as opposed to those predicted by simplified numerical models with a low meshing of the

superconducting domains, therefore enabling a faster computation, an appropriate estimate of the AC losses when compared to experimental evidence can be argued to depend on specific factors, such as the soundness of the material law chosen for the superconducting tape, and or instrumentation effects inherent to the experimental measurements, which both can be accounted by the relative tolerance above mentioned. The illustration of this above statement can be understood by Figure 4.6, as our numerical results (in renormalised units) for the perfectly wound 20-turns pancake and the experimentally measured AC losses for a 10-turns HTS pancake coil fabricated by Gömöry et al., [190] is compared. Consequently, from the numerical perspective, when the problem is such that changes on the spatial characteristics of the system are of the same dimensional order than the size of the finite elements invoked, and the physical quantities to be determined also depend on their spatial derivatives, it would be normal to expect larger discrepancies between the experimental and numerical results. These differences allow us to explain why some numerical models that take into account an artificial increase of the thickness for the ReBCO layer within the 2G-HTS tape, with a proper renormalisation of the physical quantities [162] is insufficient for the numerical modelling of 2G-HTS coils [126], when compared to models with homogenised meshes [116, 120]. Nevertheless, for a superconducting coil with a minimum turn-to-turn displacement factor δ_m, it becomes imperative to use a mesh with finite elements of a size smaller than the spatial displacement between the adjacent turns, as this high-level meshing approach renders a much higher accuracy for the calculation of the AC-losses by allowing an adequate discernment of local changes on the physical variables of magnetic field and current density. Thus, for the coils considered in our study which are made of a 4 mm wide 2G-HTS tape split into 200 finite elements along its width, the minimum displacement that could be conceived while maintaining the relative tolerance between the calculation is 20 μm, which corresponds to a turn-turn displacement factor of $\delta_m = 1/50$ in Figure 4.6, 4.7, & 4.8.

On the basis of these considerations, the community of researchers and companies with interests in the deployment of superconducting technologies could use the results presented within this sections as a practical benchmark to determine the actual dependence of the AC losses on the axial alignment of misalignment in HTS wound coils with a large number of turns. In this sense, to avoid conjectural conclusions bonded to the coil dimensions and to provide a clear insight on the effect of the misalignment factor on the AC losses of HTS pancake and racetrack coils, our numerical results are presented as a percentage function of their corresponding predicted AC losses for perfectly wound coils (see Figure 4.7 & 4.8, respectively), where the relative difference between perfectly aligned and misaligned coils that cannot be seen in the clas-

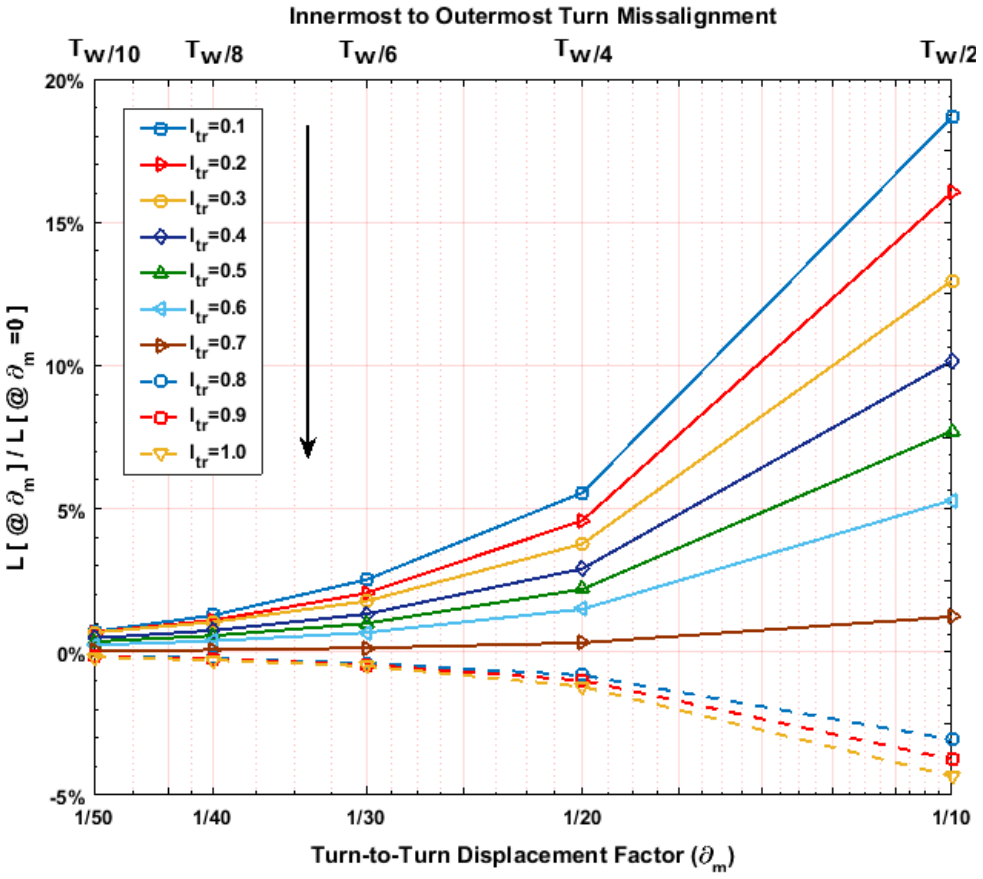

Figure 4.7: The curves of AC losses displayed as a function of the innermost to outermost turns misalignment distance (top abscissa) which for general purposes is measured in units of the 2G-HTS tape width, corresponding therefore to the shown turn-to-turn displacement factor δ_m (bottom abscissa) for the 20 turns SCS4050 pancake coil with the profiles of current density reported in [191].

sical representation of the AC-losses curve in logarithmic scale (Figure 4.6), is shown.

Thus, concerning to our results for the deformed 2G-HTS pancake coil (Figure 4.7), it is to be noticed that for low to moderate amplitudes of the applied transport current, $I_a/Ic0 \leq 0.6$, i.e., when the occurrence of magnetisation currents dominates the local profiles of current across the turns of the HTS coil, the turn-to-turn misalignment in the wound coil is capable of producing a large increase in the AC-losses from the base value, when the latter refers to the hysteretic losses of a perfectly wound pancake coil. This noticeable increase becomes larger as the turn-to-turn displacement factor is greater, reaching up to a $\sim 19\%$ increment in the lateral maximum condition,

i.e. when the relative displacement between the innermost and the outermost turn is about half the tape width, a condition that could be reached for a coil with a much large number of turns than the one presented in this study (Figure 4.3).

Although on these cases, the ratio of the AC-losses between perfectly wound and misaligned coils will be equivalent, given the fact that the similar physical principles govern the distribution of profiles of current shown in Figures 4.1 & 4.3 onto the local dynamics of flux front profiles described above; in Figures 4.1 & 4.3, it is to be noticed that any increment or decrement on the AC-losses is bounded to the displacement or consumption of magnetisation currents by the injected transport current, and ultimately to the disappearance of a flux-free core into the coil turns as the applied current is greater than 0.7 I_{c0}. Then, although an increment in the AC-losses can always be expected for $I_{tr} \leq 0.7\ I_{c0}$, due to Lorentz force on the motion of magnetisation currents induced by the transport current, this increment is gradually smaller as the size of the flux-free core decreases. Besides, from our analysis of Figures 4.1 & 4.3, in conjunction with Figure 4.7, it is conclusive that the increment of the AC losses is affected by the deformation of the flux fronts caused by the introduced wound misalignment. In other words, the larger the deformation of the turn-to-turn displacement of the flux fronts, the higher the AC losses would be. Thus, although from a practical perspective, a perfect winding of a coil is recommended in order to maintain the homogeneity characteristics of the magnetic field, we have proven that at least for these transport current conditions, $I_a \leq 0.7\ I_{c0}$, misalignments generally larger than $T_w/6$ in a pancake coil (i.e., $\geq 33\ \mu$m turn-to-turn displacement in 4 mm tape-width pancake coils) results in a non-negligible increment of the AC-losses (see Figure 4.7). Moreover, for applied currents of amplitude $I_a \geq 0.7\ I_{c0}$, a striking decay on the ratio of the AC-losses curve can be observed, which is linked to the disappearance of the flux free core in Figure 4.3. This decrease in the AC-losses becomes more evident as the winding misalignment is exacerbated, and although this improvement could be almost negligible for very small winding displacements, which is remarkable about this unique feature on the curve of AC losses, is that this allows a direct macroscopic method to determine the actual intensity of the applied transport current when the full disappearance of the flux free core is achieved inside an HTS coil, an event that cannot be determined by any other method, including the magnetisation measurements, as in the later a magnetisation signal will still be observed at $I_a \geq 0.7\ I_{c0}$.

Likewise, the AC losses calculation for the deformed racetrack HTS coil is shown in Figure 4.8, where a remarkable feature is observed between the results of the misaligned coils and perfectly wound coil, showing robust increments in the AC losses increments for low amplitudes of the transport current,

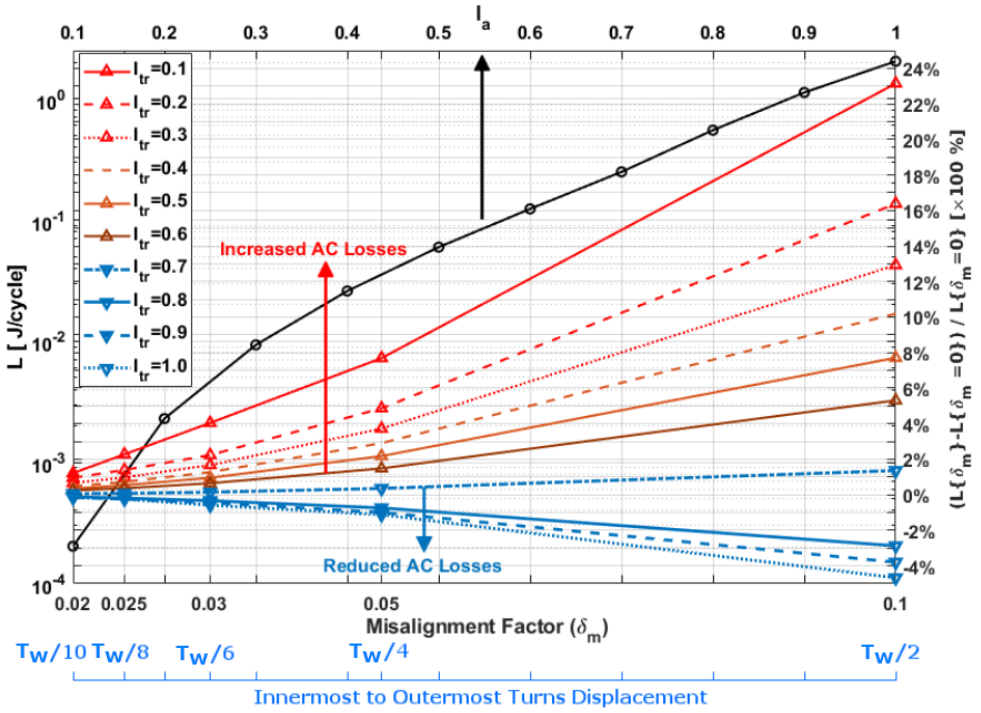

Figure 4.8: Top-left axes: AC losses (Joules/cycle) for the perfectly wound HTS racetrack coil with $\delta_m = 0$, as a function of the normalised transport current $I_{tr} = I_a/I_c = i_a$. Bottom-right axes: The AC losses curves for the misaligned coils in relative percent units are also depicted as a function of the individual misalignment factor δ_m for a 20 turns SCS4050 racetrack coil, and in more general terms as a function of the coil deformation or innermost-to-outermost turn displacement for a generic 2G-HTS tape of width T_w.

and a notable but slight reduction of the hysteresis losses for applied currents reaching the critical threshold I_{c0}. Thus, within a general framework for the coil dimensions, we report that for displacements measured between the positioning of the innermost turn to the outermost turn of the HTS coil, on the one hand, the AC losses decreases as a function of the misalignment factor at currents $I_a \geq 0.8I_{c0}$, obtaining approximately 5% reduction at $I_a = I_{c0}$ with $\delta_m = 0.1(100\mu\text{m})$. On the other hand, for moderate to low currents, $I_a/I_{c0} < 0.6$, the magnitude of the AC losses rises monotonically up to an outstanding increase of nearly 24% at $I_a = 0.1I_{c0}$ and $\delta_m = 0.1$. These intriguing observations in the curves of AC losses can be understood with relation to the distribution of profiles of current density displayed in Figure 4.5, where by observing the profiles for applied current $I_a \geq 0.8I_{c0}$, the flux-free core within the turns of the HTS coil disappears, which implies that by increasing the magnitude of I_{tr}, the associated injected lines of transport current con-

sume the remaining magnetisation currents inside the superconducting coil, diminishing the hysteretic losses provided by the latter, a phenomenon that has been evinced also in type-II rounded superconducting cables within the critical state model [182]. On the other hand, the reported increase in the AC losses for misaligned coils is a result of the deformation of the flux front with axisymmetric distributions of the profiles of current density and magnetic field across the different turns of the coil, which impacts in a more extensive measure the magnetisation currents that need to be diverted towards one of the edges of the HTS tapes.

It is worth mentioning that further details about the results above mentioned, as well as high resolution figures for the electromagnetic quantities here discussed, can be found also in [145, 191].

Chapter 5

Impact of the Material Law Selection on the Modelling of 2G-HTS Coils

As previously mentioned, the advances in the development of 2G-HTS coils composed of ReBCO tapes have instigated several studies not only focused on the formulation of modelling tools for describing the electromagnetic and thermal properties of such tapes, but also on the simplification of numerical models due to the inherent complexity of the material law that governs the electrical properties of the superconducting compound (i.e., their critical current density), and the computational burden imposed by the large cross-sectional aspect ratio of the 2G-HTS tape against the actual size of the superconducting coils, which need to be computationally modelled before investing in usually large and customised cryogenic facilities for their experimental testing. Also, multiple publications have already reported that the intensity and direction of externally and self-induced applied magnetic fields can robustly impact the electrical properties of most 2G-HTS tapes [141, 142, 172], although no strong agreement has been reached in terms of the material law that governs their critical current density properties, because different material laws can give comparable results depending on the physical quantity being studied [143, 144, 192]. Moreover, this complication exacerbates in conditions where the simulation of the electromagnetic behaviour of 2G-HTS coils considers the in-field dependence of the critical current I_c with the magnitude and orientation of externally or self-induced magnetic field at each turn of the coil, as pointed out in early experiments for the measurement of the magnetic field distribution and AC losses of HTS thin films in the superconducting coils [115, 153]. Nevertheless, regardless of the 2G-HTS tape being used, a definitive agreement has been

reached in terms of describing the current-voltage characteristics of all type-II superconductors, known as the power-law approach law, $V \propto (I/I_c)^n$, with $n \gg 1$, and from a computational point of view, it invokes a new material law for the electric field behaviour in a superconductor called $E - J$ power-law, $\mathbf{E}(\mathbf{J}) = E_0 \cdot \mathbf{J}/J_c \cdot (|\mathbf{J}|/J_c)^{n-1}$, previously discussed in Chapter 3.1. However, the intrinsic difficulties of measuring the critical current density over the different turns of relatively large superconducting coils, which might demand the use of specialised experimental facilities not easily accessible to all researchers, have led to the search of theoretical methods or approaches where the critical current density at the different turns can be numerically extracted by the electromagnetic modelling of observed physical quantities, or where the ansatz of this value renders a good qualitative or quantitative match with other experiments. Therefore, this indirect approach raises questions such as, Is the computational ansatz adopted for the E-J power law a sufficiently stringent material law to reproduce all other macroscopical electromagnetic quantities within a more quantitative perspective for the superconducting tapes?, and Would be any other material law capable for accounting the different electromagnetic phenomena of type-II superconductors, simultaneously?, or Can we reduce the computing time by the previous knowledge of simplified material laws which under certain experimental or numerical conditions could render the same results?, and if so, What will be the conditions and material laws that will allow the researchers to make a safe decision in this regard, specially when the principal quantity of interests is the AC-losses of the system?

Thus, in this chapter we present a comprehensive study of the impact of the E-J material law selection on the electromagnetic properties of superconducting racetrack coils, using the H-formulation in chapters 3 & 4 as a benchmark for solving the partial differential equation system of Maxwell equations. In particular, we present a direct comparison between the four most popular material law models for type-II superconductors, namely: (i) a simplified critical state (CS)-like-model [137, 143], (ii) the classical Kim's model [171, 187], (iii) an empirical Kim-like model with orthonormal field dependence for SuperPower Inc. SCS4050 2G-HTS tapes [116], and (iv) the generalised form of the critical current density with magneto angular anisotropy measured on these tapes [141]. The discussion starts with outlining the main characteristics of the material law models considered in this study, and introduces the geometry and other physical conditions relevant to the solution of this problem. Then, we discuss the main findings from our numerical results, where similarities and differences between the diverse material laws are disclosed.

5.1 *Reference Models for Superconducting Materials*

In order to compare the impact of different material law models on the numerical modelling of 2G-HTS coils, below we simulated distinctive models that incorporate different material laws for describing the E-J superconducting properties, where the derived physical effects of them are equivalent to the modelling condition strategy that defines the perfectly wound racetrack magneto-anisotropic HTS coil at self-field conditions, under an AC transport current that satisfies the function $I_{tr} = I_a \sin(\omega t)$ as discussed in Chapter 3 (see Figure 3.1). Nonetheless, most studies have shown that the power law of the E-J material law in its most generic form (Equation 3.11) can be included within the four most common approaches for the behaviour of the critical current density, J_c, shown in Table 5.1, and all of them are within the isotropic hypothesis of parallelism between the vectors $\mathbf{E}$ and $\mathbf{J}$, in principle valid for the symmetry of our problem due to the perpendicularity between the vectors B and J. Similarly, for numerical purposes, the power exponent $n = 30.5$ that has been experimentally reported for the SCS4050 tape in [141] is surmised large enough to exhibit a sharp increment in the electric field when the current applied exceeds the critical current of the tape, i.e., $I > I_{c0}$, which allows neglect the thermal activation of vortices and other statistical effects on the conventional magneto-quasi-steady (MQS) approach [137], and therefore emulate Bean's classical statements [39, 193] for the critical-state model [143]. Nevertheless, for practical purposes linked to the case for 2G-HTS tapes where finite differences in the homogeneity properties of the superconducting material need to be averaged, the use of the $E - J$ power-law formulation in Equation 3.11 is conceivable, provided that the values of the parameters for I_{c0} and n are experimentally measured. Based on these considerations, we emphasise on the fact that the parameters of the 2G-HTS utilised for this study correspond to that of a specific standard tape (SCS4050) manufactured by SuperPower Inc. [134], whose measurement and validation of their properties have been broadly conducted by many research groups [141].

To begin our attempt to unveil the impact of the material law selection in the modelling of 2G-HTS coils, the critical-state-like model, C_M, was simulated first. Note that within a purely theoretical framework, the critical state model allows to efficiently capture the main physics characteristics from the macroscopic electromagnetic behaviour of type-II superconductors in the mixed or vortex state [39, 193]. However, in most practical applications of type-II superconductors including the 2G-HTS tapes, it is well known that in the manufacturing of superconducting materials, achieving widely homogeneous electrical properties is something that cannot be assured ad hoc. This is mainly due

Table 5.1: Material law models and related variables considered within the $E-J$ power law formulation for the ReBCO material in Equation 3.11.

Model	Legend	Simplified Description	Material Law $J_c =$	Microstructure Parameters
Critical-State (CS)-Like model [137, 143]	C_M	$J = \pm J_c$	J_{c0}	$J_{c0} = 2.85 \times 10^{10}\text{A/m}^2$ [134]
Kim's Model [171]	K_{M1}	$J_c(\mathbf{B})$	$\frac{J_{c0}}{\left(1+\frac{\lvert\,\mathbf{B}\,\rvert}{B_0}\right)^{\alpha}}$	$B_0 = 240$ mT [134, 142] $\alpha = 0.7$
Kim-like model [194]	K_{M2}	$J_c(B_\parallel, B_\perp)$	$\frac{J_{c0}}{\left(1+\frac{\sqrt{k^2\lvert B_\parallel\rvert^2+\lvert B_\perp\rvert^2}}{B_0}\right)^{\alpha}}$	$B_0 = 42.65$ mT $\alpha = 0.7$ $k = 0.29515$ [116, 134, 194]
Magneto-Angular Anisotropy Model [141]	R_M	$J_c(\mathbf{B}, \theta)$	$\frac{J_{c0}}{\left(1+\epsilon_\theta\left(\frac{\lvert\,\mathbf{B}\,\rvert}{B_0}\right)^{\beta}\right)^{\alpha}}$	$\epsilon_\theta = \sqrt{\gamma^{-1}\sin^2(\theta)+\cos^2(\theta)}$ $B_0 = 240$ mT, $\beta = 1.5$ $\alpha = 1$, $\gamma = 5.02$ [134, 141, 142]

to the granular properties that these kinds of materials commonly have, and the possibility of having impurities within the structure of the superconductor (i.e., having added materials or alloys with non-superconducting properties during the fabrication of the HTS material). This situation that is not necessarily unfavourable for the actual use of superconducting materials gave rise to the flux creep concept in the early 1960s, where the occurrence and motion of local profiles of current density predicted by Bean, were not only caused by the thermally activated motion of flux structures (vortices) proposed by Anderson [186], but the local Lorentz force between collective groups of vortex lines whose intensity depends on the microstructure of the HTS material, which can be averaged within the semi-empirical parameters B_0 and α introduced by Kim [171, 187]. These parameters can be obtained from I-V measurements, either under self-field conditions or externally applied magnetic fields [116, 134, 192, 194], which had lead to variants of the classical version of Kim's model, K_{M1} (Table 5.1), as the empirical Kim-like model K_{M2} (Table 5.1) introduced by Thakur et al. [194], which has been used regularly for the modelling of 2G-HTS tapes from different manufactures, including the SCS4050 tape made by SuperPower Inc. [116], where $\mathbf{B}_\parallel$ and $\mathbf{B}_\perp$ are the local orthonormal components of the magnetic flux density, being parallel or perpendicular to the wider surface of the 2G-HTS tape. However, the in-field dependence of the critical current density of K_{M2} does not account for the experimentally measured magneto-angular dependence of the critical current density of the 2G-HTS tapes, whose theoretical extension has been introduced by Dr Harold Ruiz at the University of Leicester, in collaboration with the experimentalist group led by Dr Tim Coombs at the University of Cambridge [141], which is denoted in this work as R_M. It accounts for the flux creep parameters derived by Kim's approach [171] (i.e., the microstructure parameters B_0 and α

in Table 5.1), and incorporates the Blatter's angular anisotropy factor ϵ_θ, which is a function of the electron mass anisotropy ratio (γ) of the ReBCO layer and the angular direction θ of the local magnetic field. Remarkably, this model is capable of reproducing the full magneto-angular anisotropy properties of the critical current density, $J_c(\mathbf{B}, \theta)$, for large number of market-available 2G-HTS tapes [141, 172], currently manufactured by companies such as SuperPower Inc. [134], American Superconductor [195], Shanghai Superconductor Technology Co., Ltd. [196], and SuperOx [197]. The R_M model completes the full set of material laws, and the validity and scope of them will be critically analysed in the following section, highlighting the main observations derived from the critical analysis on the use of one or another material law for the modelling of 2G-HTS racetrack coils. We pay special attention to measurable (experimental) quantities such as the critical current density, the magnetic field, and the AC losses, all from the local dynamics of current density across the cross section of the superconducting coil.

5.2 *Anisotropy Features on the Turn-by-Turn Current Density Distribution*

The comprehensive comparison of the time-dependent distribution for the flux front of current density is presented for different J_c functions, from which it is possible to analyse the distinctive features between the four most popular superconducting material laws shown in Table 5.1. Thus, as the main physical characteristics found in the evolution of flux front profile for the diverse material law models have been observed to be equivalent to those shown in Chapter 4, and recalling that the magnitude of the self-field strongly affects the intensity of the critical current across each turn of the coil (see Figure 4.2), which is evident from moderate to high applied currents (practical operation level of a superconducting system), for simplicity, in this chapter the profiles of current density are presented for only moderate and high applied currents, $I_{tr} = I_a \sin(\omega t)$, with amplitudes $I_a = 0.5 I_{c0}$ and $I_a = I_{c0}$, respectively (see Figure 5.1). These are shown for the two steady steps representing either the self-field condition, $I_{tr}(t) = 0$, or the positive peak of current, $I_{tr}(t) = I_a$, that is, at $\omega t = 2\pi$ and $\omega t = 5\pi/2$, respectively, after completing a full cycle of the external excitation, i.e., where the magnetic relaxation process has already taken place, and the electrodynamics of the HTS coil is within a hysteretic behaviour.

In summary, with the C_M model it is possible to qualitatively observe the

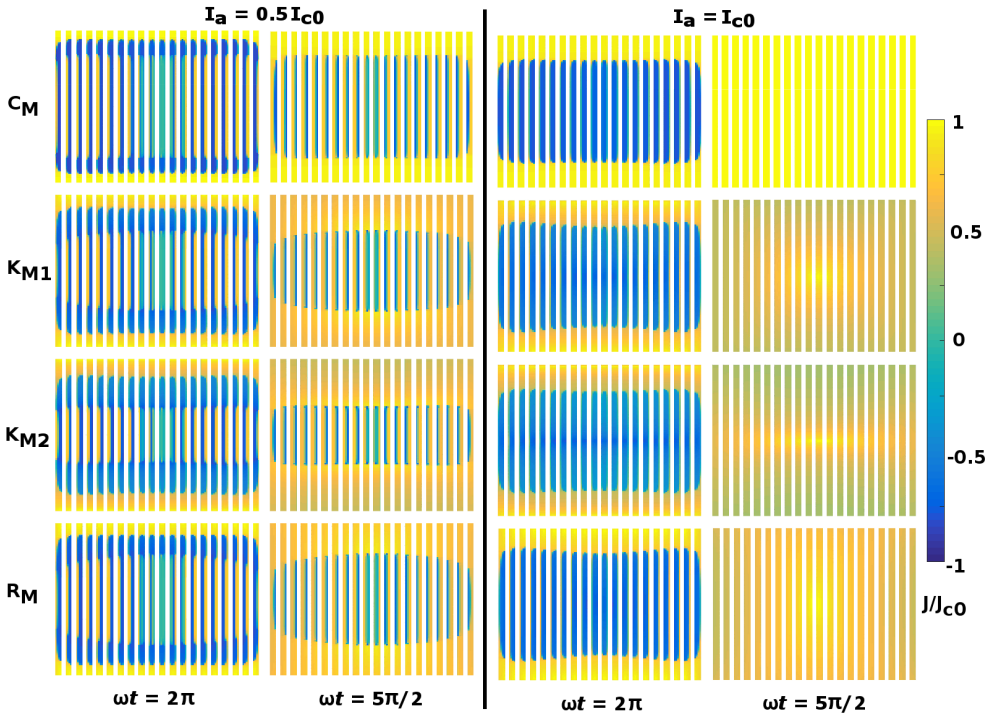

Figure 5.1: Local profiles of normalised current density J/J_{c0} inside each of the superconducting layers for a 20-turn second generation of high-temperature superconducting (2G-HTS) racetrack coil (not to scale), with the innermost turn being the leftmost 2G-HTS domain (layer) shown in each of the displayed subplots, and with applied AC currents of amplitude $I_a = 0.5\ I_{c0}$ (left pane) and $I_a = I_{c0}$ (right pane), conditioned to the HTS material laws introduced in Table 5.1. For an easy visualisation of the current-density distributions, results are shown by artificially expanding the thickness of the REBCO layer inside the 2G-HTS tape, as no electrical current flows in any of the other composite layers.

physical nature of the dynamics of current density profiles at a local level where a concomitant existence of both positive and negative currents across the thickness of the tape directly can be seen. These currents refer to the self-induced magnetisation currents, enclosed by regions within the magneto-transient history of the applied transport current, in good agreement with the predictions of Bean's model. For instance, for $I_a = 0.5I_{c0}$ at $\omega t = 2\pi$, an equal balance of positive and negative current-density profiles of the same intensity (J_{c0}) appears to satisfy the global condition $I_{tr} = 0$. This condition indicates that as the applied transport current penetrates inside the ReBCO layer from its surface towards the geometric centre of the coil as the amplitude of the current increases, i.e., $I_a \neq 0$, firstly, a certain amount of current flows in the positive direction within each ReBCO turn, which then encloses the region of

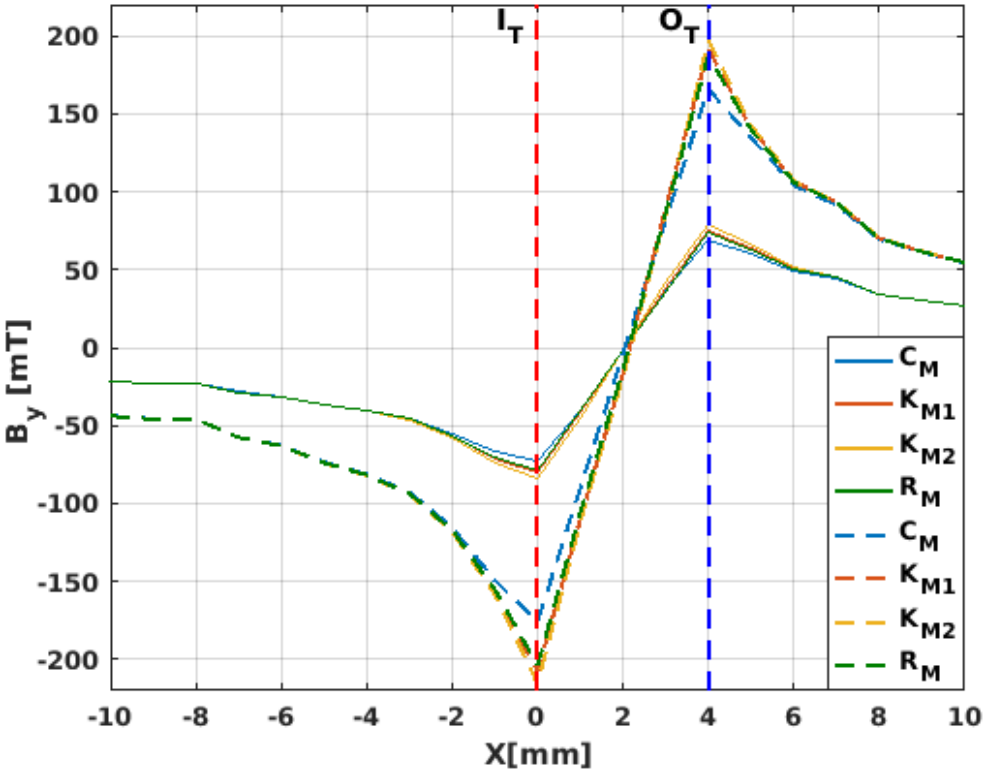

Figure 5.2: Magnetic field profile over the middle axisymmetric line (x-axis) of the $\sim$ 4-mm coil section (20 turns) displayed in Figure 5.1 in the direction parallel to the wider surface of the wound 2G-HTS tape, B_y, measured within and near the coil section for applied currents of amplitude $I_a = I_{c0}$ (dashed curves) and $I_a = 0.5I_{c0}$ (solid curves), at the peak condition $\omega t = 5\pi/2$. The vertical dashed lines at $x =$ 0 mm and $x = \sim 4$ mm respectively refer to the innermost (I_T) and outermost (O_T) turns of the HTS coil.

negative current-density profiles, accounting for the transient history of the applied current, and secondly, the region occupied by the local distribution of the magnetisation currents decreases as that of the applied current increases until its complete disappearance at the threshold current condition $I_{tr} = I_{c0}$. Nevertheless, the flux-free core is visible within the central turns of the superconducting coil at $I_{tr} < I_{c0}$, where the local distribution of current density across the turns of the HTS coil shows a strong dependence on the self-induced magnetisation currents. Thus, while the other material law models in Table 5.1 cannot assume a constant critical current density (as is the case for the C_M model), all the above-mentioned physical features can be considered as general. However, a slight difference has been observed in the pattern of the flux front profiles between the different models, which reveals substantial quan-

titative differences observed not only in the definition of the critical current density, determined at each turn of the HTS coil, but on the magnetic field measurement and AC losses discussed in the following sections.

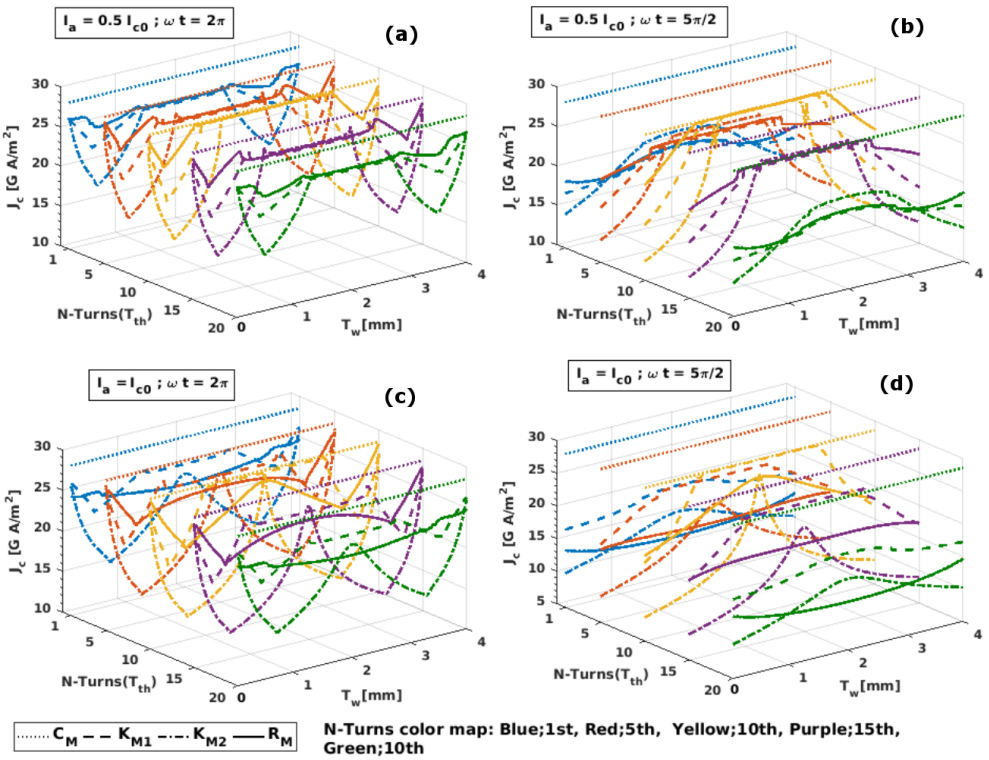

Figure 5.3: Critical current distribution across the 4-mm-width (T_w) of the 2G-HTS tape measured at the inner surface of the 1st, 5th, 10th, 15th, and 20th turn (T_{th}) of the modelled coil (Figure 5.1), under the different material law conditions in Table 5.1. The Figure shows (a) the results for an applied current of amplitude $I_a = 0.5I_{c0}$ at the self-field condition $\omega t = 2\pi$ and (b) the peak transport current condition at $\omega t = 5\pi/2$. Likewise, (c) shows the results for an applied current of amplitude equal to the threshold value of the critical current density I_{c0} at $\omega t = 2\pi$ and (d) at $\omega t = 5\pi/2$. It is to be noticed in Figure 5.1 that for $I_a = 0.5I_{c0}$, the only turn which displays a flux free core across the entire thickness of the SC wire is the 11th turn, otherwise for any of the other turns a value of current density can be measured along the surface of the SC wire.

Thus, Figure 5.1 demonstrates the local dependence of the critical current density with the magnetic field incorporated into the different material laws K_{M1}, K_{M2} and R_M, showing not only how such dependence creates a reduction in the critical current density across the width of the coil turns but an acute deformation of the flux-front profiles envisaged within the C_M model, as for instance, at $\omega t = 2\pi$ it can be observed that the magnitude of J_c decreases

from the lateral edges of the ReBCO layer towards their centre.

The local variance in the magnetic field (see Figure 5.2) produces the imbalance in the critical current density across the width of the ReBCO layers as shown in Figure 5.3, which limits the area of the magnetisation and flux-free cores of the superconducting coil, with a more robust reduction achieved for the empirical K_{M2} model, where the orthonormal components $B_{\parallel}$ and $B_{\perp}$ are explicitly included. Nonetheless, such substantial reduction in the magnetisation core is not observed for the experimentally measured J_c function, i.e., the R_M model, where θ defines the direction of the magnetic field vector at a local level (see Table 5.1). It is worth mentioning that even though the mathematical structure of K_{M2} and R_M are similar, given that the conditions $\theta = 0$ and $\theta = \pm\pi/2$ in the R_M model resemble the parallelism and perpendicularity conditions of the magnetic field assumed in the K_{M2} model, the latter model substantially increases the influence of the perpendicular component of the magnetic field when arbitrarily reducing the effect of its parallel component through the empirical microstructure parameter k. However, it has already been demonstrated that the actual dependence of J_c with the magnetic field vector can be accurately described by either the semi-analytical model [171, 187], or for those materials showing a strong magneto-angular anisotropy [141, 172], by the local components of the magnetic field averaged by the electron mass anisotropy ratio (γ) of the REBCO layer which results, at least for the case of the SCS4050 tape, in the distribution of flux front profiles at self field conditions between the K_{M1} and R_M models showing nearly the same trend (Figure 5.1). This is because robust changes in the critical current density of the SCS4050 tape have been observed only for parallel components of the magnetic field ($\theta = 0, \mathbf{B} = \mathbf{B}_y$) greater than 50 mT [141], which is a condition that manifests only for first three-to-seven innermost and outermost turns of the HTS coil at moderate to high applied transport currents, $I_{tr} \geq 0.5I_{c0}$ (see Figure 5.2). Then, observing the full penetration condition (i.e., $I_{tr} = I_{c0}$ at $\omega t = 5\pi/2$ in Figure 5.1), this reveals how the critical current density of the superconducting coil changes across the width and thickness of each one of the ReBCO turns (with exemption of the C_M model), which is a phenomenon that was experimentally observed in [110, 128].

However, in order to be able to properly see how the J_c changes across the different turns of the HTS coil for the different material law models, their local profiles of current density are quantitatively analysed. Therefore, in Figure 5.3 we show how the measurable critical current density over the surface of the individual turns of the HTS coil not only varies along the width of the superconducting tape but, from the numerical point, how these predictions can change as a function of the different material laws that can be invoked. Hence, it has already been mentioned that the critical current density under the critical state

model (C_M), can only equal the specific critical value J_c determined by the flux density of the pinning forces across the domain of the REBCO layers, as it can be noticed from the dotted lines in Figure 5.3. This defines the threshold value of the critical current density at self-field conditions, J_{c0}, which is reduced by the influence of the magnetic field in any of the Kim-like approaches. In this sense, as the intensity of magnetic fields experienced at the innermost and outermost turns is greater in comparison to the middle turns (see Figure 5.2), the critical current density of these turns ($T_{th} = 1$ or 20) will always be lower irrespective of the material law $J_c \propto B$. However, the intensity of magnetic field also varies along the width of each HTS coil turns, decreasing from the tape edges ($T_{th} = 1$ or 20) towards the centre of the coil, and the increment of J_c follows the penetration of the magnetic field inside the of HTS turns, reaching their maximum at the midpoint of the tape width and, following a similar evolving pattern from the innermost and outermost turns. This occurrence can be identified as the plateau in the J_c distribution at the middle turn ($T_{th} = 10$) for the K_{M1} model (dashed lines), in the peak transport current conditions shown in the right pane plots of Figure 5.3 (b) & (d). Therein, it is evident that for measurements at the peak transport current conditions other than the innermost and outermost turns of the coil, the classical K_{M1} model generally overestimates the critical current density across the width of the tape, which is actually one of the main reasons why further approximations for the $J_c(\mathbf{B})$ function have been adopted with time [116, 141, 142, 194].

However, in a different scenario when the computation is performed at a threshold condition $I_{tr} = I_{c0}$, simulating the actual conditions for the experimental measurement of J_c as shown in Figure 5.3 (d), it can be clearly seen why the semi-empirical models K_{M2} and R_M, respectively, can render under certain conditions to the same experimental measurements across the width of a 2G-HTS tape. For this, it is worth mentioning that the general practice for the electrical measurement of the I-V curves and consequently the magnitude of J_c are taken from a position where the intensity of the J_c is maximum, and the efficiency of these measurements mainly relies on the position of the voltage taps, usually at the centre width of the HTS tape. Therefore, by observing the local profile of J_c at the central turn of the HTS coil ($T_{th} = 10$ at $T_w = 2$ mm), where the x component of the magnetic field (perpendicular to the wider surface of the tape) is null, a similar intensity of the critical current density can be obtained from the K_{M2} model (dash-dotted yellow line) and the R_M model (solid yellow line). Conversely, when the measurement position moves from the midpoint, the impact of the parallel component of the magnetic field (B_y) on the local J_c profiles for the HTS coil is underestimated with the K_{M2} model, showing significant differences in their measurements on long sections of individual 2G-HTS tapes. This occurrence is also evident from the last column of

subplots shown in Figure 5.1, where the colours contrast allows to see how the maximum threshold of J_c for each model at the midpoint of the coil section decreases towards the coil periphery, where the detriment is is more notorious within the K_{M2} model, in good agreement with our previous analysis.

Thus, based on these discussions, if the physical quantity aimed to be measured and explained in a superconducting coil is the magnitude of the critical current density for the different turns of the wound 2G-HTS coil, particular attention must be given in terms of the adequate selection of a material law that describes the complete magneto-angular anisotropic properties of the ReBCO layer (from the theoretical perspective), and the correct position of the voltage taps for efficient experimental measurement. Otherwise, almost 50% difference could be conceivable between the theoretical and experimental measurements at the innermost and outermost turns of the coil. However, in an instance where magneto-optical imaging techniques [198–201] have been used to measure the critical current density, showing the full dynamics of the critical current density along the tape width (T_w), for the self-field and partial penetration conditions of the HTS coil (i.e., at the transport current condition $I_a = 0.5I_{c0}$ and $\omega t = 2\pi$ in Figure 5.3), a remarkable qualitative agreement with the experimental measurements reported in [201] has been found when compared with the results of the R_M model [44]. This study confirms that the actual current distribution inside the YBCO tape when C_M model is invoked does not show any plateau-like feature during the initial flux penetration, but instead it develops strong peaks near the tape edges, as determined by Kim's hypothesis ($J_c \propto \mathbf{B}$) contained within the K_{M1}, K_{M2}, and R_M models. However, further investigation of the magnetisation properties of single tapes under applied magnetic fields at different orientations (out of the scope of this thesis) will need to be conducted to determine if whether the complete validity between these models needs to be established beyond the broad success that the R_M model has already achieved over a large set of commercially available 2G-HTS tapes [141, 172].

5.3 *Magnetic Field and AC-Losses Assessment for Diverse Material Laws*

In an attempt to systematically analyse how the influence of the intensity of the magnetic field component B_y over and near the surface of the innermost turn of the HTS coil changes as a function of the applied transport current at the self-field condition ($\omega t = 2\pi$), and in the peak transport current condition

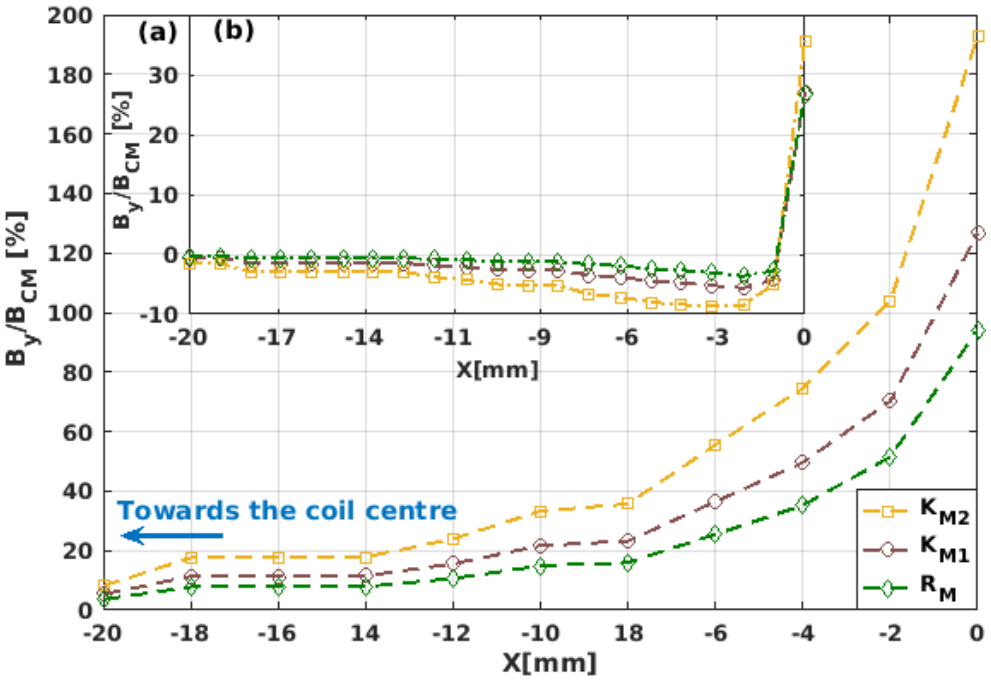

Figure 5.4: Magnetic field component B_y along the middle axisymmetric line (x-axis) of the 2G-HTS coil calculated within the Kim-like approaches K_{M1}, K_{M2}, and R_M (Table 5.1) as a percentage function relative to the field predicted by the isotropic C_M model. The measured field is presented from the innermost turn of the coil at 0 mm (see Figure 5.2) towards the coil centre at the self-field condition $\omega t = 2\pi$, when the applied current has an amplitude of (**a**) $I_a = 0.5I_{c0}$ (i.e., with the central turns of the HTS coil partly magnetised (see Figure 5.1)), and (**b**) $I_a = I_{c0}$ (inset), that is, with the HTS coil fully saturated by the transport current and no magnetisation currents.

($\omega t = 5\pi/2$), for different material laws (Table 5.1), in this section we continue our discussion by analysing Figures 5.4 to 5.6. Note that due to the relatively large width of the coil former ($R = 5\ cm$), where the magnetic field induced by the axisymmetrical branch of the coil is low due to the relative distance between the coil branches, the specific position *over the external surface of the innermost coil turn* was selected to display the magnetic field ratio between the different Kim-like material laws and the magnetic field predicted by the critical state model B_{CM} (Figure 5.5 & 5.6), otherwise these relative ratios can be seen to be rapidly lowered towards the centre of the coil former (see Figure 5.4). Therefore, in an actual experimental setup where the measurement of the magnetic field is at the centre axis of the HTS coil, our numerical results allow us to conclude that the dominant factors is not necessarily the selection of a well-established material law model (as in the K_{M1}, K_{M2}, and R_M models) but on the size of the coil itself and therefore the computational time required

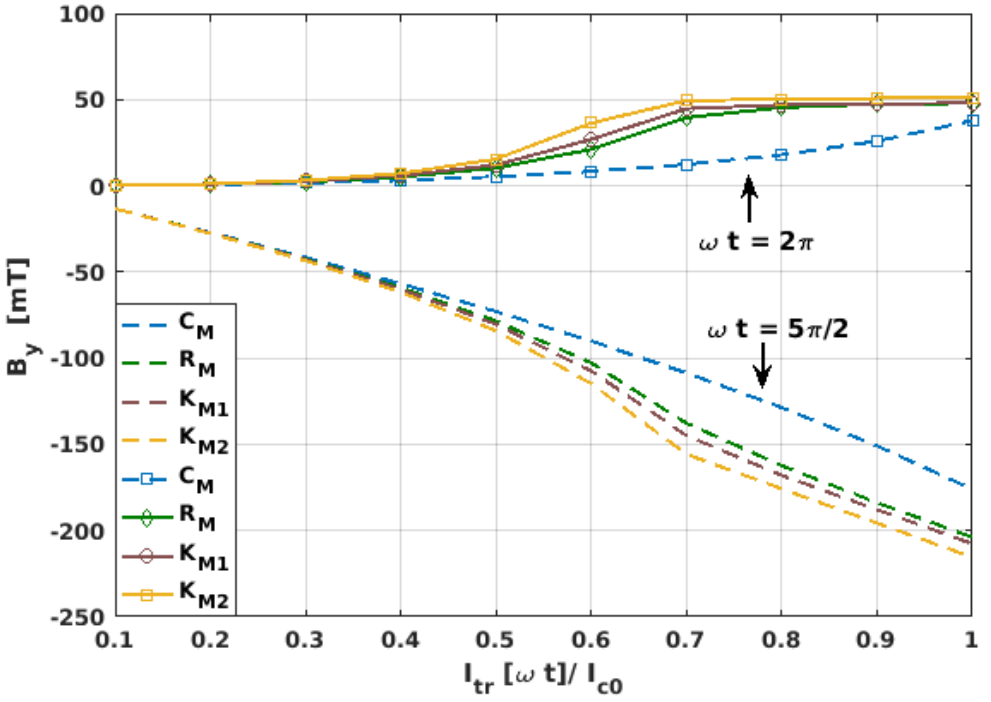

Figure 5.5: Magnetic field component B_y at the middle point of the external surface of the innermost turn of the 2G-HTS coil as a function of the applied transport current $I_{tr}(\omega t)$ at the self-field ($\omega t = 2\pi$) and peak transport current ($\omega t = 5\pi/2$) conditions, and the different material laws reported in [44].

by each model. In this sense, it is essential to note that in average, the C_M model always results in the fastest computational solution, making it the best-suited material model provided that the interest of the modeller targets the measurement of the magnetic field at the centre axis of the coil former.

On the other hand, it is evident that a clear difference between the magnitude of the magnetic field predicted by the C_M and Kim-like models is more extensive as the intensity of the applied current increases, as shown in Figure 5.5. However, the macroscopic measurement of B_y shows a remarkable difference between the C_M and the Kim-like models as a function of the applied transport current for self-field ($\omega t = 2\pi$) and peak transport current ($\omega t = 5\pi/2$) conditions, which we have found to be connected to the dynamics of the flux front profiles described above. To illustrate this, for low intensities of the applied current, $I_{tr} \leq 0.4 I_{c0}$, in Figure 5.5 almost negligible difference in the magnitude of the derived field has been observed, which suggest that no substantial discernment of local flux front profiles between the material law models at this transport current level. Then, for higher amplitudes of the transport current, for instance, $I_a = 0.5 I_{c0}$, a more noticeable difference between the

different material laws should be observed (see Figure 5.1). In fact, for moderate intensities of the applied current $\sim 0.4I_{c0} \leq I_a \leq 0.8I_{c0}$, the magnetic field curves derived for the Kim-like models rapidly deviate the isotropic C_M model, showing a "kink-like" curvature that separates the physical behaviour between the moderate and high applied currents (see Figure 5.5). More specifically, the magnetic saturation of the superconducting coil which is achieved at high applied currents, $I_{tr} \geq 0.8I_{c0}$, exhibits a plateau in the measurement of B_y at $\omega t = 2\pi$, meaning that for such level of currents, none of the turns of the superconducting coil can exhibit a flux-free core with local condition $J_i = 0$. Nevertheless, the physics of the HTS coil at moderate currents are characterised by transient states, where the Lorentz force between the local profiles of transport current and the induced magnetisation current reduces the dimensions of the flux-free core, by the flux-creep of transport currents which consumes and pushes the pre-existing magnetisation current lines. The reader is encouraged to follow references [145, 182, 202–204] for more a detailed explanation of this cumbersome phenomenon, which corresponds to the actual response of any type-II superconductor under the concomitant action of a magnetic field and a transport current, where the physical richness of the full dynamics of flux-front profiles in simplified geometries has been exploited.

In a more quantitative approach, in Figure 5.6 we show the percentage ratio between the Kim-like material laws and the C_M model (Table 5.1), where the larger differences were found at the self-field condition $\omega t = 2\pi$. Therein, the Figure shows an appropriate discernment for the change of the flux creep dynamics between fully isotropic samples that conform to the C_M model and, those with the magneto-anisotropic properties introduced by the Kim-like models. For instance, concerning to the low-intensity regime ($I_{tr} \leq 0.4I_{c0}$), the increment of the B_y/B_{CM} curves as a function of the transport current follows a linear relation, which implies that the physical mechanism leading to the flux creep in the coil turns, is primarily the linear consumption of the magnetisation currents caused by the global condition of the transport current. Also, the resulting amount of magnetisation currents inside the individual coil turns, remains at the same time almost constant for each of them. On the other hand, two different phenomena can be recognised for the so-called moderate-intensity regime ($0.4I_{c0} \lesssim I_{tr} \lesssim 0.8I_{c0}$) [145]. The first one being that the field B_y/B_{CM} quickly rises to a maximum value where the spatial balance of the magnetisation currents and the transport currents for each turn of the coil is impossible to sustain. Consequently, it causes a change in the profile of the flux front from a square-like shape towards an elliptical shape (see Figure 5.1), even though in this transient regime the dimensions of the flux-free core at the centre of the coil remained the same. The second phenomenon corresponds to the rapid drop of the B_y/B_{CM} curve displayed in Figure 5.6, where the flux

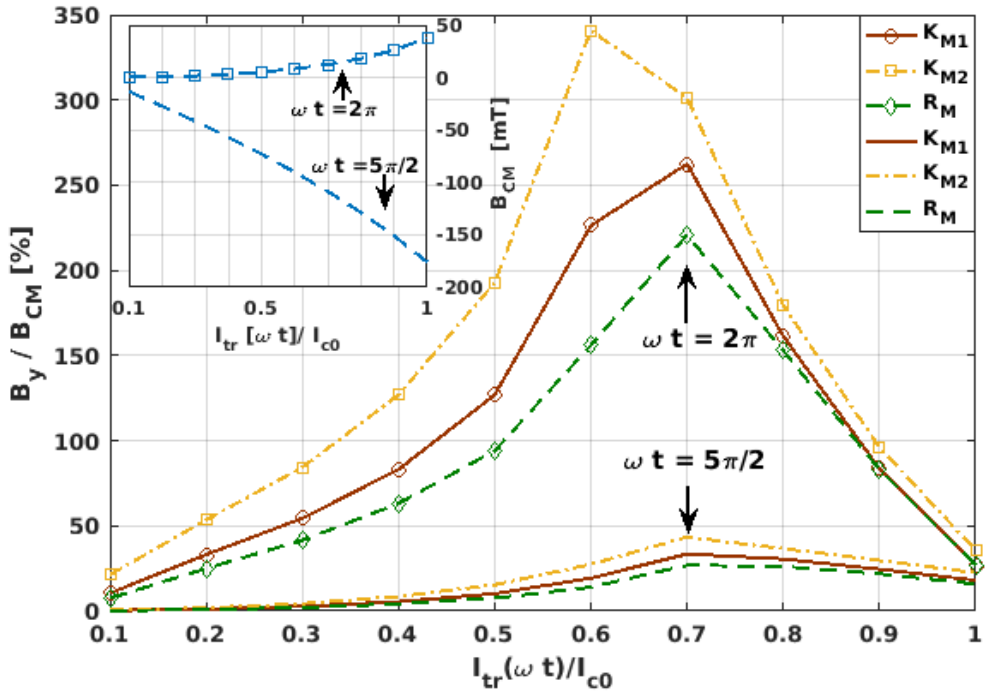

Figure 5.6: The relative percent ratio between the different material laws, taking as a reference the B_y-field obtained within the critical-state-like-model C_M (inset).

creeps occur in two positions; the first is where the applied transport current consumes the induced magnetisation currents, and the second is where the occurrence of innermost magnetisation currents exert a superconducting Lorentz force towards the centre of the coil. This manifestation reduces the dimensions of the flux-free core, which was previously unaltered. This phenomenon continues until a current level ($I_{tr} \approx 0.8I_{c0}$) reaching complete disappearance of the flux-free core, after which it realises a linear behaviour of B_y/B_{CM}. Therefore, understanding the electromagnetic behaviour of an HTS coil within the boundaries of the C_M model has to be regarded as a practical approach. Reasons not only limited to its computational affordability but simple concept of extracting the local profiles of current density with less sophisticated experimental techniques, this by comparing the actual measurement of the B_y profile near the centre of the coil with the predicted B_{CM} values.

Likewise, this concept is in good agreement with our recent analysis concerning the flux front profiles and local distribution of current density as a function of the material law, where all Kim-like models predict an increment of about 2 to 3 times the intensity of the magnetic field over the surface of the innermost tape compared to that of the C_M model, and therefore, the K_{M1} model acts as a mean-field approach for the magneto-angular anisotropic

characteristics of the ReBCO tapes which can be explicitly introduced by the R_M model. In this sense, this study has demonstrated that the C_M model can be considered as a valid approach not only for the measurement of the magnetic field at the centre of the coil former but it also provides a detailed approach for the dynamics of the flux front profiles for magnetically anisotropic materials. However, for magnetic field measurements near the coil turns, the C_M model cannot be considered quantitatively. Instead, the simplified Kim's model K_{M1} can be assumed if a relative tolerance between the experimental and numerical results of $\sim$25% is accepted. Otherwise, a more general approach such as the R_M model can be considered, under the expense of possibly increasing the computing time by a factor of 1.5-2.

In conclusion, Figure 5.7 & 5.8 presents the calculated AC loss curves for the benchmarked 20-turn SCS4050 racetrack coil, which reveals disparity between the hysteresis losses corresponding to the use of a magnetically isotropic model (e.g., the critical-state-like model, C_M) and the dissimilar Kim-like magneto-anisotropic models R_M, K_{M1}, and K_{M2} (see Table 5.1). Here, it is important to note that C_M reasonably predicts all the macroscopic electromagnetic characteristics of the type-II superconductors, however, its validity relies mainly on the qualitative figures of the model, and not on the quantitative scope added by the Kim-like models. For this reason, it is evident from Figure 5.7 that the C_M model generally underestimates the actual AC-losses of the superconducting system, as the intensity of the magnetic field created by the superconducting coil at different excitation conditions. Also, the case of a racetrack coil agrees with our previous findings concerning the flux front dynamics and the local distribution of profiles of current density, in which at low-intensity regime ($I_a \leq 0.4 I_{c0}$), the different material law models render almost equal value of the hysteretic losses, with relative differences no greater than twice the losses predicted by the C_M model. Although this factor may seem significant for some readers, the AC losses of a type-II superconducting coil influenced by the intensity of the applied current tend to increase by orders of magnitude as the I_{tr} increase, and in this sense, an increment of about two times the estimated losses by the C_M model can be absorbed by the ratio of tolerance between the numerical and experimental measurements. However, we had previously confirmed that the effect of the magneto-angular anisotropy of the REBCO layer is significant for moderate-to-high intensities of the applied current, ($I_a \gtrsim 0.4 I_{c0}$). For that reason, the difference in the AC losses estimated by the C_M model increase largely as I_a moves towards its critical threshold value I_{c0} (see Figure 5.8).

For instance, let us consider the hysteresis losses of the racetrack coil observed at the threshold condition $I_a/I_{c0} = 1$, where the C_M model predicts losses of $L_{CM} \simeq 0.4193$ J/cycle, whilst the magneto-anisotropic model, i.e.,

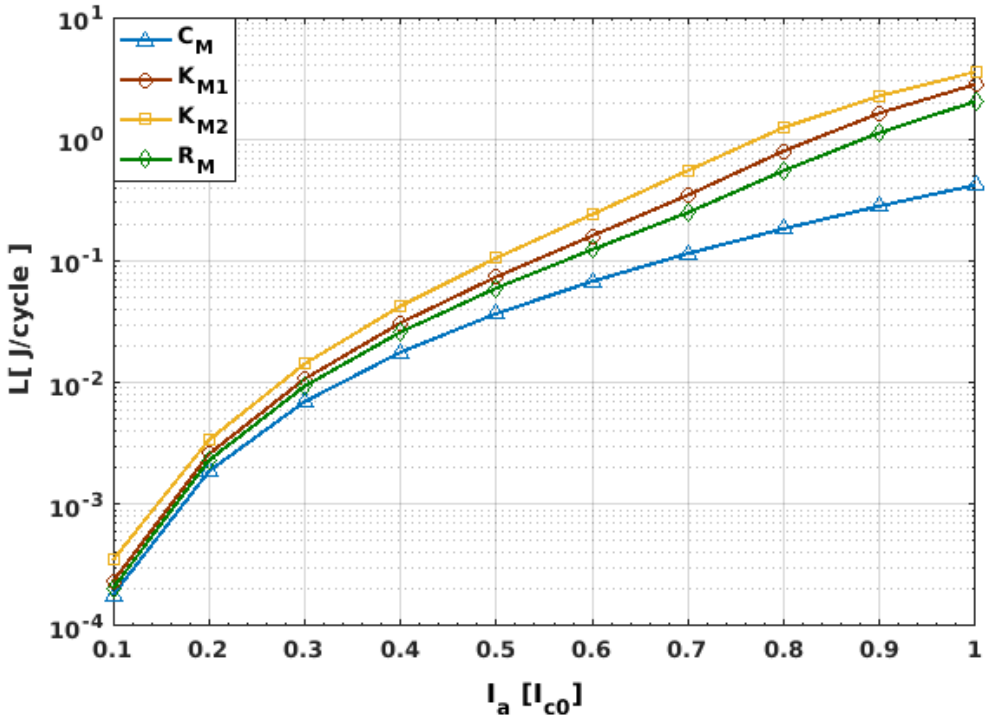

Figure 5.7: The predicted AC losses in Joules/cycle for a 20-turn SCS4050 racetrack coil is presented as a function of the amplitude of the applied transport current, I_a, and the material law models introduced in [44].

R_M estimates losses of $L_{RM} \simeq 2.039$ J/cycle, which is 4.86 times greater than that of the C_M model. Similarly, the empirical J_c-function for the K_{M2} material law estimates losses of $L_{KM2} \simeq 3.57$ J/cycle, which shows a maximum increment of about 8.5 times the L_{CM} losses. This increment of L_{KM2} is due to the increment in the intensity of the critical current density caused by the arbitrary reduction of the parallel component of the magnetic field in the function $J_c(B_\parallel, B_\perp)$, which was assumed by the K_{M2} model (see Table 5.1). However, as mentioned previously, within a transport current condition $I_a = I_{c0}$, the most classical and generic approach of the $J_c(B)$ function based on generalised Kim model, where no angular anisotropy is considered, i.e., the K_{M1} model, serves as an average model between the most tailored approaches K_{M2} and R_M, with $L_{KM2} \simeq 2.816$ J/cycle. Thus, the use of different material laws, especially in the case where the anisotropic magnetic properties of the REBCO layer are considered, shows robust differences in the predicted energy losses of superconducting racetrack coils. Therefore, we can conclude that at least for qualitative purposes where the reduction of the computing time is the priority, the classical Kim's model described by the function K_{M1} in Table 5.1 might result as the best option, especially when the actual material law governing

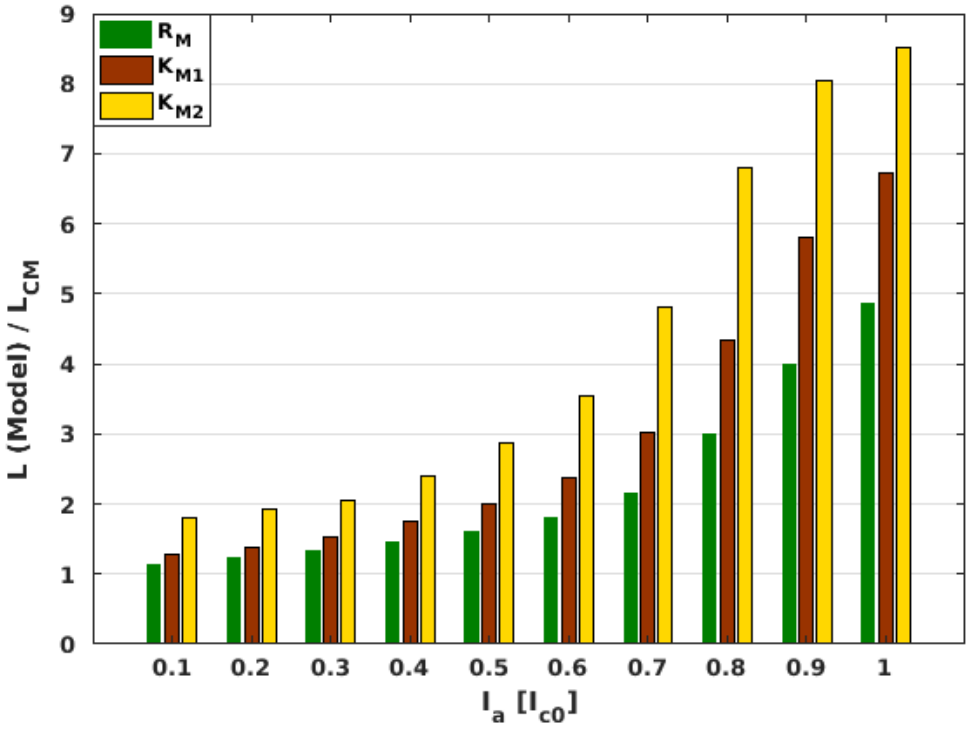

Figure 5.8: Presented as a function of the amplitude of the applied transport current, I_a, and the material law models introduced in [44], It shows the relative difference between the Kim-based anisotropic models (R_M, K_{M1}, and K_{M2}) and the magnetically isotropic C_M model.

the J_c properties of the 2G-HTS tape is not known, i.e., when most of the microstructural parameters that have been already connected with other physical quantities, such as in the case of the R_M model, are unknown and, by providing that the hysteresis losses between the experimental and numerical results fall within a tolerance range of approximately $\pm 28\%$, which is the maximal deviation obtained between the different models.

Conclusions II

As a benchmark, the different experimental conditions within Part II considers 2G-HTS coils with racetrack and pancake configurations under AC transport current conditions. The coils are conformed by 20 turns of commercially available 2G-HTS tapes (SCS4050) manufactured by SuperPower Inc., wound on a 5 cm mid-width former with 4 mm width and overall thickness of approximately 0.1 mm, which at a self-field conditions exhibit a maximum critical current density of I_{c0} = 114 A (i.e., the critical current density measured in the absence of external magnetic field) [141].

From a computational perspective, the high aspect ratio of the 2G-HTS tapes impose significant challenges for the understanding of their performance in practical superconducting machines, reason why this study adopted a unified numerical approach for high-level meshing conditions which allows to observe the dynamics of flux front profiles at a local level. The numerical simulations performed in Chapters 4 & 5 within the framework of the celebrated 2D H-formulation for both configurations have been implemented in COMSOL Multiphysics 5.3a [164], taking into account the most general material law for describing the E-J properties of the 2G-HTS tapes at constant temperature, which extends the conventional Kim's critical state model to an experimentally validated magneto angular dependent E-J power law [141]. Also, in this study we have assumed a magnetically isotropic and homogeneous behaviour for the magnetic permeability (μ) of the different materials, such that the magnetic flux density vector $\mathbf{B}$ can be presented in terms of the magnetic field vector $\mathbf{H}$, with $\mathbf{B} = \mu\mathbf{H}$, where μ equals the magnetic permeability of free space (μ_0) in the case of a Superconductor in the quasi-static approximation. It enables an appropriate modelling of the superconducting domains, provided that the different materials involved behave as non-dispersive (frequency-independent) mediums, with non-magnetic intrinsic properties in their "normal" state. This assumption can be adopted for a superconducting ReBCO layer, under the condition that the frequency of the applied transport current or any external magnetic field remains constant, and does not alter the microstructural properties of the superconducting material [194].

From the physical point of view, the governing equations, Faraday's and

Ampère's law are implemented within the magneto quasi-steady approach [137]. This approach takes into account that the displacement current densities $\delta_t \mathbf{D}$ are much smaller compared to the current density $\mathbf{J}$ inside a superconductor, i.e., $\delta_t \mathbf{D} \simeq 0$ and vanishes in a first-order treatment. Thus, it is possible to assume that for uniform and slow sweep rates of the external excitations (transport current or magnetic field sources), the transient variables of electric field $\mathbf{E}$ and electrical resistivity ρ are both small and proportional to $\dot{\mathbf{B}} = \partial B/\partial_t$, while $\ddot{\mathbf{B}}$, $\dot{\mathbf{E}}$, and $\dot{\rho}$ are negligible. Computationally, the PDE system is expressed by means of Ampère's law $\nabla^2 \mathbf{H} - \mu\sigma\partial_t \mathbf{J} = 0$, with approximate integrability condition $\nabla \cdot \mathbf{J} \simeq 0$. In this sense, the electrical field behaviour inside a ReBCO layer is introduced by the electrical resistivity function $\rho(J) = \sigma^{-1}$, which plays the role of a nonlinear and possibly nonscalar resistivity for the superconducting state, $\sigma^1 = E_0/|\mathbf{J}| \cdot (|\mathbf{J}|/J_c)^n$, with the critical current density J_c defined by the different material laws presented in Table 5.1, whilst for the non-superconducting materials the classical Ohm's law, $\mathbf{J} = \sigma\mathbf{E}$, remains valid.

We have revised the impact of different superconducting material law derivatives and the influence of turn-to-turn misalignment on the local electromagnetic properties of each turn for racetrack and pancake coil configurations. The latter gave rise to questions linked to the practical importance of 2G-HTS tapes under such misalignment factor, such as,

1. How does an unintentional misalignment in the winding of a superconducting coil impact its energy losses and magnetic field profile?
2. Is the misalignment factor commonly assumed negligible?
3. or Can it actually effect the coil energy efficiency features?

Thus, to tackle these questions, the experimental conditions in Chapter 4 takes into account the influence of systematic misalignments in the winding of 2G-HTS tapes on the hysteresis losses for both coil configurations under AC condition. To numerically model such scenarios, we have assumed a collateral turn-to-turn displacement of 20 μm, 25 μm, 33 μm, 50 μm, and 100 μm for a 20 turns SCS4050 coil of tape-width $T_w = 4$ mm, which correlate to innermost to outermost turn-misalignments of 1/10, 1/8, 1/6, 1/4, and 1/2 the width of the HTS tape.

Likewise, in Chapter 5 we have studied the impact of different superconducting material law models into the modelling of 2G-HTS coils as an attempt to solve the following questions:

1. Have computational modellers adopted a sufficiently stringent material law capable to reproduce all macroscopical electromagnetic quantities within a more quantitative perspective for 2G-HTS coils?

2. Is this material law valid when the superconducting material is known to exhibit magneto-anisotropic properties?

Thus, as a benchmark, we considered the four most popular material law models for type-II superconductors, such as (i) a simplified critical state (CS)-like-model [137, 143], (ii) the classical Kim's model [171, 187], (ii) an empirical Kim-like model with orthonormal field dependence for SuperPower Inc. [134] SCS4050 2G-HTS tapes [116], and (iv) the generalised form of the critical current density with magneto angular anisotropy measured on the SCS4050 tapes [141]. We have demonstrated how these models can strongly influence the accurate estimation of macroscopically measurable physical quantities such as the critical current density per coil turn, the magnetic field near the coil armature, and the prediction of the hysteresis losses per cycle in the system. For doing so, we have focused our study on the local understanding of the physical properties of the flux front profiles, and not on mesh simplifications for reduced computational difficulty. Within this scope, we presented the main observations derived together with the comprehensive analysis for the understanding of the local physical behaviour of macroscopic quantities such as critical current density at each turn of the superconducting coil, the calculation of the magnetic field at specific positions, and the hysteresis losses in the overall system.

We have found that almost no physical discernment can be seen between the dimensions of the local flux front profiles for pancake and racetrack coils with the same axial dimensions, i.e., when the width of a long racetrack coil former is equal to the radius of the pancake coil former, with exception to their derived AC losses. For this reason, the summary on the effect of misalignment factors on the measurable electromagnetic properties inside each 2G-HTS layers refers to both coil, unless when stated otherwise. Thus, we found that for $I_a \leq 0.2\ I_{c0}$, approximately 30% of the central turns within the SC coil exhibits a bulk-like behaviour, with a well-shaped flux-free core enclosed by the occurrence of extrinsic profiles of transport current at the edges of each HTS turns, and a complete absence of magnetisation currents. Then, the remaining 70% of the coil shows the preservation of the transport current flux front profile, and a strong dominance of magnetisation currents along the width of each tape where local flux-free cores do not appear due to the full penetration of the the induced magnetic field inside HTS turns, by the neighbouring HTS turns and the injected transport current. However, the size of the flux-free core reduces as the amplitude of the applied transport current increases, this increment exerts a Lorentz force that pushes the magnetisation currents towards the middle turns of the coil in anticipation of the full disappearance of the flux free core, which occurs under critical current conditions $I_a \geq 0.9\ I_{c0}$ (see Figure 4.1 & 4.2).

Moreover, we have demonstrated that for applied currents $I_a \leq 0.6\ I_{c0}$, a negligible difference has been observed in the distribution of flux-front profiles between the magneto-angular anisotropy features of 2G-HTS tapes and the critical-state model predictions, but for a current level at $0.6\ I_{c0} \leq I_{tr} \leq I_{c0}$, the critical state model will render a slight overestimation of the magnetisation losses that decreases as I_{tr} increases. Nonetheless, concerning the different J_c models (See Table 5.1), no significant difference have been encountered, with exemption of a striking concave-shaped feature of the flux-front profile between the different Kim-like models (K_{M1}, K_{M2}) and the magneto angular model (R_M) as shown in Figure 5.1.

Likewise, for the misaligned coils studied in Chapter 4, the study concludes that the resulting size of the flux front profiles remains unaltered regardless of the magnitude of misalignment factor. Therefore, in these cases, the induced Lorentz-force between the transport current and the magnetisation currents is the physical mechanism that contributes to the additional AC-losses in such system, where the collateral displacement of the HTS turns, and critical current density dependence on the magneto-angular anisotropy of the 2G-HTS tape, contribute to the additional source of AC losses. These conclusions are demonstrated by observing the dynamics of the flux front for misaligned pancake and racetrack coils ($\delta_m > 0$) in Figure 4.3 & 4.4, respectively. Therein, a robust deflection of the semi-elliptical vertices has been noticed compared to the case of a perfectly wound coil or $\delta_m = 0$. This deflection evolves towards the uppermost and bottommost edges of the innermost and outermost turns of the coil, which induces a clockwise repositioning of the co-vertices to form a "worm-like" flux-front shape. It triggers an imbalance in the local magnetic field at the opposite coil edges, introduced by the breakdown in the ordinal symmetry of the mutual inductance between the coil turns (see Figure 4.5). In this sense, the magnitude of the critical current drops at the region where the intensity of the magnetic field increases at the edges of the misaligned coils, i.e., the edges of the innermost and the outermost turns. This drop is due to the magneto-angular anisotropy of the 2G-HTS tape, which exerts an accumulation of transport current in the lateral edges of the 2G-HTS turns (with higher critical current density), leading to the Lorentz motion of magnetisation currents towards the edge with the weakest critical current density.

Analogously, it has been found that for low to moderate applied currents $I_a \leq 0.6 I_{c0}$ in misaligned racetrack coils, with I_{c0} the self-field critical current of the wound tape, the AC losses increases in a racetrack coil can increase in up to 25% over the hysteresis losses of perfectly wound coils ($\delta_m = 0$) for extreme winding deformations. However, the change in the AC losses is almost negligible for higher amplitudes of the transport current ($I_a/I_{c0} \geq 0.7$), although at the critical current $I_a/I_{c0} = 1$ it shows a decrease of about 5% of

the losses calculated for a perfectly wound coil. These striking variations on the AC losses are linked physically to the local motion of magnetisation currents (increased losses) or the disappearance of the flux free core (reduced losses). Also, irrespective of the misalignment factor, we confirm that at the outermost and innermost turns of a 2G-HTS racetrack coil, the averaged critical current density in each turn experiences a detriment of about 50% the self-field critical current density J_{c0} when $I_a \geq 0.5I_{c0}$. This remark is in good agreement with the previously reported studies for perfectly wound coils under simplified $J_c(B)$ Kim-like models[136, 180].

Likewise, the effect of misalignment on the AC losses of a wound 2G-HTS pancake coil can reach up to a 19% with the perfectly aligned coil, under similar transport current conditions, $I_a \leq 0.6I_{c0}$. However, for higher intensities of the applied current, and pancake coils exposed to relatively large deformations of $> T_w/4$ in the wound coil (larger than a quarter of the tape width, between the innermost and outermost turn of the coil), unpredictably, the AC losses of the deformed pancake coil results lesser compared to that generated by a perfectly aligned coil with the same overall dimensions and 2G-HTS tape.

It is worth mentioning that our results for the case of perfectly wound coils, although computationally expensive due to the augmented mesh required for the study of the local distribution of profiles of current density inside each turn of the superconducting coil, it also validates some of the most intriguing electromagnetic features already predicted by integral and variational formulations such as the Minimum Magnetic Energy Variation Method [119, 205] and the $A - J$ formulation [138] where reduced meshing topologies have been invoked. Furthermore, we confirm one of the essential theoretical findings in [138] under the full spectrum of current and magneto angular anisotropic conditions of real 2G-HTS tapes. Therein, it was shown that the incorporation of magnetic field dependence on J_c through the classical Kim-like critical state model [187] for perpendicular and transverse components of the magnetic field in a racetrack coil with $I_a = 0.7I_{c0}$, could result in a marked non-uniformity of J_c on a few of the innermost and outermost turns turn of the HTS coil. In fact, the high-resolution approach adopted in our study has allowed as to show how the magneto dependence of the critical current density alters the expected homogeneity of the critical current density over the width of the outer tapes, where this influence does not extends only up to the second and penultimate turn of the coil predicted in [101], but at least up to the turn where the elliptical-like shape flux front (encapsulating magnetisation currents) is observed, as it can be seen in Figures 4.1 and 4.2 for the case of perfectly aligned pancake and racetrack coils, respectively, and Figures 4.3 and 4.4 for the corresponding misaligned coils.

Thus, our findings could be used as a practical benchmark to understand the physical characteristics of 2G-HTS wound pancake or racetrack coils capable of determining the source of possible deviations in the measured AC losses by manufacturing defects inherent to the winding process, or by mechanical deflections of the HTS tapes when positioning the superconducting coil within a particular fixture.

Finally, concerning to our analysis of the four different material laws for the formulation of the critical current density of 2G-HTS tapes within the E-J power law, which shows distinctive characteristics through the direct comparison between an isotropic critical-state-like model, C_M, and different versions of the so-called Kim-based models: K_{M1}, K_{M2}, and R_M in Table 5.1, we have found that despite these material laws allow an adequate qualitative description of the electromagnetism of superconducting coils, significant quantitative disparities exists between their predictions. From a computational veiwpoint, this difference can assist modellers to reach a conclusion on the soundness of the material law to adopt when time and computing power are deciding factors. From this perspective, our findings indicate that for the measurement of physical quantity linked to the turn-by-turn critical current density by I-V measurements, the position of the voltage taps becomes a determinant factor for the local magneto-angular anisotropy of the superconducting tape. This statement is demonstrated in Figure 5.3, as inappropriate placement of the voltage taps across the width of the coil could generate about 50% deviation between the theoretical and experimental measurements. Unlike the C_M model, the J_c over the different turns of the superconducting coil remains constant. Conversely, the use of Kim-like model exhibits a local variation of the critical current density across the surface of the superconducting tape, which is consistent with the reported observations by magneto-optical imaging [201]. However, the C_M model is the best option if the physical quantity of interest to be measured is the intensity of the magnetic field at the central axis of the 2G-HTS coil (see Figure 5.2), as no difference was obtained when compared with the prognostics of the Kim-like models and also, the C_M model offers a simplified framework and minimum computing time in comparison with the other models. Otherwise, the C_M model will tend to underestimate the intensity of the magnetic field for measurements beyond the central axis of the coil. Under such situations, the simplified Kim's model K_{M1} serves as the best option for the numerical modelling of the superconducting properties, and it can be invoked given an acceptable relative tolerance between the experimental and numerical results of $\sim$25%, unless the expected increase in the computing time by a factor of at least 1.5 times can be afforded, on which a more "tailored" approach such as the R_M model is recommended.

Likewise, concerning to the AC losses, we found that for low intensities of

the applied current ($I_a \leq 0.4I_{c0}$), all the models render almost the same losses prediction with a relative difference of maximum twice the expected losses calculated by the critical state model. On the other hand, the meaningful impact of the magneto-angular anisotropy of 2G-HTS tape was evinced for moderate-to-high intensities of the applied current ($I_a \geq 0.4I_{c0}$), where the difference in the estimated losses is approximately 3 to 8 times of the isotropic C_M model. In this sense, it is evident that if the power and computing time are not the deciding factors for the modeller of superconducting machines, the suitable option for selecting material law for quantitative purposes is the R_M model. This because experimental measurements have already determined the majority of the microstructural parameters for the superconducting tape, and it applies to other simplified models not considered here. However, in the case where the $J_c(\mathbf{B}, \theta)$ function for 2G-HTS tape is not known, the use of the classical Kim's model connotes the best advisable choice with the requisite that the experimentalists and numerical modellers bear in mind a relative tolerance of $\sim$28% in the estimation of the AC losses.

To conclude, the results presented in each Chapter of this thesis are original and highly useful results that significantly advance the knowledge in the numerical modelling of superconducting coils under rigorous data methods and analysis, and also useful for the design of 2G-HTS machines. The results from Chapter 2 to 5 have been published in high impact factor peer- reviewed journals, as evidence that our results are of high interest for the community of scientists and engineers in the diverse fields of applied superconductivity. Therefore, these results are considered of enough soundness to motivate other researches in these fields, and to expand the studies towards the practical optimisation of superconducting devices

References

[1] H. Ruiz Rondan, *Material laws and numerical methods in applied superconductivity*. Zaragoza, Spain: University of Zaragoza Press, 2013.

[2] M. Oomen, W. Herkert, D. Bayer, P. Kummeth, W. Nick, and T. Arndt, "Manufacturing and test of 2g-hts coils for rotating machines: Challenges, conductor requirements, realization," *Physica C: Superconductivity and its applications*, vol. 482, pp. 111–118, 2012.

[3] K. S. Haran, S. Kalsi, T. Arndt, H. Karmaker, R. Badcock, B. Buckley, T. Haugan, M. Izumi, D. Loder, J. W. Bray, *et al.*, "High power density superconducting rotating machinesâ€"development status and technology roadmap," *Superconductor Science and Technology*, vol. 30, no. 12, p. 123002, 2017.

[4] M. Leghissa, J. Rieger, H.-W. Neumuller, J. Wiezoreck, F. Schmidt, W. Nick, P. Van Hasselt, and R. Schroth, "Development of hts power transmission cables," *IEEE transactions on applied superconductivity*, vol. 9, no. 2, pp. 406–411, 1999.

[5] P. M. Grant, "Superconductivity and electric power: promises, promises... past, present and future," *IEEE transactions on applied superconductivity*, vol. 7, no. 2, pp. 112–133, 1997.

[6] D. W. Hazelton, V. Selvamanickam, J. M. Duval, D. C. Larbalestier, W. D. Markiewicz, H. W. Weijers, and R. L. Holtz, "Recent developments in 2g hts coil technology," *IEEE Transactions on Applied Superconductivity*, vol. 19, no. 3, pp. 2218–2222, 2009.

[7] J. Welstead and J. L. Felder, "Conceptual design of a single-aisle turboelectric commercial transport with fuselage boundary layer ingestion," in *54th AIAA Aerospace Sciences Meeting*, p. 1027, 2016.

[8] H. Karmaker, D. Sarandria, M. T. Ho, J. Feng, D. Kulkarni, and G. Rupertus, "High-power dense electric propulsion motor," *IEEE transactions on industry applications*, vol. 51, no. 2, pp. 1341–1347, 2014.

[9] D. Uglietti, "A review of commercial high temperature superconducting materials for large magnets: from wires and tapes to cables and conductors," *Superconductor Science and Technology*, vol. 32, no. 5, p. 053001, 2019.

[10] O. Maruyama, T. Ohkuma, T. Masuda, Y. Ashibe, S. Mukoyama, M. Yagi, T. Saitoh, T. Hasegawa, N. Amemiya, A. Ishiyama, *et al.*, "Development of 66 kv and 275 kv class rebco hts power cables," *IEEE transactions on applied superconductivity*, vol. 23, no. 3, pp. 5401405–5401405, 2012.

[11] J. Maguire, J. Yuan, W. Romanosky, F. Schmidt, R. Soika, S. Bratt, F. Durand, C. King, J. McNamara, and T. Welsh, "Progress and status of a 2g hts power cable to be installed in the long island power authority (lipa) grid," *IEEE Transactions on Applied Superconductivity*, vol. 21, no. 3, pp. 961–966, 2010.

[12] N. Kelley and J. Jipping, "Hts cable system demonstration at detroit edison," in *2002 IEEE Power Engineering Society Winter Meeting. Conference Proceedings (Cat. No. 02CH37309)*, vol. 1, pp. 136–139, IEEE, 2002.

[13] D. I. Doukas, "Superconducting transmission systems: review, classification, and technology readiness assessment," *IEEE Transactions on Applied Superconductivity*, vol. 29, no. 5, pp. 1–5, 2019.

[14] S. J. Lee, M. Park, I.-K. Yu, Y. Won, Y. Kwak, and C. Lee, "Recent status and progress on hts cables for ac and dc power transmission in korea," *IEEE Transactions on Applied Superconductivity*, vol. 28, no. 4, pp. 1–5, 2018.

[15] C. Lee, H. Son, Y. Won, Y. Kim, C. Ryu, M. Park, and M. Iwakuma, "Progress of the first commercial project of high-temperature superconducting cables by kepco in korea," *Superconductor Science and Technology*, vol. 33, no. 4, p. 044006, 2020.

[16] W. V. Hassenzahl, S. E. Eckroad, P. M. Grant, B. Gregory, and S. Nilsson, "A high-power superconducting dc cable," *IEEE transactions on applied superconductivity*, vol. 19, no. 3, pp. 1756–1761, 2009.

[17] S. Eckroad *et al.*, "Program on technology innovation: a superconducting dc cable," *Electric Power Research Institute, Final Report*, vol. 1020458, 2009.

[18] X. Liang, S. Dai, Z. Gao, N. Song, Y. Wang, D. Zhang, Z. Zhang, F. Zhang, Z. Zhu, X. Xu, *et al.*, "Design of a 380 m dc hts power cable," *IEEE Transactions on Applied Superconductivity*, vol. 20, no. 3, pp. 1259–1262, 2010.

[19] J.-G. Kim, S.-K. Kim, M. Park, I.-K. Yu, H. Lee, Y.-G. Kim, H.-M. Kim, Y.-J. Won, K.-W. Jeong, and B. Yang, "Loss characteristic analysis of hts dc power cable using lcc based dc transmission system," *IEEE transactions on applied superconductivity*, vol. 22, no. 3, pp. 5801304–5801304, 2012.

[20] M. Hamabe, T. Fujii, I. Yamamoto, A. Sasaki, Y. Nasu, S. Yamaguchi, A. Ninomiya, T. Hoshino, Y. Ishiguro, and K. Kawamura, "Recent progress of experiment on dc superconducting power transmission line in chubu university," *IEEE transactions on applied superconductivity*, vol. 19, no. 3, pp. 1778–1781, 2009.

[21] V. Sytnikov, S. Bemert, Y. V. Ivanov, S. Kopylov, I. Krivetskiy, D. Rimorov, M. Romashov, Y. G. Shakaryan, R. Berdnikov, Y. A. Dementyev, *et al.*, "Hts dc cable line project: On-going activities in russia," *IEEE transactions on applied superconductivity*, vol. 23, no. 3, pp. 5401904–5401904, 2013.

[22] S. Kopylov, V. Sytnikov, S. Bemert, Y. Ivanov, I. Krivetskiy, M. Romashov, Y. Shakaryan, V. Keilin, A. Shikov, V. Patrikeev, *et al.*, "Hts dc transmission line for megalopolis grid development," in *J. Phys. Conf. Ser*, vol. 507, 2014.

[23] M. Stemmle, F. Merschel, M. Noe, and A. Hobl, "Ampacityâ€"installation of advanced superconducting 10 kv system in city center replaces conventional 110 kv cables," in *2013 IEEE International Conference on Applied Superconductivity and Electromagnetic Devices*, pp. 323–326, IEEE, 2013.

[24] S.-H. Sohn, H.-S. Yang, J.-H. Lim, S.-R. Oh, S.-W. Yim, S.-K. Lee, H.-M. Jang, and S.-D. Hwang, "Installation and power grid demonstration of a 22.9 kv, 50 mva, high temperature superconducting cable for kepco," *IEEE transactions on applied superconductivity*, vol. 22, no. 3, pp. 5800804–5800804, 2012.

[25] S.-K. Kim, S.-K. Ha, J.-G. Kim, B.-G. Jang, M. Park, I.-K. Yu, S. Lee, K. Sim, and A.-R. Kim, "Development and performance analysis of a 22.9 kv/50 mva tri-axial hts power cable core," *IEEE transactions on applied superconductivity*, vol. 23, no. 3, pp. 5400804–5400804, 2013.

[26] H. S. Yang, D. L. Kim, S. H. Sohn, J. H. Lim, H. O. Choi, Y. S. Choi, B. S. Lee, W. M. Jung, H. S. Ryoo, and S. dole Hwang, "Long term performance test of kepco hts power cable," *IEEE transactions on applied superconductivity*, vol. 19, no. 3, pp. 1782–1784, 2009.

[27] B. Yang, J. Kang, S. Lee, C. Choi, and Y. Moon, "Qualification test of a 80 kv 500 mw hts dc cable for applying into real grid," *IEEE Transactions on Applied Superconductivity*, vol. 25, no. 3, pp. 1–5, 2015.

[28] O. Tonnesen, S. Hansen, P. Jorgensen, K. Lomholt, S. D. Mikkelsen, J. Okholm, S. Salvin, and J. Ostergaard, "Power applications for superconducting cables," in *CONFERENCE SERIES-INSTITUTE OF PHYSICS*, vol. 167, pp. 1103–1108, Philadelphia; Institute of Physics; 1999, 2000.

[29] Z. Zhang, S. Venuturumilli, M. Zhang, and W. Yuan, *Superconducting Cables – Network feasibility study work package 1.* Innovation, Next Generation Networks, Western Power Distribution, August 2016.

[30] H. Thomas, A. Marian, A. Chervyakov, S. Stúckrad, D. Salmieri, and C. Rubbia, "Superconducting transmission lines - sustainable electric energy transfer with higher public acceptance," *Renewable and Sustainable Energy Reviews*, vol. 55, no. Supplement C, pp. 59 – 72, 2016.

[31] H. K. Onnes, "Investigations into the properties of substances at low temperatures, which have led, amongst other things, to the preparation of liquid helium," *Nobel Lectures, Physics*, vol. 1901-1921, p. 306, Dec 1913.

[32] J. Bardeen, L. N. Cooper, and J. R. Schrieffer, "Microscopic theory of superconductivity," *Phys. Rev.*, vol. 106, pp. 162–164, Apr 1957.

[33] W. Meissner and R. Ochensenfield, "Ein neuer effeckt bei eintritt der supraleitfaehigkeit," *Naturwissenschaften*, vol. 21, p. 787, 1933.

[34] C. Rey and A. Malozemoff, "2 - fundamentals of superconductivity," in *Superconductors in the Power Grid* (C. Rey, ed.), Woodhead Publishing Series in Energy, pp. 29 – 73, Woodhead Publishing, 2015.

[35] A. A. Abrikosov, "On the magnetic properties of superconductors of the second group.," *Zh Eksperim.i Teor Fiz*, vol. 5, p. 1174, 1957.

[36] V. Ginzburg and A. E.A, *Superconductivity.* Singapore: World Scientific, 2005.

[37] A. Campbell and J. Evetts, "Flux vortices and transport currents in type ii superconductors," *Advances in Physics*, vol. 21, no. 90, pp. 199–428, 1972.

[38] A. Campbell, J. Evetts, and D. Dew-Hughes, "Pinning of flux vortices in type ii superconductors," *Philosophical Magazine*, vol. 18, no. 152, pp. 313–343, 1968.

[39] C. P. Bean, "Magnetization of high-field superconductors," *Rev. Mod. Phys.*, vol. 36, pp. 31–39, Jan 1964.

[40] H. S. Ruiz and A. Badía-Majós, "Exotic magnetic response of superconducting wires subject to synchronous and asynchronous oscillating excitations," *Journal of Applied Physics*, vol. 113, no. 19, p. 193906, 2013.

[41] L. Prigozhin, "On the bean critical-state model in superconductivity," *European Journal of Applied Mathematics*, vol. 7, no. 3, pp. 237–247, 1996.

[42] J. W. Barrett and L. Prigozhin, "Bean's critical-state model as the $p \to \infty$ limit of an evolutionary $p-$laplacian equation," *Nonlinear Analysis: Theory, Methods & Applications*, vol. 42, no. 6, pp. 977–993, 2000.

[43] F. Sirois and F. Grilli, "Potential and limits of numerical modelling for supporting the development of hts devices," *Superconductor Science and Technology*, vol. 28, no. 4, p. 043002, 2015.

[44] B. C. Robert, M. U. Fareed, and H. S. Ruiz, "How to choose the superconducting material law for the modelling of 2g-hts coils," *Materials*, vol. 12, no. 17, 2019.

[45] G. P. Mikitik, Y. Mawatari, A. T. S. Wan, and F. Sirois, "Analytical methods and formulas for modeling high temperature superconductors," *IEEE Transactions on Applied Superconductivity*, vol. 23, pp. 8001920–8001920, April 2013.

[46] A. Badía-Majós, C. López, and H. S. Ruiz, "General critical states in type-ii superconductors," *Phys. Rev. B*, vol. 80, p. 144509, Oct 2009.

[47] W. J. Carr Jr., M. S. Walker, and J. H. Murphy, "Alternating field loss in a multifilament superconducting wire for weak ac fields superposed on a constant bias," *Journal of Applied Physics*, vol. 46, no. 9, pp. 4048–4052, 1975.

[48] A. V. Gurevich, R. G. Mints, and A. L. Rakhmanov, *Physics of Composite Superconductors*. Begell House, New York, 1997.

[49] J. D. Jackson, *Classical Electrodynamics*. New Jersey, USA: John Wiley & Sons, Inc., 3 ed., 1991.

[50] A. D. Huxley, "Ferromagnetic superconductors," *Physica C: Superconductivity and its Applications*, vol. 514, pp. 368 – 377, 2015. Superconducting Materials: Conventional, Unconventional and Undetermined.

[51] J. W. Barret and L. Prigozhin, "A quasi-variational inequality problem in superconductivity," *Mathematical Models and Methods in Applied Sciences*, vol. 20, no. 05, pp. 679–706, 2010.

[52] A. M. Wolsky and A. M. Campbell, "A new method for determining the critical state of three-dimensional superconductors: explanation and examples," *Superconductor Science and Technology*, vol. 21, no. 7, p. 075021, 2008.

[53] A. M. Campbell, "A direct method for obtaining the critical state in two and three dimensions," *Superconductor Science and Technology*, vol. 22, no. 3, p. 034005, 2009.

[54] L. E. Svistov and S. A. Vitkalov, "High frequency electromagnetic action on dc magnetic moment of ybacuo granular superconductor," *Czechoslovak Journal of Physics*, vol. 46, pp. 1267–1268, Mar 1996.

[55] A. Badía and C. López, "Critical state theory for nonparallel flux line lattices in type-ii superconductors," *Phys. Rev. Lett.*, vol. 87, p. 127004, Aug 2001.

[56] L. S. Pontryagin, V. G. Boltyanshii, R. V. Gamkrelidze, and E. F. Mishenko, "The mathematical theory of optimal processes," 1962.

[57] X. Zhang, Z. Zhong, H. S. Ruiz, J. Geng, and T. A. Coombs, "General approach for the determination of the magneto-angular dependence of the critical current of ybco coated conductors," *Superconductor Science and Technology*, vol. 30, no. 2, p. 025010, 2017.

[58] H. S. Ruiz, X. Zhang, and T. A. Coombs, "Resistive-type superconducting fault current limiters: Concepts, materials, and numerical modeling," *IEEE Transactions on Applied Superconductivity*, vol. 25, pp. 1–5, June 2015.

[59] W. Rudin, *Principles of mathematical analysis*. New York: McGraw-Hill Book Co., third ed., 1976. International Series in Pure and Applied Mathematics.

[60] H. S. Ruiz and A. Badía-Majós, "Smooth double critical state theory for type-ii superconductors," *Superconductor Science and Technology*, vol. 23, no. 10, p. 105007, 2010.

[61] M. Baghdadi, H. S. Ruiz, and T. A. Coombs, "Crossed-magnetic-field experiments on stacked second generation superconducting tapes: Reduction of the demagnetization effects," *Applied Physics Letters*, vol. 104, no. 23, p. 232602, 2014.

[62] A. Campbell, M. Baghdadi, A. Patel, D. Zhou, K. Y. Huang, Y. Shi, and T. Coombs, "Demagnetisation by crossed fields in superconductors," *Superconductor Science and Technology*, vol. 30, no. 3, p. 034005, 2017.

[63] F. Liang, T. Qu, Z. Zhang, J. Sheng, W. Yuan, Y. Iwasa, and M. Zhang, "Vortex shaking study of rebco tape with consideration of anisotropic characteristics," *Superconductor Science and Technology*, vol. 30, no. 9, p. 094006, 2017.

[64] S. Celebi, F. Sirois, and C. Lacroix, "Collapse of the magnetization by the application of crossed magnetic fields: observations in a commercial bi:2223/ag tape and comparison with numerical computations," *Superconductor Science and Technology*, vol. 28, no. 2, p. 025012, 2015.

[65] J. L. Giordano, J. Luzuriaga, A. Badía-Majós, G. Nieva, and I. Ruíz-Tagle, "Magnetization collapse in polycrystalline ybco under transport current cycles," *Superconductor Science and Technology*, vol. 19, no. 4, p. 385, 2006.

[66] "Superconducting wire subject to synchronous oscillating excitations: Power dissipation, magnetic response, and low-pass filtering," *Applied Physics Letters*, vol. 100, no. 11, p. 112602, 2012.

[67] J. Ogawa, S. Fukui, T. Oka, T. Sato, H. Kojima, M. Shibayama, and M. Egawa, "Influence of dc offset transport current on ac loss characteristics in hts tapes," *IEEE Transactions on Applied Superconductivity*, vol. 21, pp. 3325–3328, June 2011.

[68] F. Grover, *Inductance Calculations: Working Formulas and Tables*. New York: Dover Publications Inc., 2009. Phoenix Edition Series.

[69] F. Grover, "Tables for the calculation of the inductance of circular coils of rectangular cross section," vol. 18, pp. 451–487, New York: Department of Commerce, National Bureau of Standards, 1922. Scientific papers of the bureau of standards.

[70] E. B. Rosa and F. W. Grover, *Formulas and tables for the calculation of mutual and self-inductance (Revised)*, vol. 169. Washington, Govt. Print. Off.: Department of Commerce, National Bureau of Standards, 3rd ed., 1948. Bulletin of the Bureau of Standards.

[71] F. Grilli, E. Pardo, A. Stenvall, D. N. Nguyen, W. Yuan, and F. Gömöry, "Computation of losses in hts under the action of varying magnetic fields and currents," *IEEE Transactions on Applied Superconductivity*, vol. 24, pp. 78–110, Feb 2014.

[72] A. Stenvall, V. Lahtinen, and M. Lyly, "An h -formulation-based three-dimensional hysteresis loss modelling tool in a simulation including time varying applied field and transport current: the fundamental problem and its solution," *Superconductor Science and Technology*, vol. 27, no. 10, p. 104004, 2014.

[73] A. Conn, G. Gould, and P. Toint, *Lancelot: A Fortran Package for Large-Scale Nonlinear Optimization (Release A)*. Springer-Verlag Berlin Heidelberg, 1992.

[74] A. R. Conn, N. I. M. Gould, and P. Toint, "A globally convergent augmented lagrangian algorithm for optimization with general constraints and simple bounds," *SIAM Journal on Numerical Analysis*, vol. 28, no. 2, pp. 545–572, 1991.

[75] M. W. Coffey, "High-frequency linear response of anisotropic type-ii superconductors in the mixed state," *Phys. Rev. B*, vol. 47, pp. 12284–12287, May 1993.

[76] M. W. Coffey and J. R. Clem, "Theory of high-frequency linear response of isotropic type-ii superconductors in the mixed state," *Phys. Rev. B*, vol. 46, pp. 11757–11764, Nov 1992.

[77] R. Prozorov, A. Shaulov, Y. Wolfus, and Y. Yeshurun, "Frequency dependence of the local ac magnetic response in type-ii superconductors," *Phys. Rev. B*, vol. 52, pp. 12541–12544, Nov 1995.

[78] B. C. Robert and H. S. Ruiz, "Magnetic characteristics and ac losses of dc type-ii superconductors under oscillating magnetic fields," *Superconductor Science and Technology*, 2018.

[79] B. C. Robert and H. S. Ruiz, "Electromagnetic response of dc type-ii superconducting wires under oscillating magnetic excitations," *IEEE Transactions on Applied Superconductivity*, vol. 28, no. 4, p. 8200905, 2018.

[80] B. C. Robert and H. S. Ruiz, "Magnetization profiles of ac type-ii superconducting wires exposed to dc magnetic fields," *IEEE Transactions on Applied Superconductivity*, vol. 28, pp. 1–5, June 2018.

[81] S. Zannella, L. Montelatici, G. Grenci, M. Pojer, L. Jansak, M. Majoros, G. Coletta, R. Mele, R. Tebano, and F. Zanovello, "Ac losses in transport current regime in applied ac magnetic field: experimental analysis and modeling [superconducting cables]," *IEEE Transactions on Applied Superconductivity*, vol. 11, pp. 2441–2444, Mar 2001.

[82] H. Tonsho, S. Fukui, T. Sato, M. Yamaguchi, S. Torii, T. Takao, and K. Ueda, "Theoretical and experimental study on ac loss in hts tape in ac magnetic field carrying ac transport current," *IEEE Transactions on Applied Superconductivity*, vol. 13, pp. 2368–2371, June 2003.

[83] J. Ogawa, M. Shiokawa, M. Ciszek, and O. Tsukamoto, "Ac losses in ybco coated conductors carrying ac transport currents in perpendicular ac external magnetic field," *IEEE Transactions on Applied Superconductivity*, vol. 13, pp. 1735–1738, June 2003.

[84] M. Vojenčiak, J. Šouc, J. M. Ceballos, F. Gömöry, B. Klinčok, E. Pardo, and F. Grilli, "Study of ac loss in bi-2223/ag tape under the simultaneous action of ac transport current and ac magnetic field shifted in phase," *Superconductor Science and Technology*, vol. 19, no. 4, p. 397, 2006.

[85] R. Inada, K. Tateyama, Y. Nakamura, A. Oota, C. Li, and P. Zhang, "Total ac loss of ag-sheathed bi2223 tapes with various filament arrangements carrying ac transport current in ac parallel transverse magnetic field," *Superconductor Science and Technology*, vol. 20, no. 3, p. 138, 2007.

[86] Z. Jiang, N. Amemiya, N. Ayai, and K. Hayashi, "Total ac loss characteristics of untwisted and twisted bi-2223 multifilamentary tapes and interaction between self and external magnetic fields," *Superconductor Science and Technology*, vol. 17, no. 11, p. 1311, 2004.

[87] J. J. Rabbers, B. ten Haken, and H. H. J. ten Kate, "Advanced ac loss measurement methods for high-temperature superconducting tapes," *Review of Scientific Instruments*, vol. 72, no. 5, pp. 2365–2373, 2001.

[88] M. Ashkin, "Flux distribution and hysteresis loss in a round superconducting wire for the complete range of flux penetration," *Journal of Applied Physics*, vol. 50, no. 11, pp. 7060–7066, 1979.

[89] M. Ashkin and G. R. Wagner, "Comparison of calculated and measured hysteresis loss in multifilamentary superconducting wire," *Journal of Applied Physics*, vol. 60, no. 7, pp. 2477–2481, 1986.

[90] F. Gömöry, R. Tebano, A. Sanchez, E. Pardo, C. Navau, I. Husek, F. Strycek, and P. Kovac, "Current profiles and ac losses of a superconducting strip with an elliptic cross-section in a perpendicular magnetic field," *Superconductor Science and Technology*, vol. 15, no. 9, p. 1311, 2002.

[91] A. Badía and C. López, "Vector magnetic hysteresis of hard superconductors," *Phys. Rev. B*, vol. 65, p. 104514, Feb 2002.

[92] P. N. Barnes, G. L. Rhoads, J. C. Tolliver, M. D. Sumption, and K. W. Schmaeman, "Compact, lightweight, superconducting power generators," in *2004 12th Symposium on Electromagnetic Launch Technology*, pp. 158–163, May 2004.

[93] J. Gieras, "Superconducting electrical machines state of the art," vol. 85, pp. 1–19, 12 2009.

[94] S. S. Kalsi, *Applications of High Temperature Superconductors to Electric Power Equipment*. Wiley-IEEE Press, 2011.

[95] G. D. Marzi, L. Muzzi, and P. Lee, *Superconducting Wires and Cables: Materials and Processing*. Elsevier, 2016.

[96] B. Shen, C. Li, J. Geng, X. Zhang, J. Gawith, J. Ma, Y. Liu, F. Grilli, and T. A. Coombs, "Power dissipation in hts coated conductor coils under the simultaneous action of ac and dc currents and fields," *Superconductor Science and Technology*, vol. 31, no. 7, p. 075005, 2018.

[97] X. Zhang, H. S. Ruiz, J. Geng, B. Shen, L. Fu, H. Zhang, and T. A. Coombs, "Power flow analysis and optimal locations of resistive type superconducting fault current limiters," *SpringerPlus*, vol. 5, p. 1972, Nov 2016.

[98] S. Yan, L. Ren, Y. Zhang, K. Zhu, R. Su, Y. Xu, Y. Tang, J. Shi, and J. Li, "Ac loss analysis of a flux-coupling type superconducting fault current limiter," *IEEE Transactions on Applied Superconductivity*, vol. 29, pp. 1–5, Aug 2019.

[99] X. Zhang, H. Ruiz, J. Geng, and T. Coombs, "Optimal location and minimum number of superconducting fault current limiters for the protection of power grids," *International Journal of Electrical Power & Energy Systems*, vol. 87, pp. 136 – 143, 2017.

[100] H. S. Ruiz, X. Zhang, and T. A. Coombs, "Resistive-type superconducting fault current limiters: Concepts, materials, and numerical modeling," *IEEE Transactions on Applied Superconductivity*, vol. 25, p. 5601405, June 2015.

[101] G. Nam, H. Sung, B. Go, M. Park, and I. Yu, "Design and comparative analysis of mgb2 and ybco wire-based-superconducting wind power generators," *IEEE Transactions on Applied Superconductivity*, vol. 28, pp. 1–5, April 2018.

[102] Z. Zhong, M. Chudy, H. Ruiz, X. Zhang, and T. Coombs, "Critical current studies of a hts rectangular coil," *Physica C: Superconductivity and its Applications*, vol. 536, pp. 18 – 25, 2017.

[103] A. Kim, K. Kim, H. Park, G. Kim, T. Park, M. Park, S. Kim, S. Lee, H. Ha, S. Yoon, and H. Lee, "Performance analysis of a 10-kw superconducting synchronous generator," *IEEE Transactions on Applied Superconductivity*, vol. 25, pp. 1–4, June 2015.

[104] Z. Huang, H. S. Ruiz, W. Wang, Z. Jin, and T. A. Coombs, "Hts motor performance evaluation by different pulsed field magnetization strategies," *IEEE Transactions on Applied Superconductivity*, vol. 27, pp. 1–5, June 2017.

[105] Z. Huang, H. S. Ruiz, Y. Zhai, J. Geng, B. Shen, and T. A. Coombs, "Study of the pulsed field magnetization strategy for the superconducting rotor," *IEEE Transactions on Applied Superconductivity*, vol. 26, pp. 1–5, June 2016.

[106] M. Baghdadi, H. S. Ruiz, J. F. Fagnard, M. Zhang, W. Wang, and T. A. Coombs, "Investigation of demagnetization in hts stacked tapes implemented in electric machines as a result of crossed magnetic field," *IEEE Transactions on Applied Superconductivity*, vol. 25, pp. 1–4, June 2015.

[107] D. Uglietti, S. Choi, and T. Kiyoshi, "Design and fabrication of layer-wound ybco solenoids," *Physica C: Superconductivity and its Applications*, vol. 470, no. 20, pp. 1749 – 1751, 2010. Proceedings of the 22nd International Symposium on Superconductivity (ISS 2009).

[108] M. Baghdadi, H. S. Ruiz, and T. A. Coombs, "Nature of the low magnetization decay on stacks of second generation superconducting tapes under crossed and rotating magnetic field experiments," *Scientific Reports*, vol. 8, no. 1, p. 1342, 2018.

[109] M. Baghdadi, H. S. Ruiz, and T. A. Coombs, "Crossed-magnetic-field experiments on stacked second generation superconducting tapes: Reduction of the demagnetization effects," *Applied Physics Letters*, vol. 104, no. 23, p. 232602, 2014.

[110] J. Zhu, P. Chen, M. Qiu, C. Liu, J. Liu, H. Zhang, H. Zhang, and K. Ding, "Experimental investigation of a high temperature superconducting pancake consisted of the rebco composite cable for superconducting magnetic energy storage system," *IEEE Transactions on Applied Superconductivity*, vol. 29, pp. 1–4, Aug 2019.

[111] A. V. Pan, L. MacDonald, H. Baiej, and P. Cooper, "Theoretical consideration of superconducting coils for compact superconducting magnetic energy storage systems," *IEEE Transactions on Applied Superconductivity*, vol. 26, pp. 1–5, April 2016.

[112] G. Messina, L. Morici, G. Celentano, M. Marchetti, and A. D. Corte, "Rebco coils system for axial flux electrical machines application: Manufacturing and testing," *IEEE Transactions on Applied Superconductivity*, vol. 26, p. 5205904, April 2016.

[113] E. Moser, E. Laistler, F. Schmitt, and G. Kontaxis, "Ultra-high field nmr and mri-the role of magnet technology to increase sensitivity and specificity," *Frontiers in Physics*, vol. 5, p. 33, 2017.

[114] S. Noguchi and V. Cingoski, "Simulation of screening current reduction effect in rebco coils by external ac magnetic field," *IEEE Transactions on Applied Superconductivity*, vol. 27, no. 4, pp. 1–5, 2017.

[115] M. Polak, E. Demencik, L. Jansak, P. Mozola, D. Aized, C. L. H. Thieme, G. A. Levin, and P. N. Barnes, "ac losses in a yba2cu3o7-x coil," *Applied Physics Letters*, vol. 88, no. 23, p. 232501, 2006.

[116] V. M. R. Zermeno, A. B. Abrahamsen, N. Mijatovic, B. B. Jensen, and M. P. Sørensen, "Calculation of alternating current losses in stacks and coils made of second generation high temperature superconducting tapes for large scale applications," *Journal of Applied Physics*, vol. 114, no. 17, p. 173901, 2013.

[117] M. D. Ainslie, D. Hu, J. Zou, and D. A. Cardwell, "Simulating the in-field ac and dc performance of high-temperature superconducting coils," *IEEE Transactions on Applied Superconductivity*, vol. 25, pp. 1–5, June 2015.

[118] M. Zhang, J. Kvitkovic, J.-H. Kim, C. H. Kim, S. V. Pamidi, and T. A. Coombs, "Alternating current loss of second-generation high-temperature superconducting coils with magnetic and non-magnetic substrate," *Applied Physics Letters*, vol. 101, no. 10, p. 102602, 2012.

[119] E. Pardo, "Modeling of coated conductor pancake coils with a large number of turns," *Superconductor Science and Technology*, vol. 21, no. 6, p. 065014, 2008.

[120] J. R. Clem, J. H. Claassen, and Y. Mawatari, "Ac losses in a finite z stack using an anisotropic homogeneous-medium approximation," *Superconductor Science and Technology*, vol. 20, no. 12, p. 1130, 2007.

[121] F. Grilli and S. P. Ashworth, "Measuring transport AC losses in YBCO-coated conductor coils," *Superconductor Science and Technology*, vol. 20, pp. 794–799, jun 2007.

[122] E. Pardo, J. Šouc, and J. Kováč, "Ac loss in rebco pancake coils and stacks of them: modelling and measurement," *Superconductor Science and Technology*, vol. 25, no. 3, p. 035003, 2012.

[123] W. Yuan, T. A. Coombs, J.-H. Kim, C. Han Kim, J. Kvitkovic, and S. Pamidi, "Measurements and calculations of transport ac loss in second generation high temperature superconducting pancake coils," *Journal of Applied Physics*, vol. 110, no. 11, p. 113906, 2011.

[124] E. Pardo, J. Souc, M. Vojenciak, and F. Gomory, "Ac loss and voltage signal in a pancake coil made of coated conductor with ferromagnetic substrate," *IEEE Transactions on Applied Superconductivity*, vol. 19, pp. 2223–2227, June 2009.

[125] M. D. Ainslie, V. M. Rodriguez-Zermeno, Z. Hong, W. Yuan, T. J. Flack, and T. A. Coombs, "An improved FEM model for computing transport AC loss in coils made of RABiTS YBCO coated conductors for electric machines," *Superconductor Science and Technology*, vol. 24, p. 045005, jan 2011.

[126] M. Zhang, J. Kvitkovic, S. V. Pamidi, and T. A. Coombs, "Experimental and numerical study of a ybco pancake coil with a magnetic substrate," *Superconductor Science and Technology*, vol. 25, no. 12, p. 125020, 2012.

[127] E. Pardo and F. Grilli, "Numerical simulations of the angular dependence of magnetization ac losses: coated conductors, roebel cables and double pancake coils," *Superconductor Science and Technology*, vol. 25, no. 1, p. 014008, 2012.

[128] F. G. R. Martins, F. Sass, P. Barusco, A. C. Ferreira, and R. de Andrade, "Using the integral equations method to model a 2g racetrack coil with anisotropic critical current dependence," *Superconductor Science and Technology*, vol. 30, p. 115009, oct 2017.

[129] E. Pardo, J. Kováč, and J. Šouc, "Power loss in rebco racetrack coils under ac applied magnetic field and dc current," *IEEE Transactions on Applied Superconductivity*, vol. 23, pp. 4701305–4701305, June 2013.

[130] Z. Hong, W. Yuan, M. Ainslie, Y. Yan, R. Pei, and T. A. Coombs, "Ac losses of superconducting racetrack coil in various magnetic conditions," *IEEE Transactions on Applied Superconductivity*, vol. 21, pp. 2466–2469, June 2011.

[131] D. Swaffield, C. Lewis, J. Eugene, M. Ingles, and D. Peach, "Testing of machine wound second generation hts tape vacuum pressure impregnated coils," *Journal of Physics: Conference Series*, vol. 507, no. 3, p. 032046, 2014.

[132] F. Gömöry, J. Šouc, E. Pardo, E. Seiler, M. Soloviov, L. Frolek, M. Skarba, P. Konopka, M. Pekarcíková, and J. Janovec, "Ac loss in pancake coil made from 12 mm wide rebco tape," *IEEE Transactions on Applied Superconductivity*, vol. 23, p. 5900406, June 2013.

[133] M. Zhang, J.-H. Kim, S. Pamidi, M. Chudy, W. Yuan, and T. A. Coombs, "Study of second generation, high-temperature superconducting coils: Determination of critical current," *Journal of Applied Physics*, vol. 111, no. 8, p. 083902, 2012.

[134] Superpower, "http://www.superpower-inc.com."

[135] Z. Hong, A. M. Campbell, and T. A. Coombs, "Numerical solution of critical state in superconductivity by finite element software," *Superconductor Science and Technology*, vol. 19, no. 12, p. 1246, 2006.

[136] W. Yuan, A. M. Campbell, and T. A. Coombs, "A model for calculating the ac losses of second-generation high temperature superconductor pancake coils," *Superconductor Science and Technology*, vol. 22, no. 7, p. 075028, 2009.

[137] A. Badía-Majós, C. López, and H. S. Ruiz, "General critical states in type-II superconductors," *Phys. Rev. B*, vol. 80, p. 144509, Oct 2009.

[138] L. Prigozhin and V. Sokolovsky, "Computing ac losses in stacks of high-temperature superconducting tapes," *Superconductor Science and Technology*, vol. 24, no. 7, p. 075012, 2011.

[139] F. G. R. Martins, F. Sass, P. Barusco, A. C. Ferreira, and R. de Andrade, "Using the integral equations method to model a 2g racetrack coil with anisotropic critical current dependence," *Superconductor Science and Technology*, vol. 30, p. 115009, oct 2017.

[140] J. Geng, H. Zhang, C. Li, X. Zhang, B. Shen, and T. A. Coombs, "Angular dependence of direct current decay in a closed YBCO double-pancake coil under external AC magnetic field and reduction by magnetic shielding," *Superconductor Science and Technology*, vol. 30, p. 035022, feb 2017.

[141] X. Zhang, Z. Zhong, H. S. Ruiz, J. Geng, and T. A. Coombs, "General approach for the determination of the magneto-angular dependence of the critical current of ybco coated conductors," *Superconductor Science and Technology*, vol. 30, no. 2, p. 025010, 2017.

[142] S. C. Wimbush and N. M. Strickland, "A public database of high-temperature superconductor critical current data," *IEEE Transactions on Applied Superconductivity*, vol. 27, pp. 1–5, June 2017.

[143] A. Badía-Majós and C. López, "Modelling current voltage characteristics of practical superconductors," *Superconductor Science and Technology*, vol. 28, no. 2, p. 024003, 2015.

[144] F. Sirois and F. Grilli, "Potential and limits of numerical modelling for supporting the development of hts devices," *Superconductor Science and Technology*, vol. 28, no. 4, p. 043002, 2015.

[145] B. C. Robert, M. U. Fareed, and H. S. Ruiz, "Local electromagnetic properties and hysteresis losses in uniformly and non-uniformly wound superconducting racetrack coils," *Journal of Applied Physics*, vol. 126, no. 12, p. 123902, 2019.

[146] L. Quéval, V. M. R. Zermeño, and F. Grilli, "Numerical models for ac loss calculation in large-scale applications of HTS coated conductors," *Superconductor Science and Technology*, vol. 29, p. 024007, jan 2016.

[147] H. Zhang, M. Zhang, and W. Yuan, "An efficient 3d finite element method model based on the t-a formulation for superconducting coated conductors," *Superconductor Science and Technology*, vol. 30, 2 2017.

[148] F. Liang, S. Venuturumilli, H. Zhang, M. Zhang, J. Kvitkovic, S. Pamidi, Y. Wang, and W. Yuan, "A finite element model for simulating second generation high temperature superconducting coils/stacks with large number of turns," *Journal of Applied Physics*, vol. 122, no. 4, p. 043903, 2017.

[149] E. Pardo, "Calculation of AC loss in coated conductor coils with a large number of turns," *Superconductor Science and Technology*, vol. 26, p. 105017, sep 2013.

[150] R. Brambilla, F. Grilli, D. N. Nguyen, L. Martini, and F. Sirois, "AC losses in thin superconductors: the integral equation method applied to stacks and windings," *Superconductor Science and Technology*, vol. 22, p. 075018, jun 2009.

[151] Y. Ichiki and H. Ohsaki, "Numerical analysis of ac loss characteristics of ybco coated conductors arranged in parallel," *IEEE Transactions on Applied Superconductivity*, vol. 15, pp. 2851–2854, June 2005.

[152] G. Blatter, M. V. Feigel'man, V. B. Geshkenbein, A. I. Larkin, and V. M. Vinokur, "Vortices in high-temperature superconductors," *Rev. Mod. Phys.*, vol. 66, pp. 1125–1388, Oct 1994.

[153] K. Higashikawa, T. Nakamura, and T. Hoshino, "Anisotropic distributions of current density and electric field in bi-2223/ag coil with consideration of multifilamentary structure," *Physica C: Superconductivity and its Applications*, vol. 419, no. 3, pp. 129 – 140, 2005.

[154] N. Amemiya, S. Murasawa, N. Banno, and K. Miyamoto, "Numerical modelings of superconducting wires for ac loss calculations," *Physica C: Superconductivity*, vol. 310, no. 1, pp. 16 – 29, 1998.

[155] R. Brambilla, F. Grilli, and L. Martini, "Development of an edge-element model for ac loss computation of high-temperature superconductors," *Superconductor Science and Technology*, vol. 20, no. 1, p. 16, 2007.

[156] N. Enomoto, T. Izumi, and N. Amemiya, "Electromagnetic field analysis of rectangular superconductor with large aspect ratio in arbitrary orientated magnetic fields," *IEEE Transactions on Applied Superconductivity*, vol. 15, pp. 1574–1577, June 2005.

[157] S. Rao, *The Finite Element Method in Engineering*. Oxford : Pergamon Press, 1989.

[158] G. Mur, "Edge elements, their advantages and their disadvantages," *IEEE Transactions on Magnetics*, vol. 30, no. 5, pp. 3552–3557, 1994.

[159] Y. M. Desai, T. I. Eldho, and A. H. Shah, *Finite Element Method with Applications in Engineering*. Pearson: Dorling Kindersley (India) Pvt. Ltd, 2011.

[160] J. Jin, *The Finite Element Method in Electromagnetics*. Wiley - IEEE, Wiley, 2015.

[161] G. W. Bowden and M. J. Hole, "A singular finite element technique for calculating continuum damping of alfvén eigenmodes," *Physics of Plasmas*, vol. 22, no. 2, p. 022116, 2015.

[162] S. Stavrev, F. Grilli, B. Dutoit, and S. P. Ashworth, "Comparison of the AC losses of BSCCO and YBCO conductors by means of numerical analysis," *Superconductor Science and Technology*, vol. 18, pp. 1300–1312, aug 2005.

[163] O. Biró, "Edge element formulations of eddy current problems," *Computer Methods in Applied Mechanics and Engineering*, vol. 169, no. 3, pp. 391 – 405, 1999.

[164] COMSOLMultiphysics, "http://www.comsol.com," 2018.

[165] R. Pecher, "3d-modelling of bulk type ii superconductors using unconstrained h-formulation," *Proc. 6th EUCAS, Sorrento, Italy, 2003*, 2003.

[166] K. Kajikawa, T. Hayashi, R. Yoshida, M. Iwakuma, and K. Funaki, "Numerical evaluation of ac losses in hts wires with 2d fem formulated by self magnetic field," *IEEE Transactions on Applied Superconductivity*, vol. 13, pp. 3630–3633, June 2003.

[167] F. Grilli, S. Ashworth, and S. Stavrev, "Magnetization ac losses of stacks of ybco coated conductors," *Physica C: Superconductivity*, vol. 434, no. 2, pp. 185 – 190, 2006.

[168] H. Song, P. Brownsey, Y. Zhang, J. Waterman, T. Fukushima, and D. Hazelton, "2g hts coil technology development at superpower," *IEEE Transactions on Applied Superconductivity*, vol. 23, no. 3, pp. 4600806–4600806, 2013.

[169] L. Quéval, V. M. R. Zermeño, and F. Grilli, "Numerical models for ac loss calculation in large-scale applications of HTS coated conductors," *Superconductor Science and Technology*, vol. 29, p. 024007, jan 2016.

[170] M. Zhang, J. Kvitkovic, S. V. Pamidi, and T. A. Coombs, "Experimental and numerical study of a ybco pancake coil with a magnetic substrate," *Superconductor Science and Technology*, vol. 25, no. 12, p. 125020, 2012.

[171] Y. B. Kim, C. F. Hempstead, and A. R. Strnad, "Critical persistent currents in hard superconductors," *Phys. Rev. Lett.*, vol. 9, pp. 306–309, Oct 1962.

[172] X. Zhang, Z. Zhong, J. Geng, B. Shen, J. Ma, C. Li, H. Zhang, Q. Dong, and T. A. Coombs, "Study of critical current and n-values of 2g hts tapes:

Their magnetic field-angular dependence," *Journal of Superconductivity and Novel Magnetism*, vol. 31, no. 12, pp. 3847–3854, 2018.

[173] F. Grilli, R. Brambilla, and L. Martini, "Modeling high-temperature superconducting tapes by means of edge finite elements," *IEEE Transactions on Applied Superconductivity*, vol. 17, no. 2, pp. 3155–3158, 2007.

[174] M. Ainslie, Y. Jiang, W. Xian, Z. Hong, W. Yuan, R. Pei, T. Flack, and T. Coombs, "Numerical analysis and finite element modelling of an hts synchronous motor," *Physica C: Superconductivity and its Applications*, vol. 470, no. 20, pp. 1752 – 1755, 2010. Proceedings of the 22nd International Symposium on Superconductivity (ISS 2009).

[175] Y. Duan, W. Ta, and Y. Gao, "Numerical models of delamination behavior in 2g hts tapes under transverse tension and peel," *Physica C: Superconductivity and its Applications*, vol. 545, pp. 26 – 37, 2018.

[176] D. C. van der Laan, J. W. Ekin, C. C. Clickner, and T. C. Stauffer, "Delamination strength of YBCO coated conductors under transverse tensile stress," *Superconductor Science and Technology*, vol. 20, pp. 765–770, jun 2007.

[177] X. Zhang, W. Liu, J. Zhou, and Y.-H. Zhou, "A device to investigate the delamination strength in laminates at room and cryogenic temperature," *Review of Scientific Instruments*, vol. 85, no. 12, p. 125115, 2014.

[178] L. Liu, Y. Zhu, X. Yang, T. Qiu, and Y. Zhao, "Delamination properties of ybco tapes under shear stress along the width direction," *IEEE Transactions on Applied Superconductivity*, vol. 26, pp. 1–6, Sept 2016.

[179] Y. Zhang, Y. Song, L. Wang, and X. Liu, "Simulation of superconducting tapes and coils with convex quadratic programming method," *Superconductor Science and Technology*, vol. 28, no. 8, p. 085002, 2015.

[180] W. Yuan, A. M. Campbell, Z. Hong, M. D. Ainslie, and T. A. Coombs, "Comparison of ac losses, magnetic field/current distributions and critical currents of superconducting circular pancake coils and infinitely long stacks using coated conductors," *Superconductor Science and Technology*, vol. 23, no. 8, p. 085011, 2010.

[181] E. H. Brandt, "Superconductors of finite thickness in a perpendicular magnetic field: Strips and slabs," *Phys. Rev. B*, vol. 54, pp. 4246–4264, Aug 1996.

[182] H. S. Ruiz, A. Badía-Majós, Y. A. Genenko, H. Rauh, and S. V. Yampolskii, "Superconducting wire subject to synchronous oscillating excitations: Power dissipation, magnetic response, and low-pass filtering," *Applied Physics Letters*, vol. 100, no. 11, p. 112602, 2012.

[183] V. M. Rodriguez-Zermeno, N. Mijatovic, C. Traeholt, T. Zirngibl, E. Seiler, A. B. Abrahamsen, N. F. Pedersen, and M. P. Sorensen, "Towards faster fem simulation of thin film superconductors: A multiscale approach," *IEEE Transactions on Applied Superconductivity*, vol. 21, pp. 3273–3276, June 2011.

[184] A. Badía-Majós and C. López, "Critical-state analysis of orthogonal flux interactions in pinned superconductors," *Physical Review B*, vol. 76, no. 5, p. 054504, 2007.

[185] H. S. Ruiz, A. Badía-Majós, Y. A. Genenko, and S. V. Yampolskii, "Strong localization of the density of power losses in type-II superconducting wires," *IEEE Transactions on Applied Superconductivity*, vol. 23, pp. 8000404–8000404, June 2013.

[186] P. W. Anderson, "Theory of flux creep in hard superconductors," *Phys. Rev. Lett.*, vol. 9, pp. 309–311, Oct 1962.

[187] Y. B. Kim, C. F. Hempstead, and A. R. Strnad, "Resistive states of hard superconductors," *Rev. Mod. Phys.*, vol. 36, pp. 43–45, Jan 1964.

[188] H. S. Ruiz and A. Badía-Majós, "Nature of the nodal kink in angle-resolved photoemission spectra of cuprate superconductors," *Phys. Rev. B*, vol. 79, p. 054528, Feb 2009.

[189] G. Apollinari, S. Prestemon, and A. V. Zlobin, "Progress with high-field superconducting magnets for high-energy colliders," *Annual Review of Nuclear and Particle Science*, vol. 65, no. 1, pp. 355–377, 2015.

[190] F. Gömöry, J. Šouc, E. Pardo, E. Seiler, M. Soloviov, L. Frolek, M. Skarba, P. Konopka, M. Pekarcíková, and J. Janovec, "Ac loss in pancake coil made from 12 mm wide rebco tape," *IEEE Transactions on Applied Superconductivity*, vol. 23, pp. 5900406–5900406, June 2013.

[191] B. C. Robert, M. U. Fareed, and H. S. Ruiz, "Flux front dynamics and energy losses of magnetically anisotropic 2g-HTS pancake coils under prospective winding deformations," *Engineering Research Express*, vol. 1, p. 015037, sep 2019.

[192] S. C. Wimbush and N. M. Strickland, "A public database of high-temperature superconductor critical current data," *IEEE Transactions on Applied Superconductivity*, vol. 27, pp. 1–5, June 2017.

[193] C. P. Bean, "Magnetization of hard superconductors," *Phys. Rev. Lett.*, vol. 8, pp. 250–253, Mar 1962.

[194] K. P. Thakur, A. Raj, E. H. Brandt, J. Kvitkovic, and S. V. Pamidi, "Frequency-dependent critical current and transport ac loss of superconductor strip and roebel cable," *Superconductor Science and Technology*, vol. 24, p. 065024, apr 2011.

[195] "American superconductor, amsc amperium ®hts wire. technical information available at." `www.amsc.com/solutions-products/hts_wire.html`.

[196] "Shangai superconductor technology co. ltd. 2g hts strip. technical information available at." `www.amsc.com/solutions-products/hts_wire.html`.

[197] "Superox 2g hts wire. technical information available at." `http://www.superox.ru/en/products/`.

[198] M. Baziljevich, T. H. Johansen, H. Bratsberg, Y. Shen, and P. Vase, "Magneto-optic observation of anomalous meissner current flow in superconducting thin films with slits," *Applied Physics Letters*, vol. 69, no. 23, pp. 3590–3592, 1996.

[199] C. Jooss, K. Guth, V. Born, and J. Albrecht, "Electric field distribution at low-angle grain boundaries in high-temperature superconductors," *Phys. Rev. B*, vol. 65, p. 014505, Nov 2001.

[200] C. Jooss, J. Albrecht, H. Kuhn, S. Leonhardt, and H. Kronmüller, "Magneto-optical studies of current distributions in high-tc superconductors," *Reports on Progress in Physics*, vol. 65, pp. 651–788, apr 2002.

[201] F. S. Wells, A. V. Pan, I. A. Golovchanskiy, S. A. Fedoseev, and A. Rozenfeld, "Observation of transient overcritical currents in ybco thin films using high-speed magneto-optical imaging and dynamic current mapping," *Scientific Reports*, vol. 7, p. 40235, 2017.

[202] H. S. Ruiz, A. Badía-Majós, and C. López, "Material laws and related uncommon phenomena in the electromagnetic response of type-II superconductors in longitudinal geometry," *Superconductor Science and Technology*, vol. 24, no. 11, p. 115005, 2011.

[203] H. S. Ruiz, C. López, and A. Badía-Majós, "Inversion mechanism for the transport current in type-II superconductors," *Phys. Rev. B*, vol. 83, p. 014506, Jan 2011.

[204] H. S. Ruiz and A. Badía-Majós, "Exotic magnetic response of superconducting wires subject to synchronous and asynchronous oscillating excitations," *Journal of Applied Physics*, vol. 113, no. 19, p. 193906, 2013.

[205] J. Šouc, E. Pardo, M. Vojenčiak, and F. Gömöry, "Theoretical and experimental study of ac loss in high temperature superconductor single pancake coils," *Superconductor Science and Technology*, vol. 22, no. 1, p. 015006, 2009.

APPENDIX

Glossary

In order to provide an easiest reading of this report, below we introduce a list of the most used abbreviations in text. Greek symbols are either incorporated by their phonetic translation into Latin.

- **A**

  A. Magnetic vector potential.

  AC. Alternate Current.

- **B**

  B. Magnetic induction field (Bold-facing means vector).

  $B_{\mathtt{a}}$. Peak amplitude for the AC excitation B_0.

  B_0. Applied magnetic flux density.

  B_p. Penetration field.

  B_{ind}. Self (induced) magnetic flux density.

  Bi2212. $Bi_2Sr_2CaCu_2O_{8+x}$.

  Bi2201. $Bi_2Sr_{1.65}La_{0.35}CuO_{6+x}$.

  Bi-2221. $(Bi,Pb)_2Sr_2Ca_2Cu_3O_x$

- **C**

  CS. Critical state.

- **D**

  Δ. Variation (increment) of ...

  $\Delta_{\mathbf{r}}$. Material law for the critical state problems.

  DC. Direct current.

  DCSM. Double critical state model.

- **E**

  E. Induced transient electric field (In bold means vector).

  E_c. Critical electrical field.

  Eq(s). Equation(s).

- **F**

  $\mathcal{F}$. Minimization functional or so-called Objective function.

  FEM. Finite Element Methods

  Fig(s). Figure(s)

  FC. Field cooling

- **H**

  H. Magnetic field (In bold means vector).

  H_a. Components of magnetic field applied.

  HTSC. High-temperature superconductor.

- **I**

  $I_{\mathtt{a}}$. Peak amplitude for the AC excitation I_{tr}.

  I_c. Critical current.

  I_{tr}. Transport current.

- **J**

  J. Electrical current density (In bold means vector).

  J_c. Critical current density.

- **L**

  $\mathcal{L}$. Lagrange density.

  L. Hysteretic AC loss.

  LANCELOT. A FORTRAN package for large-scale nonlinear optimization.

  LSCO. $La_{2-x}Sr_xCuO_4$.

- **M**

  μ_0. Permeability of the free space.

  μ_r. Relative permeability associated to a ferromagnetic. material.

  M. Magnetization (In bold means vector).

  M_{ij}. Mutual/Self inductance matrix.

  MRI. Magnetic resonance imaging.

- **N**

  n. Smoothing index in a power law, or a defined time step

- **O**

  ω. Electromagnetic oscillating frequency.

  Ω. Superconducting volume.

- **P**

  Φ. Electric scalar potential.

  p. Lagrange multiplier.

  PDE. Partial Differential Equation.

  Pag(s). Page(s).

- **R**

  R. Radius of the cylinder.

  $REBCO$. Rare-Earth Barium-Copper-Oxide

- **S**

  SC. Superconductor or Superconducting.

  SFCL. Superconducting fault current limiters.

  2G-HTS. Second Generation of High Temperature Superconductor/Superconducting.

  SIF. Standard Input Format.

  SC-II. Type-II Superconductor.

  SC-I. Type-I Superconductor.

- **T**

  T_c. Superconducting critical temperature.

  T. Temperature.

  2D. Two Dimensional.

- **Y**

  YBCO or Y123. $YBa_2Cu_3O_{6+x}$.

- **Z**

  ZFC. Zero field cooling.

Publications

6 first author peer reviewed journal publications + 1 second author publication:

1. **B.C. Robert**, M.U. Fareed, and H.S. Ruiz. How to Choose the Superconducting Material Law for the Modelling of 2G-HTS Coils. **Materials** 2019, 12, 2679.

2. **B.C. Robert**, M.U. Fareed, and H.S. Ruiz. Local electromagnetic properties and hysteresis losses in uniformly and Non-Uniformly wound Superconducting Racetrack Coils. **Journal of Applied Physics** 2019, 126, 123902.

3. **B.C. Robert**, M.U. Fareed, and H.S. Ruiz. Flux front dynamics and energy losses of magnetically anisotropic 2G-HTS pancake coils under prospective winding deformations. **IOP Engineering Research Express** 2019, 1,015037.

4. M. U. Fareed, **B. C. Robert**, and H. S. Ruiz. Electric Field and Energy Losses of Rounded Superconducting/Ferromagnetic Heterostructures at Self-Field Conditions. **IEEE Transactions on Applied Superconductivity** 2019, 29, 1-5.

5. **B. C. Robert** and H.S. Ruiz. Magnetic characteristics and AC losses of DC type-II superconductors under oscillating magnetic field. **Superconductor Science & Technology** 2018, 31, 035006.

6. **B. C. Robert** and H. S. Ruiz. Electromagnetic response of DC type-II SC wires under oscillating magnetic excitations. **IEEE Transactions on Applied Superconductivity** 2018, 28, 1-5.

7. **B. C. Robert** and H. S. Ruiz. Magnetization profiles of AC type-II superconducting wires exposed to DC magnetic fields. **IEEE Transactions on Applied Superconductivity** 2018, 28, 1-5.

Conference Proceedings and Workshops

Some of the published results where presented in following conferences:

1. The Solar future, Lagos, Nigeria 'Powerful collaboration, Energy innovations -All on and United States African development foundation.' Dec 2019.

2. European Conference on Applied Superconductivity, EUCAS 2019, SEC Centre, Glasgow; **Poster Presentation** 'Impact of material law selection for 2H-HTS coils' Sept 2019.

3. Applied Superconductivity Conference, ASC 2018, Washington state convention centre, Seattle USA; **Oral presentation** 'AC Losses for non-uniform wound 2G-HTS racetrack coils' Oct 2018.

4. 13th Biennial European Conference on Applied Superconductivity, CERN - Geneva, Switzerland; **Poster presentation** 'Electromagnetic Response of DC type-II SC under AC magnetic field' Sept 2017 .

Likewise, the workshops attended that contributed to the content of this thesis

1. Energy research accelerator (ERA) - UKs first cross-disciplinary energy innovation initiative-series of doctoral training- specially tailored events, workshops and joint conferences for the growth of ERA student community both within and across Institutions and Industrial partners. 2018-2019 .

2. 2nd International workshop on Cooling of High-Temperature Superconductor Applications, Karlsruhe, Germany. Sept 2017.